Visualising infections across scales

Calum Bentley-Abbot

A thesis submitted in fulfilment of the degree of

Doctor of Philosophy

MRC - Centre for Virus Research (CVR) - School of Infection and Immunity - College of Medical, Veterinary and Life Sciences (MVLS) - University of Glasgow

September 2025

Abstract

The ability to visualise biological structures and processes at the microscale has been instrumental in the development of modern medicine and the control of disease. In recent years, technological innovations have enabled imaging of large, mesoscale tissues, from organs to whole mammalian organisms. However, the development of these methods demonstrates the inherent weaknesses of imaging modalities designed to function at specific length scales. While modern microscale methods enable imaging at resolutions beyond the diffraction limit of light, resolving objects tens of nanometers apart, the field of view and working distance of these systems prevents analysis of mesoscale samples. Conversely, cutting-edge mesoscale imaging methods are capable of imaging whole mice, but lack the resolution of modern confocal microscopes. Holisic analyses are crucial in understanding biological processes and only by designing imaging pipelines capable of coupling high resolution microscopy with large sample mesoscopy can we develop a complete understanding of processes occurring within organisms. Influenza A virus (IAV) exemplifies the need for multiscale imaging approaches. Viral replication is governed by microscale, intracellular processes, while pathology and spread on the scale of the whole lung dictates virus transmission and patient outcomes. Here, I develop methods for imaging tissues across length scales, primarily using IAV as a model pathogen. On the mesoscale, I develop means of visualising infections in whole murine lungs, as well as skin, nerve, and bone tissue without the need for sectioning. On the microscale, I develop computational tools and laboratory assays capable of visualising interactions between viruses, elucidating the processes governing the emergence of viral strains with pandemic potential. By designing

holistic imaging pipelines capable of analysing IAV infections across scales, these insights develop a more complete understanding of the spatial context of IAV infection, the interactions between viral populations, and the relationship between microscale processes and meso- and macroscale pathology.

Table of Contents

List of Tables

List of Figures

Acknowledgements

I would firstly like to thank my PhD supervisor, Ed, your willingness to talk a physicist through basic biology has been instrumental to my growth as a researcher and your enthusiasm and support has been invaluable, thank you! The Hutchinson lab, past and present, are amazingly supportive people and have made even the most stressful lab days enjoyable. Thank you so much to Colin Loney for being both a friend and a mentor, and in large part inspiring my interest in pursuing a career in microscopy. Finally, thank you to my fellow PhD students at the Garscube campus for reminders that experiments will work eventually, and that there are more important things even if they don't.

Declaration

I declare that all work described here is my own, other than when explicit reference is made to the contributions of others. This work has not been submitted for any other degree at any institution.

Abbreviations

ALI Air Liquid Interface

ARRIVE Animal Research: Reporting of *In Vivo* Experiments

AU Airy Unit

BABB Benzyl Alcohol/Benzyl Benzoate

Breg Regulatory B-cell

BSA Bovine Serum Albumin

cDNA Complementary Deoxyribonucleic Acid

CPE Cytopathic Effect

CRUK Cancer Research United Kingdom - Scotland Institute

CSV Comma Separated Value file

CT Computed Tomography

CUBIC Clear, Unobstructed Brain/Body Imaging Cocktails

CVR MRC-University of Glasgow Centre for Virus Research

DAB 3,3'-Diaminobenzidine

DAPI 4',6-Diamidino-2-Phenylindole

DMEM Dulbecco's Modified Eagle Medium

DNA Deoxyribonucleic Acid

dpi Days Post Infection

dSTORM Direct Stochastic Optical Reconstruction Microscopy

ECi Ethyl Cinnamate

EDTA Ethylenediaminetetraacetic Acid

EtOH Ethanol

FBS Fetal Bovine Serum

FFPE Formalin Fixed Paraffin Embedded

FISH Fluorescent *In Situ* Hybridisation

FLIM Fluorescence Lifetime Imaging

GFP Green Fluorescent Protein

HA Haemagglutinin

IAV Influenza A virus

iDISCO Immunolabeling-enabled three-Dimensional Imaging of Solvent-Cleared Organs

IF Immunofluorescence

IgG Immunoglobulin G

IHC Immunohistochemistry

IP Intraperitoneal

IQR Interquartile Range

LiSM Light Sheet Microscopy

LSM Laser Scanning Microscope

MDCK Mardin-Darby Canine Kidney cells

MOI Multiplicity Of Infection

MRI Magnetic Resonance Imaging

mRNA Messenger Ribonucleic Acid

NA Neuraminidase

NP Nucleoprotein

NS Non-structural segment

NS1 Non-Structural protein 1

OCT Optimal Cutting Temperature compound

PALM Photoactivated Localisation Microscopy

PBA Phosphate Buffered Saline (PBS) treated with Bovine Serum Albumin (BSA)

PBS Phosphate Buffered Saline

PB2 Polymerase Basic protein 2

PCR Polymerase Chain Reaction

PET Positron Emission Tomography

PFA Paraformaldehyde

PFU Plaque Forming Units

PLP Periodate-Lysine-Paraformaldehyde

PR8 A/Puerto Rico/8/1934

PSF Point Spread Function

qPCR Quantitative Polymerase Chain Reaction

RI Refractive Index

RIN RNA Integrity Number

RLT Qiagen cell lysis buffer

ROI Region Of Interest

SIE Superinfection Exclusion

SMLM Single Molecule Localisation Microscopy

SNP Single Nucleotide Polymorphism

SPIM Selective Plane Illumination Microscopy

STED Stimulated Emission Depletion

T. b. brucei *Trypanosoma brucei brucei*

T. b. rhodesiense *Trypanosoma brucei rhodesiense*

T. b. gambiense *Trypanosoma brucei gambiense*

TPCK N-tosyl-L-phenylalanine chloromethyl ketone

ULI Unique Library Identifier

UV Ultraviolet

VGM Virus Growth Media

Publications

Publications arising from work presented in this thesis:

Bentley-Abbot C, Heslop R, Pirillo C *et al.* An easy to use tool for the analysis of subcellular mRNA transcript colocalisation in smFISH data. Sci Rep. 2024, 14, 8348, https://doi.org/10.1038/s41598-024-58641-3

Quintana J.F, Chandrasegaran P, Sinton M.C, Briggs E, Otto T.D, Heslop R, Bentley-Abbot C *et al.* Single cell and spatial transcriptomic analyses reveal microglia-plasma cell crosstalk in the brain during Trypanosoma brucei infection. Nat Commun. 2022, 13, 5752, https://doi.org/10.1038/s41467-022-33542-z

Publications arising from work not included in this thesis:

Weir D, Bentley-Abbot C, McCowan J, Loney C, Roberts E, Hutchinson E. Induction of tunnelling nanotube-like structures by influenza A viruses requires the onset of apoptosis. PLoS Pathog. 2025, 21(6): e1013191, https://doi.org/10.1371/journal.ppat.1013191

Work performed as part of Weir *et al.* (2025) builds upon the methods developed in **chapter 3**. Work performed as part of Bentley-Abbot *et al.* (2024) and Quintana *et al.* (2022) collectively form the basis for **chapter 4**.

Chapter 1

Introduction

1.1 Microscopy in medicine

The importance of imaging in modern medicine cannot be overstated. From simple procedures like x-rays experienced by the majority of people at some point, to cutting edge, high resolution microscopy approaches used in diagnostic and research environments. Improvements in technology have enabled higher resolution imaging, giving researchers the ability to visualise subcellular structures on the scale of tens of nanometers (Bates et al., 2008; Schmidt et al., 2008). Meanwhile, clinical applications of magnetic resonance imaging (MRI), positron emission tomography (PET), and computed tomography (CT) scans allow for high throughput diagnostic scanning of the whole human body (Grover et al., 2015; Trotter et al., 2023).

There is, of course, a significant size range between cells and the whole human body. Given that biological effects on the scale of organs or the whole body are inherently emergent properties of biological processes occurring on the microscale, ideally, it would be possible to image whole organs at microscale resolution, however, imaging modalities vary in resolution and field of view, varying their applicability at specific length scales. It is therefore useful in practice to differentiate phenomena based on the length scale across which they occur. This length scale, including everything from cell cultures, to tissue structures such as organoids, up

to whole organs, is becoming an increasingly common area of study in medical science and is typically referred to as the "mesoscale" (Tyson and Margrie, 2022). For the purposes of the work performed in this thesis, microscale will be used to describe events on the intercellular and subcellular level, mesoscale for studies of tissue-scale effects incorporating populations of numerous cells, such as infection dynamics in the airway epithelium for example. Macroscale will be used for everything beyond the scale of whole organs, for example, whole body systems such as the lymphatic system or systems incorporating numerous organs such as the respiratory tract (figure 1.1).

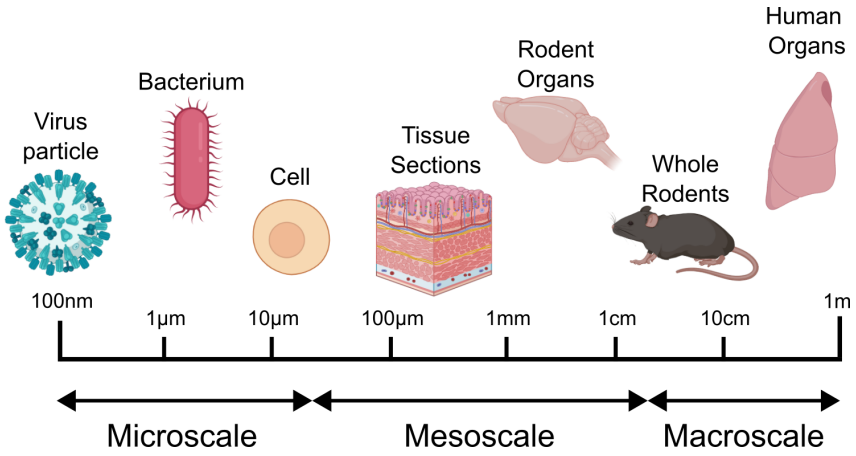

Figure 1.1: Comparison of scales of biological samples.

However, it is crucial to remember that macroscale and microscale phenomena are not distinct and that only through a holistic understanding of conditions can we fully understand the development and spread of diseases such as infectious conditions or cancers within the host. This thesis develops methods for visualising infections across length scales. I develop light sheet microscopy, fluorescence *in situ* hybridisation (FISH), and spatial transcriptomics methods to visualise infection from the meso- to the microscale. By validating these visualisation approaches for a range of infectious conditions, this body of work seeks to both highlight the importance of holistic imaging approaches in medicine, and to develop pipelines for conducting multi-scale imaging of disease.

1.1.1 The importance of imaging across scales

In order to understand the dynamics and pathology of infection it is crucial to understand that all infections are multi-length scale phenomena. The processes taking place on the microscale within and between cells ultimately shape behaviour on the macroscale of the whole body.

In parasitic diseases such as *Trypanosoma brucei* infection, the macroscale multi-stage lifecycle of the microscopic *T. brucei* parasite takes place across numerous tissues of the mammalian host (Matthews, 2005). Viral infections arguably function across an even wider length scale with intracellular mechanisms governing viral replication and evolution (Dou et al., 2018). While understanding these microscopic processes offer significant insights relevant to human health, for example the evolution of novel viral strains, it is often the macroscale effects of disease attract greater clinical interest and typically define the health outcomes for patients. These multi-scale effects are not limited to infectious disease, with the study of the tumour microenvironment in cancers proving highly informative in understanding the immunological factors resident in live tumours, potentially shaping future immunotherapy interventions (Moody et al., 2021). Meanwhile, metastasis occurring on the macroscale remains a primary clinical method for defining progression between stages in a cancer diagnosis. Furthermore, the growth (and shrinkage) of individual tumours on the mesoscale during immuno-, chemo- and radiotherapy is a common standard for determining efficacy of therapeutic interventions and progression from disease to remission.

Given the multi-scale nature of disease, it is unsurprising that we must be able to image pathogens and their effects across scales in order to gain meaningful insights into infection. Many systems have long existed for imaging at various scales, with x-rays first being used in clinical applications shortly after the discovery of their imaging potential in 1985 and use of light microscopy for microscale imaging beginning in the 1600s (Hooke, 1665; Van Leeuwenhoek, 1675). Despite the range of imaging methods available for imaging at scales from the entire human body to individual viral particles, coupling these methods to create a truly multi-

scale imaging method capable of imaging across scales remains difficult. This is primarily due to the inherent limitations of optical physics, meaning that optimising a system for imaging at a particular scale impacts on the capability of that system at other scales. However, in developmental biology this has been attempted, albeit not at the scale of the whole human body. Researchers have successfully imaged live zebrafish at subcellular resolution. Similarly, neurologists have successfully mapped *drisophila* brains at subcellular resolution. Through collaboration with developmental biologists, perhaps such techniques could be extended to larger samples on the scale of whole human organs.

1.1.2 Principles of optical physics

The electromagnetic spectrum comprises low energy radiowaves with wavelengths on the order of tens of meters to high energy gamma rays with wavelengths of picometers. Wavelength, λ, and energy, E, are related by the following formula:

$$E = \frac{hc}{\lambda} \tag{1.1}$$

Where h is Planck's constant, and c is the speed of light in a vacuum. As such, wavelength is inversely proportional to energy.

Visible light comprises electromagnetic waves of wavelength 380-700nm (Martynov et al., 2016). Optical microscopy predominantly functions in this range of the spectrum, with fluorescent dyes and illumination sources typically being designed in this range. However, markers which fluoresce in the ultraviolet and far red are becoming increasingly common (Martynov et al., 2016).

Because light propagates as a wave, it exhibits two interesting interactions crucial to microscopy, namely diffraction and interference. Light from a continuous illumination source comprises multiple photons. These photons travel as a wavefront consisting of multiple waves. When encountering an aperture, diffraction causes the wavefront to deform, propagating as a series of spherical waves (Young, 1802).

If we now imagine light encountering a pair of apertures, diffraction at each

aperture results in a pair of spherical wavefronts (figure 1.2). As these spherical wavefronts propagate they overlap and interact with one another, these interactions result in interference. Propagating waves have regions of high and low amplitude, if the high amplitude peaks of two interacting waves align, the waves are in phase and interact constructively. Constructive interference results in a increase in amplitude of the combined wave. Conversely, if the "peak" of one wave aligns with the "trough" of the interacting wave, the waves are 180°out of phase resulting in destructive interference and a reduction in amplitude (Young, 1802).

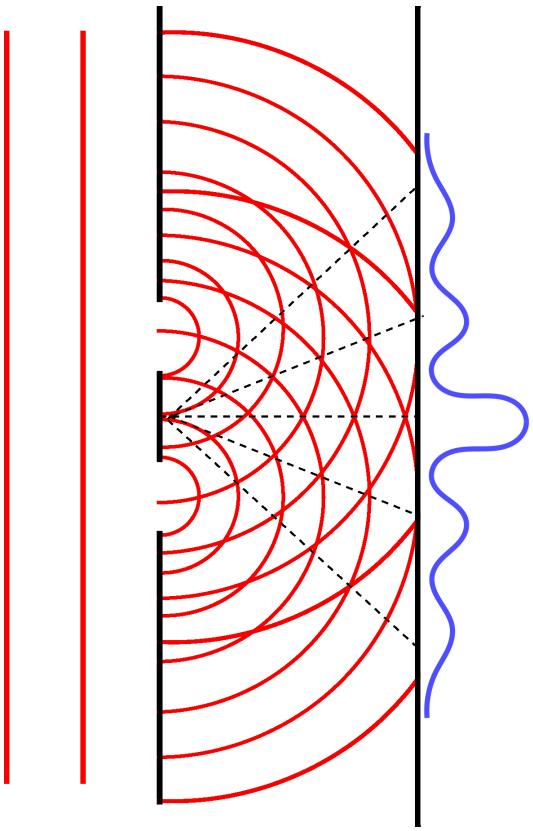

Figure 1.2: Linear wavefront (Red) diffracting through two apertures (Black), the resulting spherical waves interfere producing an interference pattern on the black screen beyond the apertures. The intensity at each position in the interference pattern is shown in blue. Dotted black lines show the regions of constructive interference between waves and correspond to intensity maxima in the interference pattern.

In the case of the double slit experiment described above, if waves propagating from each aperture travel the same distance before interacting (i.e. at the central axis between the apertures) the waves will be in phase and interfere constructively. If the distance traveled by each wave differs by $\frac{\lambda}{2}$ waves will be out of phase and destructively interfere. Generalising this idea it is clear that path differences of $n\lambda$ result in constructive interference and differences of $\frac{n\lambda}{2}$ result in destructive interference. The result is an interference pattern with a central intensity maximum surrounded by bands of decreasing intensity separated by dark bands resulting from destructive interference (figure 1.2) (Young, 1802).

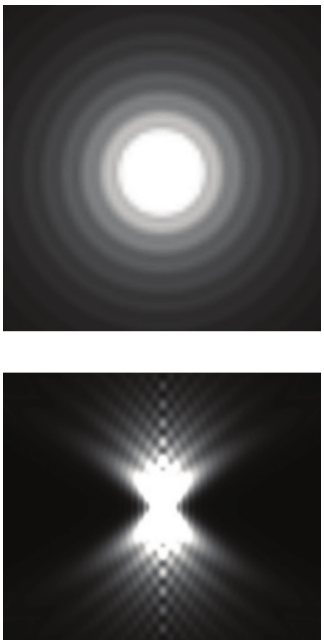

Figure 1.3: Example point spread function (PSF) in the lateral direction (Above) and axial direction (Below). Adapted from Single-Molecule Localization Super-Resolution Microscopy: Deeper and Faster by Herbert *et al.* (Herbert et al., 2012).

In the case of apertures wider than the wavelength of the incident light, light propagates as a series of spherical waves rather than a single spherical wave. This effect occurs at the aperture in the objective lens of a light microscope (Enders, 1996). Imaging a point source, for example a fluorescent spherical bead, results in a similar diffraction pattern occurring in the lateral direction at the focal plane of the microscope, referred to as the Airy disk (figure 1.3) (Herbert et al., 2012). Outside of the focal plane the rings surrounding the central maximum spread out in the axial direction and decrease in intensity. In the example of the fluorescent bead, the result is a 3D image shaped somewhat like an hourglass, this is the point spread function (PSF) of the microscope (figure 1.3) (Herbert et al., 2012).

The central maximum of the PSF has a gaussian shape, the radius of which is approximately equal to the width of the gaussian at half maximum amplitude (referred to as the full width half maximum (FWHM)). The FWHM of the lateral direction can be mathematically expressed as:

$$FWHM_{lat} = \frac{0.61\lambda}{NA} \tag{1.2}$$

Where NA is the numerical aperture of the lens. The numerical aperture defines the angle at which light can be detected by the lens. The higher the NA, the wider the cone of light which can be gathered by the lens and the higher the resolution (Juškaitis, 2006). However, because the angle of acceptance is higher, the working distance (the distance from the lens to the sample) is smaller, thus limiting the thickness of tissues which can be imaged.

Similarly, the axial component of the PSF has a gaussian profile and the FWHM can be expressed as:

$$FWHM_{ax} = \frac{2n\lambda}{NA^2} \tag{1.3}$$

Where n is the refractive index (RI) of the immersion media. RI dictates the speed of propagation of light in a medium and is discussed in detail below.

Resolution is typically defined as the ability to differentiate two objects. The higher the resolution, the closer two objects can be while still being differentiable.

The Rayleigh criterion is the commonly used metric for determining whether two objects are differentiable (Kubalová et al., 2021). The Rayleigh criterion states that two objects are just discernible if the centre of the central maximum of the airy disk of one object overlaps with the first minimum of the second object (figure 1.4) and can be mathematically expressed as:

$$\theta = \frac{1.22\lambda}{D} \tag{1.4}$$

Where θ is the angle of separation between the two objects measured from the aperture, D is the diameter of the aperture, and λ is the wavelength.

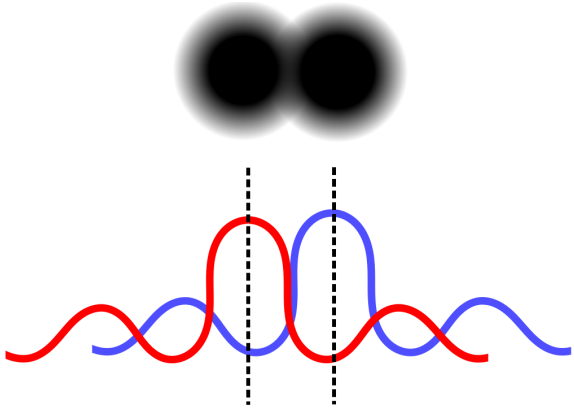

Figure 1.4: Two objects which are at the limit of differentiability under the Rayleigh criterion. Below are the PSFs for each of the two objects showing that the central maximum of each object is aligned with the first minimum of the other.

Based on this resolution criterion and the size of the PSF, Ernst Abbe formulated an equation for the resolution limit of any given microscope in the lateral and axial directions:

$$R_{lat} = \frac{\lambda}{2NA} \tag{1.5}$$

$$R_{ax} = \frac{2\lambda}{NA^2} \tag{1.6}$$

Where R is the resolution limit. In practical terms, high numerical aperture lenses typically have numerical aperture of around 1.45. Using an illumination wavelength of approximately 550nm the lower limit on the resolution of light microscopy can be derived as:

$$R_{lat} = \frac{550}{2\times1.45} = 190nm \tag{1.7}$$

$$R_{ax} = \frac{2\times550}{1.45^2} = 523nm \tag{1.8}$$

Thus no traditional confocal microscope can resolve objects separated by less than approximately 200nm in the lateral direction or 500nm in the axial direction (Abbe, 1873).

The PSF is convolved with every fluorescent signal imaged by the microscope (Lee et al., 2017). This convolution is most easily imagined as a stamp which the microscope imprints on the image of every fluorescent source in the image. As such, no signal can appear smaller than the PSF of the microscope in the raw image. However, provided the PSF of the microscope is well determined, computational tools can deconvolve images, improving the resolution (Lee et al., 2017).

Despite the limitations on the resolution of optical microscopy determined by Abbe, in the following century researchers have found many innovative methods for surpassing this apparent limit (Lelek et al., 2021; Neupane et al., 2014; Wu et al., 2021). Collectively, these methods are referred to as super-resolution microscopy.

1.2 Modern light microscopy methods

1.2.1 Macroscale imaging

Macroscale imaging modalities are the most prevalent imaging methods in clinical applications, with x-ray, MRI, PET, and CT scanning being common diagnostic tools (Hawkes et al., 1980). While microscale imaging is commonly used for clinical studies of tissue sections, biopsies and other excised, fixed tissues, the capacity to image the entire human body non-invasively makes macroscale imaging ideal for direct live diagnosis of patients. Such macroscale approaches typically rely on either contrast between natural tissues, as for many x-ray imaging applications, or non-toxic tracers, as for PET scanning, (Rong et al., 2023; Trotter et al., 2023). However, the large field of view afforded by macroscale imaging comes at the cost of resolution, with modern macroscale imaging approaches attaining a maximum resolution on the order of hundreds of microns (Feinberg et al., 2023; Z. Liu et al., 2022; Moses, 2011). This limits the scope of macroscale imaging to the investigation of mesoscale structures and tissues within the body. Comparatively, modern mesoscale and microscale imaging approaches achieve sub-micron resolution, with superresolution confocal microscopes achieving resolutions on the order of tens of nanometers, enabling a detailed description of subcellular structures(Bates et al., 2008; Schmidt et al., 2008; Yang et al., 2022).

Additionally, macroscale imaging is limited in the diversity of targets these techniques can visualise. While microscopy techniques such as immunofluorescence and FISH enable the fluorescent marking of proteins and RNA respectively, these techniques require the incubation of tissues with antibodies and probes (Bauman et al., 1980; Im et al., 2019). Such reagents are typically neither safe, nor viably available in sufficient abundance, for use in live patients. Macroscale imaging is therefore predominantly limited to endogenous markers such as tissue density in x-ray imaging or electric dipoles in MRI (Grover et al., 2015; Smith et al., 1981). Exceptions to this rule include radioactive tracers used in PET scanning and luciferase reporters (Rong et al., 2023; Trotter et al., 2023). Luciferase reporter

assays enable the study of gene expression by fusing a luciferase encoding sequence to the promoter region of the gene of interest. Following transcription and translation, chemical reactions between luciferase and substrates such as luciferin result in bioluminescence at sufficient intensity to be visualised at the macroscopic level through solid tissue (Luker and Luker, 2010; McLatchie et al., 2013). However, similar to immunofluorescence and FISH, luciferase assays involve toxic compounds and are therefore inappropriate for use in live patients.

1.2.2 Microscale imaging

Innovations in the design of lenses can be traced back to early civilisation, with polished crystalline lenses having been discovered at many archaeological sites across the middle east (Gerhard, 2021). The production of clear silicate glass in 13th century Europe was the next significant innovation in the design of optical components and enabled the design of lenses with improved magnification and visual acuity. Thus the first microscopes were created (Wollman et al., 2015). These early microscopes functioned essentially as magnifying glasses, comprising a single lens. While simple in their design, these early microscopes, such as those designed by van Leeuwenhoek, enabled the visualisation of microorganisms van Leeuwenhoek described as "animalcules", now protozoa and bacteria, likely for the first time ("IX. An account of Mr. Leeuwenhoek's microscopes", n.d.; Kutschera, 2023).

Contemporaries of van Leeuwenhoek sought to improve on the design of the simple microscope, incorporating a second lens, referred to as the objective lens, between the eyepiece lens and the sample (figure 1.5) (Wollman et al., 2015). This design, referred to as a compound microscope, incorporates a secondary lens, the objective. The magnified image produced by the objective lens is then secondarily magnified by the eyepiece, rather than the eyepiece directly viewing and magnifying the sample (figure 1.5).

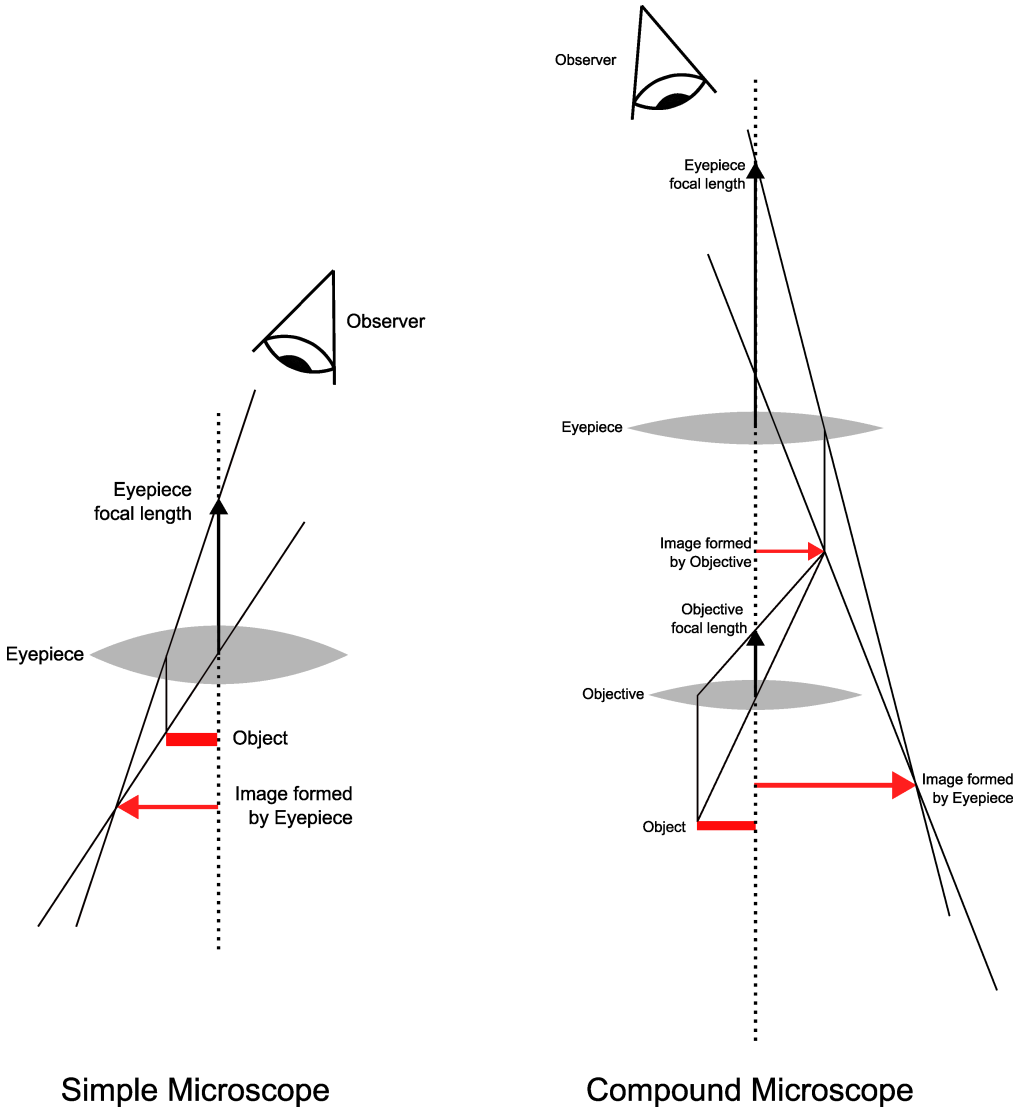

Figure 1.5: Comparison of the working principles, and magnification, of a simple and compound microscope.

The total magnification of a compound microscope, **M**, can simply be calculated as;

$$M = M_{obj} \times M_{eye} \tag{1.9}$$

Where $\mathbf{M}_{obj}$ and $\mathbf{M}_{eye}$ are the magnification of the objective and eyepiece lenses respectively.

The invention of the first compound microscope is commonly attributed to the Dutch glasses makers, Hans and Zacharias Janssen around the year 1600 (Wollman et al., 2015). Though it is Hooke whose use of the compound microscope heralded

the next major step in the timeline of optical microscopy. Through the use of compound microscopy Hooke studied the microstructure of tissues, describing the cell for the first time. Hooke published his findings as a series of highly detailed illustrations and descriptions of microorganisms in his work "Micrographia" (figure 1.6) (Hooke, 1665).

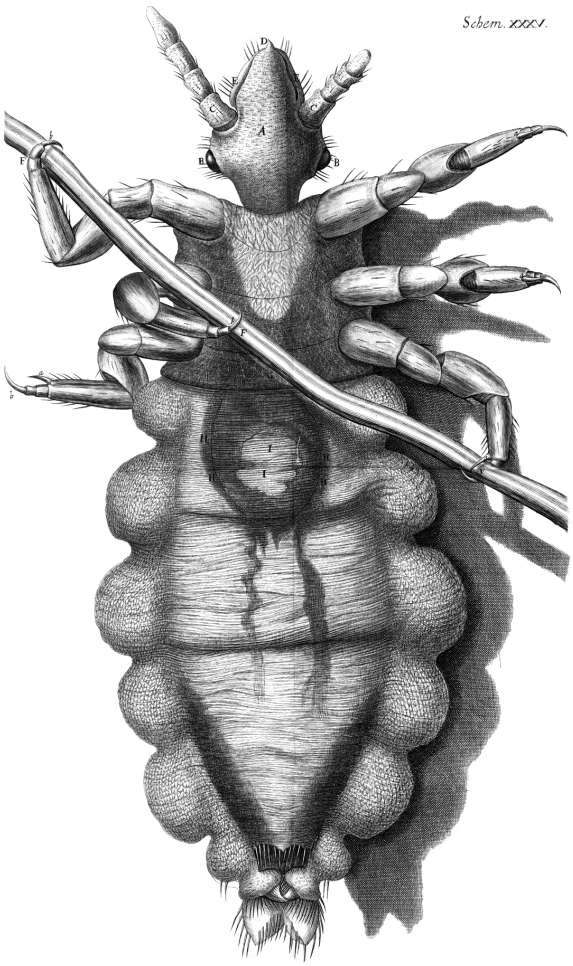

Figure 1.6: Hooke's illustration of a louse observed via his compound microscope from his publication Micrographia (Hooke, 1665).

Despite the level of detail provided in "Micrographia", this work highlights a limitation of these early compound microscope systems; the capture of data. Hooke created illustrations, which were later passed along to engravers, based on his findings. This approaches leaves relies on the subjective interpretation of the data by both Hooke and the engravers. It would not be until the 20th century when digital microscope systems reduced this subjectivity by integrating cameras

capable of capturing micrograph information (X. Chen et al., 2011).

The work of 20th century researchers such as Carl Zeiss and Ernst Abbe yielded breakthroughs both in technology and optical theory. Abbe demonstrated that the relationship between wavelength and numerical aperture set a limit on the resolution of light microscopes as described above (Abbe, 1873; B. Huang et al., 2010). Meanwhile, Zeiss was instrumental in the practical application of optical theory in microscope design. Advancements in illumination sources, particularly the use of monochromatic lasers, during this period enabled fine control over the wavelength of illumination (Elliott, 2020). The ability to illuminate samples at specific wavelengths gave rise to fluorescence microscopy, revolutionising the visualisation of biological structures within samples. When illuminated with light of a specific wavelength, fluorescent molecules will emit light of a longer wavelength (Berezin and Achilefu, 2010). This occurs as electrons absorb incident light. Following absorption, electrons will remain excited for a brief period (typically on the order of nanoseconds) before decaying to the ground state, releasing that energy as a photon (Berezin and Achilefu, 2010). However, during the excited period the electron loses some small amount of energy to vibration, decaying between multiple closely packed vibrational energy states. Due to the conservation of energy, the energy emitted as light following excitation must definitionally be lower than the energy of the excitation light due to these vibrational loses. This lower energy corresponds to a longer wavelength emitted photon as described in equation 1.1. In practice, fluorophores, being molecules comprising multiple atoms thus complicating the structure of electron energy levels, are not perfect absorbers or emitters and as such don't emit at a single wavelength. Rather, each has a peak excitation and emission wavelength surrounded by a range of excitation/emission wavelengths of decreasing likelihood, collectively, these are the fluorophores excitation and emission curves (figure 1.7) (Heim and Tsien, 1996).

This difference in excitation and emission energy represented a powerful opportunity for microscopists of the 20th century. Many optical materials had been created capable of filtering light based on wavelength (Elliott, 2020). By illuminat-

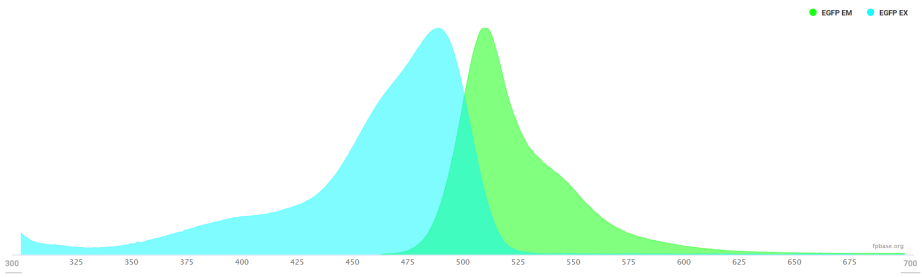

Figure 1.7: Excitation (Blue) and emission (Green) curves for the commonly used fluorophore EGFP. The width of excitation and emission curves varies between fluorophores. In all cases excitation and emission curves have some non-zero width, resulting in overlap when using numerous fluorescent markers in a single sample ("FPBase", 2025).

ing tissues comprising fluorescent molecules with monochromatic laser light, such materials could be used to filter out the excitation light, leaving only emitted fluorescence. Following the invention of fluorescence microscopy many such fluorescent molecules, known commonly as fluorophores, were developed with excitation wavelengths across the visible, UV and near infrared spectrum (Martynov et al., 2016; S. Wang et al., 2020). By affixing fluorophores to antibodies (Immunofluorescence) or nucleic acid sequences (FISH) or by genetically modifying organisms to express fluorophores endogenously, tissue structures, pathogens, or transcribed gene products can be fluorescently labeled (Bauman et al., 1980; Calvo-Alvarez et al., 2018; Im et al., 2019).

The invention of the first confocal microscope systems also occurred in the 20th century and marked another step forward in resolving power (Davidovits and Egger, 1969). The confocal microscope incorporates a pinhole between the illumination source and the sample, and the sample and the detector/eyepiece (figure 1.8). The pinhole between the illumination source and the sample enables incident light to be focused to a precise point in the sample, reducing illumination of, and signal from, tissue above or below the focal plane. The primary purpose of the second pinhole is to prevent out-of-focus light from reaching the detector, further sharpening the focus of the instrument. In many modern confocal systems, the light path enables

these functions to be performed by a single pinhole (Elliott, 2020).

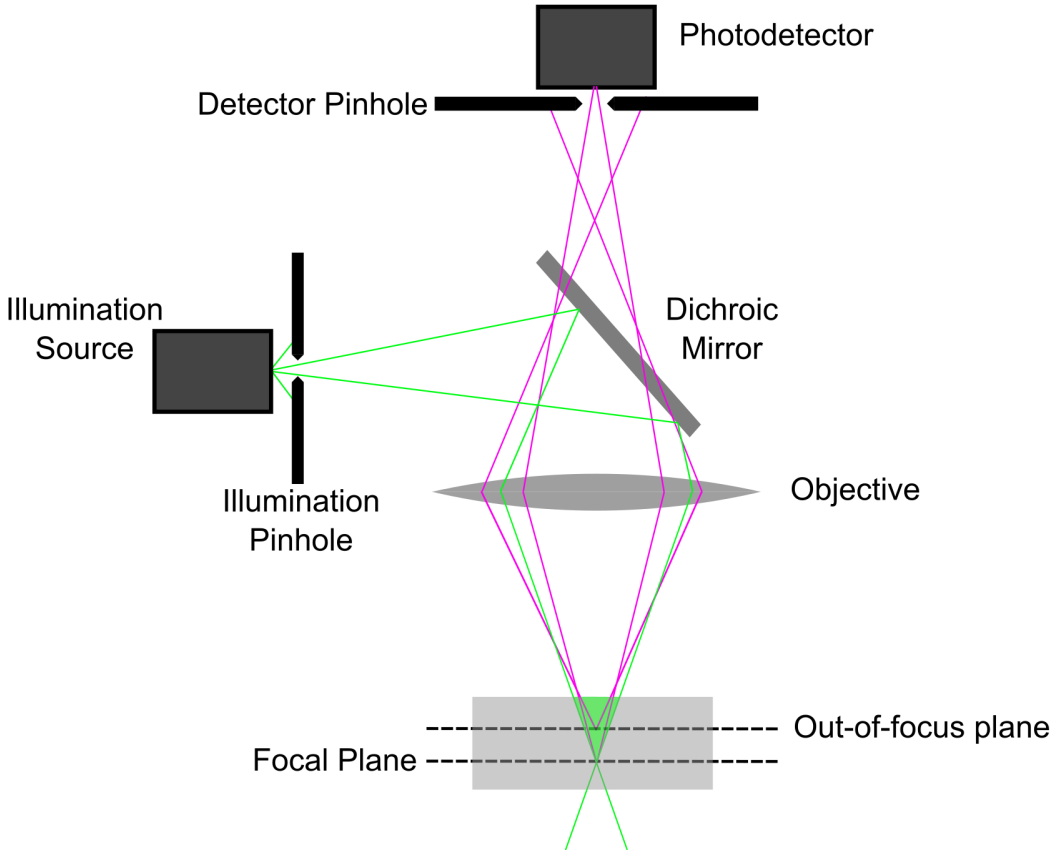

Figure 1.8: Working principle of a confocal microscope. Illumination (green) is performed using a shorter wavelength of light due to loses of energy in the excited state. A dichroic mirror reflects this shorter wavelength light but transmits lower wavelength emitted light. Light emitted from the out-of-focus plane is blocked by the detector pinhole.

The result is a microscope with a narrower depth of field compared to traditional microscopes, commonly referred to as widefield microscopes. Decreasing the size of the pinhole exacerbates this effect, further sharpening the image, however care must be taken as decreasing pinhole size also reduces how much light reaches the detector, decreasing signal-to-noise ratio. The airy unit (AU) describes the size of the central bright spot in the diffraction pattern of an illuminated object, commonly 1 AU is regarded as the optimal size of pinhole (Elliott, 2020).

Modern confocal fluorescence microscope systems combine these advancements in optics from the last 500 years, enabling the precise labeling of biomarkers

and the visualisation of structures at resolutions approaching the diffraction limit of light (Elliott, 2020). While the working principles of confocal fluorescence microscopy were largely established in the 20th century, recent innovations continue to develop the scope of light microscopy. For example, fluorescence lifetime imaging (FLIM) exploits the subtle differences in the duration of excitation of different fluorescent molecules to distinguish between fluorophores (Datta et al., 2020). This means that even if two fluorophores emit at similar wavelengths, they can still be distinguished from one another. Due to the width of emission curves described above, it can be difficult to distinguish between fluorophores with similar emission curves using a traditional confocal microscope (Bhakdi and Thaicharoen, 2018). Such systems are often limited to imaging 5-7 fluorophores depending on available excitation lasers and filters. By offering an alternative scheme for separating fluorescent signals, FLIM can significantly expand the number of fluorophores used in parallel, as well as allowing for combinations of fluorophores too similar in emission spectra to be viable in traditional confocal experiments.

Surpassing resolution limits: Superresolution

The diffraction limit demonstrated by Abbe limits the resolution of traditional confocal microscope systems (Abbe, 1873). However, modern innovations have introduced numerous technologies capable of surpassing this limit. These methods, collectively referred to as superresolution microscopy, improve the resolution limit to tens of nanometers (B. Huang et al., 2010). Structured Illumination Microscopy (SIM) exploits the interactions between structured light to visualise structures below the Abbe diffraction limit (Long et al., 2025). Structured light refers to light which is repeating but not homogeneous across the field of illumination. For example, illumination may take the form of a series of illuminated bands or a grid, with dark regions between illuminated bands. By overlapping these structures, interference between illuminated bands results in Moire patterns. These emergent structures are lower resolution than the structured light which interfere to create them, but crucially, by knowing the structure of one of the structured illumination

sources creating the Moire pattern, the structure of the other illumination source can be solved. In the case of SIM, a structured illumination method is used to illuminate samples, interference between this illumination and light emitted from the sample results in Moire patterns. Given that the structure of the illumination source is known, the resulting lower resolution Moire pattern can be used to visulaise the structure of the sample at higher resolution than a traditional confocal microscope. A similar result can be achieved using unstructured light by scanning multiple point detectors across the sample, known as instant SIM (iSIM) (Long et al., 2025). In practice, this is achieved by replacing the traditional pinhole with an array detector, This is the working principle of the AiryScan technology from Zeiss, for example (Weisshart, 2025). By reducing the size of the pinhole in a confocal microscope we can increase resolution, however, reducing the pinhole below 1 AU significantly decreases signal. An iSIM detector array allows for a sub-airy unit sized detector without losing signal from the central node of the airy disk. In the case of the AiryScan from Zeiss, the pinhole is replaced with a hexagonal array of detectors. Each detector is 0.2 AU, thereby improving on the resolution of a traditional pinhole set to 1 AU. Each element in the array captures a separate image of the structure (i.e. a fluorophore) being imaged. Each of these images is higher in resolution, but lower in intensity, than that of a traditional confocal. Additionally, the images from each of the array elements other than the central element are offset from the illumination axis. By aligning and summing images captured by each element, the resulting image is of higher resolution and of comparable intensity to that of a confocal microscope. A similar method, 4Pi microscopy, employs coherent illumination and detection of light from a sample from multiple angles simultaneously (Schmidt et al., 2013). By illuminating samples from multiple angles a coherent image of fluorescent emitters in the focal plane of both objectives can be acquired, significantly improving the resolution of the resulting image when compared with a traditional confocal approach relying on single-direction illumination of the sample.

Other superresolution methods rely on the emission properties of fluorophores.

As described above, excitation and emission wavelengths differ due to vibrational relaxation of the excited electron prior to decay to a lower energy state. This relaxation occurs as the electron transitions between vibrational energy levels in the excited state and similar vibrational levels exist in the ground state. In addition to this natural emission, excited electrons can be forced to emit light through a process called stimulated emission. Stimulated emission involves illuminating a fluorescent molecule with light of a wavelength equal to the fluorophore's emission wavelength (Neupane et al., 2014). This illumination causes the spontaneous emission of photons of wavelength equal to the illumination wavelength (figure 1.9). Due to the numerous vibrational energy levels within each energy state, stimulated emission can result in the emission of photons of various wavelengths, depending on the wavelength of the illumination laser (figure 1.9).

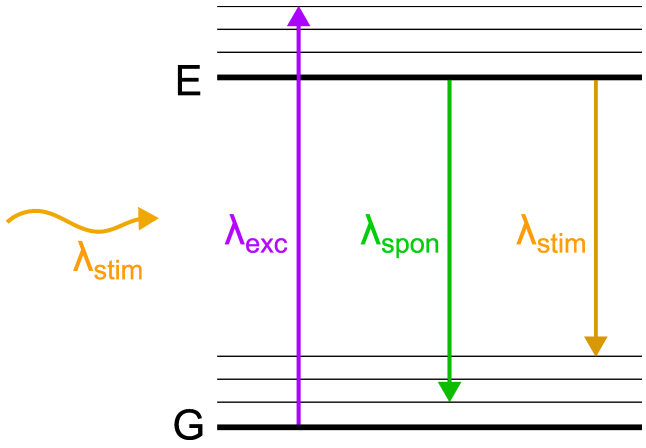

Figure 1.9: Working principle of stimulated emission depletion (STED). Ground and Excited states are represented by G and E respectively. Thin black lines represent vibrational energy levels. Excitation with wavelength of λ_{exc} exc results in spontaneous emission of wavelength λ_{spon}. STED interrupts this process via illumination with shorter wavelength light, λ_{stim}

Stimulated emission depletion (STED) microscopy exploits this behavior to increase resolution (Neupane et al., 2014; Wu et al., 2021). Samples are first illuminated at the excitation wavelength of the fluorophore using a traditional illumination beam. Within the excitation lifetime of the fluorophore, the sample is illuminated with a wavelength at the tail of the fluorophore's emission curve. This

secondary illumination, referred to as the depletion beam, results in the stimulated emission of photons, and by extension the decay of excited electrons back to the ground state. Importantly, this depletion beam is shaped into a torus, this ensures that stimulated emission occurs only in the periphery of the illuminated spot (figure 1.10). As a result, only the small spot in the centre of the toroidal depletion beam emits photons via the natural decay of electrons back to the ground state. These electrons will decay into a number of vibrational levels in the ground state, releasing photons with a range of wavelengths across the emission curve of the fluorophore. By selecting a depletion wavelength in the tail of the emission curve, the majority of photons emitted naturally will be of shorter wavelength. The longer wavelength photons emitted via stimulated emission can therefore be filtered out without significant losses of fluorophore signal. Filtering these longer wavelengths removes signal from the torus illuminated by the depletion beam, resulting in a central spot of improved resolution. The size of this central spot can be tuned by increasing the laser power of the depletion beam, however, the high powers required for depletion can result in photobleaching. Hypothesised and later demonstrated experimentally by Steffan Hell, STED typically provides lateral resolutions between 30-80 nm, though Wildanger *et al.* report a resolution of 2.4 nm (Schmidt et al., 2008).

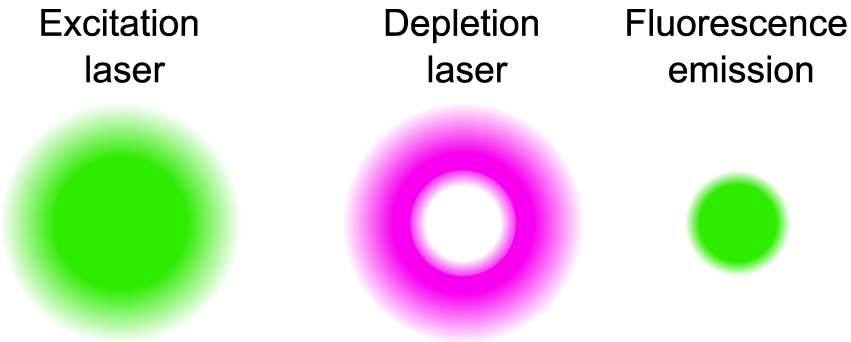

Figure 1.10: Mechanism by which the depletion beam improves resolution in STED microscopy.

In 2014, Hell was awarded the Nobel prize in Chemistry for his work on STED. He shared the prize with Eric Betzig and William E. Moerner who demosntrated another superresolution method: Single Molecule Localisation Microscopy (SMLM)

(Betzig et al., 2006; Moerner and Kador, 1989). SMLM exploits switchable fluorophores whose fluorescence can be controlled, allowing fluorophores to "blink" (Dickson et al., 1997). This enables only a subset of fluorophores to fluoresce, and by extension be imaged, at one time. By iteratively imaging subsets of fluorophores and superimposing these images, a superresolution image comprising all fluorophores can be created. The mechanism by which fluorophores are switched on and off varies between SMLM methods. Photo-Activated Localisation Microscopy (PALM) uses photo-activated proteins. These proteins are typically non-fluorescent and only fluoresce after illumination with an activtion light, typically UV (Betzig et al., 2006). In some PALM applications photoswitchable rather than photo-activated proteins are used. These fluorophores have switchable emission wavelength, rather than being turned on or off, though the triggering mechanism is the same. Stochastic Optical Reconstruction Microscopy (STORM) exploit the photochemical properties of fluorescent molecules to control blinking (Rust et al., 2006). The excited state discussed thus far is, more precisely, the excited singlet state. This state is characterised by the presence of an electron with opposite spin to that of the electron in the ground state (Rust et al., 2006). Further exploration of electron spin states is outwith the scope of this work, all that is necessary for the understanding of STORM is that electrons can exist in one of two spin states; spin up or spin down. The Pauli exclusion principle states that no two electrons can occupy the same state (Kaplan, 2020). This results in complementary pairs of electrons occupying energy levels, one with spin up, the other with spin down (figure 1.11). The excited singlet state arises when a complementary pair of electrons exist between the ground and excited state. The excited triplet state arises when the electron in the excited state exhibits the same spin as the electron in the ground state and are thus not a complementary pair. The triplet state can also arise from an electron transition from the singlet state following a change of spin (Endesfelder and Heilemann, 2015).

Excited triplet states are less common than singlet states due to the required change of spin of the excited electron, however, this also results in triplet states

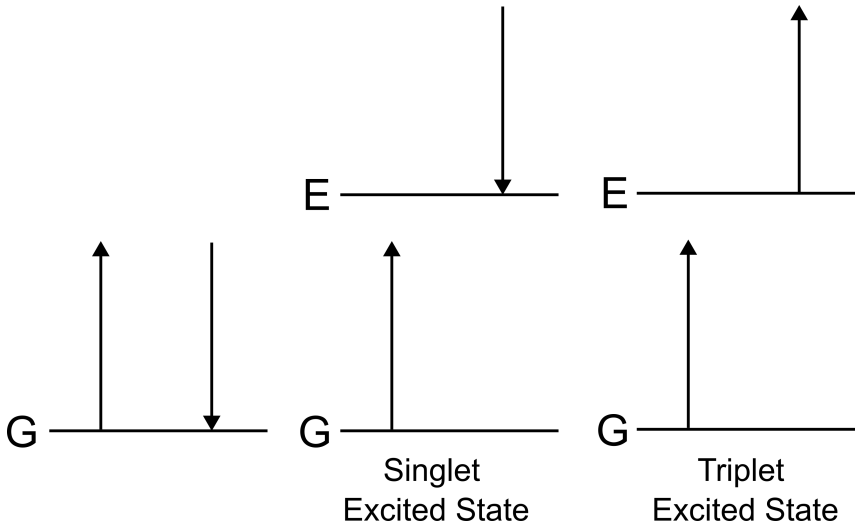

Figure 1.11: Excitation states allowed under the Pauli exclusion principle. Direction of arrows represents an electron with either spin up or spin down.

being longer lasting. These long lasting triplet states result in fluorophores containing long lasting, high-energy, highly reactive electrons which do not readily decay to the ground state. Through reaction with reducing agents in imaging buffers these highly reactive electrons can form stable radical anions. This process renders fluorophores temporarily non-fluorescent, with fluorescence being recovered following exposure to high energy illumination (UV) or oxidisation which returns the electron to the ground state (figure 1.12) (Goossen-Schmidt et al., 2020). By controlling the concentration of oxygen and reducing agents in imaging buffers the concentration of fluorophores non-fluorescent anionic state can be controlled, thus controlling fluorescent blinking.

This blinking results in only a subset of fluorophores emitting at any given time. By capturing many images of the sample as this blinking process continues, an image of the entire sample can be built up. This enables fluorophores which are separated by distances smaller than the diffraction limit to be imaged sequentially, rather than simultaneously. By capturing these images sequentially, these signals can be differentiated, where as in a conventional micrograph these signals would fall below the separation distance enforced by the Rayleigh criterion and be inseparable.

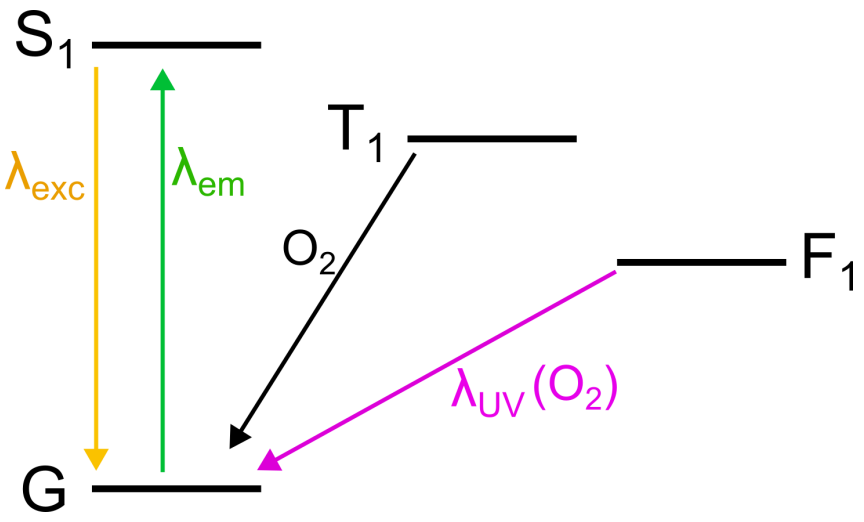

Figure 1.12: Working principle of dSTORM. Excitation from the ground state (G), results in population of the singlet excited state, S_1. Internal electron transitions result in the excited triplet state, T_1. Reactions between triplet states and reducing agents results in the formation of anions, F_1. Electrons are returned to the ground state via oxidisation or excitation with UV.

Surpassing resolution limits: Expansion microscopy

While superresolution approaches focus on imaging nanoscopic structures by surpassing the diffraction limit of light, other researchers have explored alternative methods. Expansion microscopy seeks to chemically alter the structure of samples, isotropically inflating tissues via immersion in a polyelectrolyte hydrogel in order to spatially separate structures which are otherwise unresolvable (Zhuang and Shi, 2023). Samples are first incubated with a reagent, often referred to as "molecular handles", which readily binds to both biomarkers within the sample and the structure of the hydrogel. Samples are then permeated with the hydrogel, binding biological structures to the gel matrix. As biological markers are now affixed to the hydrogel matrix, sample integrity is no longer reliant on the structure of the tissue. The mechanical properties of the sample are therefore chemically homogenised such that they do not interfere in the isotropic expansion of the sample. Finally, the hydrogel is permeated with an aqueous solution. This frees charged electrolytic compounds within the gel and repulsion between these charged compounds results in the expansion of the hydrogel and embedded tissue (Wassie et al.,

2019). Expansion microscopy is appropriate for use with fluorescence microscopy approaches, with fluorophore binding being incorporated either prior to handle incubation or following hydrogel embedding (F. Chen et al., 2016; Chozinski et al., 2016).

Expansion microscopy is capable of 10-fold linear expansion of samples, though most protocols result in approximately a 5-fold linear expansion (Zhuang and Shi, 2023). This expansion results in structures at or below the resolution limit being sufficiently far apart that they become distinguishable. Structures separated by 70-80nm would be 350-400nm apart following 5-fold expansion, being separable using many modern confocal systems (Elliott, 2020). Additionally, embedded samples can be iteratively expanded for a second time yielding expansion of approximately $4.5 \times 4.5 =$ 20-fold (J.-B. Chang et al., 2017). This iterative expansion method has been demonstrated to effectively distinguish structures separated by only 25nm in the native tissue using traditional confocal microscopy.

Expansion microscopy has enabled the study of ultra-fine structures in a variety of tissues including viruses, organs, organelles, and in model organisms such as *C. elegans* (Rodriguez-Gatica et al., 2022; Scherer et al., 2021; C.-C. Yu et al., 2020). The method has gained particular popularity in neuroscience due to the complexity and size of tissue components. Here, expansion microscopy has been used to image individual synapses beyond the resolution limit of traditional imaging approaches (F. Chen et al., 2015; Murakami et al., 2018; Sarkar et al., 2022).

Immunofluorescence

Immunofluorescence exploits antibody binding to label proteins (Im et al., 2019). Antibodies bind to target antigens with high specificity, enabling the targeting of pathogens, cell types, and tissue structures with a high level of precision. By labeling antibodies with fluorophores, labeled proteins can be visualised via confocal microscopy. Immunofluorescence was conceptualised by Hewett Coons in the 1940s. Through a collaboration with researchers working on the development of fluorophores, Coons successfully fluorescently stained bacteria via incubation

with an antibody bound to the fluorescent dye, anthracene isocyanate (Coons and Kaplan, 1950). Despite this, application of early fluorescent dyes in tissues was unsuccessful. All tissues produce some degree of autofluorescence due to the excitation of electrons within the tissue. The intensity and wavelength of autofluorescence will vary between tissue types however significant autofluorescence in blue-green portion of the visible spectrum (approximately 420-520nm) is common (Jacob et al., 2024). As such, Coons and his contemporaries struggled to distinguish anthracene isocyanate signal (approximately 400-450nm) from tissue autofluorescence. Additionally, the fluorescence of all flourophores decays following repeated illumination due to photobleaching, resulting from molecular changes to the fluorophore altering its absorption and emission characteristics (Boudreau et al., 2016; Neuman et al., 1999; Zheng et al., 2014). This effect is attributed to reactions between excited electrons and reactive molecular oxygen within the sample mounting environment, evidenced by the effects of oxygen depleting buffers on photobleaching (Dempsey et al., 2011). This prompted the development of brighter fluorophores and fluorophores with a diverse range of emission spectra. These efforts have led to the invention of highly photostable fluorophores capable of maintaining fluorescence over minutes of continuous illumination (Hirano et al., 2022).

Signal intensity was further improved by the invention of indirect immunofluorescence by Beutner and Jordan in 1964 (Beutner and Jordon, 1964). Early immunofluorescence (direct immunofluorescence), bound fluorescent dyes/proteins directly to the labeling antibody (Coons and Kaplan, 1950). Indirect immunofluorescence is a two step protocol; Primary antibodies are bound to the biomarker of interest, secondary antibodies carrying fluorophores are then bound to the primary antibodies (figure 1.13). Fluorophores in close proximity exhibit self-quenching effects and thus a fluorescence from a primary antibody cannot simply be increased by binding more fluorescent molecules directly. Thus, binding of secondary antibodies enables far greater amplification of signal than could be achieved using direct immunofluorescence (Bae et al., 2021).

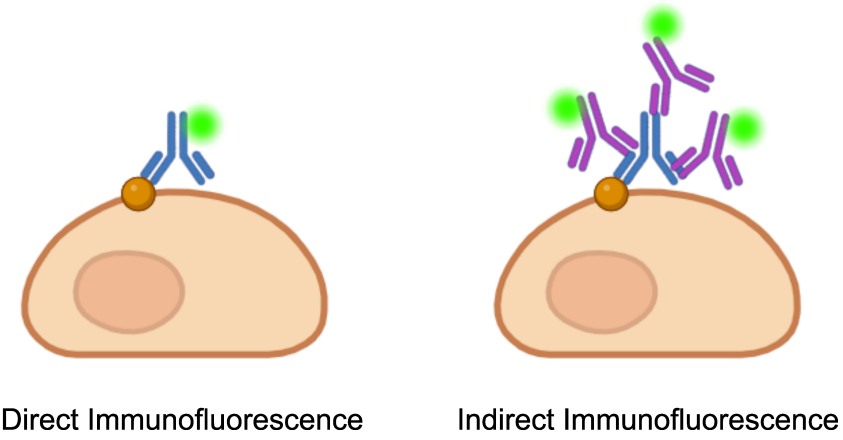

Figure 1.13: Working principle of direct and indirect immunofluorescence labeling. In both cases antibodies (Blue) bind to specific proteins of interest (Orange). Fluorophores (Green) are either conjugated directly to the antibody, as in direct immunofluorescence, or to secondary antibodies (Purple) which bind the primary antibody, as for indirect immunofluorescence.

Importantly, primary antibodies are produced in a different host to that of the sample being stained, commonly being of the abundant Immunoglobulin G (IgG) subtype (Vidarsson et al., 2014). Secondary antibodies target IgG specific to that host species, the secondary antibody will bind only the primary antibody IgG rather than the IgG endogenously expressed by the host of the sample (Beutner and Jordon, 1964).

Because multiple secondary antibodies can bind to a single primary antibody, indirect immunofluorescence significantly amplifies signal intensity (Beutner and Jordon, 1964). Additionally, indirect immunofluorescence allows any primary and secondary antibodies to be used together, provided the host species are correct, improving the diversity of antibody and fluorophores combinations available. Modern innovations in nanobodies, small fluorescently labeled secondary antibodies capable of penetrating further into tissues, continue to improve the scope of immunofluorescence by enabling the visualisaiton of signals in thicker tissues (Schneider et al., 2021). Immunofluorescence is commonly used in high magnification confocal studies in which highly specific, highly localised staining is required (Im et al.,

2019). The ability to visualise and distinguish numerous fluorophores in parallel, referred to as multiplexing, has resulted in significant popularity among researchers working at the cellular and subcellular level. For widefield studies, such as pathology studies of large tissue sections immunohistochemistry (IHC) is more common (de Matos et al., 2010). IHC was developed shortly after the work of Coons on immunofluorescence and also relies on antibodies targeting proteins of interest. Unlike immunofluorescence, IHC conjugates antibodies to enzymes which produce colour through reaction with a substrate. IHC staining does not rely on fluorescence and is therefore visible under white light illumination as is typical in widefield microscopy. Additionally, relying on chromogenic rather than fluorescent staining means IHC stained tissues are not subject to photobleaching allowing for long term preservation and repeated imaging of samples. While IHC staining does not provide the resolution or multiplexing capacity of immunofluorescence, the reduced cost, improved throughput and longevity of samples associated with IHC have resulted in popularity among pathologists and oncologists (de Matos et al., 2010).

FISH

Where immunofluorescence enables the labeling of proteins, FISH enables the labeling of RNA and DNA. Rather than antibodies, FISH probes comprise nucleic acid sequences complimentary to genes of interest. The hybridisation of probes within samples enables *in situ* targeting of RNA and DNA (Bauman et al., 1980), with probes typically range from tens to hundreds of nucleotides (F. Wang et al., 2012).

Initially, *in situ* hybridisation probes were bound to radioactive isotopes and detected by autoradiography (Gall and Pardue, 1998). Later, histochemical reactions with HRP substrates expanded detection of ISH probes via choromogenic IHC, and subsequently via immunofluorescence, either by designing fluorophores directly into the probe or attached after hybridisation in a similar manner to secondary antibody staining (Femino et al., 1998). Many early FISH approaches relied on the binding of single fluorophores to probes, however, this resulted in a

low abundance of fluorophore and low signal to noise ratio (Huber et al., 2018). Modern applications therefore rely on amplification of fluorescence, with multiple fluorophore molecules being attached to each probe to ensure high signal. Such methods typically involve binding amplification reagents comprising numerous fluorophore binding sites, rather than constructing probes capable of binding large numbers of fluorophores directly, reducing the size and complexity of probes (F. Wang et al., 2012). One innovative solution to amplification is hybridisation chain reaction (HCR) (Dirks and Pierce, 2004; Evanko, 2004). HCR relies on a stable mixture of two DNA or RNA species each of which exists in a self-bound hairpin formation. These species are capable of hybridising with one another, but cannot due to the hairpin formation. When an indicator sequence capable of binding one of the two stable species (in the case of FISH, the target gene) hybridises with one of these hairpins, the reaction results in the opening of the hairpin species. This subsequently results in a reaction which opens, and hybridises with, the second hairpin species, resulting in a hybridisation chain reaction between the two species. If these species provide a binding site for fluorescence, this can significantly increase the number of fluorophores which can be bound to the target sequence.

Some modern applications also incorporate innovative solutions to non-specific probe binding, incorporating pairs of probes targeting adjacent sequences in target genes. These probes pairs collectively encode a binding site for fluorophores or amplification reagents, meaning fluorophores only bind when both probes are in place. Thus, non-specific binding of single probes does not yield fluorescence (F. Wang et al., 2012).

While it is possible for antibodies to be highly specific, in some cases, antibody cross-reactivity makes differentiation of similar proteins difficult. For example in virology, the structure of influenza A virus (IAV) proteins differs between variants, however, differences are typically not sufficient to prevent antibody cross-reactivity (Beest et al., 2017) due to conservation of binding epitopes between proteins. Targeting the encoding RNA sequence rather than the translated protein enables an alternative target for identification and differentiation of viral genes of different

variants which cannot be differetiated via antibody. The ability to visualise pre-translational processes and the increased specificity of RNA targeting have led to an influx of interest in FISH technologies in biological imaging, supplementing well-established immunofluorescence technologies.

In the work presented here, FISH experiments were performed using the RNAScope platform (ACD-BioTechne). The RNAScope platform is a commercial FISH technology capable of conducting multiplex fluorescent FISH assays marking upto 4 distinct RNA or DNA species. The platform has gained popularity in recent years due to it's ease of use and the support avaialble from ACD-BioTechne. This existing ecosystem was the primary motivator for it's use in this work. However, the RNAScope platform has drawbacks not present in other FISH platforms such as HCR-FISH or smFISH. Namely, RNAScope reagents are significantly more expensive than HCR-FISH and smFISH probes which many researchers produce in-house. Possibly most problematic is that while ACD-BioTechne offer a custom probe design service, this service involves the user providing a sequence of approximately 1000 nucleotides which they desire a probe against. The RNAScope team then design a proprietary probe targeting a subsequence within this 1000 nucleotide string, however, the exact position of this target sequence within the 1000 nucleotide string is not provided to the user. As such, the user is not aware of the specific sequence their probe targets, and thus has little recourse if the probe fails to bind or binds non-specifically. With probes which are designed in house, these issues can be avoided easily.

1.2.3 Mesoscale imaging

While low-resolution macroscale imaging methods and high-resolution microscale imaging methods have continued to improve, it has proven difficult to combine these approaches to create techniques capable of imaging such as large tissue sections or organs at high resolution. This is largely due to the relationship between field of view, working distance, and resolution described above. These inherent physical barriers make imaging large samples with traditional confocal microscopes

difficult. Microscopists have devised multiple solutions to surpass these physical limitations, however, each method comes with compromises.

The simplest solution to image large samples is simply to dissect tissues prior to imaging. Many sectioning platforms exist such as vibratomes and cryotomes which are capable of precisely sectioning tissues without damaging morphology within the tissue section (Germroth et al., 1995; Simpson and Hawes, 2022). Resulting tissue sections typically range from 10-300 μm thick depending on the microscope system being used for imaging and the experimental design (Q. Wang et al., 2023). Such sections can then be imaged at high resolution using existing microscale imaging methods. However, while advanced computational tools exist for reconstructing mesoscale structures from images of multiple adjacent tissue sections, these tools are imperfect and the sectioning process introduces aberrations between sections, significantly impacting spatial accuracy in the resultant reconstructed tissue volume.

Alternatively, the limitations on field of view and depth of focus incurred by working with high numerical aperture, high magnification lenses can be circumvented by simply increasing the size of components. By working with a larger condenser and objective lens, the working distance can be increased, enabling the imaging of larger samples. This approach has been employed by McConnell *et al.* at the University of Strathclyde when designing the Mesolens, a confocal system exploiting a large objective lens to enable to imaging of samples on the order of whole fruit flies and murine embryos with subcellular resolution throughout the imaging volume (McConnell and Amos, 2018; McConnell et al., 2016; Rooney et al., 2024). However, given the point-scanning imaging modality employed in confocal microscope systems, increasing sample size significantly increases imaging time, with samples on this scale taking days to capture. Additionally, during the confocal imaging process, the tissue is repeatedly exposed to out-of-focus excitation light as data is gathered from other areas of the sample (figure 1.14). This exposure can lead to photobleaching, the process by which fluorophores' capacity to fluoresce is reduced following repeated excitation, and photodamage of tissue

structures (Zheng et al., 2014).

Light sheet microscopy

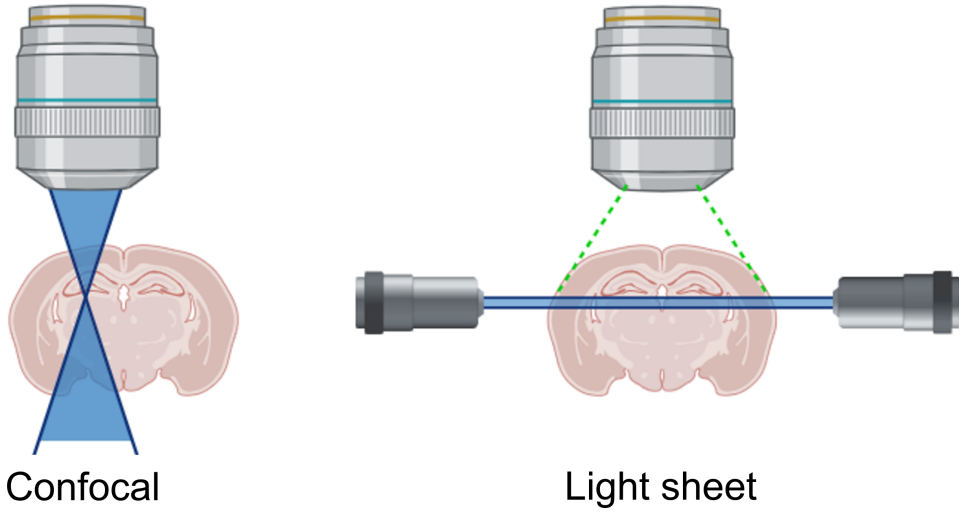

Figure 1.14: Working mechanism of a confocal microscope (left) and a light sheet microscope (right). Incident light is shown in blue. The imaging objective lens is shown above the sample in each case, with illumination objective to the left and right of the sample in the light sheet case, ("BioRender", 2025).

Light sheet microscopy (LiSM) provides an alternative means of imaging mesoscale samples without the need for dissection and at improved speeds compared to confocal imaging (Battistella, Schniete, et al., 2022; Daetwyler and Fiolka, 2023). LiSM (known also as selective plane illumination microscopy (SPIM)) was invented by Huisken *et al.* in 2004 (Huisken et al., 2004b). In the two decades since numerous light sheet systems have been developed capable of imaging increasingly large tissues, while retaining cellular resolution (Battistella, Quintana, and McConnell, 2022; Cai et al., 2023). The principle optical difference between LiSM and confocal microscopy is the decoupling of the illumination and imaging planes (figure 1.14). While confocal systems rely on a spherical lens to focus excitation light to a single point, LiSM uses a cylindrical lens to focus light only in one axis, producing a "sheet" of light which can illuminate a plane through the sample simultaneously. By orienting the objective lens perpendicular to this light sheet, emitted light from

the illuminated plane can be captured at once, significantly improving imaging speed compared to point-scanning confocal systems. Additionally, by illuminating only the imaging plane, each plane of the tissue is only exposed to light as that plane is imaged, reducing the photodamage resulting from repeated exposure required in confocal microscopy (Daetwyler and Fiolka, 2023).

Effect of attenuation and refraction on imaging of thick tissues

Irrespective of imaging method, the size of mesoscale samples means that refraction and attenuation of incident light has a significant impact on imaging (Hamdy et al., 2022).

The speed of light in a vacuum, **c**, the "universal speed limit", is approximately 3.00×10^8 meters/second. However, the speed of light varies between materials, for example, the speed of light in water is only approximately 2.26×10^8 meters/second. Interestingly, while the speed of light in a vacuum cannot be exceeded, this is not true in other media, with high energy particles exceeding light speed in water, for example. This "breaking of the light barrier" releases Cherenkov radiation, similar to the emission of a sonic boom when breaking the sound barrier, and is the cause of the blue glow seen in the water cooling systems in nuclear reactors (Jelley, 1983).

When passing from one medium to another, this change in speed results in a change of direction of incident light, known as refraction (Khan et al., 2021). The RI of a material is a dimensionless quantity which relates the speed of light in that medium to the speed of light in a vacuum. For example, the RI, **n**, of water is 1.33, therefore we can calculate the speed of light in water, **v**, stated above simply as:

$$v = \frac{c}{n} = \frac{3 \times 10^8}{1.33} = 2.26 \times 10^8 meters/second \quad (1.10)$$

Given the heterogeneous nature of tissue, numerous changes in RI occur as light passes through an organ (Hamdy et al., 2022). Refractive indices of tissue components such as lipid droplets and proteins typically vary between 1.35 and 1.5,

with particularly dense structures such as bone and enamel exhibiting refractive indices of approximately 1.4-1.6. Such tissue components all exist in aqueous substrates, such as cytoplasm, which have similar refractive indices to that of water, being around 1.33-1.35 (Khan et al., 2021).

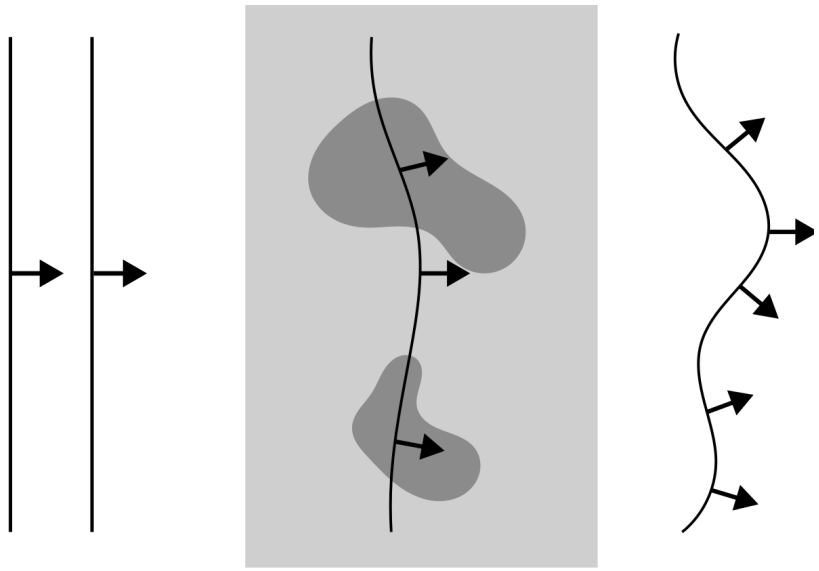

Figure 1.15: Example of the deformation of a wavefront due to refraction, arrows represent the direction of propagation of the wavefront. A uniform wavefront (black) propagating to the right will undergo refraction when entering a tissue (grey). The degree of refraction will depend on tissue composition, with regions of high RI (dark grey) refracting light more, thus deforming the wavefront.

Such mismatches in RI result in significant deviation of the light path through the tissue volume. Importantly, this deviation will vary across the tissue. This means that a well structured wavefront will be substantially deformed after passing through a tissue (figure 1.15). In addition to sources of deformation of signal arising from within the tissue, spherical aberration in the lens also distorts captured signals. Spherical aberration describes the process in which light rays are focused to different focal lengths depending where they pass through the lens due to differences in refraction. Light passing through the centre of the lens is focused further from the lens than light passing through the periphery of the lens In practice, these sources of deformation and aberration alter the appearance of fluorescent signals and tissue structures and morphology, making measurements of

distances and signal intensity unreliable. In addition to refraction, attenuation can significantly impede the imaging of thick tissues. Attenuation is simply the loss of intensity of light as it passes through a medium due to scattering and absorption (Shariati B. K. et al., 2023). Scattering describes the process by which a wave deviates from its incident path through interaction with a particle. Within tissues, scattering events arise when incident light interacts with small particles within the medium (Miles et al., 2001). When interacting with atoms, incident light waves accelerate charged particles, such as electrons. This acceleration leads to oscillation of the electron about the nucleus, and the resultant energy is emitted as light, since the direction of emission is random, this is referred to as "scattered" light. The strength of the interaction between the incident light and the particle, and by extension the degree to which light is scattered, is strongly correlated with how closely the frequency of incident light matches the resonant frequency of the particle (Miles et al., 2001). Given that frequency and wavelength are associated via equation 1.1, the intensity of scattered light, **I**, can be written in terms of wavelength of incident light, λ, and is found to be inversely proportional to λ^4:

$$I \propto \frac{1}{\lambda^4} \tag{1.11}$$

In the case of biological tissues, resonant frequencies of constituent particles are most similar to higher energy (bluer) visible light. As such, blue light lasers are scattered more readily than red light lasers and penetrate less far before attenuating (Sandell and Zhu, 2011). Such scattering events can reduce the intensity of both excitation light arriving at the focal plane and emitted light making it from the focal plane to the detector. Many tissue components scatter light, though lipid droplets and calcified tissue have strong scattering effects and are often detrimental to imaging (Masselink and Tanaka, 2023). Absorption is particularly problematic in tissues containing large amounts of haem such as the liver and kidneys, and highly melanised tissues, such as the skin and eyes (J. Huang et al., 2019; Masselink et al., 2019). Often, absorptive pigments are highly localised, for example in the pupils, or in melanomas. However, these small pigmented regions can have a

substantial effect on imaging due to shadowing. In the majority of microscope systems, excitation light is unidirectional, meaning absorptive structures cast shadows which occlude the region behind them (figure 1.16). While modern LiSM systems have incorporated multiple light sheets or means of varying the angle of the light sheet during imaging to circumvent this, shadowing still impedes the imaging of thick tissues (CarlZeissMicroscopy, 2011).

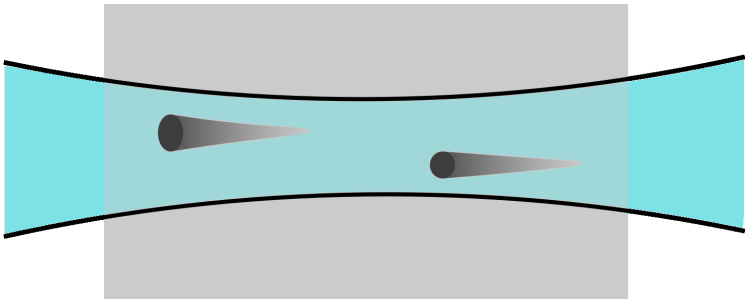

Figure 1.16: Example of shadowing by highly pigmented structures during LiSM imaging. A unidirectional light sheet (Blue) illuminating a sample (Grey) from the left. Pigmented structures (Black) prevent illumination of the region immediately behind them.

The effects of refraction can be combated via components with adjustable refractive indices. A simple approach is the use of optical components with a correction collar enabling the user to tune the refractive index of the lens to better match that of the immersion medium. Similarly, silicone immersion lenses directly match the refractive index (approximately 1.41) of many common immersion mediums Scientific, 2025. Adaptive optics exploits a deformable mirror the surface of which is manipulated in real time based on the deformation of the wavefront, such that after reflection the deformations in the wavefront are normalised (Hampson et al., 2021). Cumulatively, the effects of refraction and attenuation make imaging of tissues of thickness greater than around 200 μm very challenging with traditional microscopy approaches (Centonze and White, 1998). Due to the inverse relationship between the wavelength of incident light and the intensity of scattered light described above, longer wavelength light can penetrate deeper into tissues. This is exploited in multi-photon microscopy in which multiple low energy (typi-

cally near infrared) photons are used to excite fluorophores with comparatively high excitation energy (figure 1.17) (Centonze and White, 1998; Soeller and Cannell, 1999). However, this extends the imaging limit only to approximately 1 mm before attenuation again occludes imaging deeper tissue sections. Clearly, this is not sufficient for the imaging of whole organs. To this end, chemical processes have been invented for rendering tissues transparent, this process is known as optical clearing.

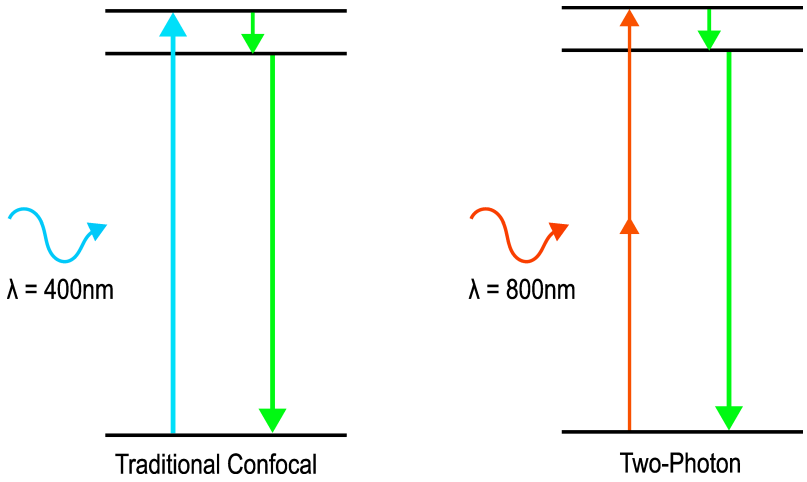

Figure 1.17: Working mechanism of multi-photon microscopy, displayed here in terms of a two-photon excitation system. Pairs of low energy photons (right) are used to excite electrons rather than a single high energy photon as in traditional epifluorescence confocal (left). Emitted light is of lower energy than the excitation energy due to losses in energy to vibration resulting in small changes in energy state of electrons prior to emission.

Optical clearing of tissues

Optical clearing involves the alteration of the chemical composition of tissues in an attempt to increase transparency (Azaripour et al., 2016). As described above, RI boundaries inhibit visualisation of deep sections in thick tissues. RI matching offers a solution to this, reducing RI boundaries within tissues by dehydrating and permeating tissues with oil of a similar RI to that of tissue components (Splateholz, 1914). While RI differences exist between cellular structures such as organelles and

plasma membranes, the majority of RI changes within tissues occur between cells and the surrounding aqueous medium (Khan et al., 2021). This aqueous medium primarily comprises water and so has a RI of approximately 1.33. By replacing water with oil of an RI similar to that of the surrounding tissue, the effects of refraction throughout the tissue can be significantly reduced. The refractive indices of tissue components (i.e. organelles, extracellular matrix) are difficult to define precisely as measuring the RI of tissues inherently incorporates a contribution from this aqueous medium. However, oils of RI = 1.45-1.58 are typically well matched to the RIs of dehydrated tissues.(Foster et al., 2019; L. Liu et al., 2021; Masselink and Tanaka, 2023 This is logical as bone, a tissue with a low water content and therefore an RI more representative of non-aqueous tissue components, has an RI = 1.4-1.6 (Khan et al., 2021).

Dehydration is typically performed by gradually replacing water with a highly osmotic medium, typically an alcohol such as ethanol (Masselink et al., 2019; Subiran Adrados et al., 2021). This dehydrating agent is then subsequently replaced with a high RI medium, such as mineral oil, rendering the tissue transparent (figure 1.18 A, B).

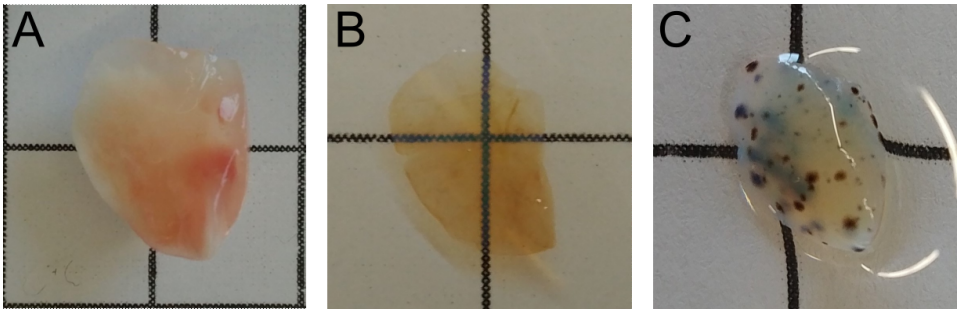

Figure 1.18: Example of mouse lung tissue cleared using an ethyl cinnamate (ECi) based clearing protocol. Harvested mouse lung tissue, **A**, is dehydrated and perfused with ECi to match refractive indices across the volume, **B**. In lungs from mice treated with a carcinogen, highly pigmented melanoma are not affected by clearing, **C**. Work from this thesis, sections 3.2.1 and 3.2.4.

In addition to RI matching, the removal of highly scattering compounds is crucial to achieving transparency (figure 1.18 C) and many common optical clearing

approaches incorporate reagents specifically for the removal of scattering compounds (Ren et al., 2021). Similarly, depigmentation of highly absorptive compounds is necessary to improve clarity and reduce shadowing (Ugolini et al., 2021). In haem-rich tissues it is advisable to repeatedly perfuse samples to remove excess blood, using an anticoagulant such as heparin in extreme cases (M. Qiu et al., 2021). Bleaching using hydrogen peroxide is typically employed to depigment highly melanised tissues, however, care must be taken as extended H_2O_2 exposure can significantly damage tissue structures and degrade morphology, inhibiting image analysis (Ugolini et al., 2021; D. Wang et al., 2024). Furthermore, H_2O_2 bleaching can damage fluorophores, reducing signal (Platkov et al., 2014).

In each case, steps can be added to optical clearing protocols to accommodate depigmentation, delipidation or decalcification of tissues, typically, these steps precede dehydration as the required reagents interfere with the dehydration of tissues (Ren et al., 2021). However, it is important to consider the effects of optical clearing on the accuracy of downstream imaging. Optical clearing is definitionally an alteration of the chemical composition of a tissue and dehydration and replacement of water with oil can lead to significant expansion or contraction of tissues. Such changes differ between tissue types and can therefore alter morphology non-isotropically (Masselink and Tanaka, 2023). Delipidation and decalcification have even more dramatic effects, directly removing tissue components. Without optical clearing, imaging of thick tissues would not be possible, however, the effects of optical clearing reagents on imaging and image interpretation must be carefully considered.

Optical clearing approaches broadly fall into two categories; aqueous and solvent-based. Aqueous clearing methods involve immersing tissues in a high RI aqueous medium, raising the RI across the tissue volume via diffusion (Chung et al., 2013a; Ren et al., 2021; Susaki et al., 2014). While aqueous protocols may include delipidation, depgigmentation, or decalcification steps (such as the commercial CUBIC method (Tokyo Chemical Industry)) the aqueous nature of reagents means no dedicated dehydration step is required. Aqueous clearing methods are typically

non-hazardous so are appropriate in the open chambers common on modern LiSM systems. These methods also preserve endogenous fluorescent signals, making them appropriate for the clearing of immunostained samples (L. Liu et al., 2021).

Solvent-based approaches involve the direct replacement of water within tissues with high RI oils and involve a dedicated dehydration step (Masselink and Tanaka, 2023). As for aqueous protocols, steps can be incorporated to remove scattering and absorptive compounds. By replacing water with oil, solvent-based approaches enable much higher final RI to be achieved, with common RI matching solutions such as Ethyl Cinnamate, iDISCO, and Benzyl Alcohol/ Benzyl Benzoate (BABB) exceeding n = 1.55 (Ertürk et al., 2012; Genina, 2022; Renier et al., 2014). Comparatively, aqueous RI matching protocols such as CUBIC and SeeDB result in a final RI of approximately n = 1.48 (Ke et al., 2013; Susaki et al., 2014). The higher RI offered by solvent-based approaches can better match certain objectives and tissues such as bone. Additionally, solvent-based approaches are often faster than aqueous protocols, taking hours to a couple of days to achieve optical clearing (Hofmann et al., 2021; Kontny et al., 2024). When compared with the incubation periods involved in aqueous clearing methods (multiple weeks for CUBIC experiments involving decalcification and delipidation for example) solvent-based approaches reduce time between tissue harvesting, staining, and imaging, reducing tissue and fluorophore degradation. Traditionally, solvent-based approaches have relied on highly toxic reagents which readily quench fluorophores, significantly decreasing their usefulness in fluorescence microscopy (Becker et al., 2012; Chung et al., 2013b). However, recent innovations in dehydration compounds have significantly improved fluorescent signal retention (Alves et al., 2016; Schwarz et al., 2015). Additionally, recent optical clearing developments have yielded RI matching solvents such as Ethyl Cinnamate which are safe for bench top and open sample chamber use and preserve fluorophores, combining the speed of solvent-based approaches with benefits traditionally reserved for aqueous methods (Foster et al., 2019; Masselink and Tanaka, 2023). By reducing the effects of refraction and scattering, optical clearing enables the visualisation of large *in vivo* samples such

as thick tissue sections in excess of 1 mm thick, and whole organs.

1.3 Influenza A virus as a model system

The primary goal of this thesis is to develop imaging methods capable of visualising infections across length scales. Throughout the work described here, IAV is used as the primary model system for the development and validation of these microscopy imaging and analysis methods. Other biological model systems are introduced throughout where relevant.

The dynamics of IAV infection are highly heterogeneous across length scales, particularly during co-infection, this makes IAV a useful model for the microscopy methods development conducted throughout this work (Amato et al., 2022; Fu, 2018; Ganti et al., 2022; Sims et al., 2022). Additionally, IAV is of importance for public health and food security, with annual seasonal outbreaks and pandemics causing a significant burden on national healthcare and agricultural systems (Fischer et al., 2014). Therefore by investigating the replication and emergence of IAV across length scales, this work may elucidate interventions pertinent to the health of both livestock and the human population.

On the microscale, intracellular processes occurring during co-infection can dramatically alter viral genetic diversity, with the exchange of genetic material between infecting viral strains (reassortment) leading to the emergence of novel strains with the potential to cause future pandemics (Sims et al., 2022)

Similarly, mesoscale pathology can dramatically differ between lobes of the lung, with single viral strains having been found to dominate within individual lung lobes during co-infection (Amato et al., 2022; Ganti et al., 2022)

Meanwhile, on the macroscale, IAV infection can lead to significant clinical complications distinct from these micro- and mesoscale effects, such as extensive tissue damage within the lower respiratory tract and, in extreme cases, subsequently pneumonia (Sharma-Chawla et al., 2016)

Cumulatively, these distinct, length-scale specific behaviors, in addition to the

clinical interest in the study of IAV, makes this pathogen an appropriate model system for the studies performed here.

1.3.1 Single vs co-infection

The replication and spread of IAV infections involving a single viral strain are well established both *in vitro* and *in vivo* (Gaush and Smith, 1968; Mansell and Tate, 2017; Rodriguez-Frandsen et al., 2020). Mice are a popular laboratory hosts for IAV studies and the progression of disease within these animals is well documented (Czakó et al., 2017; Mansell and Tate, 2017).Viral burden gradually increases following infection, peaking around 6 days post infection (dpi), typically resolving between 9 and 12 dpi (Reuman et al., 1983). Similarly, the growth of singly infected IAV lesions has been studied extensively both under plaque assay conditions *in vitro* and via histological imaging in lung sections (Gaush and Smith, 1968; Rodriguez-Frandsen et al., 2020).

Like many RNA viruses, IAV has a high mutation rate and viral evolution during single infections occurs due to mutations resulting from replication errors (Nobusawa and Sato, 2006; Petrova and Russell, 2018). The IAV genome comprises eight gene segments encoding the viral proteins, which are collectively packaged into virus particles (Jakob et al., 2022). Following the infection of a host cell, gene segments are replicated individually and packaging signals in the terminal regions of gene segments facilitate the incorporation of genes within virus particles which are then released from the cell enabling further infection (Jakob et al., 2022; X. Li et al., 2021). Despite the specificity of the packaging signals for each gene segment, the packaging of viral genes remains error-prone. This results in many viral particles which lack one or multiple gene segments, or particles comprising multiple copies of the same gene. Referred to as semi-infectious particles, such viruses lack the complete genome and therefore cannot replicate successfully (Diefenbacher et al., 2018). However, should semi-infectious particles co-infect a cell alongside either a competent virus (a virus comprising a full genome) or another semi-infectious particle with a complementary array of gene segments, all eight genes will be present

within the infected cell, enabling replication. Thus, co-infection enables production of competent virus particles from incompetent semi-infectious particles by packaging replicated genes from multiple incomplete genomes into single particles.

While these semi-infectious particle interactions can occur in both single and co-infections, this packaging behavior gives rise to an alternative evolutionary mechanism during co-infection, known as reassortment. Reassortment describes the process in which genes from genetically distinct co-infecting strains are packaged together, resulting in virus particles carrying novel genomes (Sims et al., 2022). The result of this behavior is that evolution during co-infection can arise both through mutation and reassortment between strains. Thus, viral evolution during co-infection is considerably more complex and less well understood than that of single infection (Nobusawa and Sato, 2006; Petrova and Russell, 2018)

In addition to the evolutionary complexities incurred by reassortment, the spatial dynamics of co-infections are also considerably more complex than single infections. Imaging work studying microscale interactions between co-infecting strains has demonstrated that co-infecting viruses do not simply mix, rather, infection of a cell with an IAV particle restricts that cell from being infected with another viral strain. Following infection with an IAV particle, there is a relatively short time frame during which infection with a secondary IAV virus can occur (Sims et al., 2022). The mechanism by which this prevention of secondary infection occurs is currently unknown, however the length of time during which secondary infection can occur is inversely related to the genetic similarity of the two co-infecting viruses, with IAVs of the same subtype exhibiting shorter SIE response than those of different subtypes (Sims et al., 2022). This process, known as superinfection exclusion (SIE), has also been observed in coronaviruses, suggesting this is a cellular response to viral infection rather than a phenomenon unique to IAV infection. SIE means that only cells encountering multiple virus strains within this time frame can become co-infected, and thus facilitate reassortment. SIE has been observed both *in vitro* and *in vivo* (Sims et al., 2022) and while it is clear that the restrictions imposed on viral interaction by SIE will have effects on gene exchange and evolu-

tion, these effects are poorly understood. This understanding is crucial to public health as interactions between viral strains, particularly those adapted for different hosts, can result in the emergence of viral strains with pandemic potential (Ganti et al., 2022). Similarly, the effects of co-infection on the growth of IAV across the wider lung and respiratory tract are not well established. Broadly, the progression of disease is similar between single and co-infections, with infections peaking around 6dpi and clearing around 9-12dpi (Reuman et al., 1983). However, the development and spread of lesions across the lung has not been well studied, with no mesoscale imaging studies of co-infected lungs having been performed. It is therefore unclear whether the exclusionary effects observed at the microscale result in similar isolated viral populations at the mesoscale. The forward transmission of viral progeny following co-infection is more well documented.

Transcriptomic studies of swabs from the noses of mammalian hosts co-infected with IAV enable the differentiation of viral strains (Fu, 2018). Such studies have shown that a significant proportion of viruses from co-infected mammalian hosts at 9dpi combine genetic material from multiple viruses used to inoculate the host. These viruses can only arise through the exchange of genetic material between co-infecting viruses. However, the mechanisms involved in the emergence of these viruses, the timepoints during infection and the location within the respiratory tract where they emerge, and the growth of these novel populations within the host are all poorly understood. This is particularly interesting because these findings are seemingly at odds with the exclusionary properties observed at the microscale. These exclusionary effects isolate viral populations, limiting mixing and the exchange of genes (Sims et al., 2022). Despite this, these novel viral populations are common in late stage studies of the cells in the upper respiratory tract (Fu, 2018) As mentioned, the exchange of material between viruses during co-infection is a key driver in pandemic strain emergence, so a better understanding of the mechanisms involved in the generation and spread of these viruses is of significant importance to public health. Modern mesoscale imaging approaches such as optical clearing and light sheet microscopy provide a means to resolve this disconnect between

microscale mechanisms governing viral interaction, and macroscale studies of forward transmission of viral progeny (Daetwyler and Fiolka, 2023; Masselink and Tanaka, 2023). Moreover, the development of multimodal imaging approaches aims to combine techniques for imaging samples across scales. Such imaging pipelines would allow researchers to construct a more cohesive understanding the relationship between micro-, meso-, and macroscale processes.

1.3.2 Microscale effects of co-infection: Pandemic strains, reassortment, and superinfection exclusion

As described above, the segmentation of the IAV genome enables reassortment between co-infecting viruses (Sims et al., 2022). Often, such reassortment events fail to provide a genetic advantage in the resultant IAV variant and this novel virus is quickly outcompeted (Ganti et al., 2022). Additionally, the inconsistencies in IAV replication mentioned above often result in poor replication of genes, for example, large internal deletions can occur, resulting in short sequences which maintain the packaging signals in the terminal regions of the gene but which are missing a large central sequence. These genes can be successfully packaged, but cannot replicate due to this deletion, thus further confounding viral emergence. However, despite these limitations, reassortment has the capacity to generate strains of significant concern to public health, with the 1918, 1957, 1968 and 2009 pandemic strains arising from reassortment events (F. Wang et al., 2020; Worobey et al., 2014). Reassortment between variants adapted for different host species are notable in pandemic strain emergence with reassortment of avian (1918, 1957, and 1968) and swine (2009) influenza with human infectious viruses resulting in four major pandemic strains over the last 110 years. Particularly notable are reassortment events involving the surface glycoprotein encoding genes, segments 4 and 6, encoding haemagglutinin and neuraminidase respectively. The surface glycoproteins adorn the surfaces of viral particles and are instrumental in viral binding and entry into host cells and the release of progeny virions from cells following replication and packaging (S. Jiang et al., 2010; McAuley et al., 2019). Changes to surface

glycoprotein structure and function can therefore dramatically affect the infectious viability of viral particles, increasing the efficacy of receptor binding, cell entry, and forward passage of progeny.

Co-infection studies of swine have demonstrated that reassortant progeny represent a significant proportion of viral progeny at later stages of IAV co-infection (Fu, 2018). It is interesting then, that the microenvironment of the co-infected lung does not readily support reassortment events. SIE limits viral interaction, restricting co-infection to cells encountering multiple viral particles within a short period following initial infection. Due to the relatively short distances traveled by virus particles between release from an infected cell and binding to a new host cell, viral lesions growth rate is slow in comparison to the time afforded for co-infection by SIE (Johnson et al., 2022). The combination of SIE and this slow lesion growth rate result in the emergence of networks of viral microdomains, comprising collections of cells infected with a single viral strain. These microdomains have been infected for a sufficiently long time that the effects of superinfection exclusion prevent secondary infection (Sims et al., 2022). Co-infection is therefore limited to cells at the boundaries of these microdomains. These regions where viral lesions meet are the only cases where uninfected cells encounter particles from both adjacent viral lesions within the co-infection timeframe allowed by SIE. *In vitro* studies have demonstrated that in cell culture this limits co-infection to around 2% of cells (Sims et al., 2022). However, the size of the co-infected region will vary with the cellular density of tissue and the distance traveled by viral particles both of which likely differ between *in vitro* and *in vivo* systems. So while SIE has been documented in mouse lungs, these values may not be entirely representative of the prevalence reassortment within the host.

1.3.3 Mesoscale effects of co-infection: Lung anatomy and viral islands within lung lobes

The lower respiratory tract comprises the trachea (windpipe) and the lungs (Schönbach, 2013). The bronchiole tree, the network of airways permeating the lungs enables

the exchange of oxygen between inhaled air and deoxygenated blood within the alveoli. The first bifuraction of the trachea separates the left and right main bronchi which feed the respective lungs (figure 1.19).

Immediately upon entry into the lungs the main bronchi immediately branch into the lobar bronchi, each of which feeds a separate lung lobe (Fujii et al., 2020). As such, each lobe is a semi-independent respiratory structure, having a dedicated air supply. Within each lobe the bronchi branch into tertiary bronchi and subsequently into smaller bronchioles - minor airways which lack the cartilage found in the walls of the larger bronchi. These minor airways continue to branch, terminating in alveoli in which gas exchange occurs. The surfaces of these airways comprise dense populations of goblet and ciliated cells which produce and move mucus respectively to remove contaminants from the lungs (Alberts et al., 2002). The bronchiole tree is then surrounded by the parenchyma consisting of a collagen matrix with low cellular density containing alveoli which provides structure to the lungs (Suki et al., 2011).

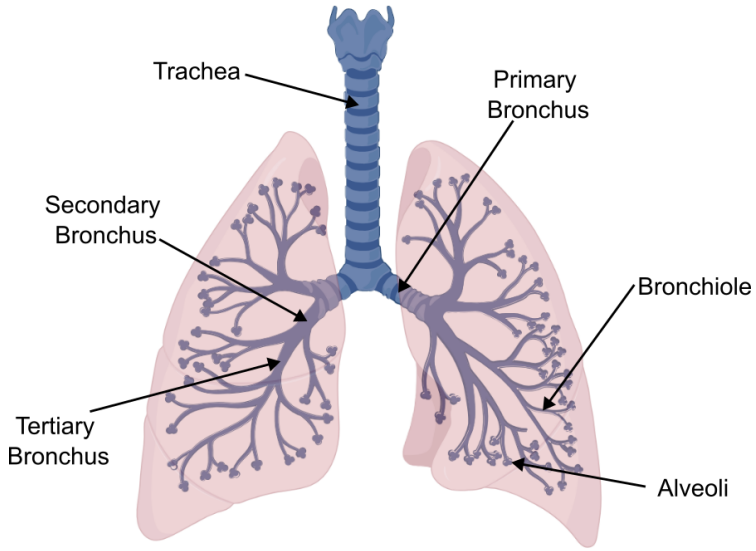

Figure 1.19: An example of the mammalian bronchiole tree. Adapted from an illustration produced in BioRender, ("BioRender", 2025)

The number of lung lobes varies between species with human lungs comprising three lobes in the right lung and two lobes in the left (Nikolić et al., 2018). In mice, used as hosts throughout the experiments conducted in this thesis, the right

lung comprises three lobes while the left lung consists of a single lobe (Irvin and Bates, 2003)

Similar exclusionary effects to those observed at the microscale have been observed at the mesoscale. In 2022, Amato *et al.* infected ferrets with a population of 10 IAVs encoding a genetic barcode (a sequence unique to each viral strain the sequencing of which enables the discrimination of strains) (Amato et al., 2022). Ferrets were inoculated in the upper respiratory tract and the virus was allowed to spread to the lower respiratory tract naturally. Amato *et al.* found that viral diversity remained high in the upper respiratory tract throughout the timecourse of infection. However, bulk transcriptomic analysis of the trachea and lung lobes of infected animals showed a significant reduction in diversity in comparison to the upper respiratory tract. Additionally, rather than a well-mixed population, the majority of trachea and lung lobes exhibited a single IAV strain which dominated the population. The specific strain which dominated differed between hosts and between lobes within individual hosts, demonstrating that this effect was not the result of selection for a specific strain.

The authors suggest this is the result of bottlenecks which reduce the number of virions seeding lower respiratory tract infections, thus reducing viral diversity. While Amato *et al.* detect a clear reduction in the number of unique viral variants in the lower respiratory tract, thousands of unique IAV lineages are detected in the majority of lobes. It is therefore reasonable to assume that interactions between viruses within lobes would occur prior to the emergence of a single dominant variant.

Also in 2022, Ganti *et al.* conducted a similar study, co-infecting ferrets, guinea pigs and swine with a pair of viruses; a wildtype H1N1 IAV and a variant comprising a single nucleotide mutation to each gene segment (Ganti et al., 2022). This single nucleotide mutation was synonymous so the resultant proteins structures were the same for each gene segment. This yields upto 254 variants through reassortment. Bulk transcriptomic analysis of lung lobes revealed a decrease in genetic diversity in the lungs of ferrets in comparison to their upper respiratory tracts, similar to the

findings of Amato. Furthermore, in the majority of lobes a single strain dominated the population, as for Amato's data. Study of viral diversity in swine revealed similar results with a dominant strain it the majority of lobes from swine culled at 3 and 6 dpi. Interestingly, while ferrets were intranasally inoculated, as in Amato's study, swine were both intranasally and intratracheally inoculated. The emergence of a dominant strain in swine lung lobes despite direct inoculation fo the lower respiratory tract suggests that if genetic bottlenecks are the cause of decreased diversity, as suggested by Amato, bottlenecks below the trachea are sufficient to produce a dominant strain.

In both cases it is unclear whether dominant variants arise due to SIE or a distinct mechanism. Previous studies appear to suggest that SIE is a microscale effect, separating infectious lesions into singly infected microdomains spanning hundreds of microns (Sims et al., 2022). This effect would isolate viral populations within airways and portions of the parenchyma of the lung, but would not isolate entire lobes. The studies by Ganti and Amato rely on bulk transcriptomic analysis of each lobe of the lung to draw their conclusions. Bulk transcriptomics is a powerful tool, enabling the identification of specific genes via sequencing (X. Li and Wang, 2021). In these cases, this enables researchers to differentiate specific viral strains based on a small number of genetic mutations. However, bulk sequencing homogenises samples, meaning the spatial context of the tissue is lost. Here, since each lung lobe is sampled separately, we can see differences in viral gene expression between lobes, but the interactions between co-infecting viruses within lobes is lost. Recent innovations such as spatial transcriptomic approaches enable the conservation of spatial information about transcript distribution (X. Li and Wang, 2021). However, spatial transcriptomics is expensive and limited to small tissue sections so is not viable for analysis of whole lung lobes. Through combination with mesoscale imaging methods, spatial transcriptomics may provide insights into the spread of co-infecting viruses within the host and elucidate the mechanisms underpinning the behavior documented by Amato and Ganti.

1.3.4 Macroscale effects of co-infection: Exchange between the upper and lower respiratory tract

The upper respiratory tract of mammals comprises the nasal cavity, pharynx (throat) and larynx (voice box) while the lower respiratory tract comprises the trachea and lungs (Schönbach, 2013). IAV particles typically enter the respiratory tract via aerosolised droplets released through respiration, sneezing, or coughing by an infected host (Richard et al., 2020). These droplets deposit in the respiratory tract and infection of the lower respiratory tract occurs primarily through respiratory transport of replicated viral particles (Haghnegahdar et al., 2019). As described by Amato and Ganti, viral populations in the upper and lower respiratory tract can differ significantly with the lower respiratory tract showing decreased viral diversity (Amato et al., 2022; Ganti et al., 2022)

It is unclear whether reassortment events occur more readily in the upper or lower respiratory tract. Ganti observes more reassortant viruses in the nasal tracts of ferrets at 1, 2, 3, and 4 dpi, however, while the diversity of reassortant viruses is lower in the lungs, the dominant virus in the lungs of the majority of ferrets is a reassortant virus. Importantly, the dominant reassortant virus in the lungs does not correlate with the major viral population in the upper respiratory tract. This suggests these reassortant viruses were likely generated within the lungs rather than deposited through seeding of reassortant viruses emerging in the upper respiratory tract.

In the swine data reported by Ganti, reassortant viruses were uncommon in both the upper and lower respiratory tract, with the dominant variant being one of the two inoculation strains in the nasal tracts and lung lobes of the majority of biological replicates. Conversely, work performed by Jinqi Fu using a library of barcoded IAVs to conduct co-infections of swine reports a high prevalence of reassortant viruses in both the upper and lower respiratory tract (Fu, 2018). Fu reports that viral populations in swabs of peripheral and deep nasal tissue were highly correlated, however these populations were not well correlated with samples from the trachea and lungs (Fu, 2018)

These studies focus on the bottlenecks imposed on transmission of variants from the upper respiratory tract to the lungs. The rate at which reassortant viruses emerging in the lungs progress to the upper respiratory tract is not well established. Recent transmission studies suggest that viruses from the upper respiratory tract are more readily transmitted (Lakdawala et al., 2015; Richard et al., 2020; Varble et al., 2014). However, without an understanding of the transmission of viruses from the lungs to the upper respiratory tract, the origin of these transmitted reassortant viruses remains unknown. Understanding the transmission of viral populations between the upper and lower respiratory tract is therefore crucial in understanding the transmission of reassortant viruses between hosts.

In the work described in this thesis, I conduct mesoscale imaging of the lower respiratory tract to investigate the dynamics of IAV co-infection. Given the differences in viral landscape between the upper and lower respiratory tract, it would be productive to conduct similar studies of the upper respiratory tract. However, thus far imaging of the upper respiratory tract has been limited due to complexities in optical clearing. Visualising the nasal cavity *in situ* would require the simultaneous clearing of multiple soft tissue types and bone. Simultaneous clearing of multiple tissues has been performed, however, it is time-consuming and complex (Cai et al., 2023). Additionally, while mice are commonly hosts in IAV experiments, ferrets lung morphology and IAV transmission capacity is much more representative of that of humans and are widely regarded as being preferable for transmission studies (Amato et al., 2022). However, the ferret nasal cavity is structurally complex, further complicating clearing and imaging (Johnson-Delaney and Orosz, 2011). Correlative upper/lower respiratory tract studies may soon be feasible; with innovations in light sheet imaging enabling the imaging of progressively larger samples, it will soon be possible to image the entire ferret respiratory tract *in situ* (Cai et al., 2023)

1.3.5 Barcoded viruses and spatial transcriptomics

The studies conducted by Amato, Ganti, and Fu rely on the genetic barcoding of IAVs in order to track specific variants (Amato et al., 2022; Ganti et al., 2022). This method, initially documented by Varble *et al.*, significantly improves on the specificity of immunofluorescence and even the majority of FISH approaches by directly sequencing viral genomes (Varble et al., 2014). However, the use of barcoded viruses does come with caveats. The introduction of a barcode sequence into a genetic sequence, particularly a short genetic sequence such as those of IAV gene segments, can dramatically alter the function of a gene, or even render it incapable of transcription and translation (Fu, 2018). Barcode designs typically circumevent this by encoding barcodes as synonymous mutations, as for the barcodes designed by Ganti and Fu. Amino acids are encoded by codons, sequences of three nucleotides. Due to the relative abundance of 3-bit permutations of nucleotides in comparison to amino acids, numerous codons encode the same amino acid (Fu, 2018). These codons are synonymous and often differ only in the third nucleotide of the codon. This third position of synonymous codons is referred to as the wobble base. By mutating the wobble base of synonymous codons, the genetic sequence can be varied without altering the resultant protein sequence, hence barcoding the virus while preserving function (Fu, 2018)

The robustness of barcodes is of particular concern in IAVs because of the high mutation rate mentioned above. If barcodes rely on single nucleotide mutations, such as the system used by Ganti, mutation at the barcode position can compromise the ability to distinguish variants. Increasing the number of bits used to encode the barcode increases robustness, however, if multiple barcodes differ by a single bit (i.e. at only one position) a change to this bit can turn one barcode into another. The most robust method involves the use of an error correcting system such as a Hamming code, as is employed by Fu.

Error correcting codes enable the accurate reading of a sequence despite some loss of information. The simplest example of this is to imagine if each barcode were repeated three times within each segment. It would then be possible to com-

pare the three barcode sequences and, for bases where a mutation had occurred, take the base shared by two of the three barcodes as being the true value for that base. However, this would involve using 2/3rds of barcode space for redundancy, as mentioned above, minimising barcode length minimises effects on viral stability and function. More complex error correcting codes minimise the space used for redundancy while maintaining error robustness. Hamming codes rely on the inclusion of parity bits which tell the reader whether there has been a modification to a bit (H. Wang, 2011). Each parity bit provides information on a subset of the code so through the combination of parity bits, the exact location of the error can be determined. The Hamming distance describes the number of bits which can be modified before any two barcode sequences are no longer distinguishable. In the case of Fu's system, the minimum Hamming distance is three, meaning any two bases can be compromised and the variants will still be distinguishable. Through collaboration with Jinqi Fu (University of Cambridge), I have used the barcoded library she developed throughout the experiments involving barcoded viruses in this thesis (Fu, 2018)

These barcoded viruses are useful in transcriptomics, however, prior transcriptomic studies have relied on bulk transcriptomics (Amato et al., 2022; Ganti et al., 2022; Varble et al., 2014). As mentioned, this removes the spatial context of the tissue. Spatial information is crucial to understanding the interactions between IAVs yielding dominant strains, reassortment, and novel variants. Recent innovations in spatial transcriptomics offer a solution. 10× Genomics have developed the Visium spatial transcriptomics assay, capable of recovering RNA from tissues while preserving spatial context (Cheng et al., 2023). Spatial transcriptomics visualises a sample in a similar fashion to microscopy, providing a visual representation of a tissue section. However, while microscopy provides a visual representation of optical signals (emission of photons by fluorophores, tissue autofluorescence, etc.) across a tissue, spatial transcriptomics provides a visual "map" of RNA expression. The Visium assay relies on a slide covered in an array of capture spots, within these capture spots are lawns of oligonucleotides. These oligonucleotides comprise a poly-A

sequence along with a spatial identification sequence unique to that capture spot (figure 1.20). When lysing tissues affixed to the slide, poly-adenylated RNA binds to oligonucleotides. When sequencing captured RNA, the spatial identifier allows researchers to reconstruct the tissue landscape. This process constructs an RNA "map" of the tissue section, revealing where each RNA sequence originated.

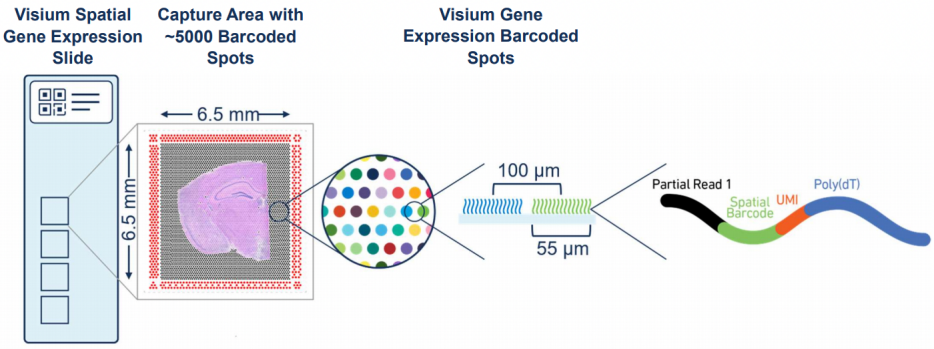

Figure 1.20: Visium gene expression slide design from 10× Genomics. Slides contain four capture areas. Each capture area contains a lawn of spots filled with poly-dT oligonucleotides which bind poly-adenylated RNA.

The Visium assay can capture all poly-adenylated RNA from fresh samples, however, formalin fixed paraffin embedded (FFPE) tissue is common as this process enables the long term storage of samples (Cheng et al., 2023). Cross-linking and RNA degradation involved in the FFPE process make direct capture of RNA difficult. The Visium assay can be adapted using probes which bind to RNA targets within the tissue, these probes are then captured by oligonucleotide binding. The Nanostring Geomics platform enables similar probe based spatial transcriptomics as the FFPE Visium assay.

In both cases, specific probes are required for each transcript of interest. For barcoded IAV studies this comes with two issues; the specificity of probes may not be sufficient to distinguish variants, as in FISH studies, and the cost of spiking in probes for every variant of each gene is high. For these reasons, spatial transcriptomic work carried out in this thesis was performed using the Visium assay for fresh frozen tissue.

1.3.6 Burden on human health

Further to the benefits of IAV as a model organism, the pathogen is of importance to global public health. IAV infection results in influenza, an infection of the respiratory tract characterised by sore throat, dry cough and headache. While the majority of influenza cases resolve within weeks without treatment, infection can be fatal, particularly in vulnerable people such as the elderly and immunodeficient individuals (Fischer et al., 2014)

Vaccination efforts have significantly decreased the burden of influenza in many countries, however, the mutation rate of IAV requires that new vaccines be developed annually (Petrova and Russell, 2018; Trombetta et al., 2022). In addition to annual outbreaks, the emergence of novel strains through reassortment between viruses poses a risk of generating pandemic strains (Ganti et al., 2022). Reassortment events between IAVs adapted for different species are of particular concern, with four pandemics of the last 120 years comprising surface glycoprotein encoding genes of zoonotic origin (F. Wang et al., 2020; Worobey et al., 2014). Spillover events from avian species, which comprise a significant natural IAV reservoir, are of particular concern presently, with outbreaks of highly pathogenic avian influenza documented in mammalian hosts in 2025 (Alexakis et al., 2025; Mostafa et al., 2025)

A goal of the work described in this thesis is to explore the mechanisms governing reassortment in the host and pandemic strain emergence. Insights into the mechanisms of reassortment and the evolution of novel IAV strains may yield approaches capable of inhibiting their emergence and spread, significantly decreasing the burden of influenza pandemics on global human health.

1.4 Thesis overview

In this work, I seek to develop methods for imaging infections across scales, with a particular interest in IAV co-infections. As described above, the effects of SIE have been well established at the microscale but the understanding of co-infection

dynamics at the mesoscale is limited. Therefore, the goals of this project are as follows:

1.4.1 Aim 1: Developing mesoscale imaging methods for imaging infection

Here I aim to develop imaging methods capable of imaging infections on the mesoscale, focusing on whole organs. This will entail the development of optical clearing approaches capable of rendering a range of tissues transparent. Additionally, mounting and imaging methods for large tissue samples, namely light sheet microscopy, will be explored.

1.4.2 Aim 2: Developing microscale imaging methods for imaging infections

The second goal of this project was to develop methods for visualising infection at the microscale, initially via FISH and subsequently via spatial transcriptomics. As for the mesoscale imaging methods developed here, these microscale methods were developed with the intention of better understanding the dynamics of infection in tissues.

1.4.3 Aim 3: Coupling multi-length scale imaging methods to visualise IAV co-infection

The imaging methods developed here will be employed to visualise IAV co-infections across length scales. On the mesoscale, LiSM will be used to investigate the dynamics of IAV co-infection on the scale of whole lung lobes, providing spatial context to previous studies by Ganti and Amato (Amato et al., 2022; Ganti et al., 2022) On the microscale, the emergence of novel IAV strains within the interstitial spaces between infecting viruses exhibiting SIE will be explored via spatial transcriptomics. By enabling the targeting of specific IAV gene segments, these

methods can identify novel combinations of genes, expanding on previous studies of SIE via immunofluorescence.

1.4.4 Thesis chapter composition

Materials and methods are discussed in chapter 2.

In chapter 3, I develop a novel optical clearing approach for light sheet microscopy. The method developed here is based on an existing popular ethyl cinnamate (ECi)-based method. I validate this method for a variety of tissues common in light sheet microscopy studies including skin, lung, nerve, and lymphatic tissue. Additionally, I validate this clearing and imaging approach for the study of both endogenously tagged molecules and for immunofluorescence. This work improves on the existing ECi approach, improving fluorophore retention by altering the method used to dehydrate tissues and improving the transparency of cleared tissues. Using the methods developed in this chapter, I study IAV co-infection on the mesoscale, imaging co-infections of whole lung lobes for the first time. By comparing the light sheet imaging of whole lung lobes to images of co-infections of the airway epithelium captured at higher resoultion via cofocal microscopy, I identify length-scale specific co-infection dynamics and determine the effect of microscale SIE on the mesoscale pathology of IAV infection across the wider tissue. Additionally, these studies support previous *in vitro* findings which report on the extent to which SIE inhibits co-infection of cells. By identifying similar SIE behavior as observed in previous studies within airways, these studies determine the limited regions which may enable reassortment between co-infecting viruses. Such regions are of significant academic and clinical interest, as the mechanisms governing reassortment are not only poorly understood, but also underpin the emergence of novel strains with pandemic potential.

Having explored the mesoscale dynamics of IAV infection and identified microscale regions which may enable reassortment events, chapter 4, I shift focus towards the microscale. I explore FISH methods for the identification of reassotant progeny arising within the interstitial regions between superinfection excluding viral

populations during co-infection events. To this end, I create a software tool for the analysis of FISH data, FISHtoFigure. This tool acts as a downstream analysis tool for the popular image analysis software QuPath and enables the analysis of complex cell types based on user-selected markers (In the example of IAV reassortment, cells expressing mRNA from segments from co-infecting viral lineages, indicating a reassortant strain). FISHtoFigure is packaged such that no interaction with the underlying code is required to conduct such analyses, so can be used by anyone, regardless of computational image analysis experience. This tool is then validated by analysing a data set from a murine *T. brucei* infection study conducted by a fellow research group at the University of Glasgow. This analysis is now published as part of a study in Nature Communications and the software tool is published in Scientific Reports (Bentley-Abbot et al., 2024; Quintana et al., 2022)

Chapter 5 continues to probe the reassortment events occurring between adjacent viral populations via spatial transcriptomics. Using a library of genetically barcoded IAVs and the Visium spatial transcriptomics platform from 10× Genomics, I study co-infection dynamics *in vivo* and subsequently *in vitro*. Prior to this work, spatial transcriptomics platforms described in the literature were validated only for *in vivo* studies. Here, I develop a method for conducting spatial transcriptomics experiments *in vitro* for the first time. Using cells cultured on permeable membranes as surrogates for tissue sections, I successfully capture poly-adenylated RNA from cell cultures, this RNA is then successfully converted to cDNA tagged with a Visium spatial barcode which subsequently enables the recapitulation of spatial information following sequencing. This experiment provides the first validation of a novel method for performing the Visium spatial transcriptomics assay *in vitro*.I validate this *in vitro* application of spatial transcriptomics through an IAV co-infection study using a barcoded library of IAV viurses.

Finally, a general discussion of results is given in chapter 6.

Chapter 2

Materials and Methods

2.1 Materials

2.1.1 Cell lineages

Table 2.1: Cell lines used throughout this thesis

Cell Line	**Origin**	**Source**
Madin-Darby Canine Kidney (MDCK)	Dog Kidney Carcinoma	Professor Paul Digard (University of Edinburgh)
Human Embryo Kidney (HEK) 293T	Human Embryonic Kidney	Professor Sam Wilson (University of Cambridge)

2.1.2 Pathogens: Viruses and Parasites

Table 2.2: Pathogens used throughout this thesis

Pathogen	**Source**
Influenza A virus A/Puerto Rico/8/1934 (PR8; H1N1)	Professor Ron Fouchier (Erasmus MC Rotterdam) Plasmids provided by Professor Paul Digard (University of Edinburgh)
Influenza A virus A/X31 (H3N2)	Doctor Ed Roberts (University of Glasgow)
Influenza A virus ColorFlu-eGFP (Fukuyama et al., 2015)	Professor Yoshihiro Kaowaoka (University of Wisconsin-Madison, University of Tokyo)
Influenza A virus ColorFlu-mCherry (Fukuyama et al., 2015)	Professor Yoshihiro Kaowaoka (University of Wisconsin-Madison, University of Tokyo)
Influenza A virus BrightFlu-ZsGreen (Pirillo et al., 2023)	Doctor Ed Roberts (University of Glasgow)
Influenza A virus BrightFlu-ZsGreen minOVA	Doctor Huailong Zhao (University of Glasgow)
Influenza A virus BrightFlu-DsRed	Doctor Huailong Zhao (University of Glasgow)
Influenza A virus BrightFlu-mCherry	Doctor Huailong Zhao (University of Glasgow)
Barcoded influenza A virus library	Doctor Laurence Tiley (University of Cambridge)
T. b. brucei Antat 1.1E	Professor Annette MacLeod (University of Glasgow)
T. b. brucei Antat 1.1E - tdTomato reporter (Calvo-Alvarez et al., 2018)	Doctor Brice Rotureau (Pasteur Institute)

2.1.3 Antibodies

Table 2.3: Antibodies used throughout this thesis

Target	**Species**	**Primary/ Secondary**	**Conjugate**	**Origin**	**Dilution**
IAV nucleoprotein (NP)	Sheep Polyclonal	Primary	N/A	Influenza toolkit (Dundee University)	1:500 (IF) 1:200 (IHC)
IAV hemagglutinin (HA)	Rabbit Polyclonal	Primary	N/A	ThermoFisher	1:400 (IHC)
Anti-sheep IgG	Donkey Polyclonal	Secondary	AF 561	ThermoFisher	1:1000 (IF)

2.2 Cell culture and viruses

2.2.1 Passaging cells

Cells were maintained in Dulbecco's modified eagle medium (DMEM, Gibco) treated with 10% fetal bovine serum (FBS, Gibco) in tissue culture flasks (Corning). Between passages, cells were incubated at 37°C, 5% CO_2. During passage, cells were washed with phosphate buffered saline solution (PBS, Gibco) and detactched from flasks via an incubation with TrypLE trypsin (Gibco) at 37°C, 5% CO_2. Cells were then resuspended in DMEM treated with FBS as above and seeded into fresh flasks.

2.2.2 Passaging virus

Marin-Darby canine kidney (MDCK) cells were seeded in T75 flasks (Corning). Prior to infection, cells were washed with DMEM. Once cells reached 70% conflu-

ence, cells were infected at a multiplicity of infection (MOI) of 0.01 plaque forming units (PFU)/cell in 1ml virus growth media (VGM) (DMEM treated with 1mg/ml TPCK trypsin) as per (Equation 2.1). After 1 hour incubation, an additional 15ml of VGM was added. Infected cells were incubated at 37°C, 5% CO_2 for a minimum of 48 hours or until signs of cytopathic effects were visible. Supernatant was centrifuged at 1300rpm, 4°C for three minutes. Supernatant was aliquoted and stored at -80°C.

$$MOI(PFU/cell) = \frac{No.\,of\,infectious\,virus\,particles}{No.\,of\,cells} \quad (2.1)$$

2.2.3 Titration of viruses

MDCK cells were seeded into 6-well plates at 1×10^6 cells per well in DMEM treated with 10% FBS. Plates were incubated for 24 hours at 37°C, 5% CO_2.

A 10-fold dilution series was prepared for the virus being titrated. Virus dilutions were prepared in VGM. Prior to infection, cells were washed in DMEM. Each well was then inoculated with 400 μl of diluted virus and incubated at 37°C, 5% CO_2 for 1 hour with regular rocking of the plate. Inoculum was then removed and each well was then overlayed with 3ml of 50/50 vol/vol dilution of 2.4% low melt agarose (ThermoFisher) and DMEM treated with 2 μl/ml. Plates were incubated at 37°C, 5% CO_2 for a minimum of 48 hours until plaques were visible beneath the agarose overlay.

Plates were stained with Coomassie blue (2g Coomassie brilliant blue (Thermofisher), 75ml acetic acid, 500ml ethanol in 1250ml PBS) for 20 minutes at room temperature. Following the removal of Coomassie stain, plaques can be counted and titre determined via equation 2.2.

$$Titre(PFU/ml) = \frac{No.\,of\,Plaques\,(PFU)}{Volume\,of\,inoculum\,(ml) \times Dilution} \quad (2.2)$$

2.3 Animal Work

2.3.1 Mice

Housing and handling

All mouse handling, infection, culling, and tissue harvesting was performed by collaborators, either at the Cancer Research UK-Scotland Institute (CRUK) or University of Glasgow MRC-Centre for virus research (CVR). Mice were bred and housed at the CRUK (Lung samples; C57BL/6, Spleen samples; C57BL/6, Bone samples; C57BL/6) and CVR (Skin samples; C57BL/6, Brain samples; C57BL/6). All mice were sourced from Charles River. All animal work was carried out in line with the EU Directive 2010/63/eu and Animal (Scientific Procedures) Act 1986 and was approved by the University of Glasgow Animal Welfare and Ethics Review Board prior to the start of experiments. All work at the CVR was covered by project license PC8C3B25C (to Dr. Jean Rodgers), all work at the CRUK was cover by project license P72BA642F (to Dr. Ed Roberts). This work was carried out in accordance with the Animal Research: Reporting of *In Vivo* Experiments (ARRIVE) guidelines.

Sample collection and preparation for light sheet experiments

Light sheet experiments performed here imaged murine lung, skin, and bone tissues. All animal work was performed by collaborators Dr. Ryan Devlin and Jack McCowan (Lung samples), and Dr. Chiara Pirillo (Bone samples) at the CRUK - Scotland Institute, and Dr. Anneli Cooper (Skin samples) at the CVR.

Lung samples

Mice were intranasally inoculated with free virus particles. Free virus particle inoculations were performed by collaborators Dr. Ryan Devlin and Jack McCowan at the CRUK. Free virus particle inoculations were performed with IAV A/Puerto Rico/8/1934 (H1N1) (PR8), one of several BrightFlu variants of PR8 described in section 2.1.2, or as co-infections using the pair of isogenic fluorescently tagged

ColorFlu viruses described in section 2.1.2. PR8 infections were performed at an MOI of 500 plaque forming units (PFU) and BrightFlu infections were performed at an MOI of 1000 PFU, ColorFlu infections were performed at MOIs of 1000 PFU for each of the two co-infecting viruses.

In all cases mice were culled 3-6 dpi by collaborators at the CRUK via intraperitoneal (IP) injection of pentobarbital and severance of the femoral artery, death was confirmed by pedal response. Whole lungs were harvested immediately. Lungs were inflated with 1ml of 1% low melt agarose and perfused via cardiac puncture with phosphate buffered saline solution (PBS) to remove blood. Infected mice were weighed to monitor disease progression as per the ethical regulations of animal licence P72BA642F. Lung samples were fixed in PLP buffer for 24 hours at 4°C. Fixed samples were stored in PBA buffer for a maximum of three days before optical clearing. Lungs were dissected in to constituent lobes in all cases other than in section 3.2.8, in which whole lungs were imaged. Lungs from uninfected male C57BL/6 mice, culled by the same method, was harvested by collaborators at the CRUK to act as naïve controls.

Skin samples

Mice were infected via intraperitoneal injection of with *Trypanosoma brucei brucei* by collaborator Dr. Anneli Cooper at the CVR and monitored for parasitemia via tail venesection and clinical signs over the timecourse of infection. All work was carried out as per the ethical regulations of animal license PC8C3B25C. Mice were culled via cervical dislocation and death was confirmed via pedal response. Skin samples were harvest from C57BL/6 mice 45 dpi by Dr. Anneli Cooper at the CVR. Samples were stored in PBA buffer for a maximum of three days prior to optical clearing.

Bone samples

Sample harvesting and staining was performed by Dr. Chiara Pirillo at the CRUK. 9 week-old, naive C57BL/6 mice were culled via IP injection of pentobarbital and severance of the femoral artery. Death was confirmed via pedal response. Femur samples were immediately harvested and bone samples were fixed via immersion in 4% PFA at room temperature for 24h. Decalcification was performed by Dr. Pirillo prior to optical clearing by immersing tissues in 0.5M EDTA at pH 7.4, incubated at 4°C for 24h. Samples were stored in PBA for a maximum of three days prior to optical clearing.

2.3.2 Sample collection and preparation for FISH experiments

All animal work was performed either at the CVR by collaborators Dr. Juan Quintana and Dr. Matthew Sinton (brain samples), or the CRUK by collaborators Dr. Chiara Pirillo (Spleen and lung samples).

Brain samples

All brain samples were collected from 6 – 8-week-old, female C57BL/6 mice. Two mice were infected with *T. brucei* Antat 1.1E Quintana et al., 2022 by collaborators at the CVR. Mice were culled 45 dpi via rapid decapitation following isoflurane anaesthesia and whole brains were harvested immediately. Mice were monitored for disease severity using the following clinical scoring method, score (0) normal, healthy, and explorative mouse; score (1) slow, sluggish, or displaying stary coat; score (2) animals with reduced coordination of hind limbs and/or altered gait; score (3) animals with flaccid paralysis of one hind limb. Mice with clinical scores higher than (3) were humanely killed as per the ethical regulations of animal licence PC8C3B25C. Whole brains from two uninfected female mice, culled by the same method, were harvested to act as naïve controls. Brain samples were fixed in 4% paraformaldehyde (PFA) at room temperature for 24 hours.

Spleen samples

All spleen samples were collected from nine week old, male C57BL/6 mice by Dr.Chiara Pirillo at the CRUK. A mouse was intranasally inoculated with IAV A/Puerto Rico/8/1934 (PR8; H1N1). The infected mouse was culled 6 dpi via IP injection of pentobarbital and whole spleens were harvested immediately. The infected mouse was weighed to monitor disease progression as per the ethical regulations of animal licence P72BA642F. The spleen from an uninfected male C57BL/6 mouse, culled by the same method, was harvested to act as a naïve control. Spleen samples were fixed in 4% paraformaldehyde (PFA) at room temperature for 24 hours.

Lung samples

All lung samples were harvested from nine week old C57BL/6 mice by collaborators Dr. Chiara Pirillo and Dr. Ryan Devlin at the CRUK. For FISH experiments, mice were co-infected via intranasal inoculation with IAV A/Puerto Rico/8/1934 (H1N1) and IAV A/X31 (H3N2) at a multiplicity of infection (MOI) of 500 and 10,000 plaque forming units (PFU) respectively. Mice were culled by collaborators at the CRUK via intraperitoneal (IP) injection of pentobarbital and death confirmed by severance of the femoral artery. Lung tissue was immediately harvested and fixed for via 24 hour immersion in PLP buffer at 4°C. All samples for FISH experiments were embedded in paraffin by University of Glasgow Veterinary Diagnostic Services. From paraffin blocks, sections were cut on a microtome (Thermo Scientific) and mounted on glass slides for histology by the University of Glasgow Veterinary Diagnostic Facility.

2.3.3 Sample collection and preparation for spatial transcriptomics experiments

All animal work was performed by Jack McCowan at the CRUK. Mice were intranasally inoculated via single cell instillation of co-infected MDCK cells as de-

scribed below in section 2.4.6. Mice were inoculated with 5000 co-infected cells. Mice were culled 6 dpi via IP injection of pentobarbital and severance of the femoral artery. Death was confirmed by pedal response. Lungs were immediately harvested and transferred from the CRUK animal unit to the CRUK primary facility for further processing. Lungs were then flash frozen via immersion in liquid nitrogen-cooled isopentane for 2 minutes. Frozen tissue was stored at -80°C for a maximum of 2 weeks prior to sectioning. Samples were cryosectioned and mounted onto Visium tissue optimisation or Visium spatial gene expression slides by the CRUK histology department.

2.3.4 Mosquitoes

Wildtype *Anopheles coluzzii* mosquitoes were provided by Professor Steven Sinkins (University of Glasgow). The lineage originates from Burkina Faso. Mosquitoes were housed at the CVR, University of Glasgow, managed and handled by Dr. Ewan Parry.

Other tissues were imaged and are described in chapter 3. These other tissues were imaged as part of collaborations with external users. Rather than describe methods for each case here, animal handling, infections, and culling details are provided in relevant subsections of chapter 3.

2.4 In vitro experiments

2.4.1 Plaque assays on transwell membranes

Transwell plates (8 μm pore pore size, polycarbonate membrane (Corning)) were incubated in DMEM treated with FBS at room temperature for one hour. Membranes were then seeded with MDCK cells at 1×10^6 cells per well. Plates were incubated for 24 hours at 37°C, 5% CO_2. Membranes were then washed in DMEM. A 10-fold dilution series of the influenza A virus (IAV) IAV/Puerto Rico/8/1934(H1N1) (PR8) was prepared in VGM. DMEM wash was removed and membranes were underlayed with 2 ml of VGM. Membranes were inoculated with

400 μl of diluted virus and incubated at 37°C, 5% CO_2 for one hour, rocking every 10 minutes.

Following incubation, media (inoculum within the transwell and underlay in the outer well) was removed and membranes overlayed with 2 ml of 50/50 vol/vol dilution of 2.4% low melt agarose and DMEM treated with 2 μl/ml. Agarose was allowed to set for 20 minutes before membranes were again underlayed with fresh VGM. Plates were incubated at 37°C, 5% CO_2 for 48 hours.

Underlayed VGM was discarded and agarose removed from memrbanes. Membranes were stained with Coomassie blue (2g Coomassie brilliant blue (Thermofisher), 75 ml acetic acid, 500 ml ethanol in 1250 ml PBS) for 20 minutes at room temperature. Stain was removed and membranes washed in water.

2.4.2 Comet assays on transwell membranes

Transwell plates (8 μm pore pore size, polycarbonate membrane (Corning)) were incubated in DMEM treated with 10% FBS for one hour at room temperature before seeding with MDCK cells at 1×10^6 cells per membrane. Plates were incuabted for 24 hours at 37°C, 5% CO_2. Membranes were washed with DMEM. IAV PR8 was prepared in a 10-fold dilution series in VGM. DMEM wash was removed and membranes were underlayed with 2ml of VGM. Each membrane inoculated with 400 μl diluted virus and plates were incubated at 37°C, 5% CO_2 for one hour, rocking the plate every 10 minutes. Membranes were overlayed with 2ml VGM and incubated as above for 48 hours without motion or disturbance. Following incubation, underlay and overlayed media was removed and membranes were stained with Coomassie blue for 20 minutes at room temperature. Stain was removed and membranes washed with water.

When staining membranes seeded in parallel at different timepoints post infection, transwell membranes were transferred into separate 6-well plates (Corning) prior to infection. This ensures later timepoints are not disturbed during staining.

2.4.3 Immunofluorescence on transwell cell cultures

Transwell membranes were incubated at room temperature for one hour. Membranes were seeded with MDCK cells at 1×10^6 cells per well in DMEM treated with 10% FBS before incubating for 24 hours at 37°C, 5% CO_2. Cell monolayers were washed with DMEM. Cells were then infected at an MOI of with IAV BrightFlu-ZsGreen in 400 μl VGM. Plates were incubated for 15 minutes, with rocking every five minutes, after which time wells were underlayed and overlayed with 2ml VGM. Plates were incubated for a further 24 hours.

All media was removed from transwells and monolayers were fixed in 4% formaldehyde for 20 minutes at room temperature before three washes with 2% FBS in PBS. All steps from this point were performed in the dark to prevent fluorophore bleaching. Membranes were blocked in PBS treated with 2%FBS for two hours at room temperature. Cells were then permeabilised via a seven minute incubation in 0.02% Triton X-100 (SigmaAldrich) in PBS, both the inner and outer wells were filled with reagent. Cells were washed and blocked again as above. Membranes were cut from wells with a scalpel and placed on 76×26 mm VWR microscope slides (Avantor). Cells were stained for IAV nucleoprotein (NP) (table 2.3) for one hour before washing three times with PBS and secondary staining (AF568 conjugated anti-sheep (table 2.3)) for 30 minutes, each incubation was performed in a humid environment at room temperature. Membranes were washed three times with PBS and dried before overlaying with prolong gold mounting media and coverglass. Edges of coverglass were sealed with clear nail varnish and slides stored in the dark at 4°C for no longer than three days before imaging.

2.4.4 In vitro FISH

FISH probes against IAV H1N1 and H3N2 haemagglutinin and neuraminidase were validated. Probes were designed by me and produced by the ACDBio RNAScope team, were validated *in vitro*.

13 mm diameter coverglass (Avantor) was sterilised by washing with ethanol,

dried, and placed in 24-well plates. MDCKs were seeded onto coverglass at 2×10^5 cells per well and plates were incubated at 37°C, 5% CO_2 for 24 hours.

MDCK monolayers were infected with IAV PR8 or IAV A/X31 (H3N2) at MOIs of 0.02, 0.4, and 2 in 400 μl VGM. Plates were incubated for one hour with rocking every 10 minutes before inoculum was removed and wells were overlayed with 1ml VGM. Plates were incubated as above for a further five hours. VGM overlay was removed and fixation performed via incubation in 4% formaldehyde (Aldrich) in PBS (Gibco) at room temperature for 20 minutes. Monolayers were wash three times in PBS before being transferred to 100% ethanol via an ethanol:PBS dilution series as recommended by ACDBio RNAScope. The plate was then stored at -20°C overnight.

Coverglass was removed from wells and afixed to VWR microscope slides (Avantor), cell-side up, via a drop of clear nail varnish. Cells were then rehydrated via one minute washes of an ethanol:PBS dilution series. Cells were permiabilised via a 10 minute incubation in PBS treated with 0.1% Tween-20 (Sigma Aldrich) at room temperature before a one minute wash in PBS. Cells were bleached in 3% hydrogen peroxide (Biotechne) for 10 minutes at room temperature, washed in PBS and incubated for 10 minutes with Protease 3 (Biotechne) diluted 1:15 in PBS at room temperature in a humid environment for 10 minutes. A one minute wash was performed in PBS before commencing the standard RNAScope protocol. This protocol is described in full by Biotechne, however, it is described briefly below (F. Wang et al., 2012).

Slides were placed in RNAScope slide tray (Biotechne and RNA target probes (Biotechne) were mixed and added to cells. Slide tray was then placed in a HybEZ 2 Oven (Biotechne) pre-heated to 40°C for two hours. Slides were removed from the oven and washed twice for two minutes in RNAScope wash buffer (Biotechne). Target probes were amplified via 40°incubations in a HybEZ 2 oven with Multiplex FL v2 Amp 1, 2, and 3 reagents (Biotechne) for 30, 30 and 15 minutes respectively. Slides were washed twice for two minutes in RNAscope wash buffer between steps. A fluorophore were bound to the first target probe (designated C1) via incubation

with Multiplex FL v2 HRP-C1 reagent (Biotechne), a fluorescent dye (table 2.4), and finally Multiplex FL v2 HRP blocker (Biotechne), washing as above between steps. This process was then repeated for the three remaining target probes.

Slides were washed twice as above before being mounted in Prolong gold mounting media (Invitrogen) and coverglass being applied. Edges of coverglass were sealed with clear nail varnish and slides were imaged via Zeiss LSM 710.

Table 2.4: Opal fluorophores (Akoya Bioscience) used for FISH experiments throughout this work

Fluorophore	**Dilution**	**Source**
Opal 520	1:1500	Akoya Bioscience
Opal 540	1:1500	Akoya Bioscience
Opal 570	1:1500	Akoya Bioscience
Opal 650	1:750	Akoya Bioscience

2.4.5 RNA extractions of transwell cell cultures

Transwell membranes were prepared and seeded with MDCKs as described in section 2.4.1, and incubated at 37°C, 5% CO_2 for 24 hours. Following incubation, membranes were either left uninfected or washed with DMEM, underlayed with 2ml of VGM and infected at an MOI of 0.5 with IAV PR8 in 400 μl VGM. Infected plates were incubated as above for one hour with rocking every 10 minutes. Infected plates were then overlayed with 2ml VGM and all plates were incubated for 48 hours as above. Overlayed and underlayed media was then removed and transwell membranes dried by tapping over blue roll. Membranes were cut from transwells using a scalpel and immediately transferred to an 1 ml eppendorf tube containing 1ml RLT lysis buffer (Qiagen). Membranes were incubated in lysis buffer for 10 minutes at room temperature before briefly vortexing (Scientific Industries). Following vortexing, RNA extractions were performed following the standard Qiagen RNeasy mini kit protocol (Qiagen). Eluted RNA was transferred to -80°C on ice.

2.4.6 In vitro spatial transcriptomics

Barcoded virus library

The barcoded virus library used here was developed by Jinqi Fu at the University of Cambridge during her PhD (Fu, 2018). The library comprises PR8 derived IAVs genetically modified to contain a genetic barcode comprising mutations to wobble bases of synonymous codons (table 2.5).

Table 2.5: Sequences for barcodes in each segment as reported by Jinqu Fu (Fu, 2018).

PB2 barcode sequences

Barcode	Sequence
BC1	ttg atc atc gct gcc agg aac att gtt agg
BC2	ttg atc atc gct gcc agg aac ata gta aga
BC3	ttg atc atc gct gct aga aac att gtt aga
BC4	ttg atc atc gct gct aga aac ata gta agg
BC5	ttg atc atc gca gcc aga aac att gta agg

HA sequences

Barcode	Sequence
BC1	ggc tac cat gcg aac aac tcc acc
BC2	ggc tac cat gcg aac aat tca act
BC3	ggc tac cat gca aat aac tcc act
BC4	ggc tac cat gca aat aat tca acc
BC5	ggc tat cat gcg aat aac tca acc

NP sequences

Barcode	Sequence
BC1	cag ggc tcg acc ctc cct agg agg tcc
BC2	cag ggc tcg acc ctc cct aga aga tct
BC3	cag ggc tcg acc ctt ccg agg agg tct
BC4	cag ggc tcg acc ctt ccg aga aga tcc
BC5	cag ggc tcg act ctc ccg agg aga tcc

The specific synonymous codons selected to encode the barcode were selected to avoid altering RNA sequences conserved for viral functions such as packaging and were based on the work of Gog *et al.* examining the variability of wobble bases during IAV evolution (Gog et al., 2007). Segments 1, 4, and 5 are barcoded and each segment has five barcode variants (figure 2.1). The barcodes in each segment are constructed with a minimum Hamming distance of 3. Hamming distances describe the number of errors which can occur in a sequence, via mutation or sequencing errors for example, before the sequence cannot be distinguished from another barcode. In this case, barcodes can sustain two sequencing errors and still be read accurately. Five barcoded viral stocks were produced from a stock of each virus kindly provided by Dr. Laurence Tiley at the University of Cambridge.

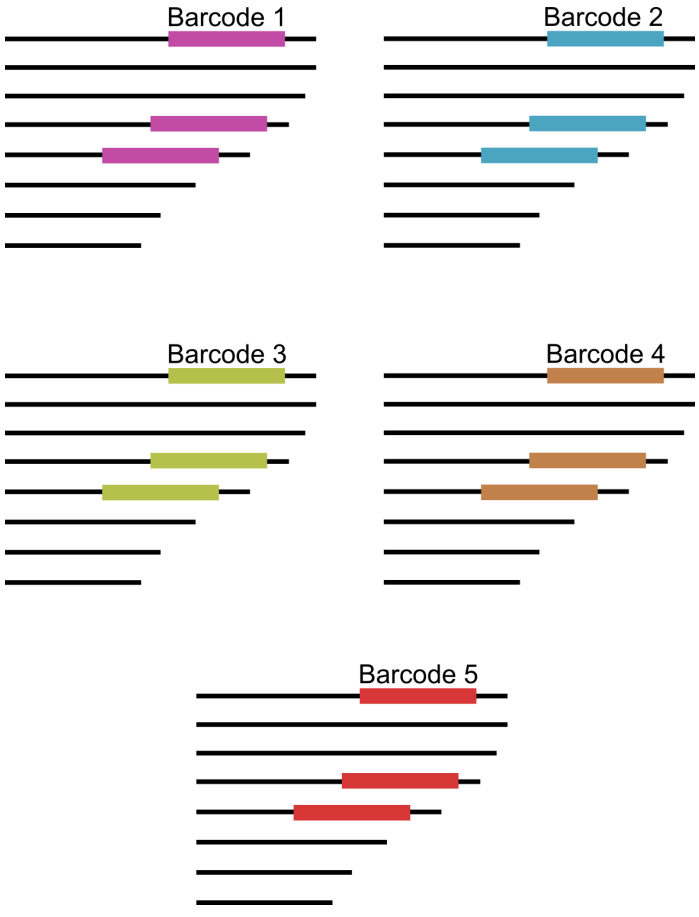

Figure 2.1: Barcode positions in barcoded IAV library. Library designed by Dr. Jinqi Fu (University of Cambridge).

Validation of barcodes

Barcode sequences were compared with those described by Dr. Jinqi Fu via Sanger sequencing (Fu, 2018). MDCK cells cultured in 6-well plates as described in 2.2.1. MDCK monolayers were infected with a single barcoded virus at an MOI of 1 PFU/cell and overlayed with VGM. Monolayers were incubated overnight at 37°C. Monolayers were then trypsinised via incubation in TPCK-trypsin at 37°C until cells detached from the plate surface. Cells were resuspended in DMEM and RNA was extracted via Qiagen RNeasy kit, as described in section 2.4.5. Barcode sequences were amplified via polymerase chain reaction (PCR) (C1000 thermal cycler, Bio-Rad) using primers described in table 2.6.

Table 2.6: PCR primers for amplification of barcode sequences

Target Gene	Direction	Start Position	End Position	Sequence	Tm	Amplicon Length
PB2	Forward	314	336	tgacatggtggaataggaatgg	59	766
PB2	Reverse	1059	1080	gtttgaagattgcccgtaagc	59	766
HA	Forward	34	54	tgaaggcaaacctactggtc	57	600
HA	Reverse	613	634	tgttaggcgggtgatgaatac	57	600
NP	Forward	57	77	aggcaccaaacgatcttacg	57	792
NP	Reverse	828	849	cctctcaatatgagtgcagacc	57	792

PCR products were visualised via agarose electrophoresis to validate that products were of the expected size for barcode sequences. Products were then sent to Eurofins for Sanger sequencing along with specifically designed primers for sequencing of each barcoded segment. Sequencing primers are described in table 2.7. Tm describes the melting temperature. Note that the primer used for sequencing of the HA segment is the same as the forward PCR primer. This was due to the proximity of the barcode region to the 5' end of the HA sequence. Sequencing and sequencing results are described in detail in section 5.2.1.

Table 2.7: Sequencing primers for Sanger sequencing of barcoded amplicons

Target Gene	Start Position	End Position	Sequence	Tm
PB2	740	763	catgctgggaacagatgtatact	58
HA	34	54	tgaaggcaaacctactggtc	57
NP	474	497	gaatgatgcaacttatcagagga	57

Performing spatial transcriptomics in vitro via the Visium spatial gene expression assay

Transwell membranes were prepared and seeded with MDCK cells as described in section 2.4.2. A 6-well plate was seeded with MDCK cells at 1×10^6 in DMEM treated with 10% FBS. Both plates were incubated at 37°C, 5% CO_2 for 24 hours.

The 6-well plate was washed with DMEM and infected at a total MOI of 3 PFU/cell with a cocktail of viruses in VGM (IAV BrightFlu-ZsGreen and five barcoded IAV PR8-derived viruses, each at an MOI of 0.5 PFU/cell). Inoculated cells were incubated at 37°C, 5% CO_2 for one hour with rocking every 10 minutes. Inoculum was then removed and cell monolayers overlayed with VGM. Plates were incubated for a further three hours as above.

Following incubation, 500 μl of TrypLE trypsin (Gibco) waas added to each well and the plate was incubated at 37°C, 5% CO_2 for 20 minutes to detach infected cells. Detached cells were resuspended in an additional 500 μl of VGM and centrifuged at 1300 rpm for three minutes at 4°C. Supernatant was removed and pelleted cells were resuspended in 500 μl VGM. Resuspended cells were diluted 100-fold in VGM.

Transwell membranes were washed in DMEM and underlayed with 2 ml of VGM. Membranes were inoculated with 400 μl of the infected cell dilution described above and incubated at 37°C, 5% CO_2 for one hour, rocking every 10 minutes. Membranes were then overlayed with 2ml VGM under comet assay conditions and incubated at 37°C for 24 hours.

Following incubation, membranes were fixed in methanol for 30 minutes at -20°C. Samples were washed using PBS and imaged via widefield fluorescence

microscope (EVOS) to identify transwells containing suitable numbers of comets for spatial transcriptomics analysis. Membranes were then cut from transwells and dissected into quarters to fit the capture areas of the 10× Genomics Visium gene expression assay slides. Membrane sections were then mounted on the Visium slide and the RNA capture and cDNA synthesis performed on the slide. This protocol is described in full by 10× Genomics (www.10xgenomics.com/support/spatial-gene-expression-fresh-frozen), however, it is briefly outlined below.

Samples were not immunostained and imaged due to the need to overlay samples with coverglass, and subsequently remove this coverglass, for imaging. This was deemed liable to delaminate membrane sections from the Visium slide. Cells were permeabilised via incubation with the 10× Genomics Visium permeabilisation reagent cocktail. RNA is captured by oligonucleotides attached to the Visium slide. cDNA and second strand synthesis is performed on the slide via incubation with proprietary 10× Genomics reagents. cDNA is aliquoted and was frozen at -80°C for approximately one week prior to library preparation for Illumina and oxford nanopore sequencing sequencing. All sequencing was performed by the CVR Genomics facility, specifically Dr. William Rooney.

2.5 In vivo experiments

2.5.1 Optical clearing of tissues

Optical clearing was performed using an ethyl cinnamate (ECi) (Tokyo Chemical Industries) based approach, with differences to specific steps depending on tissue type.

Certain tissue types require different preprocessing steps prior to dehydration and optical clearing to ensure clearing efficacy. The development of tissue-type-specific processing methods for clearing are discussed in greater detail in chapter 3, however, processing of each tissue type tested is briefly discussed here.

Highly melanised tissues (lungs containing melanoma and mosquitoes) were bleached prior to dehydration in 6% hydrogen peroxide (Fisher Scientific) in PBS.

Bleaching was performed in a water bath at 40°C. Bone samples were decalcified prior to dehydration via incubation in 0.5M EDTA (Fisher Scientific) at pH 7.4, incubated at 4°C for 24h. Dehydration was performed using either an PBS:ethanol (table 2.8) or PBS:tertiary butanol (table 2.9) dilution series. Tertiary-butanol was treated with triethylamine (ThermoFisher). In all cases, incubations were performed at room temperature under consistent agitation.

Table 2.8: Ethanol dehydration protocol for optical clearing

Dilution (in milli-Q water)	**Incubation time**
25% ethanol	8 hours
50% ethanol	16 hours
75% ethanol	8 hours
100% ethanol	16 hours

Table 2.9: Tertiary-butanol dehydration protocol for optical clearing

Dilution (in milli-Q water)	**Incubation time**
30% tertiary-butanol + 8μl/L triethylamine	8 hours
50% tertiary-butanol + 8μl/L triethylamine	16 hours
70% tertiary-butanol + 20μl/L triethylamine	8 hours
90% tertiary-butanol +120μl/L triethylamine	16 hours
100% tertiary-butanol + 8ml/L triethylamine	8 hours

Refractive index matching was performed using either an ethanol:ECi (table 2.10) or tertiary butanol:ECi (table 2.11) dilution series depending on the dehydration method used. All incubations were performed at room temperature under consistent agitation.

Tissues can be stored in ECi at room temperature for up to one month before imaging without any sign of degradation to the tissue.

Table 2.10: Ethyl cinnamate refractive index matching following ethanol dehydration

Concentration	**Incubation time**
50% ethyl cinnamte (in ethanol)	8 hours
100% ECi	24 hours

Table 2.11: Ethyl cinnamate refractive index matching following tertiary-butanol dehydration

Concentration	**Incubation time**
50% ethyl cinnamte (in tertiary-butanol + 8ml/L triethylamine)	8 hours
100% ECi	24 hours

2.5.2 Tissue embedding for light sheet microscopy

1% low melt agarose (Thermofisher) was prepared in PBS (Gibco) and allowed to set before use. Agarose was dissolved by heating and cooled until it could be comfortably held by hand to avoid damaging tissues during embedding. Samples for embedding were immersed in 1% agarose in a 35 mm dish (ThermoFisher). The tapered end was removed from a 1 ml syringe (Becton Dickinson) and this modified syringe was used to take up a volume of agarose containing the sample. Agarose was allowed to set for 30 minutes at room temperature. The agarose plug was ejected from the syringe and optically cleared using tertiary butanol and ethyl cinnamte dilutions similarly to above but with incubation times decreased to one hour per dilution.

2.5.3 Preparation of thick tissue sections

Fixed lung tissue was sectioned via vibratome (Campden Instruments). 300 μm thick sections were cut and stored in PBA (in the dark for sections containing endogenous fluorophores) at 4°C prior to optical clearing. To optically clear tissue, sections were incubated in Ce3D (BioLegend) for two hours at room temperature under consistent agitation. Cleared sections were mounted on VWR microscope slides (Avantor) and 1mm tall microscope slide gaskets (ThermoFisher) were placed around tissues to ensure that tissues were not deformed between slide and coverglass. The chamber formed by the gasket was filled with Ce3D reagent and covered with coverglass (Avantor). Edges of coverglass were sealed with clear nail polish.

Thick sections were imaged via Zeiss LSM 880. Images were captured via 20$\times$ objective lens (Zeiss), 488nm and 561nm laser lines (Zeiss) using Zen black (Zeiss) software. Downstream processing was performed in Imaris (BitPlane)

2.5.4 Immunohistochemistry staining of tissues

Immunohistochemistry (IHC) staining was performed by University of Glasgow Veterinary Diagnostic Services.

PLP fixed lungs were embedded in paraffin and 10μm thick tissue sections were cut and mounted onto VWR microscope slides (Avantor). Sections were deparaffinised by two five-minute incubations in xylene (May and Barker) at room temperature. Sections were rehydrated using an ethanol:distilled water dilution series followed by wash in distilled water.

Antigen retrieval was performed via 30 minute incubation at 90°C in sodium citrate antigen retrieval buffer at pH 6. Sections were washed with distilled water prior to antibody staining. Sections were stained for influenza A virus NP and HA on seperate adjacent sections with secondary chromogenic staining using a DAB conjugated anti-sheep and anti-rabbit antibodies respectively, each at 1:1000. Sections were imaged via Slide scanner (Licor).

2.5.5 In vivo FISH

Tissues for FISH analysis were embedded in paraffin by University of Glasgow Veterinary Diagnostic Services. 10 μm thick tissue sections were cut and mounted on VWR microscope slides. FISH was performed via the RNAScope protocol (ACD-BioTechne). Sections were deparaffinised via two five-minute incubations in xylene and rehydrated via an ethanol:PBS dilution series, each at room temperature. RNAscope antigen retrieval buffer (BioTechne) was added to sections and slides were incubated in a HybEZ 2 oven (BioTechne) at 60°C for two hours. Slides were removed from the oven and washed for two minutes with constant rocking in RNAScope wash buffer (BioTechne), wash was repeated with fresh buffer. Sections were then treated with Protease Plus (BioTechne) for 10 minutes at room teperature in a humid environment. Sections were washed as above. From this point, the protocol was identical to the RNAScope protocol described above in section 2.4.4. Slides were mounted as described above and stored at 4°C in the dark for no longer three days before imaging. Commercial RNAScope control

slides containing mouse NIH 3T3 cells (Advanced Cell Diagnostics, US) were used as a positive control sample for RNAScope for all samples. Fresh probe mixes containing the RNAScope probes were prepared for each experiment (table 2.12).

Table 2.12: Detection channels and associated targets and fluorophores for RNAScope experiments.

Target	**Channel**	**Detection Dye**	**Peak Emission Wavelength (nm)**	**Dilution**
Pol2ra	C1	Opal 520	525	1:1500
Ppib	C2	Opal 570	570	1:1500
Ubc	C3	Opal 690	694	1:1500
Dapb	C1, C2, C3	Opal 520/ 570/690	525, 570, 694	1:1500
Cd79a	C1	Opal 520	525	1:1500
Cd4	C4	Opal 650	650	1:1500
Cx3cr1	C2	Opal 650	650	1:1500
Il10	C3	Opal 570	570	1:750
Il10-ra	C4	Opal 540	536	1:1500

2.5.6 RNA extractions from tissues

Mouse lungs were frozen immediately following tissue harvesting via plunging in isopentane (SigmaAldrich) cooled on a bed of dry ice for two minutes. Lungs were immediately stored at -80°C until cutting. 40 μm tissue scrolls were cut on a CM1950 cryotome (Leica) and stored at -80°C before RNA extraction.

To homogenise tissues, scrolls were incubated in 500 μl QIAzol (Qiagen) for one minutes at room temperature before being shredded via Qiagen TissueShredder protocol. Briefly, a ceramic ball is added to the QIAzol-tissue mixture and mixture is rapidly shaken for two minutes to disrupt and homogenise tissues. 500 μl of chloroform (SigmaAldrich) was added to QIAzol mixture and mixed before centrifuging at 12,000×g for two minutes. Supernatant was transferred to an RNeasy

mini kit spin column (Qiagen) and RNA isolated via RNeasy mini kit (Qiagen). Eluted RNA was transferred to -80°C on ice.

2.5.7 In vivo spatial transcriptomics

MDCK cells were seeded into 6-well plates at 1×10^6 cells/well in DMEM treated with 10% FBS and incubated for 24 hours at 37°C, 5% CO_2. Cells were co-infected with IAV BrightFlu ZsGreen alongside a library of barcoded viruses at a total MOI of 3 PFU/cell as described above in section 2.4.6. The MOI was selected based on the titre of barcoded stocks (on the order of 10^5 PFU/ml) and the volume limitations of 6-well plates. Higher MOI infections were not feasible due to these volume limitations. This MOI was determined to result in co-infection of a satisfactory proportion of cells to conduct transcriptomics experiments, as explained in section 5.2.2. Cells were harvested as described above. Cells were spun down and counted via Countess cell counter (Invitrogen) and diluted in VGM to a concentration of 20,000 cells/ml. C57BL/6 mice were anaesthetised and inoculated via intranasal instillation with 50 μl of co-infected cells for a total MOI of 1000 PFU. Instillations were performed by Dr. Ryan Devlin at the CRUK. Following infection, mice were housed, infected, and culled at the CRUK. Following infection mice were weighed and monitored daily, mice falling below humane weight standards were culled. Mice losing 20% of bodyweight were deemed to have reached the humane endpoint of the study and were humanely culled.

Mice were culled by collaborators at the CRUK and lung samples taken 3 and 6 days post infection (dpi). Samples were harvested and fixed as described above. Samples were transported to from the CRUK animal facility to the primary CRUK facility and flash frozen by plunging in isopentane cooled on a bed of dry ice for two minutes. Samples were then immediately transferred to -80°C and stored for a maximum of three weeks before sectioning.

10 μm thick sections were cut on a cryotome and mounted onto Visium spatial transcriptomics slides (10× Genomics) by the CRUK Veterinary histology facility. Slides were stored at -80°C for no more than 14 days before processing.

Sections were stained, imaged, and lysed, and RNA captured, cDNA generated and aliquoted as per the 10× Genomics Visium spatial transcriptomics protocol. The protocol is described in full by 10× Genomics, however, it is briefly described here (Marx, 2021).

Tissues were stained for NP as described above in section 2.4.3. Slides were then imaged via fluorescent slide scanner (Leica), 4× objective, 488nm and 561nm laser lines.

Coverglass was removed and cells permiabalised and lysed via incubation with 10× Genomics Visium permeabilisation reagent cocktail via thermocycler (ThermoFisher) enabling RNA capture on the slide. cDNA was generated on the slide by incubation with Visium cDNA synthesis and second strand generation reagents. cDNA was then aliquoted and stored at -80°C until library construction and processing.

Library construction and sequencing was then carried out by the CVR Genomics facility, via Illumina sequencing supported by long read nanopore sequencing (Oxford Nanopore Technology). Due to the position of barcoded regions within segments 1, 4, and 5 of the IAV genome, Illumina sequencing, as recommended by 10× Genomics, was deemed insufficient as library preparation for Illumina sequencing results in the fragmentation of genetic material. (Tan et al., 2019). The Visium method relies on a spatial identifier sequence attached to captured RNAs to determine the position from which that RNA was captured in the tissue section. The fragmentation associated with Illumina sequencing would separate barcodes from the spatial identifier sequences, compromising the ability to spatially reconstrcut the RNA map of the tissue. Long read sequencing was performed via Oxford Nanopore Technology (ONT) in parallel with Illumina sequencing to ensure the capture of barcode sequences (Marx, 2023).

2.6 Sample imaging and computational image analysis

2.6.1 Confocal microscopy

Imaging of cell monolayers, and thin and thick tissue sections was performed using either a Zeiss LSM 710 (thin sections probed using RNAScope FISH methods) Zeiss LSM 880 (all other sections) confocal microscopes. A Zeiss LSM 710 was used for RNAScope imaging due to the higher number of imaging channels afforded by spectral imaging.

Cell monolayers and thin sections were mounted in Prolong Gold mounting medium (Invitrogen) and covered with 22×50 mm coverglass (Avantor) prior to imaging. Thick sections were prepared using a gasket as described in section 2.5.3 before being covered with coverglass. Mounted slides were stored in the dark at 4°C for a maximum of three days before imaging.

Images were captured using 20× air immersion, 40× oil immersion, or 63× oil immersion objective lenses (Zeiss), with immersion oil (Zeiss) added between the lens and coverglass. All imaging was performed using 405 nm, 488 nm, 561 nm, and 633 nm laser lines (Zeiss).

Images were acquired in Zen black software (Zeiss) and downstream analysis was performed in FISHtoFigure for RNAScope data or Imaris (Bitplane) for all other imaging data.

2.6.2 Light sheet microscopy

All light sheet microscopy was performed on either a Zeiss Z1 light sheet microscope or a Miltenyi Ultramicroscope Blaze system.

Zeiss Z1 imaging

Sample mounting requires a flat face, therefore depending on sample morphology some samples were cut with a scalpel to provide a face for mounting. Cutting was

performed such that the minimum possible amount of tissue was removed. Samples were adhered to the Z1 mounting pin using superglue (GorillaGlue) and allowed to adhere for 20 minutes at room temperature. Samples were suspended within the sample chamber from above and the chamber filled with ECi. Samples were incubated in ECi in the sample chamber for 30 minutes before imaging to ensure no bubbles remained in the immersion media. Imaging was conducted using a 20× oil immersion lens (Zeiss) and 405 nm, 488 nm, and 561 nm laser lines (Zeiss) and 515-545 nm and 585-615 nm filter sets for emitted signal capture respectively. Image capture was performed using Zen black light sheet edition software (Zeiss) and downstream processing was performed in Imaris (BitPlane).

Miltenyi Ultramicroscope Blaze

All data captured via Ultramicroscope Blaze presented here was captured via a 4× objective lens, tuned via correction collar to an RI of 1.56. Samples were illuminated using 488 nm and 561 nm lasers and 515-545 nm and 585-615 nm filter sets. Samples were glued (GorillaGlue) to the mounting rail at the bottom of the chamber to prevent movement during imaging. ECi was used as an immersion medium. Sample data were stitched and rendered via Imaris as above.

2.6.3 FISHtoFigure

Development of the FISHtoFigure software and methodology is described in detail in chapter 4. FISHtoFigure is a Python-based analytical software tool, written in Python 3.13.0, designed to quantify cell expression profiles within FISH data. Expression profile analysis is conducted in FISHtoFigure using the Pandas library (Reback et al., 2022). A two-branched strategy is used to isolate cellular and subcellular data into two new datasets. Graphical outputs are generated using a combination of the Matplotlib and Seaborn Python libraries (Caswell et al., 2021; Waskom, 2021). In addition to the graphical outputs, data from FISHtoFigure analysis are stored in CSV format for downstream statistical analysis. The statistical tests in this paper were performed with GraphPad PRISM, non-parametric tests

were selected due to lack of normality. All processing was carried out on an ASUS vivobook laptop or Apple Macbook. The applications and efficacy of FISHtoFigure in comparison to other existing tools for FISH data analysis are discussed at length in Chapter 4.

QuPath image analysis

FISHtoFigure relies on the open source image analysis suite, QuPath, for image pre-processing. QuPath 0.3.1 Software was used to quantify the number of transcripts for each target probe in FISH micrographs (Bankhead et al., 2017). Negative control images were generated by probing spleen and brain tissue sections with the RNAScope 3-plex negative control probes. Fluorescence measurements for each detection channel in the negative control images were subtracted from final experimental images to determine background fluorescence thresholds. Subtracting background fluorescence in this way ensures that all detected fluorescent spots represent true signal from RNA transcripts. Using in-built QuPath annotation tools, one large region of interest (ROI) was specified on each image such that the whole image was encompassed in a single annotation. The "Cell Detection" function was used to determine the number and position of cells in each ROI based on the DAPI nuclear stain (under the assumption that one nucleus represented one cell), and the 'Subcellular Detection' function was used to calculate the number of transcripts for each target. The accuracy of QuPath's automated annotation features have been confirmed by comparison to annotation by expert human analysts (Bankhead et al., 2017). QuPath output data were then used as input data for FISHtoFigure. The analysis workflow was scripted to enable batch processing of all images within each dataset.

2.6.4 Zen and Imaris

All imaging performed on Zeiss LSM 710 and 880 were captured in Zeiss Zen black edition. Data were captured as tiled images and each tile was saved as an individual file. CZI (Zeiss) files were converted to IMS files (Imaris) via Imaris file

converter (Bitplane). Individual tile files were stitched into full images using Imaris Stitcher (Bitplane) and processed in Imaris (Bitplane).

All imaging performed on Zeiss Z1 sheet microscopes was captured in Zeiss Zen black (light sheet) edition. Data were captured as tiled images and processed as above. Processed image data were then visualised and analysed in Imaris.

All imaging performed via Ultramicroscope Blaze was captured in Miltenyi's proprietary Ultramicroscope imaging software. Data were processed via Imaris stitcher and visualised as above.

Chapter 3

Developing methods for imaging of large tissues

3.1 Introduction

3.1.1 History of optical microscopy

The advent of light microscopy dramatically altered the understanding of *in vitro* and *in vivo* biological systems, enabling the visualisation of constituent components of tissues at previously unattainable resolution. The basic brightfield microscope, in which a sample is illuminated from below and transmitted light captured by a spherical objective has since been steadily improved upon. Improvements in objective lens manufacturing have enabled larger, higher numerical aperture lenses to be designed, improving resolution and field of view.

A significant breakthrough came in the development of the confocal microscope. Functionally similar to a brightfield, a confocal microscope incorporates a pinhole axially locked to the focal plane of the microscope. This eliminates out-of-focus light from reaching the objective lens, significantly improving axial resolution. This is particularly important for *in vivo* studies which, unlike studies on cell monolayers, comprise cells across the depth of the tissue. The development of epifluorescence imaging and fluorescent labeling elevated confocal microscopy, enabling researchers to tag specific proteins and cellular structures, either by an-

tibody labelling or genetic modification to encode fluorescent proteins. These fluorescent proteins, fluorophores, have well characterised excitation and emission profiles and therefore by sequentially illuminating a sample with monochromatic light sources multiplex images can be built up in layers corresponding to each tagged protein.

Epifluorescence confocal microscopy, in conjunction with high numerical aperture has enabled high resolution, multiplex imaging of large tissues, up to centimeters in the x and y axes. However, imaging depth and resolution in the z axis is limited due to scattering and refraction of illumination and excited light. This effect limits confocal imaging to a maximum thickness of approximately 100 μm, depending on the tissue. High precision sectioning of tissues using tools such as a vibratome or cyrotome enables sections with thicknesses on the order of tens of microns, however, sectioning reduces spatial context of results and does not allow for imaging of larger structures in their entirety.

Multi-photon imaging has improved imaging depth through the use of long wavelength illumination. Wavelength is inversely proportional to attenuation, meaning long wavelength light can penetrate, and by extension illuminate, deeper tissues. Two-photon microscopy exploits the principle of second harmonic generation, by which excitation with two low energy photons can excite an electron to an energy state higher than the energy carried by either photon individually (figure 1.17).

Thus, traditional fluorophores can be excited by pairs of low energy photons capable of penetrating further into the tissue. However, despite this effect, multi-photon illumination only improves z axis imaging depth to approximately 1-2 mm. However, in comparison to light sheet microscopy, multi-photon illumination is slow and prone to bleaching. Additionally, while 1-2mm depth may enable the imaging of some murine organs, lightg sheet imaging has been extended to significantly larger samples on the scale of whole mice (Cai et al., 2023).

3.1.2 Optical clearing of tissues

Optical tissue clearing circumvents the effects of scattering and refraction on imaging depth by rendering tissues transparent. Many clearing methods have been developed and differ significantly depending on the composition of the tissue being cleared. Broadly, tissue clearing strategies comprise two key steps; dehydration and refractive index matching. Water has a low refractive index (1.33) relative to surrounding tissues and therefore dehydration is essential prior to refractive index matching to ensure that refraction across the tissue volume is minimised. Refractive index matching involves incubating dehydrated tissues in a compound of known refractive index capable of permeating the tissue. A change of refractive index yields a change in speed and direction of incident light, resulting in divergence of light and reduction in image clarity. This process of replacing low refractive index (RI) water with a high RI solution, aims to remove refractive index boundaries across the tissue volume and renders tissues clear (figure 3.1).

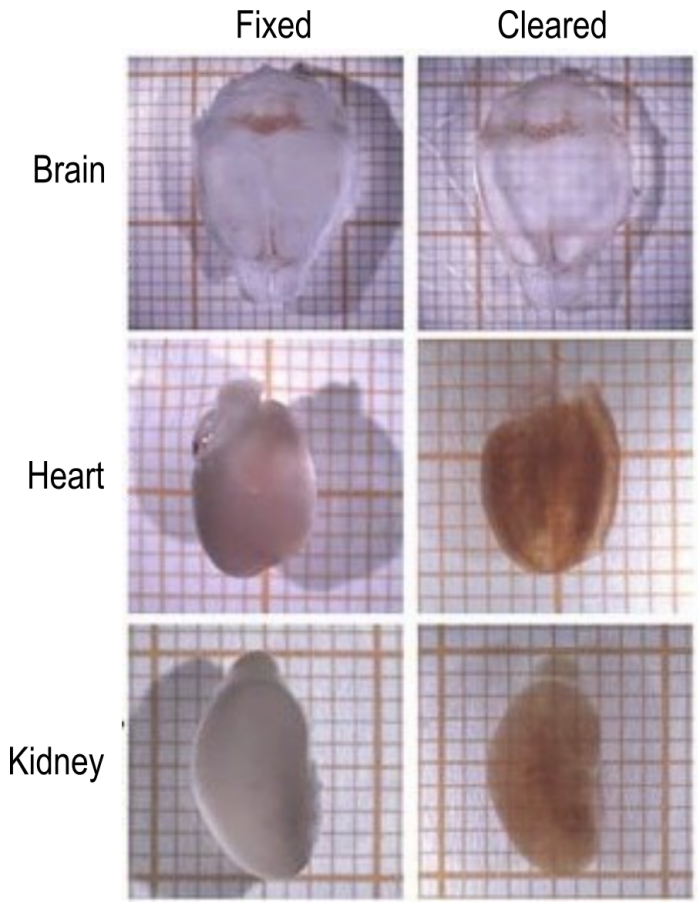

Figure 3.1: Ethyl cinnamate clearing and refractive index matching using the methodology demonstrated by Klingberg *et al.* (Klingberg et al., 2017). Tissues are dehydrated using ethanol for before refractive index matching using ECi.

Certain constituent molecules, such as lipids, scatter light significantly. These structures reduces clarity in cleared tissues, and in extreme cases result in shadowing artefacts (figure 3.2). The significance of these effects will vary depending on the tissue being cleared and many clearing approaches incorporate specific steps for delipidation, decalcification, or depigmentation.

In conjunction with large field of view, long working distance confocal microscopy, optical tissue clearing has enabled the visualisation of large samples which would previously have required extensive sectioning, such as drosophila and whole mouse organs.

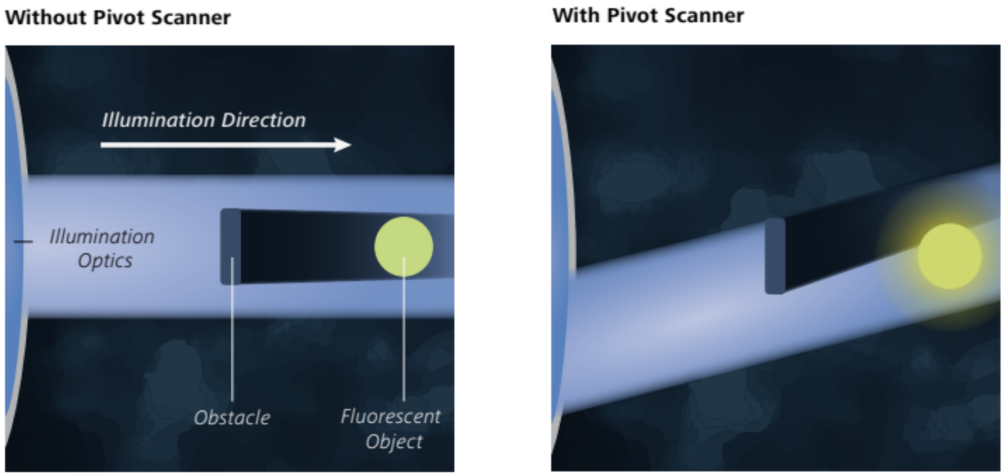

Figure 3.2: Example of shadowing resulting from endogenous absorptive structures (left). Commercial light sheet systems often have means of reducing these effects, in the case of the Zeiss Z1 "pivot scanning" (right) tilts the illumination plane to circumvent small absorptive inclusions (CarlZeissMicroscopy, 2011).

3.1.3 Light sheet microscopy

The advances in tissue clearing enabling large tissues to be imaged have highlighted limitations of confocal microscopy. In an epifluorescence confocal system, to collect data from a single diffraction-limited spot, a significantly larger region above and below this point must be illuminated. High energy laser illumination both photodamages tissue and bleaches fluorophore signal. Since a confocal system must scan through thousands of such points to image large 3D volumes, sample quality and fluorophore signal can degrade between the layers of the sample imaged at the beginning and the end of experiments. Additionally, collecting data from this number of points individually takes time, with imaging taking multiple days for samples such as drosophila.

Light sheet microscopy (LiSM) circumvents these issues. By decoupling the illumination and detection planes, a light sheet microscope illuminates planes perpendicular to the detection objective allowing all signal from a plane to be captured simultaneously, significantly decreasing imaging time (figure 1.14). This illumination method also reduces photodamage and bleaching, by illuminating only the

plane being imaged, tissue is only illuminated as it is imaged.

Despite these improvements in large sample imaging, light sheet systems cannot compete with the resolution obtained by modern confocal microscopes, particularly confocal systems capable of exploiting superresolution modalities (Bates et al., 2008; Yang et al., 2022). This is particularly clear in the axial direction in which the resolution is directly proportional to width of the light sheet used for illumination. Many light sheet systems rely on gaussian beam illumination, an in depth analysis of which is outside the scope of this thesis, but for which the width of the lightsheet in the axial direction at it's narrowest point is inversely related to the size of this narrow region in the lateral directions (B.-J. Chang et al., 2020). In practice, this means that to create a light sheet with axial resolution comparable to a confocal microscope, the size of the lateral field of view would be reduced so much as to undermine the value of the system for imaging large samples. There are alternative illumination methods for light sheet imaging such as bessel or airy beams (B.-J. Chang et al., 2020; Fahrbach et al., 2013). These methods are capable of creating narrow beams which are more stable in the lateral direction, enabling improvements in axial resolution to be maintained over larger fields of view. However, these alternative illumination methods often introduce secondary visible structures, known as sidelobes, alongside the light sheet. These interfere with imaging and must be removed computationally. Even when using these alternative illumination methods the axial resolution of light sheet microscopy remains at the scale of single cells and cannot rival the subcellular resolution achieved by confocal systems.

In recent years developments in light sheet microscopy, combined with tissue clearing have enabled the imaging of even larger tissue volumes. Using the Miltenyi Ultramicroscope Blaze, researchers from the Institute for Tissue Engineering and Regenerative Medicine in Munich cleared and imaged whole mice (Cai et al., 2023). Using a secondary nanobody labelling protocol to improve signal from endogenous fluorophores, the team visualised metastases across the entire body. These findings acutely highlight the benefits of large tissue imaging enabled by LiSM and optical

clearing; in studies of disease, immunology, and signalling, spatial context is crucial and these methods provide the most complete picture of the processes underpinning these biological phenomena. Here, I develop improved tissue clearing and LiSM imaging approaches for large tissue samples. I then validate these methods in a range biological tissues and infections.

3.2 Results

3.2.1 Tissue clearing

Tissue clearing relies on two key processes, the removal of light scattering or absorbing compounds (such as lipids or haem respectively), and the reduction of refraction of light across the tissue volume (Richardson and Lichtman, 2015). Haem is not removed by the majority of tissue clearing protocols and haem-rich tissues such as the liver and kidneys are known to be difficult to clear (T. Yu et al., 2021). The lungs majoritively comprise a collagen matrix and are not haem-rich, though in situ blood does still significantly impede clearing. To improve clarity, lungs were inflated using agarose and perfused with PBS prior, by collaborators at the CRUK, and dissected in to lobes before beginning tissue clearing protocols.

Tissue clearing was initially performed using the CUBIC protocol (Ren et al., 2021). The CUBIC protocol is a solvent based approach which has been demonstrated to clear tissues of varying composition (e.g. lipid dense brain tissue and calcium rich bone). However, CUBIC renders tissues soft, likely the result of intensive delipidation. Due to the mounting process for the Z1 in which samples are suspended from above, softened CUBIC cleared tissues could not be mounted without destruction of the tissue.

Ethyl cinnamate (ECi) tissue clearing offers numerous advantages over CUBIC and other solvent based clearing approaches. Unlike the majority of solvents, ECi is non-toxic making it significantly easier to work with on open-chamber bench top microscopes such as the Zeiss Z1 (Masselink and Tanaka, 2023). Additionally, ECi clearing can be performed in as little as 48 hours, while many solvent based

protocols require over seven days (Subiran Adrados et al., 2021). Due to the short lifetime of many common fluorophores, a shorter clearing protocol can significantly improve fluorescence during imaging.

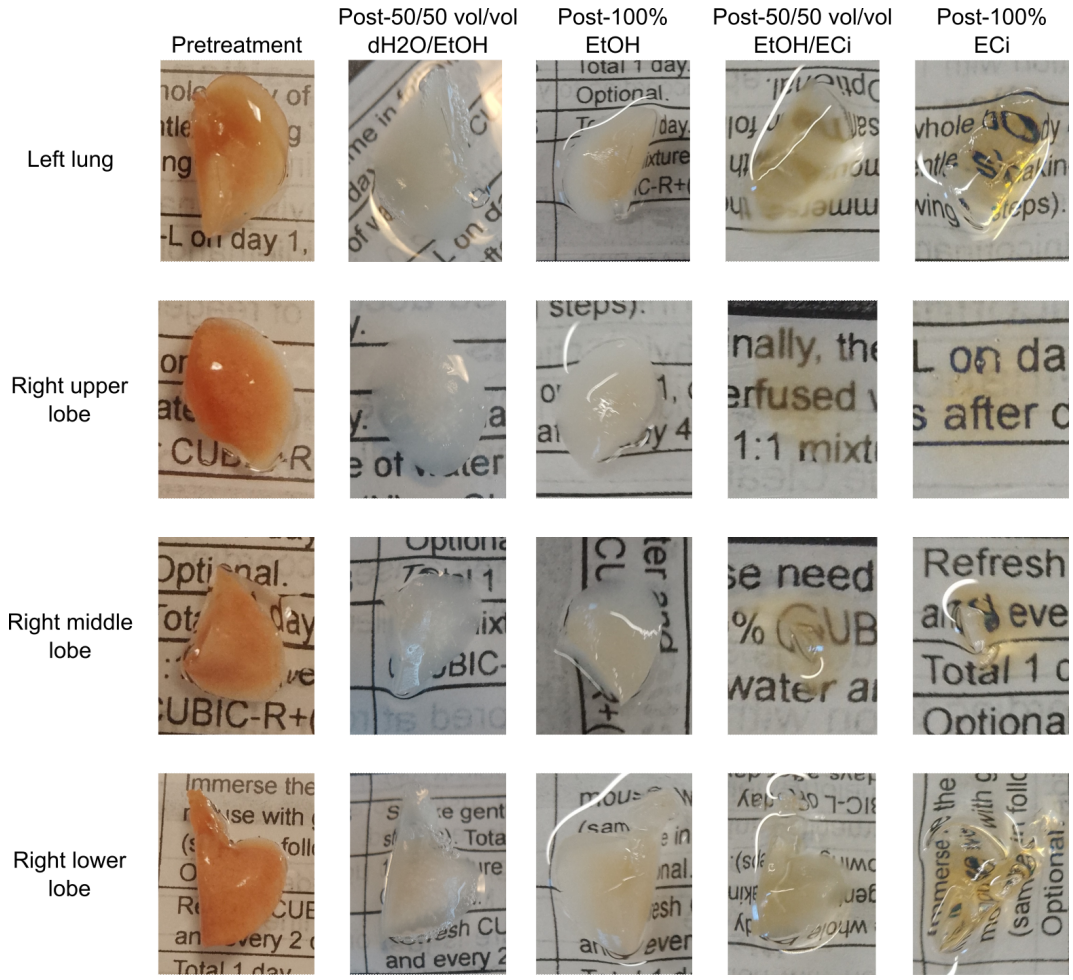

Figure 3.3: ECi clearing of lungs showing results following each step of the protocol for each lobe of a dissected lung pair. Tissues shown here were perfused to remove haem and inflated. Studies by colleagues at the CVR have shown that failure to inflate lungs significantly impedes clearing (V. Herder *et al.*, Unpublished).

The ECi clearing protocol employed here has been adapted from the protocol described by Klingberg *et al.*, increasing the incubation times to a minimum of eight hours to ensure each reagent fully permeates the tissue (Klingberg et al., 2017). Dehydration is performed using an ethanol dilution series, followed by an ethanol-ECi dilution series to achieve refractive index matching across the tissue. This

protocol resulted in a final refractive index of 1.56, confirmed by refractometer. This ECi protocol was used to clear mouse lung tissue, resulting in similar clarity to CUBIC clearing, but maintaining structural integrity of tissues, enabling mounting for light sheet imaging (figure 3.3).

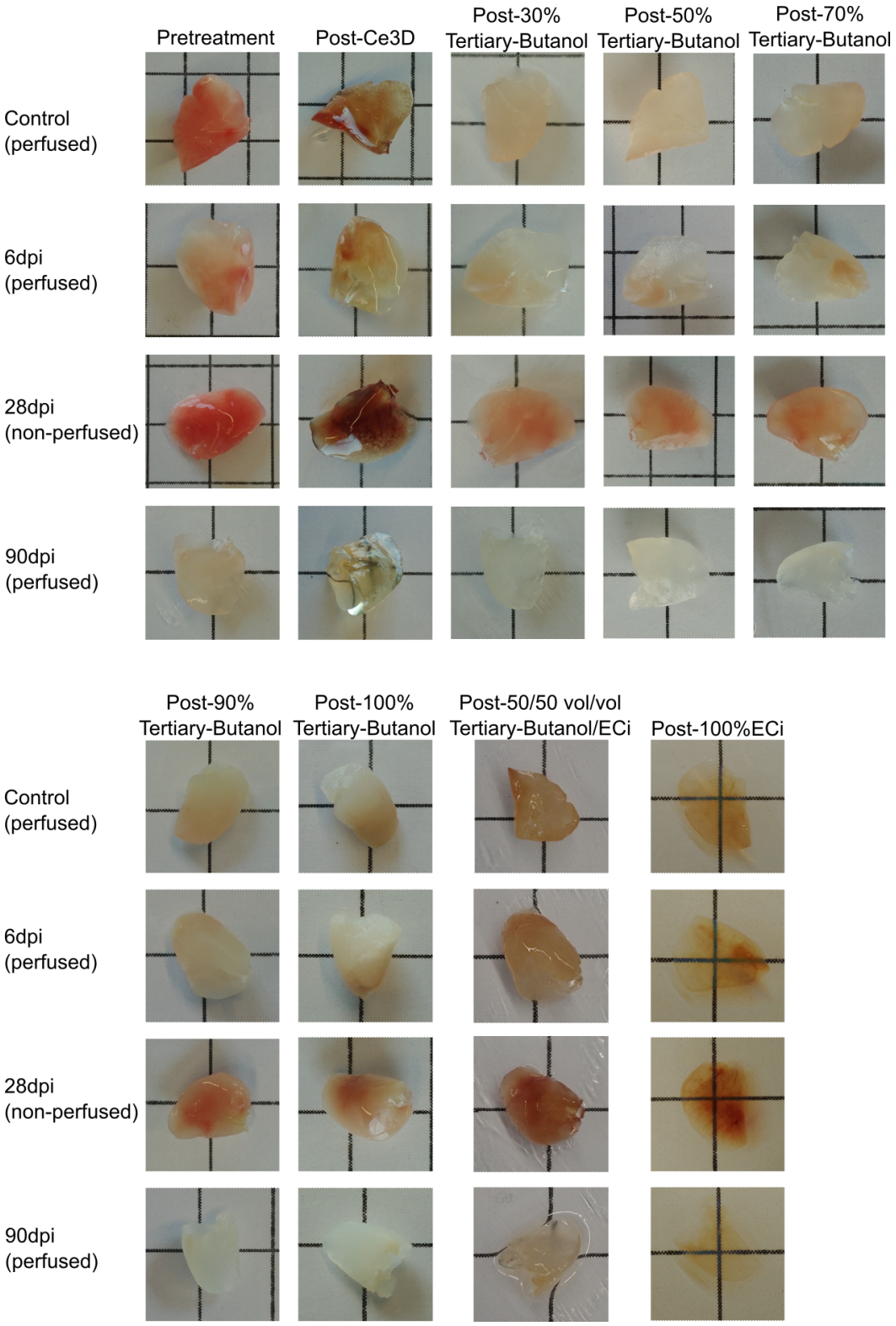

Figure 3.4: Adapted ECi clearing protocol. Lungs cleared using our newly adapted protocol employing Ce3D pre-clearing and tertiary-butanol dehydration. Four cases are shown, non-perfused tissue (28dpi), poorly perfused tissue(Control and 6dpi), and fully perfused tissue (90dpi).

Further experimentation with the novel single-step clearing medium Ce3D, and discussion with the microscopy team at Miltenyi Biotech resulted in further refinement of this ECi protocol (W. Li et al., 2019). Ce3D is a solvent based clearing method, commonly used in thick section confocal microscopy, which offers single-step clearing and refractive index matching. Due to the toxic properties of Ce3D, it was not appropriate for use with the Zeiss Z1. However, it was found that incubation with Ce3D prior to dehydration and refractive index matching using the ECi, results in improved imaging clarity (figure 3.4).

On the advice of collaborators at Miltenyi Biotech, the ethanol dehydration series was replaced with a dilution series of tertiary butanol treated with triethylamine. Ethanol quenches GFP signal and, to a lesser extent, other fluorophores, and thus tertiary butanol dehydration improves signal retention.

Lungs cleared using the existing ECi protocol and our adapted protocol including Ce3D pre-treatment appear comparatively clear to the eye (figure 3.3 and 3.4). However, clearing using the adapted protocol results in improved clarity of smaller structures, enabling finer airways to be imaged throughout the tissue volume. Additionally, the reduced fluorophore quenching when dehydrating tissues with tertiary butanol results in higher signal retention throughout the tissue volume when using our adapted clearing method.

The suitability of these clearing methods for the light sheet imaging of whole tissues was explored for a variety of tissues in both health and disease.

3.2.2 Case study 1: Trypanosoma brucei infected skin

T. brucei infection results in African sleeping sickness and poses a significant health risk in humans and livestock animals. The protozoan parasite exhibits a multistage life cycle, with parasites developing in the tsetse fly midgut before being transmitted to mammalian hosts during feeding, proliferating in the skin and vasculature and then spreading to the major organs (Matthews, 2005). *T. brucei* demonstrates a remarkable ability to infect a diverse range of tissues, with infection being observed in the majority of major organs during the first stage of infection (Hecker and Brun,

1982; Laperchia et al., 2016; Machado et al., 2021). Late stage trypanosome infection, occurring after parasites spread to the central nervous system and cross the blood-brain barrier, results in severe symptoms including seizure and death (MacLean et al., 2012). Two subspecies of *T. brucei*, *T. b. gambiense* and *T. b. rhodesiense*, are capable of infecting humans (Ponte-Sucre, 2016). The non-human mammalian infecting strain, *T. b. brucei*, is commonly used as a proxy for these strains in laboratory studies, as is the case here (Oethinger and Campbell, 2009).

The tsetse fly employs a "slash and suck" feeding strategy, creating an incision in the skin through which blood is taken up (Van Den Abbeele et al., 2010). The skin therefore represents a key environment at two stages in the trypanosome life cycle, deposition of tsetse-dwelling parasites within the mammalian host, and uptake of mature parasites during feeding. Despite this, until recently the skin was overlooked as a potential reservoir for trypanosomes (Capewell et al., 2016). In 2016, Capewell *et al.* identified the skin as a reservoir for mature trypanosomes capable of surviving in the tsetse midgut. An understanding of this overlooked reservoir is therefore essential to understanding the life cycle, transmission dynamics, and early stage proliferation and dissemination of parasites during trypanosome infections. light sheet microscopy offers a means of visualising trypanosomes *in situ* without dissection, enabling greater insights into trypanosome distribution throughout the skin than traditional confocal microscopy. This is particularly relevant in the skin due to the complex tissue composition, with tissue type differing across the depth of this organ.

Methods

Skin samples were harvested from a C57BL/6 mouse infected with a fluorescently tagged strain of *T. brucei* expressing the fluorophore TdTomato via intraperitoneal injection. Skin samples were collected from an uninfected C57BL/6 mouse to provide a negative control. All skin samples were approximately 1mm think, though thickness across individual samples and between samples varied due to thickness

of sub-dermal fat and muscle. Infections and harvesting were performed by Dr. Anneli Cooper. Samples were dehydrated via an ethanol dilution series prior to refractive index matching in ECi as described above. Samples were imaged using a Zeiss Z1 light sheet microscope.

Results

The ECi clearing protocol described above rendered skin transparent (figure 3.5), however, hair remained opaque due to the high levels of pigmentation C57BL/6 mice. When imaging the uninfected control skin sample, it was found that pigmentation in the hair did not significantly occlude tissue structure (figure 3.6).

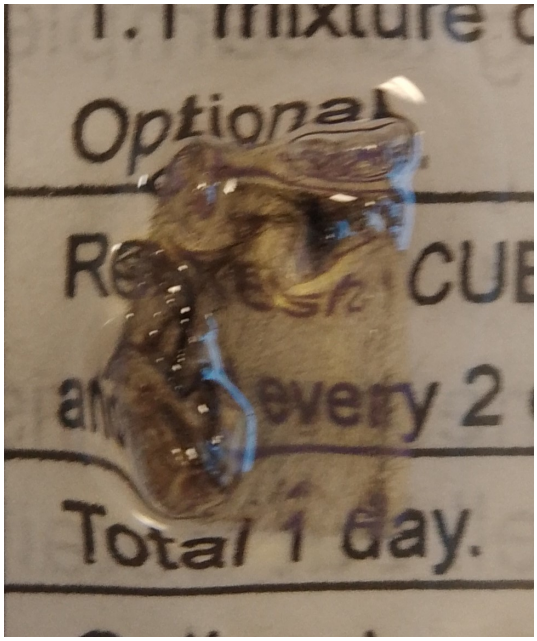

Figure 3.5: Skin sample cleared via ECi. Samples are rendered transparent excluding hair, samples are shown only after the final clearing step is complete.

In addition to providing a negative control for the removal of autofluorescence from experimental data, the imaging of uninfected skin samples provided a means to test a hypothesis that autofluorescence could be used to distinguish tissue layers in the skin. Typically, tissue-specific markers enable the differentiation of structures in LiSM data, however, the skin harbours tightly packed layers of tissue types with distinct autofluorescent properties; epidermis, dermis, and subdermal adipose and muscle tissues for example. It was therefore hypothesised that autofluorescence

could provide contextual information without the need for tissue specific markers, offering insight into the spatial distribution of skin dwelling trypanosomes.

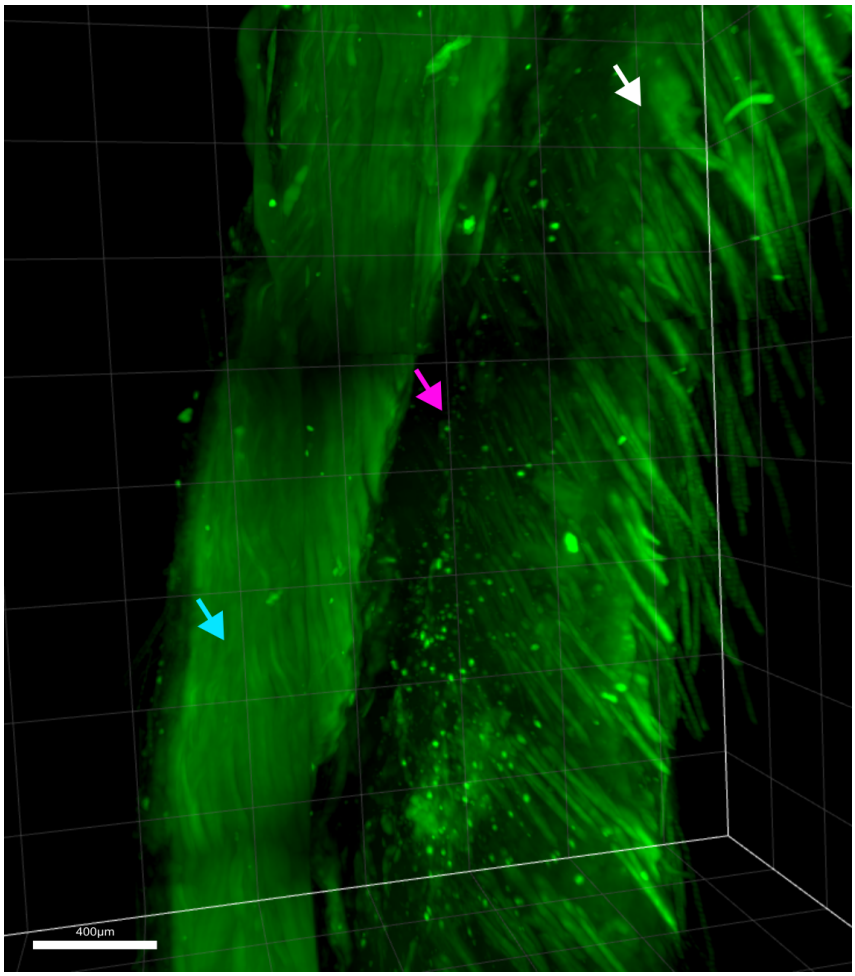

Figure 3.6: Uninfected skin imaged via light sheet microscopy (Zeiss Z1) (Scale bar = 400 μm). Autofluorescence has been captured via illumination with 488 nm laser. Skin layers are clearly visible due to differences in autofluorescence properties - epidermal layer (white arrow), unknown, non-fluorescent dermal layer (magenta arrow), subdermal layer (cyan arrow) presumed smooth muscle. These data are from an n=1 experiment.

Autofluorescence can be used to differentiate skin layers without the need for staining (figure 3.6). The epidermal layer, white arrow, exhibits significant autofluorescence and is separated from deeper layers by one or more skin layers exhibiting almost no autofluorescence, magenta arrow. The subsequent highly autofluorescent layer is hypothesised to be muscle due to the striated structure,

cyan arrow. Additionally, smaller structures such as hair follicles and vasculature are distinguishable from surrounding tissue via autofluorescence (figure 3.7).

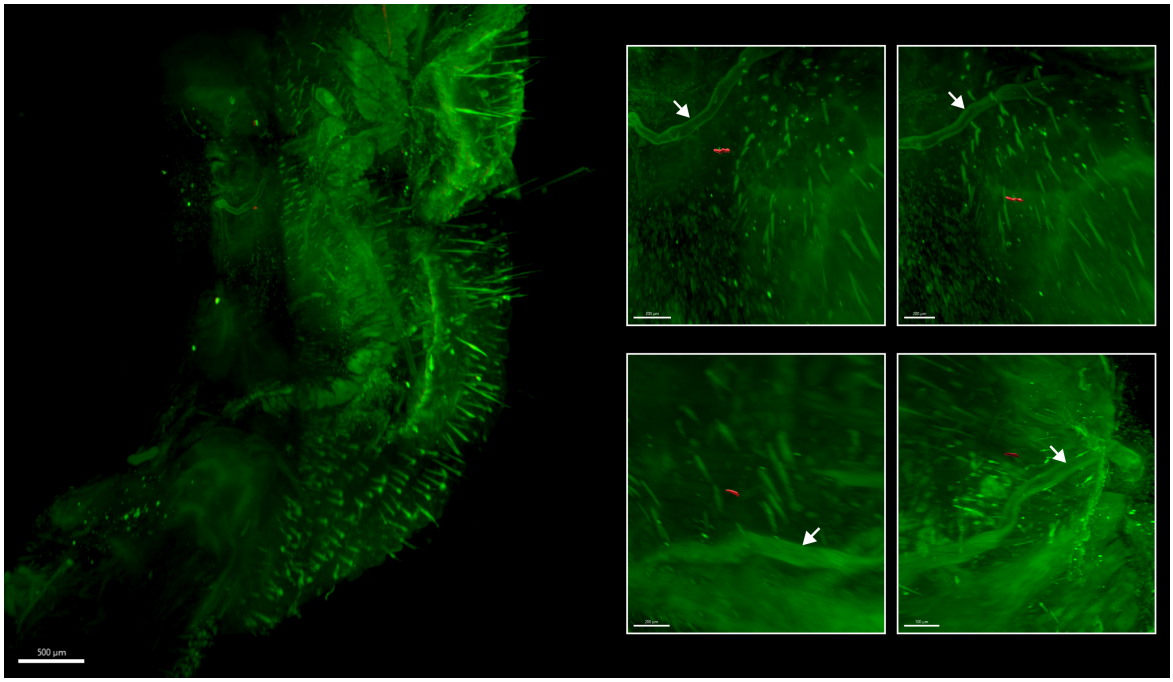

Figure 3.7: Skin from mouse infected with *T. brucei*, 45 dpi, imaged via LiSM (Zeiss Z1) (Scale bar = 500 μm). Inserts showing zoomed regions (Top left, top right, bottom left; scale bars = 200 μm. Bottom right; scale bar = 100 μm). Tdtomato tagged parasites (red) are illuminated via 561 nm laser, with background removed based on uninfected controls. Autofluorescence (green) is not removed to provide spatial context. A binary mask better quantifies parasites. Mask was generated within Imaris and fluorescence threshold was based on uninfected controls. Inserts show parasites (red) localisation to blood vessels (white arrows). These data are from an n=1 experiment.

When imaging the infected skin sample, the use of a fluorescently tagged *T. brucei* strain enabled the visualisation of parasites in situ (figure 3.7). The Imaris graphics processing suite was used to generate a binary mask based on fluorescence intensity in the negative control. Distinct structures are visible in the red channel following the binary mask. The elongated shape and size of these structures (approximately 30-40 microns) reflects the morphology expected for dividing slender form trypanosomes (Van Den Abbeele et al., 1999). These slender forms

are typically found in high abundance in the blood, however, a significant proportion of skin dwelling parasites observed by Capewell *et al.* were slender (Capewell et al., 2016). Trypanosome infection is known to cause vascular leakage, enabling the proliferation of parasites from the vasculature to major organs including the skin (De Niz et al., 2021). The position of the trypanosomes within the skin is therefore of particular interest, with both trypanosomes localising close to a major blood vessel (visible via autofluorescence) (figure 3.7). These data provide a qualitative demonstration of the localisation of trypanosomes to the vasculature. The localisation of these parasites to the vasculature suggests these fluorescent punctae represent slender parasites which have proliferated into the skin, prior to conversion to stumpy morphology.

Discussion

These experiments demonstrate that our ECi based clearing strategy is suitable for optical clearing of the skin and imaging via light sheet microscopy. Clearing was sufficient to distinguish not only distinct skin layers, but smaller structures such as blood vessels via autofluorescence. While skin-dwelling trypanosomes have been visualised previously via brightfield and confocal microscopy, these experiments focused on imaging thin sections (Capewell et al., 2016). Due to the multilayered structure of skin, in addition to the spatially heterogeneous dissemination of parasites throughout the tissue due to vascular leakage, the ability to visualise infected tissues in 3D offers significant improvements over confocal microscopy in understanding parasite proliferation and localisation. Though the localisation of parasites to the vasculature has been observed in confocal microscopy by Capewell *et al.*, the small field of view and thin tissue sections in these experiments reduce analysis to the area immediately surrounding the vasculature (Capewell et al., 2016). By visualising the entire tissue section as a single dataset, light sheet microscopy enables us to compare parasite burden between tissue regions of varying vascular density, providing a qualitative demonstration of the localisation of parasites to blood vessels and reinforcing vascular leakage as the primary entry mechanism for

slender form trypanosomes into the skin.

These experiments were performed using skin from C57BL/6 mice infected for a study on the brain. As such, conditions were not optimised for parasite skin burden, hence the relatively low density of parasites observed here compared with the experiments of Capewell *et al.* (Capewell et al., 2016). Parasite density could be increased in future studies by the use of BALB/C mice, which exhibit a higher skin burden than C57BL/6 mice, and by harvesting samples between 20-25 dpi (Šíma et al., 2011).

3.2.3 Case study 2: Cd8+ cells in the femur

Having demonstrated that ECi based clearing methods can be used to visualise microscopic signals in large tissues using light sheet microscopy. I sought to examine whether our clearing method was compatible with immunofluorescence staining. I collaborated with the Roberts lab at the CRUK Institute to visualise T-cells in the femur bone marrow in mice. These mice were not genetically modified to produce fluorescent T-cells, as such, immunofluorescent labelling was required to visualise this cell population. In addition to validating this clearing protocol for immunofluorescence, bone samples also require decalcification prior to imaging allowing us to test our clearing protocol in more demanding tissue types.

Methods

Clearing was performed using an adapted version of the ECi clearing protocol described above. Decalcification and staining was performed by Dr. Pirillo prior to optical clearing. This is crucial as staining requires the immersion of tissues in aqueous solutions, thus reversing any prior dehydration performed during clearing. Samples were stained for CD8 (Phycoerythrin). Autofluorescence provides a structural marker for the bone while CD8 staining visualises T-cells in the bone marrow. Samples were then dehydrated via ethanol dilution series, before refractive index matching via ECi dilution series and final immersion in a 80/20 solution of ECi/polyethylene glycol.

Results and Discussion

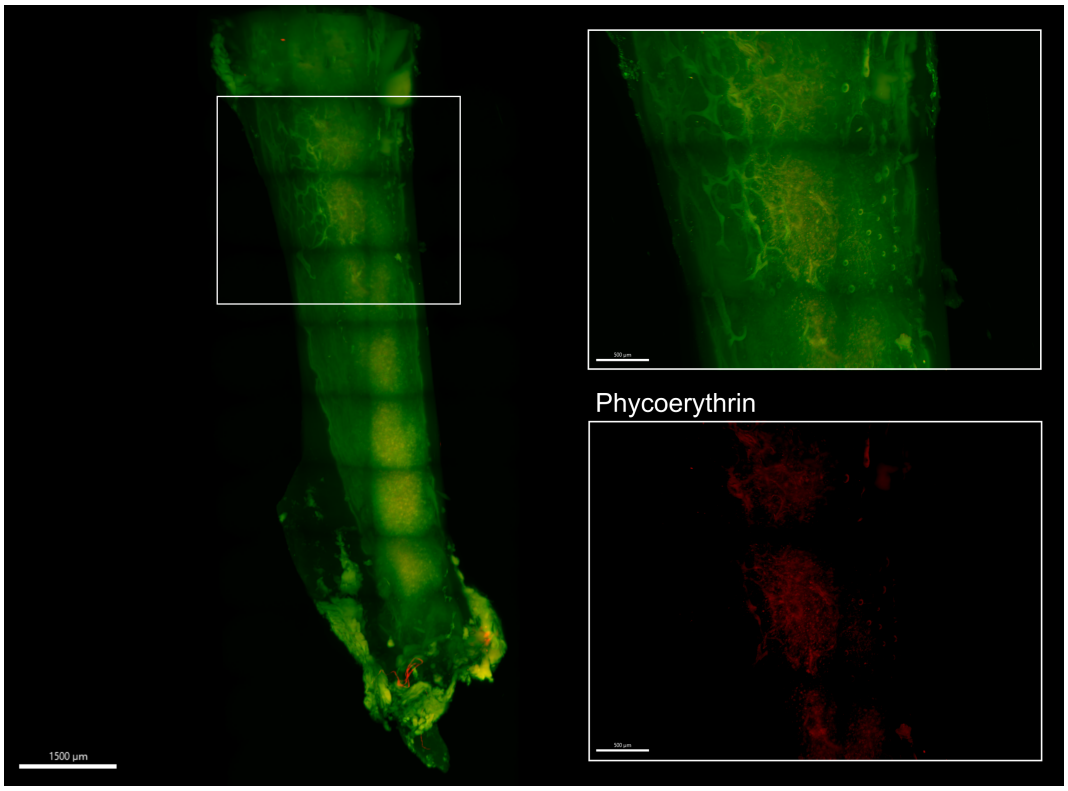

Figure 3.8: Opptically cleared bone samples imaged via LiSM (Zeiss Z1) (Scale bar = 1500 μm). Mouse femur cleared using ECi, stained for Cd4 (Red) with structure shown via autofluorescence (green). Inserts show trabecular bone structure (upper, scale bar = 500 μm) and zoomed marrow region showing possible T-cell population (lower, scale bar = 500 μm). These data are from an n=1 experiment.

Our clearing protocol produced good results in the bone with both bone structure clearly visible (figure 3.8). This work demonstrated the viability for our adapted ECi clearing protocol for clearing calcified tissues. There are some bright fluorescent spots in the red channel in the deeper tissue regions which may represent immunostained T-cells, however, these data are unclear and are only of approximately the brightness of surrounding bone structures so cannot be verified as expressing above background fluorescence (as would be expected for immunostained cells). While there data verify that the clearing protocol developed here is suitable for bone imaging, these data alone are not sufficient to draw any conclu-

sion regarding the T-cell populations in the bone marrow. In future experiments it would be better to support light sheet imaging with confocal imaging modalities, using thick sections of bone samples to better quantify immunostained populations. This is further discusssed in the general discussion at the end of this chapter.

3.2.4 Case study 3: Depigmentation and imaging of tumours in the lung

Depigmentation, particularly of melanin-rich structures in tissues, is crucial to light microscopy. Pigments both absorb and scatter incident light resulting in shadowing of tissue regions behind pigmented structures and a lack of clarity throughout the tissue as emitted light is scattered prior to collection by the objective lens. I collaborated with the Roberts lab at the CRUK to image melanoma metastases in lungs previously infected with IAV. It was hypothesised that localised immune responses in the vicinity of prior infection would alter tumour development. Samples were first cleared as described above using tertiary-butanol and ECi, however, following clearing and imaging it was found that melanin-rich tumours significantly impacted the visualisation of airways, viral lesions, and cells which survived viral infection. Here, I describe the adaptions made to the clearing protocol developed above to incorporate a depigmentation step and the application of this clearing protocol to melanoma-containing lungs.

Methods

Mice were housed, infected, culled, and harvested at the CRUK, by Dr. Ryan Devlin. Mice were intranasally inoculated with a non-lethal dose of IAV strain A/Puerto Rico/8/1934(H1N1) (MOI = 500 PFU). After 28 days, mice were intravenously injected with B16F10 melanoma cells. Mice were then culled 14 days post injection. Lungs were collected, perfused, inflated, and fixed as described in section 2.3.1. Samples were cleared via H_20_2 bleaching and dehydration with tertiary-butanol treated with triethylamine followed by ECi refractive index matching. All imaging was performed using a Zeiss Z1 light sheet microscope.

Results and Discussion

Lung samples from tdTomato Cre-reporter mice inoculated with a fluorescently tagged B16 cell line were infected with a PB2-Cre influenza virus. As such, infection events result in the expression of tdTomato in infected cells and their progeny. Lungs were first cleared with the ECi clearing protocol developed above. Optical clearing using this clearing protocol was insufficient for lungs containing melanomas (figure 3.9).

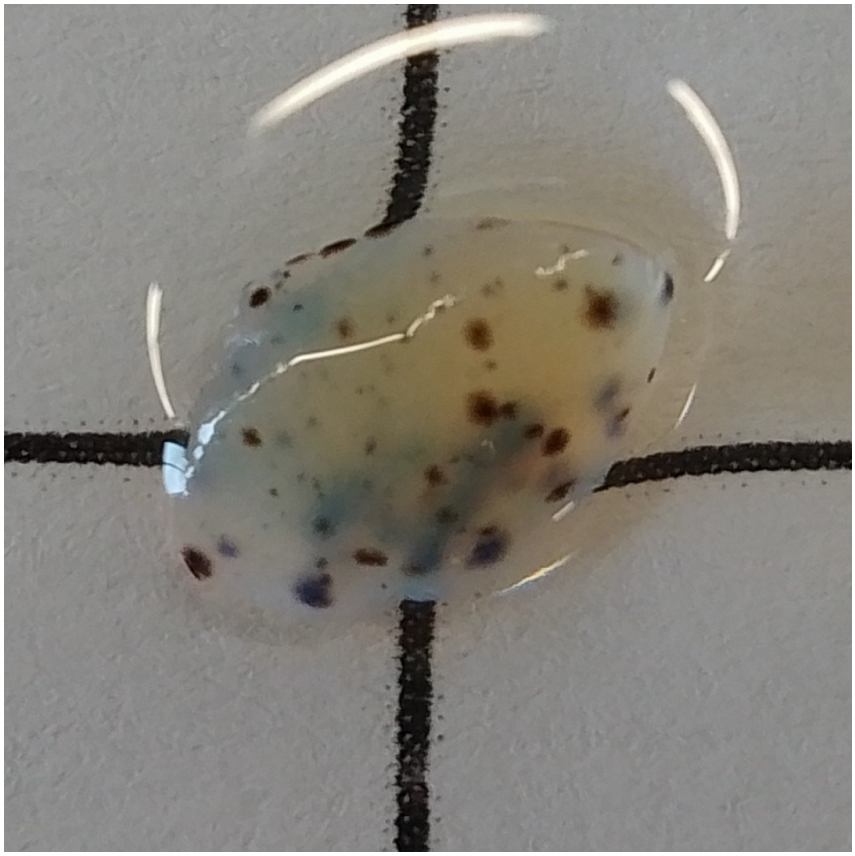

Figure 3.9: Lung lobe from a B16-inoculated mouse following clearing with Tertiary-Butanol and ECi.

Melanin inclusions are clearly visible following clearing and scattering in the surrounding tissue reduces transparency. Such inclusions cause shadowing artefacts as described above during light sheet imaging, occluding structures deeper into tissues. Additionally, the scattering observed across the whole tissue is sufficient to prevent the illumination of deeper tissue regions, resulting in non-homogenous illumination and an inability to visualise samples on the scale of whole lung lobes

accurately. Taken together, these effects render the sample non-viable for light sheet imaging.

This resulted in poor image acquisition with large portions of the tissue occluded by large surface melanomas and an overall lack of transparency of the tissue. It is hypothesised that this general lack of transparency is the result of B16-related melanin within the tissue which, while not visible as punctate tumours by eye, cause a cumulative scattering effect as light passes through the tissue volume, resulting in translucence in the deeper tissue.

To improve the transparency of cleared tissues, a melanin bleaching step was added to the beginning of the clearing protocol described above. Lung lobes cleared using the standard clearing protocol were rehydrated by immersing in 1xPBS overnight at room temperature, before transferring to fresh 1xPBS and incubating for a further 24 hours. This process reverses the tertiary-butanol dehydration and ECi refractive index matching, returning tissues to a pre-clearing state (figure 3.10).

Melanin bleaching was performed using 6% H_2O_2 in 1xPBS based on prior bleaching experiments on melanin rich structures such as the eye (Hu et al., 2008). Given the tissue damage and fluorophore degradation associated with extended H_2O_2 exposure, three bleaching times were compared; 30, 60, and 90 minutes (Platkov et al., 2014; Ugolini et al., 2021; D. Wang et al., 2024). All lobes were incubated at 55°C and immediately transferred to Ce3D following bleaching. After bleaching the established clearing protocol described above was followed.

When comparing bleaching times by eye, melanin content is visibly reduced in all samples immediately after bleaching and melanin content decreases more for longer bleaching times as expected, though clearly this is a qualitative assessment (figure 3.10). Comparing the tissues after clearing with and without the bleaching step demonstrates qualitatively that bleaching not only reduces the appearance of punctate melanoma but also largely eliminates the translucent texture in the deeper regions of the tissue. This supports the hypothesis that this translucency results from melanised structures smaller than the obvious punctae.

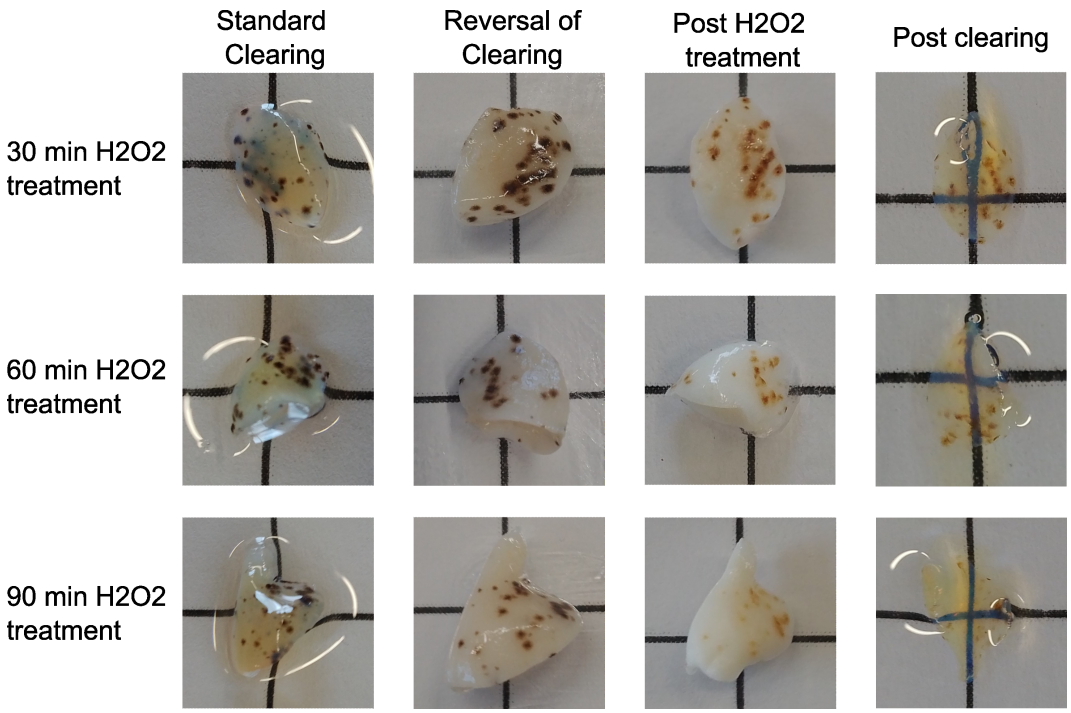

Figure 3.10: Comparison of efficacy of H_2O_2 bleaching times on reduction of visible melanoma. All samples contained approximately equivalent densities of melanin prior to clearing. Samples were initially cleared without bleaching and are shown in the left column to provide a control for validating bleaching efficacy.

Though all lobes are visibly clearer following the adapted clearing protocol when assessed by eye, it is not guaranteed that this will translate to improvements in light sheet imaging, nor that fluorophores would still be visible following bleaching. Thus, bleached and cleared lobes were imaged via Zeiss Z1 light sheet microscope (figure 3.11).

In the data gathered from imaging these bleached samples, while there are regions which appear to show structures which may be airways and tumors (white and cyan arrows in figure 3.11 respectively) the majority of the tissue is not sufficiently cleared to distinguish internal structures. This lack of clarity is primarily due to scattering of light leading to blurriness (as seen in the 90 minute bleached sample) or shadowing by highly absorptive structures. In all cases, the majority of the tissue remains insufficiently cleared for imaging. Even in regions where internal structures such as airways are more visible, clarity is not comparable to samples which do not require bleaching (as described later in this chapter). The internal

structures are dim and of poor resolution compared with structures in imaged lung, bone, and skin samples not containing melanin. Therefore, while bleaching demonstrates a clear reduction in absorption in melanin rich tumors when investigated by eye, the bleaching protocol presented here requires further refinement before it is suitable for light sheet imaging of large tissues.

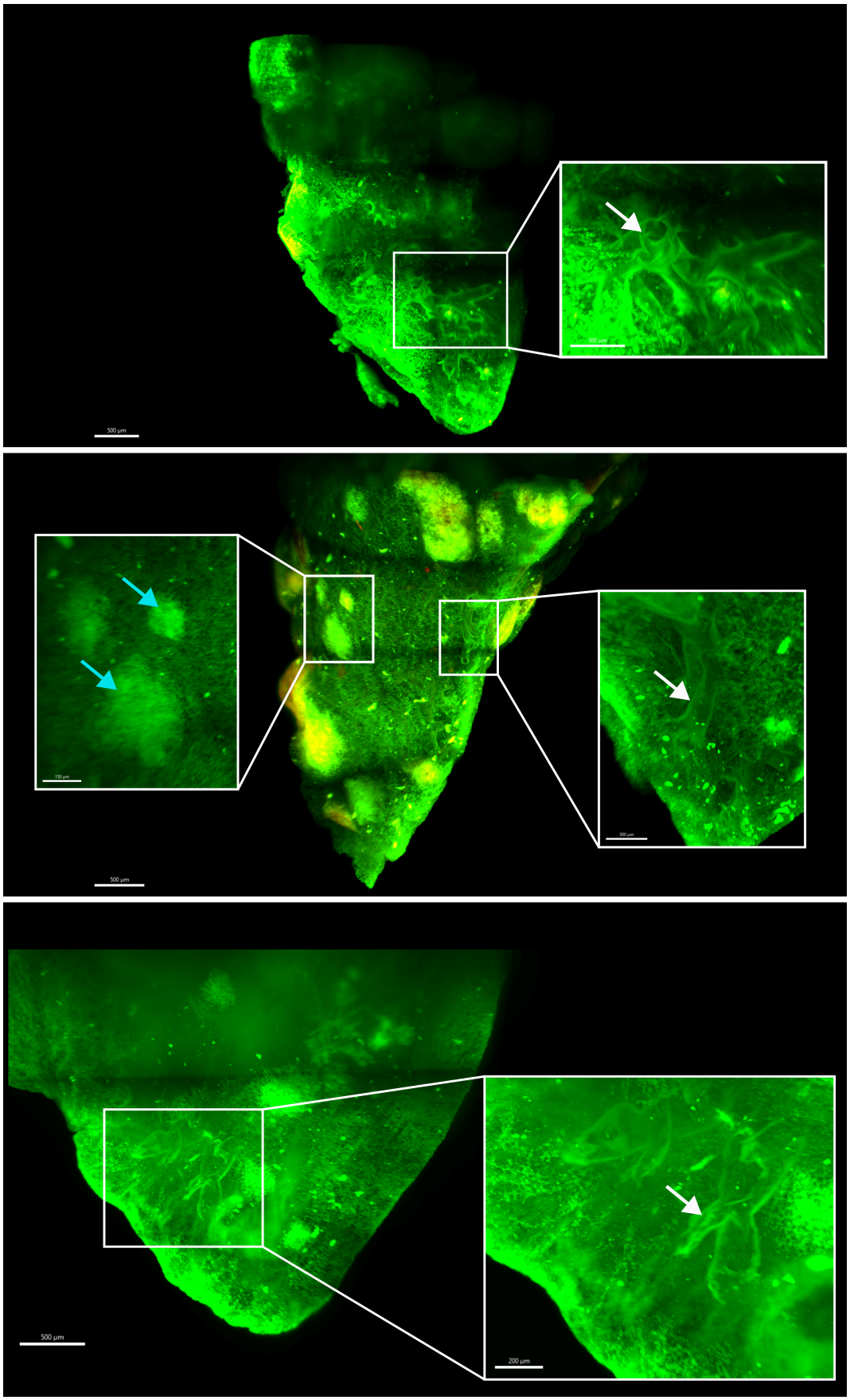

(Caption on next page.)

Figure 3.11: Comparison of lightsheet results for melanoma containing lungs following H_2O_2 bleaching. Bleaching was performed for 30 minutes (top, scale bar = 500 μm, insert scale bar = 300 μm), 60 minutes (middle, scale bar = 500 μm, insert scale bar = 150 μm (left), 300 μm (right)), and 90 minutes (bottom, scale bar = 500 μm, insert scale bar = 200 μm). Insets demonstrate the preservation of fluorescence in ZsGreen-tagged B16 tumours in all bleaching conditions along with the improved visiblity of airways proportional to the bleaching time. Data from each bleaching condition are from an n=1 experiment.

Discussion

Here, I have attempted to expand the tissues which can be cleared using our ECi clearing protocol by incorporating a H_2O_2 bleaching step. This step is added to the beginning of the clearing protocol to reduce the effects of melanin in occluding light sheet imaging. The use of H_2O_2 bleaching of melanin in sample preparation for imaging is well established, with many protocols using high concentrations for clearing melanin rich structures such as the eye (Hu et al., 2008). This bleaching step significantly reduces the opacity of both punctate melanin rich structures such as tumours, as well as improving the clarity of tissue adjacent to melanin rich structures, when making a qualitative assessment by eye (figure 3.10). However, when examining cleared tissues via light sheet microscopy the benefits of bleaching are less clear. While internal structures are visible in small regions of all samples, these regions represent only a small portion of the tissue, with the majority of the tissue being insufficiently cleared for any internal structures to be visible. Even in regions where internal structures are visible, these structures are of low resolution and clarity when compared to lungs which have not been subjected to bleaching. This method would require significant further refinement before being suitable for light sheet imaging. An important consideration during refinement is the bleaching effect of H_2O_2. Here, the longest bleaching step lasted 90 minutes. Even in the results presented here fluorescence appears relatively homogeneous across the sample, possibly suggesting bleaching has reduced the fluorescence of ZsGreen-

expressing tumors. Therefore, simply extending the bleaching time would not be an appropriate means of improving this method.

3.2.5 Case study 4: Clearing heavily melanised tissues

Having validated a clearing method for melanised tissue, this protocol was tested in *Anopheles coluzzii* mosquitoes in collaboration with the Sinkins group at the University of Glasgow. The mosquito exoskeleton comprises highly melanised chitin, entirely impeding the imaging of internal organs. Researchers in the Sinkins group have previously relied on techniques such as microdissection to enable the visualisation of internal tissues, however, this results in similar damage and morphological ambiguity as in disection of larger tissues. Here, mosquitoes were bleached and cleared to test the efficacy of our clearing protocol in a more significant case of melanisation.

Methods

Wildtype *Anopheles coluzzii* mosquitoes were culled by 20 minute incubation at -20°C by Dr. Ewan Parry at the CVR. Mosquitoes were then bleached in 6% H_2O_2. Bleaching was performed at 42°C for a variety of durations to examine optical clearing effects (figure 3.12).

Results and discussion

Following bleaching, samples were immediately transferred to 30% tertiary-butanol, treated with triethylamine as described above, and clearing was performed as previously. Following clearing, mosquitoes were mounted for imaging via Zeiss Z1 light sheet via mounting pin. Samples bleached for two, three, and four hours were imaged to investigate the tissue quality within the mosquitoes following bleaching, since extended periods of bleaching are well established to degrade tissues, DNA, and RNA (Ugolini et al., 2021; D. Wang et al., 2024). At the time of writing, the imaging data from these samples is not available. Furthermore, the bleaching study presented here in figure 3.12 does not present a negative control. While the

exoskeletons of cleared mosquitoes are visibly clear, a negative control would have make far clearer the benefits of bleaching and should have been included.

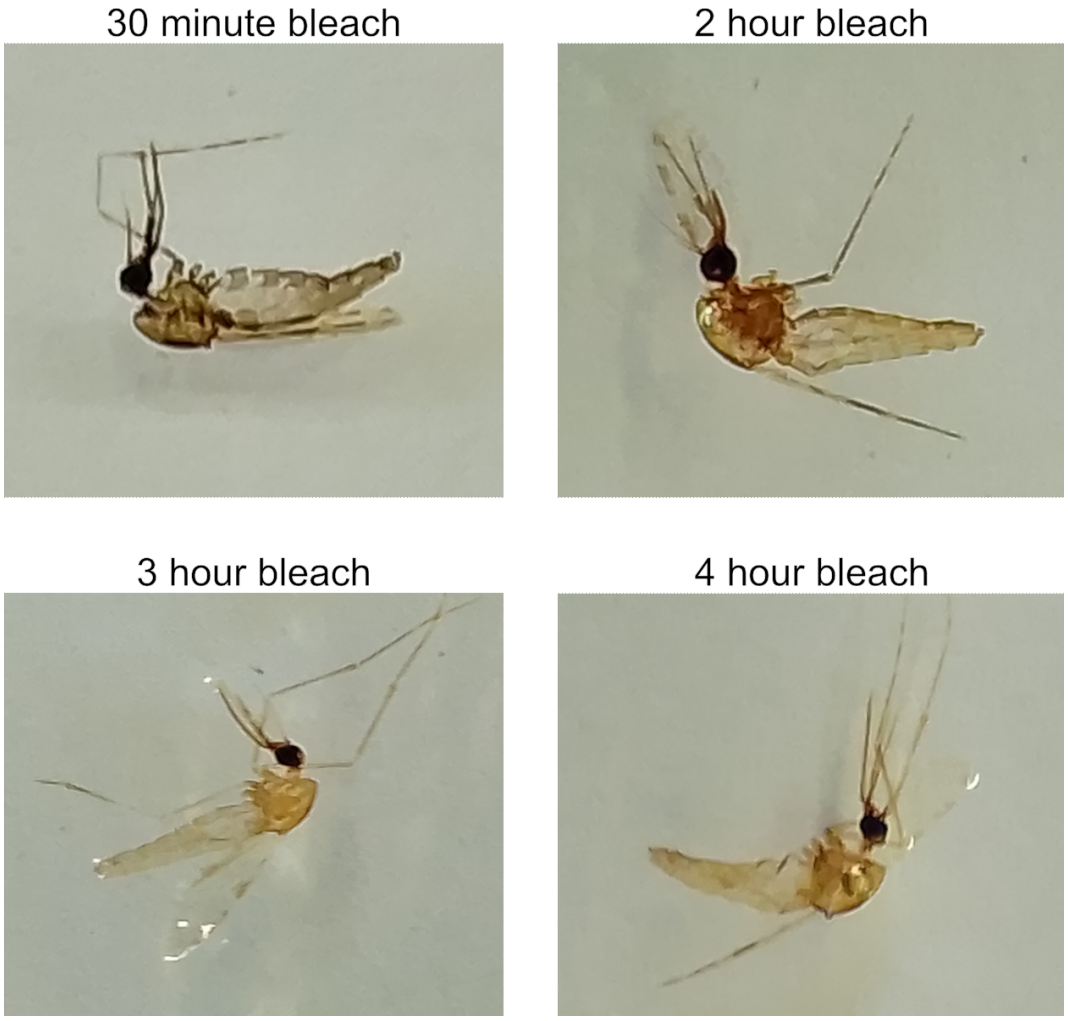

Figure 3.12: *Anopheles coluzzii* following bleaching and clearing. Clearing protocol was identical for all samples other than bleaching time. Data for each bleaching condition are from an n=1 experiment.

3.2.6 Case study 5: Agarose embedding for fragile samples

In all imaging experiments, sample handling and mounting must be carefully considered to ensure that morphology is preserved. These considerations become more consequential in light sheet microscopy experiments due to the effects of optical clearing and mobility of samples during imaging. During confocal or widefield studies of *in vitro* cell systems or thin tissue sections coverglass typically fixes

the sample in place. This ensures the relative positions of the sample and imaging objective are preserved, thus tiled images can be accurately stitched following acquisition.

Light sheet microscopy commonly works with large, irregularly shaped samples, thus samples are mounted in an open chamber. Samples are commonly mounted via adhesive, either to a rail on the bottom of the chamber or a mounting pin which suspends the sample in the chamber, as is the case for the Zeiss Z1 (CarlZeiss-Microscopy, 2011; MiltenyiBiotechnology, 2023). These mounting methods leave significantly more freedom for sample movement during imaging than confocal or widefield microscopy. This is particularly relevant when acquiring tiled images in which the sample must be moved relative to the objective lens, as is the case for most light sheet experiments due to sample size. Sample movement during acquisition will vary based on tissue, fixation and clearing method, and imaging time, however, the effect is naturally exacerbated in long, thin samples such as nerve or muscle tissues.

Additionally, many clearing methods can compromise structural integrity of samples. This is particularly common in solvent-based approaches which incorporate delipidation or decalcification steps in addition to refractive index matching (Chung et al., 2013a; Ren et al., 2021; Susaki et al., 2014). While these steps are necessary for the removal of highly light scattering material from tissues such as brain and bone, these compounds commonly comprise key structural components of the organ. Examples of such clearing methods include CLARITY and CUBIC, the latter of which I have attempted to use for imaging on the Z1, however, the sample could not be mounted without extensive morphological damage due to this softening effect (Chung et al., 2013a; Ren et al., 2021; Susaki et al., 2014).

Sample embedding has become a popular solution for light sheet imaging of fragile samples. 1-2% agarose is commonly used as an embedding matrix due to the similarity of its refractive index with water (Huisken et al., 2004a; Kaufmann et al., 2012; Keller et al., 2008). Such embedded samples can therefore be imaged using a water immersion objective without introducing additional refractive

index boundaries, compromising resolution. Alternative methods using hydrogel matrices for embedding have been employed (Poologasundarampillai et al., 2021; Shnaider and Pristyazhnyuk, 2021). Many of these approaches stem from the use of hydrogels in expansion microscopy, enabling improvements in resolution by directly increasing sample size (W. Li et al., 2019; Wassie et al., 2019). Given the increased size of expanded samples, light sheet microscopy is ideally suited to imaging such samples.

In both agarose and hydrogel cases, much of the existing literature involves working with relatively small, semi-transparent samples; zebrafish and Drosophila embryos, organoids, hydrogel cell suspensions. Such samples require little to no optical clearing prior to imaging, hence the focus on imaging using water-based objectives. For larger samples requiring optical clearing, the application of these approaches is limited. Due to the high water content of both hydrogels and agarose, embedding of optically cleared samples will result in rehydration and reduced transparency. In order to image large, fragile or flexible samples, it is crucial to develop means of embedding optically cleared tissue while retaining transparency.

Here, I develop a method for clearing and mounting large fragile tissues on the Zeiss Z1 microscope. Our approach enables transparency of optically cleared tissues to be maintained after agarose embedding and therefore is not limited to water immersion approaches. I use an optically cleared murine spinal cord prepared at the University of Glasgow Center for Neuroscience as an example tissue to evaluate this methodology.

Methods

All animal handling, infection, culling, and tissue harvesting was performed at University of Glasgow Center for Neuroscience by Dr. Magdalena Redondo Canales. Decolourisation and initial optical clearing of spinal cord samples, prior to sample embedding, was performed by Dr. Redondo Canales. Sample clearing was performed using an adapted ECi clearing protocol based on that described above. Spinal cord tissue was collected from mice aged between 8-10 weeks, two weeks

after nerve injury. Following culling, spinal cord tissue was collected and tissue fixation was performed via overnight incubation in 4% paraformaldehyde at 4°C. Tissue was decoloured prior to dehydration and refractive index matching. Decolourisation was performed by incubating in 25% Quadrol for three days at 37°C followed by 5% ammonium in water for 24 hours at 37°C. Dehydration was performed via methanol dilution series. Prior to refractive index matching, samples were delipidated to decrease light scattering during imaging. Delipidation was performed by incubating in 66% dichloromethane/33% methanol overnight at room temperature, followed by two 30-minute incubations in 100% dichloromethane at room temperature. Samples were then refractive index matched via incubation in 100% ECi, immersion media was swapped for fresh ECi after one hour.

To facilitate sample mounting during imaging, the spinal cord section was embedded in a 1% agarose plug in a 1 ml syringe. After embedding, the agarose plug was re-cleared via an ethanol dilution series followed by an ECi dilution series over a total of four hours at room temperature (figure 3.13).

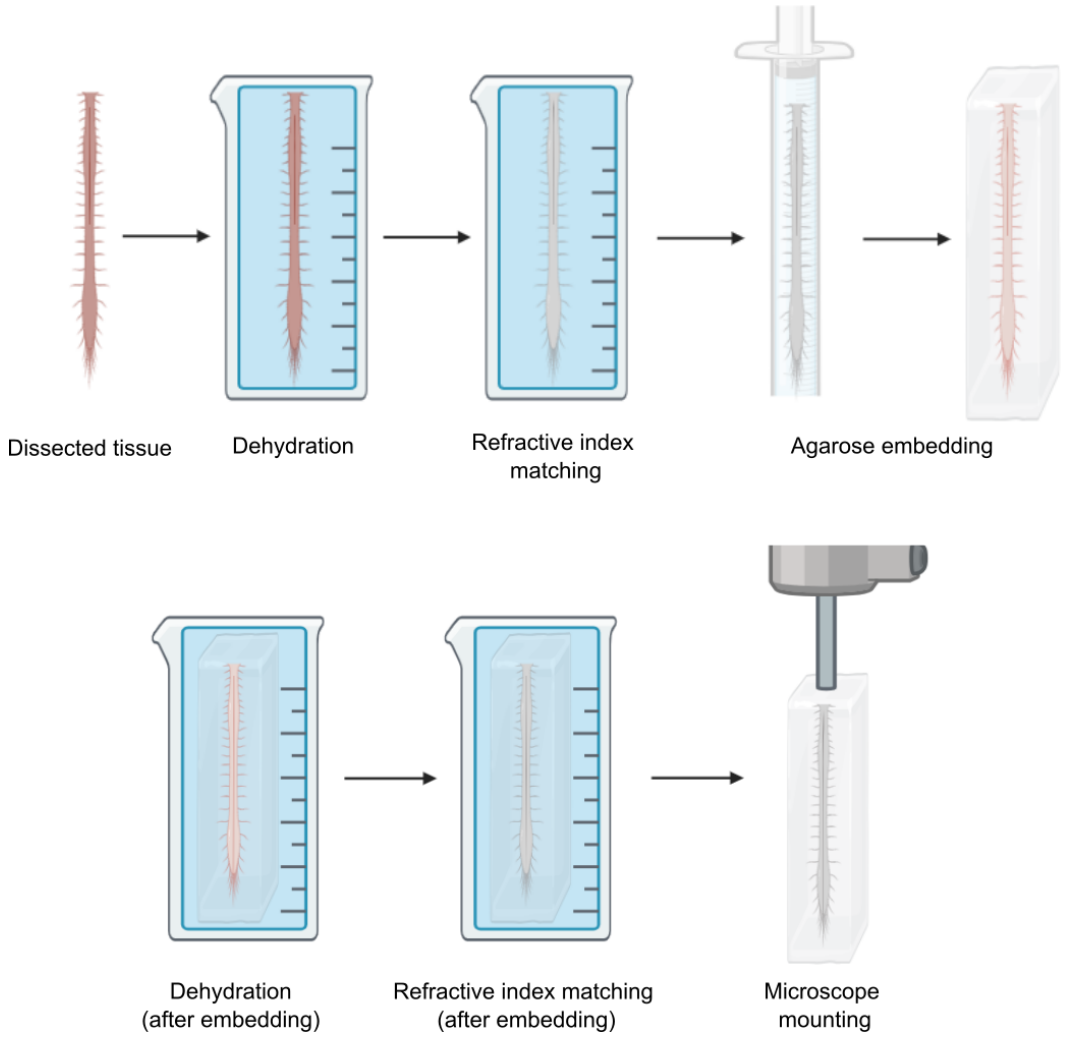

Figure 3.13: Schematic for clearing and embedding method developed for fragile samples. Standard dehydration and refractive index matching is performed as previously described. Partial reversing of clearing occurs through rehydration during embedding, requiring subsequent re-clearing of the agarose block.

Results and discussion

The Z1 light sheet microscope uses a mounting pin above the sample chamber on which samples are glued and hung during imaging. Due to the flexibility of the spinal cord section, mounting the sample directly to the mounting pin would result in significant movement of the sample during imaging. By embedding flexible samples in 1% agarose, the resulting agarose plug can be mounted for imaging without concerns over sample movement during imaging (figure 3.13). However, agarose is typically diluted in water resulting in reversal of dehydration, and by

extension optical clearing, of any tissue embedded. Here, I demonstrate that by conducting a secondary clearing protocol on agarose embedded samples optical clearing can be maintained after embedding (figure 3.14).

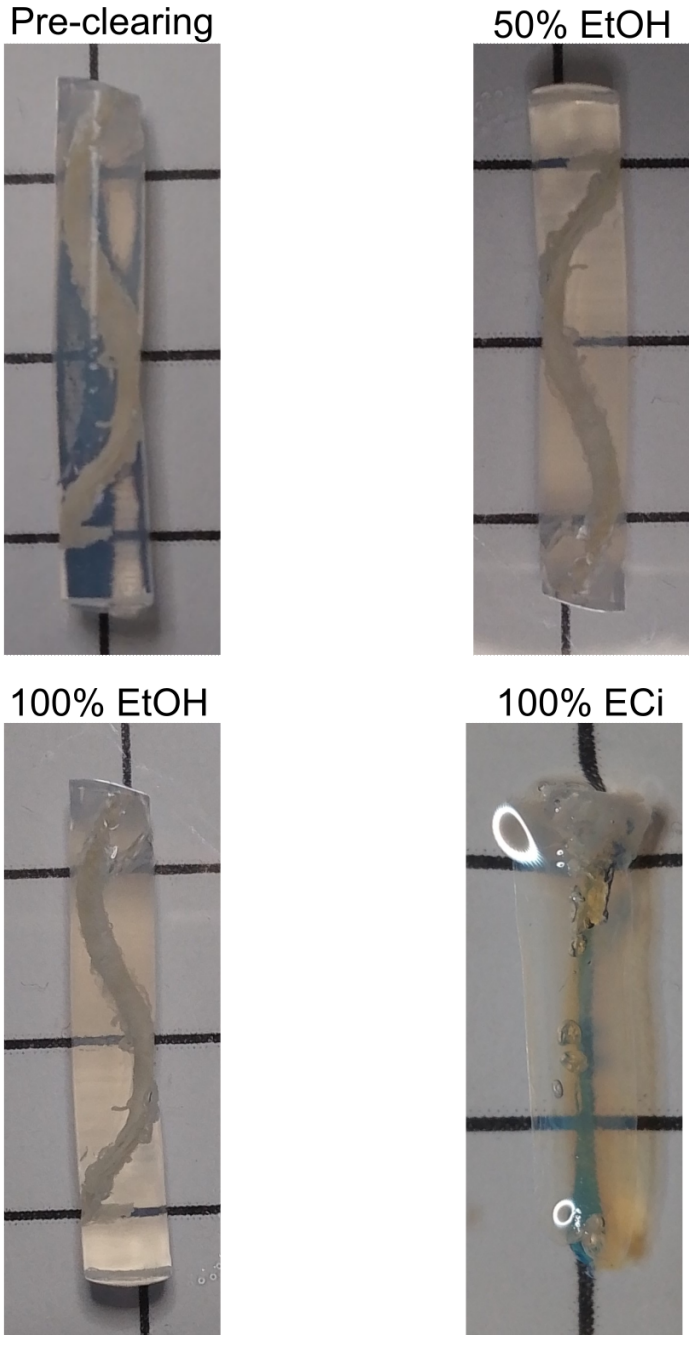

Figure 3.14: Spinal cord embedded in 1% agarose in water throughout secondary optical clearing. Each incubation was performed at room temperature for one hour. Following refractive index matching with ECi, optical clearing of the embedded sample was comparable to clarity prior to embedding.

This secondary clearing protocol can be performed in significantly less time than the initial clearing. While initial clearing took approxiamtely six days, secondary clearing was performed over four hours. This is due to the lack of decolorisation or delipidation steps in secondary clearing (since agarose embedding only reverses dehydration and refractive index matching) and the permiability of 1% agarose.

Here, secondary dehydration was performed via ethanol dilution series. As mentioned above, ethanol can lead to significant fluorophore quenching, hence the use of alternatives such as methanol and tertiary-butanol. The use of ethanol here was justified by the relatively short ethanol incubations (Three one-hour incubations in 50% ethanol (EtOH)/50% water, 100% EtOH, and 50% EtOH/50% ECi) involved in secondary clearing and the short time frame in which secondary clearing had to be performed due to project constraints.

The resulting agarose plug was then mounted via glue as per all previous samples imaged on the Z1 light sheet microscope (figure 3.15). The resolution of the spinal cord roots and dorsal root ganglia (insert) and alignment of green and red colour channels offers good evidence that the sample did not move significantly during image acquisition. Additionally, the resolution is comparable to that observed in samples imaged outwith agarose, demonstrating that agarose embedding does not noticeably impact resolution.

This work expands the tissue samples which can be visualised using the light sheet at the Center for Virus Research by demonstrating new methods for mounting flexible samples. These data demonstrate that agarose embedding allows us to image samples which would either not be sufficiently robust to mount or those too flexible to image reliably. This is particularly relevant to cleared tissue as solvent-based clearing methods such as CUBIC are known to reduce the structural integrity of tissues. This has made CUBIC-cleared brain and lung samples in particular impossible to mount on the Z1 system at the Center for Virus Research without significantly deforming the tissue and compromising morphology.

Figure 3.15: Murine spinal cord embedded in 1% agarose imaged via light sheet microscope (Zeiss Z1) (Scale bar = 1000 μm). Insert (scale bar = 200 μm) shows punctae of individual neurons in a dorsal root ganglion, demonstrating the resolution achievable with this clearing and mounting approach. These data are from an n=1 experiment.

3.2.7 Imaging of influenza A virus infections in whole lung lobes

Introduction

Having validated a clearing protocol suitable for use in various organs and imaging via Zeiss Z1 light sheet microscope, this method was employed to study our primary system of interest; the progression of disease during influenza virus co-infections.

Presently, respiratory disease pathology is reliant on immunohistochemical staining of histological sections imaged via widefield microscopy. These sections enable the visualisation of cross-sections of entire organs, however, histological sections typically range from 5-20 μm thick, therefore requiring dissection of tissues prior to imaging. This dissection is particularly detrimental to the understanding of influenza A virus co-infection as the airway epithelial surface - the point of initial virus particle deposition and infection - is effectively reduced to a single dimension.

Interactions occurring between co-infecting viruses are therefore somewhat occluded in thin section microscopy. Interactions are particularly crucial to the understanding of influenza virus co-infection studies due to the effects of superinfection exclusion (SIE). SIE inhibits the secondary infection of a cell a known time after initial infection and has been studied extensively *in vitro* (Sims et al., 2022). This inhibition of secondary infection results in the segregation of infected tissues into arrays of singly infected micro-domains (figure 3.16).

While superinfection exclusion has been studied *in vivo*, the wider effects of superinfection exclusion on disease progression, pathology, and novel strain emergence during co-infection have not been investigated (Sims et al., 2022). It is crucial then that epithelial surfaces and the wider structure of the lung be maintained in it's entirety during imaging to comprehend the complex interactions between co-infecting viruses.

Beyond improving the understanding of how SIE impacts disease progression, a better understanding of co-infecting virus interactions can yield an improved understanding of the emergence of novel strains with pandemic potential. The exchange of gene segments between co-infecting viruses, reassortment, results in the co-packaging of genes from distinct viral strains within viral progeny, and has been the primary mechanism for the emergence of the majority of pandemic strains in the last century. The inhibition of secondary infection after a short time period induced by SIE restricts co-infection, and by extension reassortment, to a band of cells at the interface between adjacent, singly-infected lesions. *In vitro* studies have shown that this co-infected region comprises approximately 2% of

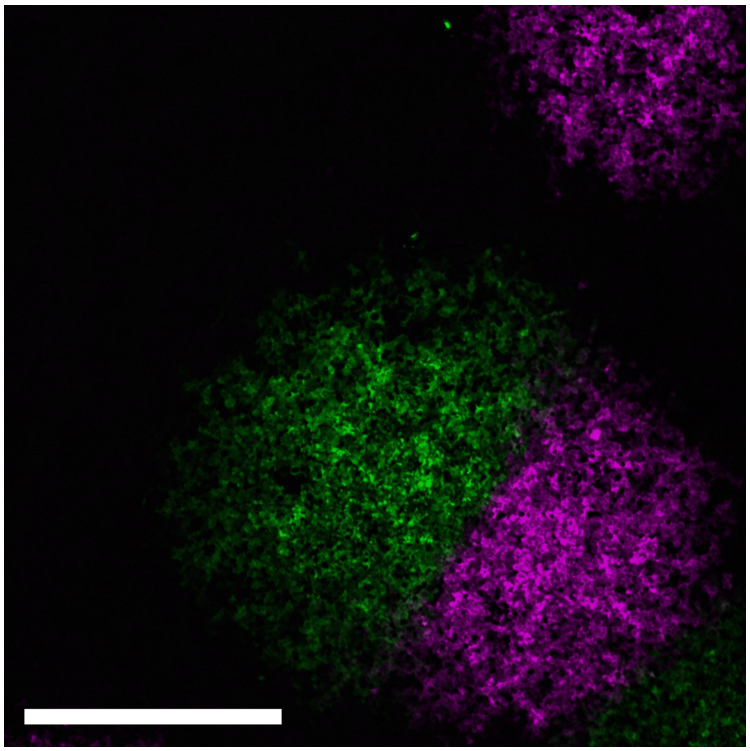

Figure 3.16: *In vitro* demonstration of superinfection exclusion and resultant micro-domain structure by Sims *et al.* Marin-Darby canine kidney (MDCK) cells were infected with a low MOI of two variants of ColorFlu (Green/Magenta) under plaque assay conditions (Scale bar = 2mm) (Sims et al., 2022).

infected cells, however, bulk transcriptomic studies have shown that reassortant progeny are common later in infection (6-9 dpi) both in nasal swabs and whole lung homogenates (Fu, 2018; Sims et al., 2022).

In addition to SIE, bulk transcriptome studies of whole lung lobes have revealed further spatial restrictions on reassortment (Amato et al., 2022; Ganti et al., 2022). In humans, and common model organisms, lungs comprise distinct lobes which are isolated from one another with the respiratory tract bifurcating immediately below the trachea. Recent transcriptome studies using viruses containing unique single nucleotide polymorphisms (SNPs) within synonymous codons, referred to hereafter as barcoded viruses, have revealed heterogeneous virus populations emerge over the timecourse of infection. Amato *et al.* showed that during co-infection with a library of barcoded viruses, a single viral population grows to dominate within a lobe, moreover, this dominant strain appears to be determined stochastically, with the

dominant strain differing between the lobes of a single lung and between biological replicates (Amato et al., 2022). Meanwhile, Ganti *et al.* have demonstrated similar effects, extending studies to include infections of the upper respiratory tract, as well as expanding studies to other mammalian hosts (Ganti et al., 2022). These findings demonstrate a similar spatial restriction mechanism to superinfection exclusion operating at the scale of the whole lung, further restricting reassortment during co-infection.

This leads to an apparent inconsistency; given the restriction of reassortment by SIE, along with the dominance of single variants within lung lobes, why are reassortant progeny so common? This study sought to develop imaging methods to examine this question and employ multimodal microscopy approaches to improve the understanding of novel strain emergence crucial to improving public health response to potentially pandemic strains.

Methods

Mice were housed at the CRUK and all handling, infection, culling and harvesting was carried out by Dr. Ryan Delvin and Jack McCowan. Mice were intranasally inoculated either with one of the four fluorescently tagged IAV BrightFlu viruses rescued by Dr. Huailong Zhao, or with a virus cocktail comprising two fluorescently tagged ColorFlu viruses, as described in section 2.3.1. Lungs were harvested by collaborators at the CRUK, and perfused, inflated, and dissected as described in section 2.3.1. Clearing was performed using the adapted ECi clearing protocol described in section 3.2.1.

Results

In order to understand the mechanisms governing spread, interaction, and reassortment between co-infecting viruses, light sheet microscopy of whole lung lobes infected with fluorescently tagged influenza A viruses were studied throughout the timecourse of infection.

Initial studies were performed on singly infected lungs, this both enabled valida-

tion of our clearing protocol in lungs and the validation of a series of fluorescently tagged influenza A viruses produced by Dr. Huailong Zhao at the CVR. These fluorescently tagged viruses, known collectively as BrightFlu, are designed on a backbone of the lab adapted IAV strain A/Puerto Rico/8/1934(H1N1). BrightFlu viruses feature a fluorophore encoding sequence within the non-structural segment (NS), following the non-structural protein (NS1) encoding sequence attached by a cleavable 2A linker. This linker sequence makes BrightFlu notably more genetically stable than the other commonly used fluorescently tagged IAV system ColorFlu which features a similar fluorophore encoding sequence within the NS segment but without a 2A linker, leading to fluorophores commonly being ejected from the genome during replication.

Four BrightFlu viruses were rescued by Dr. Huailong Zhao; BrightFlu-ZsGreen, BrightFlu-ZsGreen MinOVA, BrightFlu-DsRed, and BrightFlu-mCherry. These viruses were rescued prior to the commencment of the work carried out here. For the imaging carried out here, swapping the fluorophores, particularly those in the red portion of the spectrum, for a newer red fluorescent protein may have improved imaging (through being brighter, for example). However, as these fluorescently tagged viruses were produced by a collaborator, I had no involvement in the selection of fluorophores. This may be worth considering in future experiments. BrightFlu-ZsGreen had previously been validated for *in vivo* use via LiSM by Dr. Ed Roberts, so this work focused on validating the other viruses. Lungs were harvested at 6dpi with BrightFlu-mCherry and BrightFlu-DsRed by collaborators at the CRUK. Harvested lung tissues were then dehydrated with tertiary butanol and refractive index matched with ECi. BrightFlu-mCherry infected samples showed clear signal above mock levels in the appropriate channel (figure 3.17). The extent and distribution of fluorescent foci is representative of expected viral distribution at 6dpi based on histological data and Dr. Roberts LiSM data for BrightFlu-ZsGreen (Pirillo et al., 2023).

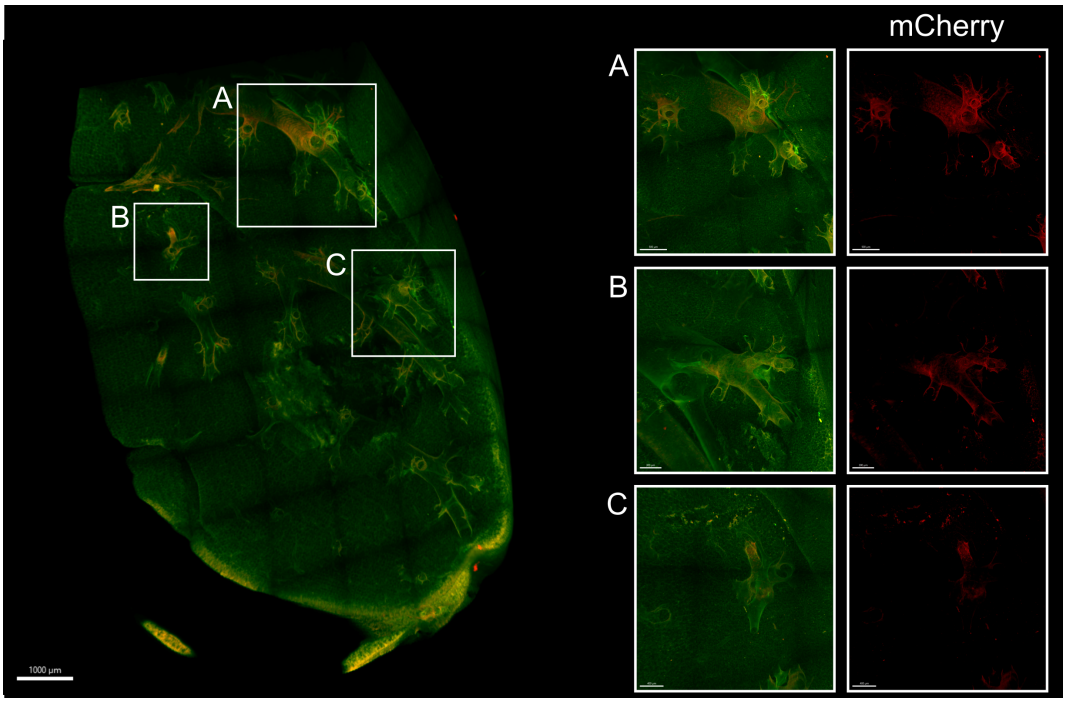

Figure 3.17: BrightFlu-mCherry (red) infected mouse lung, 6 dpi imaged via LiSM (Zeiss Z1) (Scale bar = 1000 μm). Background fluorescence in the red channel is removed based on uninfected controls. Autofluorescence (green) is not removed to provide structural context. Inserts show viral lesions (Scale bars = 500 μm (top), 300 μm (middle), 400 μm (bottom). Data is representative of results from two biological replicates. These data representative of data from an n=2 experiment.

BrightFlu-DsRed infected samples show little fluorescence above background, with the only fluorescence above mock levels co-localising with above mock level fluorescence in the green channel, suggesting this is a region of particularly high autofluorescence, rather than DsRed fluorescence (figure 3.18). This lack of signal was not unexpected due to the known cytotoxic properties of DsRed and the poor performance of BrightFlu-DsRed *in vitro* in comparison to other BrightFlu viruses (Zhou et al., 2011).

In both cases, optical clearing was successful, with lung structure being obvious based on autofluorescence. Shadowing artefacts are minimal - a result of removal of highly absorptive materials, namely haem, via perfusion - and illumination is homogeneous across the imaging volume with signal visible even in deeper section

of the tissue (figure 3.17 and 3.18).

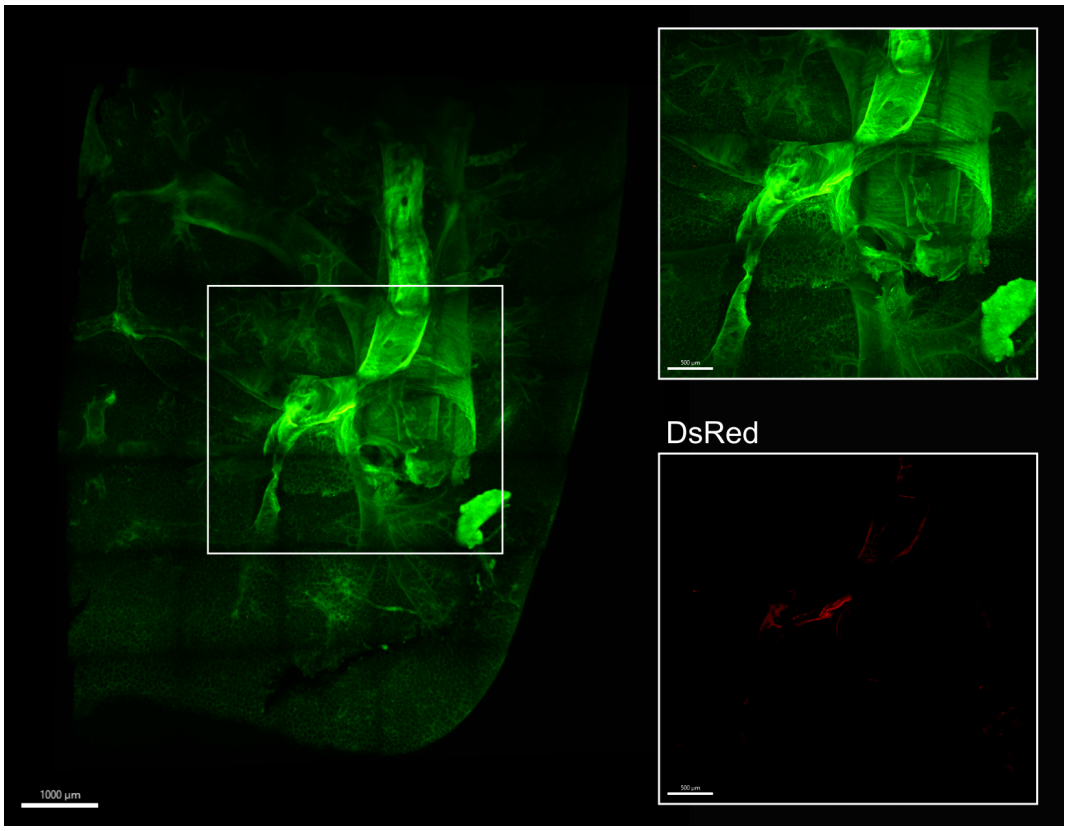

Figure 3.18: BrightFlu-DsRed (Red) infected mouse lung, 6 dpi imaged via LiSM (Zeiss Z1) (Scale bar = 1000μm). Background fluorescence in the red channel is removed based on uninfected controls. Autofluorescence (green) is not removed to provide structural context. Inserts show that the only signal in the red channel above background is aligned with regions of peak brightness in the green channel, suggesting this is not true signal (Scale bar = 500μm). Data is representative of results obtained from two biological replicates. These data are representative of data from an n=2 experiment.

Having validated our clearing approach for the visualisation of fluorescent virus within the lung, co-infected lungs were imaged to understand how co-infection alters the progression of disease. Co-infections were performed using the ColorFlu system, comprising two isogenic, fluorescently tagged IAVs (Fukuyama et al., 2015). In ColorFlu, similarly to BrightFlu, the fluorophore encoding sequence is inserted into the NS segment, however, unlike BrightFlu, ColorFlu does not contain a cleavable 2A linker between the NS1 protein encoding region and the fluorophore

sequence. In practice, this makes the virus less stable, with an increased likelihood of reversion to wildtype and generally lower titres *in vitro*. ColorFlu was chosen for these experiments as the multi-fluorophore BrightFlu system is as yet unpublished and ColorFlu remains the standard in the field.

Co-infected lungs were harvested at 3 and 6 dpi by collaborators at the CRUK. The progression of disease during co-infection is not significantly altered when compared to infection with a single IAV strain (figure 3.19). 3 dpi, the viral burden is largely confined to the proximal lung tissue, few bifurcations from the trachea (figure 3.19A). While by 6 dpi, proximal lung infection has been majoritively cleared with viral populations now present in the distal lung tissue, in the minor bronchioles and surrounding parenchyma (figure 3.19B). The exception at 6 dpi is the substantial viral burden in the trachea (top of figure 3.19B), since the trachea is not present in the 3 dpi dataset this viral burden cannot be easily compared. However, this does demonstrate that the upper respiratory tract harbours a large viral population which is likely distinct from the populations harboured in the lungs, as suggested in the literature (Amato et al., 2022; Fu, 2018; Ganti et al., 2022).

It is worth noting the reduced number of visible lesions within these data when compared to the BrightFlu studies above. The reasons for this is likely that these experiments were performed prior to the modification of the clearing protocol to use tertiary butanol rather than ethanol. Ethanol is known to disrupt GFP signals and this modification to our clearing protocol was specifically intended to improve fluorescence retention.

The largely unchanged pathology of co-infection in comparison to singly-infected tissue demonstrates that the effects of superinfection exclusion, which lead to dramatic compartmentalisation at the microscale, have no long range effects on viral distribution at the mesoscale. Additionally, the effects observed by Amato *et al.* and Ganti *et al.* in which a single strain rises in prevalence over the course of infection to dominate late stage infection are not visible here, with both strains being represented in abundance throughout (Amato et al., 2022; Ganti et al., 2022).

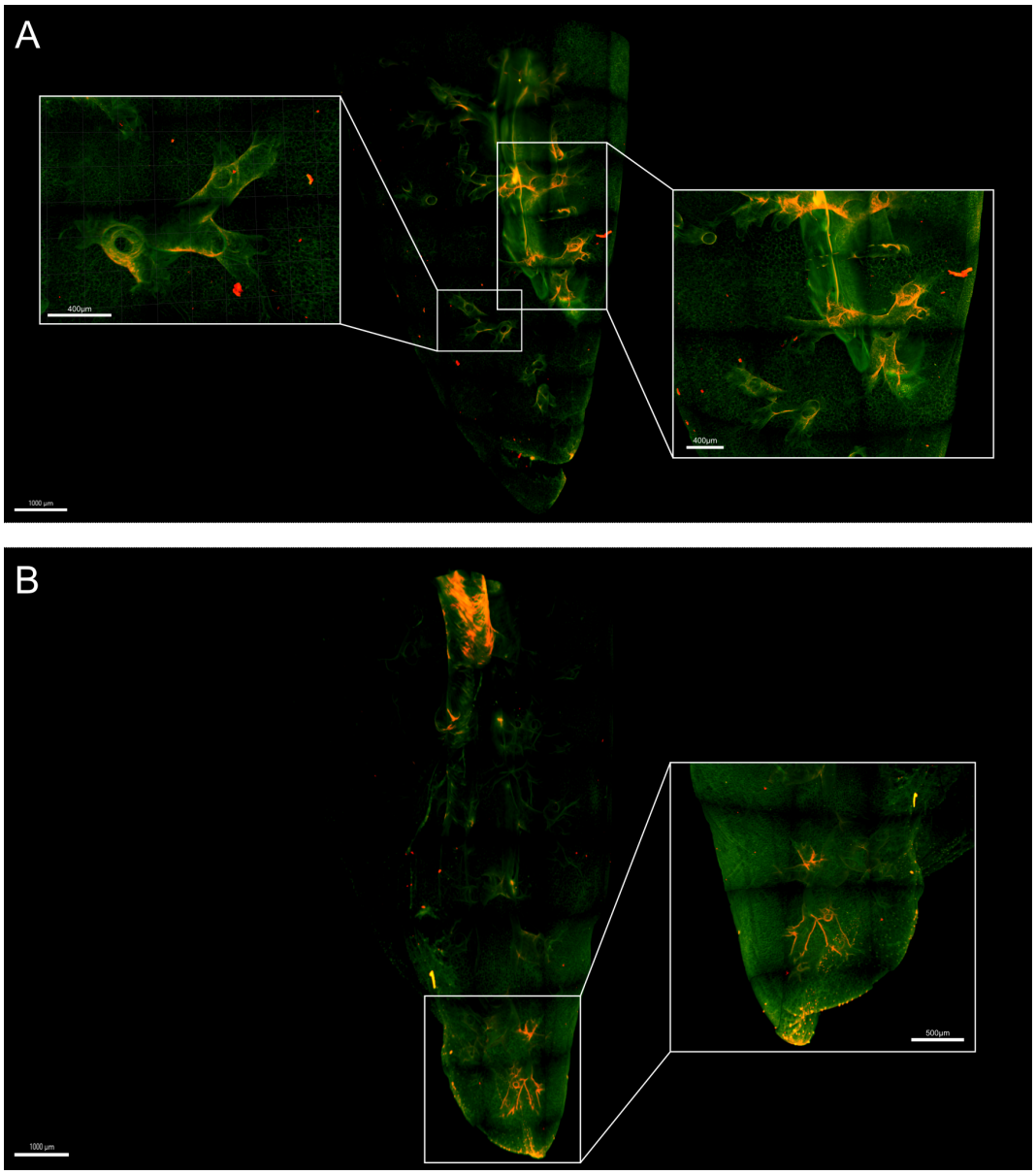

Figure 3.19: ColorFlu infected mouse lungs, harvested at 3 (A) and 6 (B) days post infection captured via light sheet microscopy (Zeiss Z1) Scale bars = 1000 μm). Autofluorescence in the red channel as been removed based on uninfected controls. In the green channel autofluorescence has been mostly removed to highlight areas of co-infection with the eGFP tagged virus, but a low level of autofluorescence has been included as a structural marker. Inserts show regions of co-infection (orange) (Scale bars = 400 μm (A, left/right), 500 μm (B)). These data are representative of data from an n=2 experiment.

Interestingly, in both cases the majority of lesions are co-infected (orange), rather than adjacent regions of single (red/green) infection. This is seemingly

at odds with the effects of superinfection exclusion observed by Anna Sims *et al.* (Sims et al., 2022). Given the spatial constraints enforced by SIE, these findings would suggest that these co-infected lesions were seeded with both viruses simultaneously (or, at least, within the approximately four hour window prior to SIE). For the number of lesions observed this is highly unlikely, particularly for lesions 6 dpi which are reliant on multiple rounds of seeding and replication.

Given this apparent discrepancy, thick section confocal imaging was employed to further study these co-infected lesions. Tissues from mice co-infected with both ColorFlu strains were harvested 3 dpi by collaborators at the CRUK. Lungs were sectioned in to 300 μm thick sections cut via vibratome. Sections were cleared via overnight immersion in Ce3D and imaged via confocal microscopy. This imaging reveals superinfection exclusion *in vivo* (figure 3.20). Given the improved resolution offered by confocal microscopy compared with light sheet microscopy (400nm and 14 microns axial resolution for the Zeiss LSM 880 and Zeiss Z1 light sheet respectively), it is hypothesised that these seemingly co-infected lesions in LiSM data actually comprise tightly constrained networks of singly infected lesions as demonstrated via thick section confocal, thereby resolving the seeming discrepancy between our LiSM findings and those of Sims *et al.*

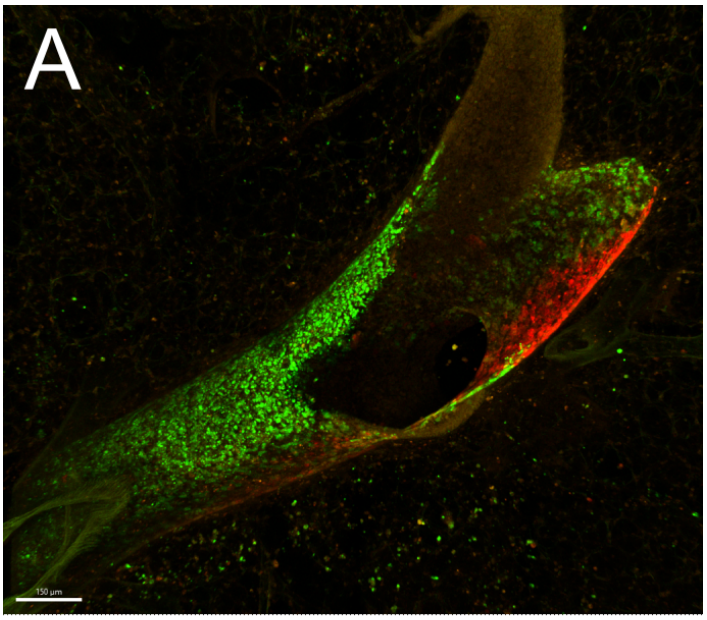

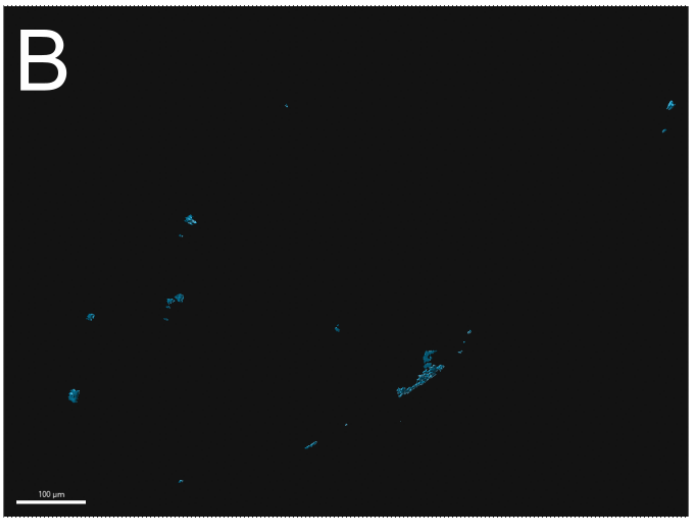

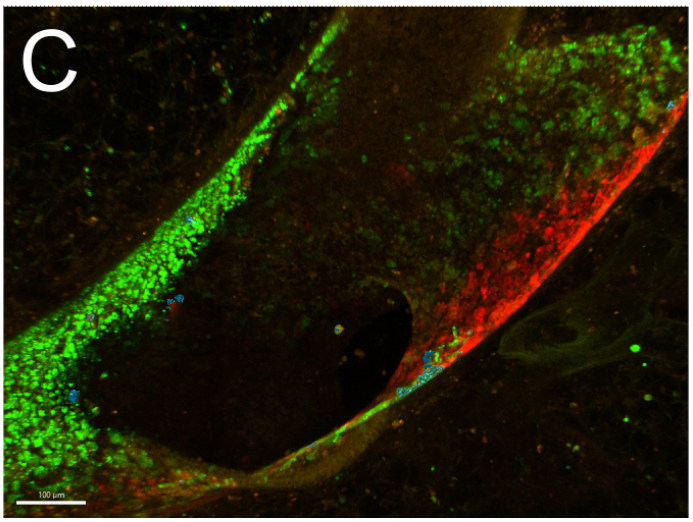

(Caption on next page.)

Figure 3.20: High resolution confocal imaging (Zeiss LSM 880) of co-infected regions reveals SIE as observed *in vitro*. A: Thick section confocal imaging of lung tissue from a ColorFlu infected mouse showing SIE between fluorescent virus strains, green and red, in the bronchi (Scale bar = 150 μm). B: Using Imaris, a surface was rendered showing co-infected cells (cyan) (Scale bar = 100 μm). C: Co-infected cell surface shown with the original image to demonstrate the restriction of co-infection to the periphery of lesions (Scale bar = 100 μm). These data are from an n=3 experiment.

In order to determine how the mechanics of superinfection exclusion *in vivo* compare with the *in vitro* findings of Sims *et al.*, I aimed to determine the quantity of co-infected cells as a ratio of cells in the two lesions. Binary masks were generated in Imaris representing the two adjacent lesions, with thresholds determined based on uninfected controls. A third volume was then created, representing the overlap between the two binary masks (shown in blue in figure 3.20B/C). The overlap between these surfaces definitionally represents co-infected cells. The volume of each surface is provided within Imaris and the ratio of co-infected cells was calculated as 2.3% of all infected cells. This finding reflects the findings of Sims *et al. in vitro* in which co-infected cells comprised approximately 2% of cells in adjacent lesions (Sims et al., 2022).

3.2.8 Miltenyi Biotech Collaboration: Validating clearing methods on alternative microscopy systems

Introduction

In order to examine how our tissue clearing method performed on equipment other than the Zeiss Z1, I collaborated with Miltenyi Biotech. This work came shortly after the release the Miltenyi Ultramicroscope Blaze, the successor of the Ultramicroscope 2 light sheet microscope (Ariel, 2018; Bhatia et al., 2022). The Blaze enables the visualisation of large samples on the order of whole mice, comprising

a 35cm^3 sample chamber illuminated by six light sheets (MiltenyiBiotechnology, 2025). Thus this collaboration also enabled us to test the efficacy of our clearing method for larger tissues such as whole lungs.

Results

Samples for imaging were selected to best compare results with existing Zeiss Z1 studies. Given the sample chamber size, whole right lungs from ColorFlu infected mice 3 and 6 dpi was selected for imaging. Mouse infections and tissue harvesting was performed by collaborators at the CRUK. Samples were cleared as described above in section 3.2.1, without the need for melanin bleaching.

In order to visualise volumes on the scale of tens of centimeters, the Ultramicroscope Blaze features a series of low magnification, high numerical aperture objective lenses with working distances on the order of centimeters, resulting in large fields of view (MiltenyiBiotechnology, 2025). This significantly improves acquisition speed when compared with the Z1 data presented above, all of which was captured with a 20× objective. Additionally, this wide field of view reduces the need for tiling and stitching. This allowed both lung and skin samples to be captured in a single field of view via the 4× objective lens, taking approximately eight minutes.

The clarity of minor structures such as airways in the lung is comparable to data gathered via Zeiss Z1 demonstrating that the clearing method developed here is suitable for tissues on the scale of whole lungs (figure 3.21). Additionally, the illumination across the entire volume of the lung is more consistent, likely due to the six light sheet illumination method and lack of tiling and stitching which results in lower illumination at tile boundaries. Lesions are also similarly visible as in single lobes imaged via Zeiss Z1. Infected cells are visible in the large lesion in the bronchi in the proximal lung. While differences between imaging platforms have an impact on the resolution of these data, the comparable resolution within lesions in lobes and whole lungs demonstrates that the method developed here is effective in clearing whole organs.

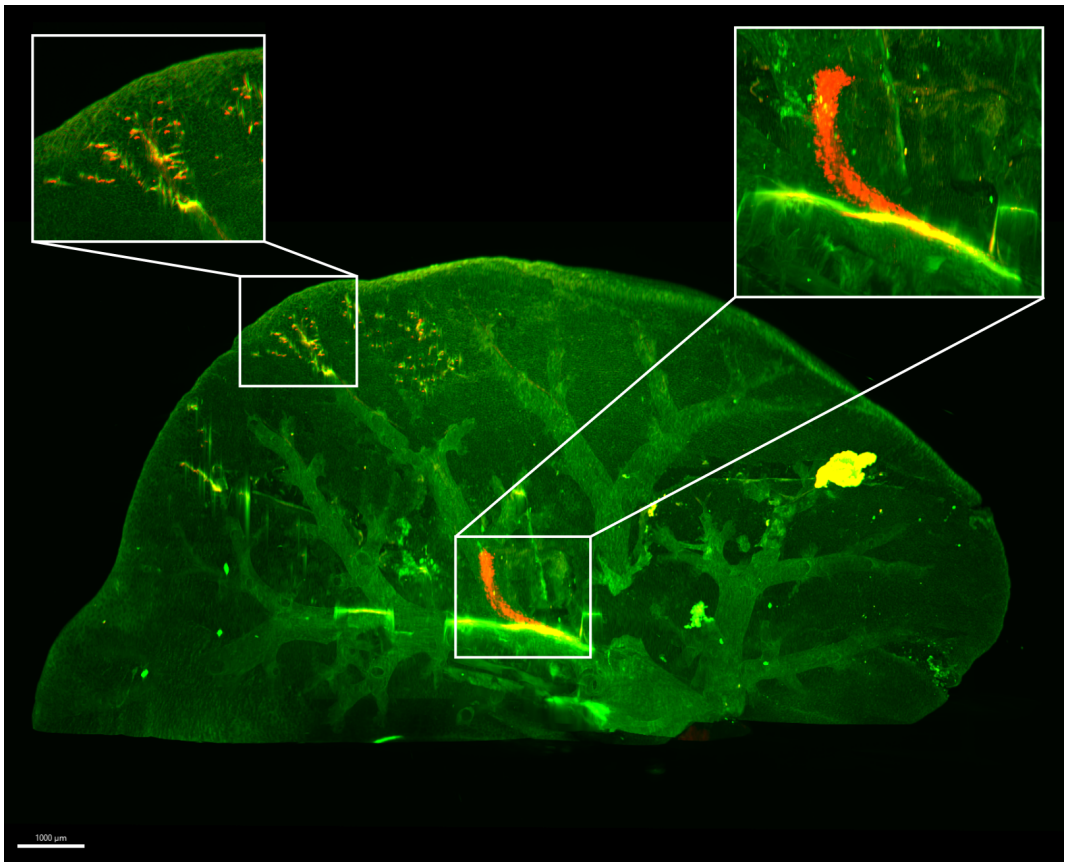

Figure 3.21: Right lungs from mice 6 dpi with ColorFlu (green and red), optically cleared via tertiary-butanol and ECi. Imaged in a single tile via Miltenyi Ultramicroscope Blaze (4× objective), using 488nm and 561nm illumination. Tissue autofluorescence (green) has been included to act as a structural marker (Scale bar = 1000 μm). These data are from an n=1 experiment.

Discussion

The Miltenyi Ultramicroscope Blaze has been used previously to visualise whole cleared mice (Cai et al., 2023). This work highlights the growing desire to image larger samples, and by extension, the need for clearing methods suitable for samples on the order of whole organs to whole rodents. While the clearing of entire mice is beyond the scope of this project, here I have demonstrated a clearing protocol relying on Ce3D priming, tertiary-butanol dehydration, and ECi refractive index matching is capable of clearing tissues on the scale of whole mouse lungs (approximately 3 cm^3). The clarity and resolution of fine tissue structures is equivalent to that observed in single lung lobes ($<$1 cm^3) using the Zeiss Z1 system at the

CVR.

The work carried out here creates a basis for more extensive studies of large tissues and collaborative projects with Miltenyi. Specifically, AstraZeneca have expressed interest in collaborating on work which would require the clearing of the upper respiratory tract of ferrets. Due to the complex structure of the ferret airway, this work would require the clearing of the entire head of the ferret (Johnson-Delaney and Orosz, 2011). Therefore, bone and skin surrounding the upper respiratory tract would remain *in situ* and require clearing. This work on clearing large tissues, in combination with the extensive studies validating our clearing method in multiple tissue types including bone, skin, and airway epithelium above offering sufficient evidence that our methods are suitable for large scale studies such as the work proposed by AstraZeneca.

3.3 General Discussion and Conclusions

Here, I have developed an improved ECi clearing protocol for fluorescence imaging via light sheet microscopy (figure 3.4). Based on the clearing protocol established by Klingberg *et al.*, I have improved both the final transparency of cleared tissue and fluorescence of endogenous signals compared with the established protocol. The addition of a pre-clearing step using Ce3D improved final clarity of fine tissue structures (figure 3.17) particularly in visualising minor airways in the lung. Comparison between tissue dehydrated using ethanol (figure 3.19) and tissue dehydrated using tertiary butanol (figure 3.17) clearly demonstrates that tertiary butanol dehydration improves fluorescence retention.

Through a series of collaborative case studies, I have demonstrated that our clearing protocol is suitable for a variety of tissues with diverse structural properties and is appropriate for imaging both endogenous markers (figure 3.7) and immunolabled structures (figure 3.8). Our clearing protocol extends the existing ECi protocol by only a single overnight incubation, and is not substantially more expensive due to the low price of Ce3D, tertiary-butanol, and triethylamine relative

to ECi.

In addition to demonstrating the range of tissue types which can be cleared and imaged using the protocol developed here, the data presented here demonstrate the resolution achievable using this clearing and imaging protocol. As described earlier in this chapter, light sheet systems are typically capable of imaging at single cell resolution but cannot reach the subcellular resolution achieved by modern confocal systems. In our data, the smallest structures which could be reliably identified were trypanosomes in the skin of mice. Trypanosomes are single cellular parasites and are roughly 40 μm long in the slender form observed here. Host cells range in size but are commonly around 20 μm in diameter. Therefore, the data presented here demonstrate that our protocol is capable of imaging structures on the scale of single cellular organisms and is approaching the size of typical host cells. This is approximately the same the expected resolution for many modern light sheet microscope approaches. Furthermore, the data presented here demonstrate that our protocol is capable of clearing and imaging tissues upto 1cm thick (the largest mouse lung lobes imaged here). The size of the Zeiss Z1 sample chamber prevented experiemnting with larger tissues on this system, however, the clarity of structures in the larger whole lung imaged on the Miltenyi Ultramicroscope Blaze demonstrates that the clearing protocol developed here is capable of imaging larger structures than can be imaged on the Z1, upto whole lungs (approximately 1.5cm in the longest axis).

A key limitation of the light sheet studies presented here is the lack of replication of results. In the case of samples handled as part of a collaboration (skin, lungs containing melanoma, mosquitoes, bone, spinal cord) samples were limited to what was made available by the collaborator (In all cases presented here n=1). In the case of IAV-infected lung samples imaged as part of my PhD, independent of any collaboration, the key limitation on replication of data was the infection, processing and imaging time required for light sheet microscopy of large samples. Infections of mice took 3-6 days depending on condition, fixation and optical clearing takes between 1 and 2 weeks, finally imaging of each sample takes 1-2

days when using the Zeiss Z1 light sheet microscope. This long imaging time is due to the magnification of the objective available on the Z1 system (20x), meaning many more tiles are required to cover the entire sample volume. In the case of the Miltenyi Ultramicroscope Blaze imaging is conducted with a 4x objective with a much larger field of view. This allows a whole lung to be imaged in a single tile, significantly improving imaging speed. In all cases, sample preparation and imaging time significantly decrease the throughput of light sheet imaging experiments on large tissue samples. A possible solution to this is to support light sheet experiments with higher through put imaging modalities such as confocal, as is done here for IAV-infected lungs.

Additionally, autofluorescence, and the relative difficultly in accounting for this in comparison to confocal images of *in vitro* samples or thin tissue sections, further confounds quantification. Biological tissues typically autofluoresce primarily in the blue-green region of the spectrum. This autofluorescence is typically highly variable across the tissue. The key drivers of this variability are two fold; Tissues are non-homogenous, with cellular density and cell types varying across the sample. Cell types vary in autofluorescence, and higher cellular density will result in higher autofluorescence. This can occur in confocal imaging of *in vitro* samples, for example in differentiated cultures, but is less common and the heterogeneity across these samples less pronounced. Secondly, illumination is variable across the sample due to the angle of incidence between the light sheet and the sample surface. Unlike tissue sections or *in vitro* cultures, organs are not flat. Therefore, the angle at which the light sheet is incident on the surface of the tissue is inconsistent. For a perfectly refractive index matched sample, this would not impact imaging, as no change in direction of propagation of light occurs when passing from the mounting medium to the tissue. However, in practice, some refractive index mismatch exists between even well cleared tissues and the mounting medium. As such, refraction at the surface of the tissue depends, to some degree, on the angle of incidence and therefore varies across the tissue volume. As described refraction effects the capacity to collect light from the sample, thus effecting the

intensity of collected light. As such, collected intensity, and therefore intensity of autofluorescence varies across the sample volume. This can be combated by improving optical clearing approaches, however, in practice, some inconsistency will remain. This effect, combined with the lack of computational tools for background removal in large 3D volume (likely due to the difficulties involved in this process arising from these differences in autofluorescence) make removal of background, and therefore quantification of data very difficult. In combination with the long lead time involved in light sheet imaging of large samples, this further supports the experimental design suggested above; supporting large tissue imaging using light sheet microscopy with higher throughput, more easily quantifiable approaches such as confocal microscopy.

Using this adapted clearing protocol, I was able to image IAV infections in the whole lung for the first time. These studies reveal that the distribution of viral lesions throughout the airway (and the localisation of these populations throughout the time course of infection) during co-infection does not differ meaningfully when compared to single infection despite SIE (figure 3.19). Early stage infection is restricted to the major airways in the proximal lung, before progressing to the distal airways and surrounding parenchyma. SIE experiments *in vitro* and single strain dominance studies may imply that large pockets of a single strain would result in a coarse, discretised infection (Amato et al., 2022; Ganti et al., 2022; Sims et al., 2022). Rather, I observe tightly constrained networks of micro-domains (figure 3.20). These networks suggest that unlike *in vitro* studies where short range particle transport prevents the seeding of secondary lesions, *in vivo*, viral particles are moving sufficiently far as to escape the spatial constraints of SIE.

Viral transport and deposition has been studied by Kevin Welsher's group using single particle tracking to visualise viral particle walks (Johnson et al., 2022). These findings offers insight into the motility of viral progeny within the mucus, demonstrating that viral particles sample many binding sites prior to cell ingress, offering ample time for longer range transport due to mucosal movement. Further to long range transport within the mucus, our data suggest that following cell

egress, viral particles become aerosolised. The distance between lesions observed at 3 and 6 dpi is beyond that expected by either plaque-like lesion growth or mucosal transport alone.

This aerosolisation of viral progeny likely also facilitates the exchange of viral material between the upper and lower respiratory tract, enabling the forward transmission of viral progeny between hosts. This is further supported by the consistent localisation of co-infecting viral populations to airway bifurcations (figure 3.19). This localisation isn't surprising as bifurcations result in the impact of large amounts of air, and by extension aerosolised particles, on the epithelium. Previously, it was not well established how upper and lower respiratory tract infections interacted.

Additionally, our findings provide a possible insight into the spatial structure of viral populations in lung lobes dominated by a single strain such as those studied by Ganti and Amato. While in both cases a single strain comes to dominate during late stage infection, other viral populations persist. Our data suggests that while a single virus dominates on the scale of the whole lobe in these studies, the spatial landscape may still be complex, with microdomains of sub-dominant strains intersperced among dominant populations. The dominance of a single strain is seemingly at odds with the significant proportions of reassortant viruses observed by Jinqi Fu in nasal swabs from ferrets during late stage infection (Fu, 2018). I hypothesise that complex spatial environments in lobes dominated by a single strain may allow significant levels of reassortment to persist despite decreasing genetic diversity on the mesoscale over the timecourse of infection.

Taken together, these findings offer insight into both the mesoscale mechanisms underpinning the pathology of co-infection and the microscale interactions between viral populations *in vivo* governed by superinfection exclusion – reflecting previous *in vitro* findings.

Chapter 4

Development of methods for FISH analysis

4.1 Introduction

Fluorescence *in situ* hybridisation (FISH) technologies such as RNAScope enable the visualisation of mRNA molecules within single cells. This method was further improved by in 1998 by the Singer lab with the development of single molecule FISH (smFISH), enabling single molecules to be quantified and distinguished using FISH probes (Femino et al., 1998; Raj et al., 2008). As described in chapter 1, many FISH platforms exist such as HCR-FISH (Choi et al., 2008; Dirks and Pierce, 2004; Evanko, 2004). Each platform has advantages which are discussed in chapter 1 however these are described here briefly; RNAScope has gained popularity as a "plug-and-play" strategy for conducting FISH experiments as it is well supported by the parent comapny ACD-Biotechne and probes targeting a range of common RNA species froma range of hosts can be purchased directly from ACD-BioTechne. However, RNAScope is expensive and the probe design is proprietary, meaning users have no scope to modify probe designs if binding is unsuccessful or non-specific. Methods in which probes are designed in hous, such as HCR-FISH circumvent both of these issues while retaining the amplification of signal seen in RNAScope assays by using a hybridisation chain reaction as described in chapter 1 (Choi et al.,

2008). RNAScope was used here due to the ease of use described above, however, issues with custom probe design discussed later in this chapter demonstrate the issues of proprietary probe sequences. mRNA transcripts are detected by fluorescence microscopy, with transcripts appearing as 'transcriptional spots' (F. Wang et al., 2012). Quantification of these signals enables the analysis of transcriptional activity at the single cell level within the spatial context of tissues (Marx, 2021). However, the large microscopy datasets produced by FISH experiments currently require custom code in order to conduct in-depth transcriptomic analyses. QuPath is a purpose-built platform for the analysis of large images such as those acquired during FISH experiments, and is recommended by ACDBio-Techne, the developer of the RNAScope platform (https://acdbio.com/qupath-rna-ish-analysis), for image analysis (Bankhead et al., 2017). QuPath has specific in-built tools for cell segmentation and fluorescent spot detection, which can be used to quantify transcriptional spots. Furthermore, the software incorporates a batch processing feature which facilitates automated analysis of data from multiple images (Bankhead et al., 2017). Following quantification, QuPath can plot quantified data, such as transcripts per cell, as a histogram (Bankhead et al., 2017). However, users wishing to conduct more complex analyses, such as differential expression analysis or co-expression analysis, must develop custom pipelines to parse raw QuPath output data, thus restricting such analysis to users with extensive programming experience. Here, I present FISHtoFigure, a standalone, open-source software tool for the in-depth analysis of transcript abundance in QuPath-quantified FISH data by users with all levels of programming experience. FISHtoFigure can concatenate the batch processed data from QuPath, enabling the analysis of large, multi-image datasets. Notably, FISHtoFigure allows users to conduct transcript abundance analysis for cells with specific, multi-transcript expression profiles. Additionally, FISHtoFigure enables users to conduct differential expression analysis between datasets, facilitating the targeted study of differential expression in specific cell types and populations. Thus, FISHtoFigure provides a means for all users to examine mRNA expression of multiple transcripts without the need for cus-

tom analysis pipelines. Many platforms similar to QuPath exist for the analysis of imaging data. Open-source examples include imageJ/FIJI, CellProfilr, and Napari. CellProfilr and ImageJ/FIJI are typically better suited to smaller datasets such as high resolution, low field of view fluorescence images, while Napari and QuPath have been designed with a focus on larger data (namely thick section confocal, lightsheet, or whole slide histological data). FISHtoFigure was designed as a downstream tool for QuPath due to a combination of existing experience with QuPath among the initial expected user base of FISHtoFigure and QuPath's capacity to handle large data, thus reducing the chance of users encountering a bottleneck when using the FISHtoFigure pipeline on large datasets. However, FISHtoFigure has been explicitly designed such that the portion of the underlying code which harvests data from QuPath datasets is intentionally separated from downstream analysis of said data. As such, the data harvesting section can be rewritten for other platforms without altering analysis and with relatively little effort. The HALO suite from Indica labs is a particlarly notable example as this platform is capable of conducting the type of cell segmentation based on transcriptomic profile which I have acheived here with FISHtoFigure. However, HALO is a proprietary software, restricting access to institutions and researchers with sufficient funding to justify this expense. With FISHtoFigure I have created a platform capable of performing analysis similar to the cell profiling function in HALO in an open-source package, significantly improving access to these tools. Similarly, many platforms exist for the analysis of FISH data. FISH-Quant is a suite of open source tools for the analysis of FISH data (Imbert et al., 2021; Imbert et al., 2022; Mueller et al., 2013). BigFISH acts as the back-end for FISH-Quant and enables the quantification of fluorescent spots within cells and analysis of the localisation of spots to cell compartments (i.e. cytoplasm, nucleus, membrane). However, by the authors own admission, use of BigFISH requires understanding of Python. A range of common methods using BigFISH are available as plugins within the graphical user interface (GUI) module, ImJoy, enabling users without coding experience to conduct these methods. These GUI-compatible methods include cell segmentation,

assignment of fluorescent spots to cells, and analysis of localisation of fluorescent spots to cellular compartments. FISHQuant is a powerful tool for the analysis of clustering and co-localisation of RNA species within cells and the localisation of RNA species to cellular compartments. However, FISHQuant is primarily focused on the localisaition of RNA species within cells, rather than the profiling of many humdreds of cells across a micrograph based on RNA expression profiles. To this end, FISHtoFigure enables users to determine cell types based on RNA expression profile and conduct analysis of these cell populations across large datasets or between biological conditions. Here, I demonstrate the use of FISHtoFigure in two biological scenarios. First, I used FISHtoFigure to analyse T-cell and B-cell populations in the spleens of influenza A virus (IAV) infected mice, hereafter referred to as the spleen dataset. Second, I demonstrate the capabilities of FISHtoFigure for the analysis of high-plex FISH data collected from highly ramified, non-round cell types, using a dataset obtained in a recent experiment by our group investigating microglia in the brains of *Trypanosoma brucei* infected mice, hereafter referred to as the brain dataset (Quintana et al., 2022).

4.2 Results

4.2.1 Development of FISHtoFigure

FISHtoFigure was designed to facilitate the conversion of QuPath-quantified image data into transcript abundance analytics. I designed a simple graphical user interface (figure 4.1) and packaged the FISHtoFigure software as a standalone executable program, enabling analysis to be conducted with no interaction with the raw data or underlying Python code. Below I outline the steps involved in analysing FISH data using FISHtoFigure, along with examples of analysis outcomes.

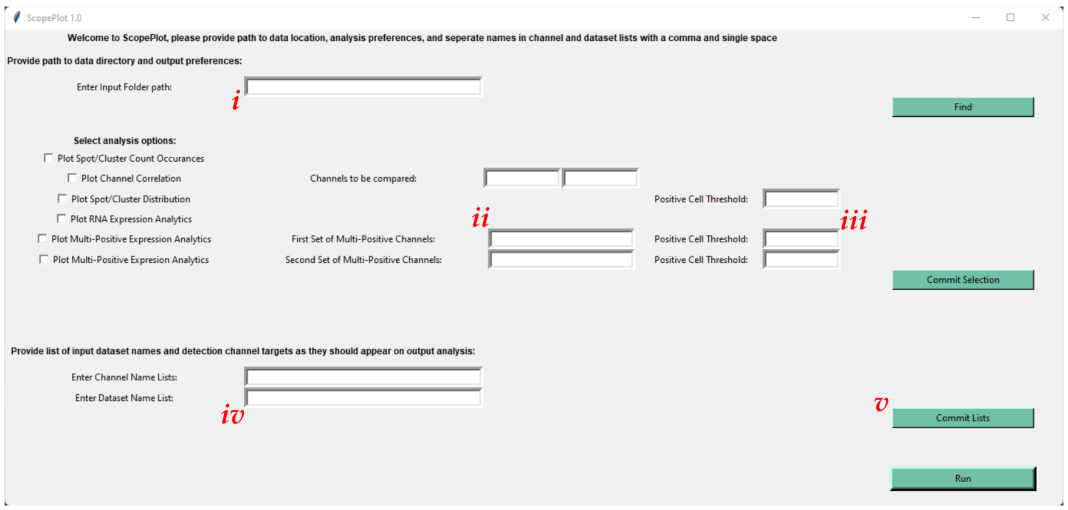

Figure 4.1: Graphical user interface designed for the use of FISHtoFigure. Here users define (i) the path to the directory containing files for analysis. (ii) Select analyses to be performed and specify names of target channels for multi-target positive cell analysis. (iii) Set positive cell thresholds (iv). Define names of all target channels (in the order they appear in the QuPath text file) and datasets (in the order they appear in the specified input directory) for analysis. (v) Before committing file location, analysis options and channel and dataset information.

Step 1: Data Harvesting and Validation of Quantified FISH Data

First, cellular boundaries and mRNA transcripts were identified using QuPath's "cell detection" function. The "cell detection" function approximates cell boundaries by expanding a region based on the nuclear staining. This approximation

method can be problematic, esspecially in highyl dendritic cell types (such as microglia) in which the structure of the cell boundary differs significantly from the structure of the nucleus. It would be preferable to use a cell boundary marker for cell segmentation. The QuPath team are currently working on cell segmentation based on a membrane marker and hope to add this functionality as part of an upcoming release. QuPath output data were then processed using FISHtoFigure (figure 4.2A) (Bankhead et al., 2017).

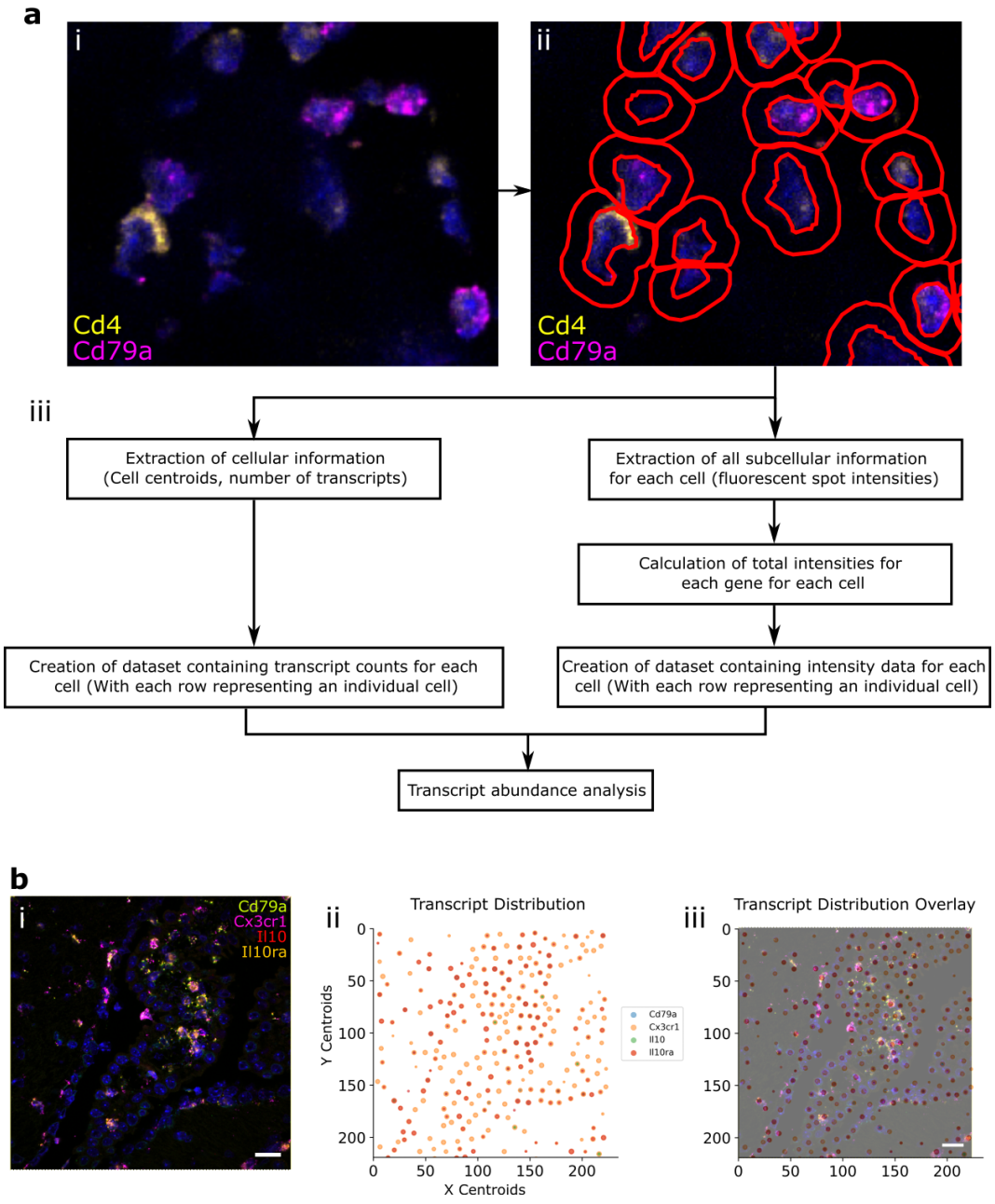

(Caption on next page.)

Figure 4.2: FISHtoFigure pipeline. (**a**) (i) A FISH image from the spleen dataset captured via Zeiss LSM 880. (ii) Cell boundaries were approximated by expanding the nuclear stain using QuPath's "Cell Detection" function was used to identify cell boundaries (red). (iii) An overview of the FISHtoFigure processing pipeline. (**b**) (i) A FISH image from the brain dataset (scale bar = 20 μm), captured via Zeiss LSM 710 and (ii) processed using FISHtoFigure's "Plot transcript distribution" function. (iii) An overlay of the captured FISH image with the plot produced by FISHtoFigure.

As experiments usually require numerous individual images, I created a dedicated pre-processing tool to concatenate individual QuPath-quantified image datasets into a single file comprising data from any number of FISH images, which can then be analysed by the main FISHtoFigure program. Due to the volume of information captured during imaging, the resulting quantified files are large and include metrics not relevant for transcript expression analysis (e.g. morphometric data, such as, cell area, nucleus and cytoplasm morphology, etc.). The desired information, i.e., the number of transcripts per cell and fluorescent intensity data, which comprise only a small portion of the quantified data, are extracted by FISHtoFigure from QuPath-quantified FISH data files and assigned to the cells from which they originate. Metrics are then calculated for each cell, i.e. the number of transcripts and total fluorescent intensities for each mRNA target. In addition to transcriptome information, cell location information is extracted in the form of the cell centroid (based on nuclear staining identified using the "Cell Detection" function in QuPath). Further information on the flags FISHtoFigure uses to harvest data are provided in the "FISHtoFigure v1.0.1 User Guide" document in the tool's GitHub repository and is recommended for developers wishing to further develop the FISHtoFigure tool. These data are then processed by FISHtoFigure using the "Plot Transcript Distribution" feature, which produces a scatter plot of points representing cell centroids, with points sized by number of mRNA transcripts within the cell and coloured by gene (figure 4.2Bii). This allows users to visualise quanti-

fied data in a format analogous to the original FISH image (figure 4.2Bi) and, by overlaying this visualised data with the original FISH image, directly validate the accuracy of data extraction by FISHtoFigure (figure 4.2Biii).

Step 2: Differential target abundance analysis from FISH data using the FISHtoFigure package

Following data extraction and assignment of transcript information to cells, differential transcript abundance analysis can be conducted using FISHtoFigure's "Transcript abundance analysis" feature. Using our spleen dataset, I investigated T-cell and B-cell populations in the spleens of mice, either uninfected or 6 dpi with influenza A virus. These cells are highly abundant in spleen tissue and have a classically "round" cellular morphology. Their morphology enabled easy identification of cell boundaries in QuPath, and thus generated a straightforward dataset for software validation. Spleen sections from naïve and infected mice were stained using DAPI to identify cell nuclei and probed for *Cd4* and *Cd79a* mRNA transcripts, enabling us to identify helper T-cells and B-cells, respectively (Luckheeram et al., 2012; Mason et al., 1995). This analysis revealed a statistically significant upregulation of *Cd4* expression within the T-cell population during infection ($p<0.01$, Mann-Whitney test (figure 4.3A)), while no statistically significant difference in *Cd79a* expression was observed. In addition to graphical outputs, FISHtoFigure analysis is saved in CSV format, meaning for further downstream analysis can be performed using a wide variety of platforms (R, Microsoft Excel, etc). Here, statistical analysis was performed on the FISHtoFigure output data using GraphPad PRISM.

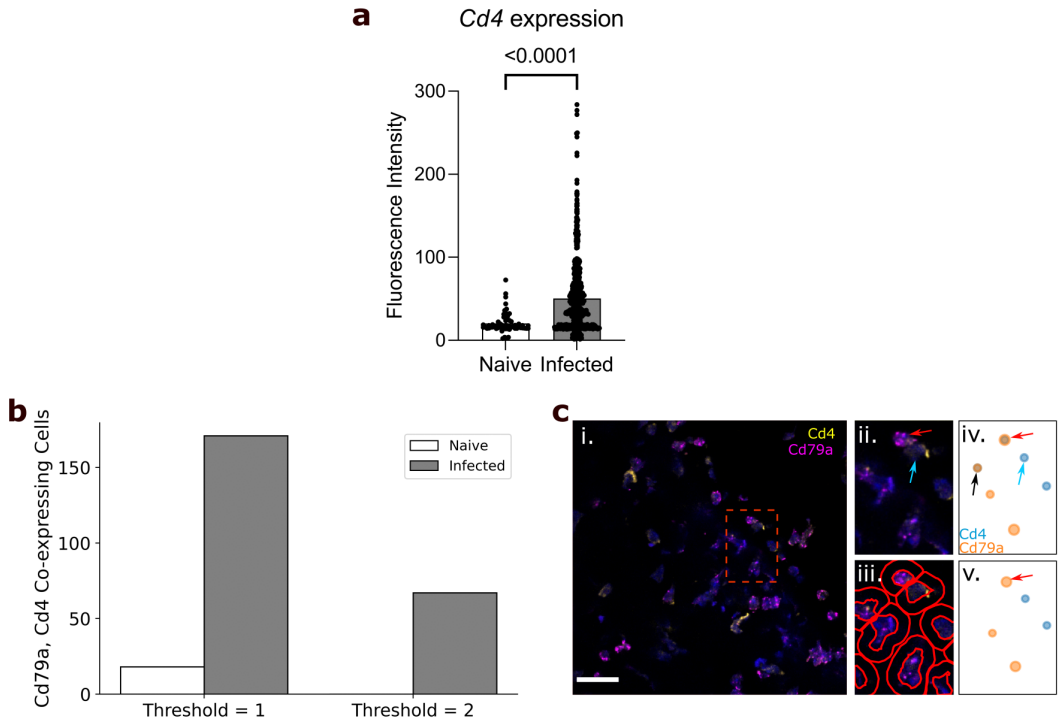

Figure 4.3: Analysis of spleen samples from naïve and IAV infected mice. (**a**) FISHtoFigure quantification of mean *Cd4* expression within cells in the naïve (n = 1228) and infected (n = 1486) spleen. Each dot represents a cell. (**b**) Total number of cells co-expressing *Cd79a* and *Cd4*, with threshold set to one or two transcripts. (**c**) (i) A FISH image from a naïve spleen (scale bar = 20 μm), captured via Zeiss LSM 880. (ii) A zoomed view of the region shown in the red square in (i) shows a B-cell (red arrow) and T-cell (blue arrow) in close proximity. (iii) Cell boundaries identified using QuPath. (iv) FISHtoFigure's "Plot Transcript Distribution" feature with a threshold of one transcript per cell, (v) two transcripts per cell; correctly categorising the B-cell and removing the ambiguous *Cd79a*+ *Cd4*+ cell (black arrow).

I expanded the analysis capabilities of FISHtoFigure by adding the "Multi-target transcript abundance" feature, enabling the identification and quantification of cell types with multiplex transcriptomic profiles. This feature can be used to identify cells expressing any combination of mRNA transcripts. Here, I present an overview of the capabilities of this feature of FISHtoFigure and example analysis on the brain dataset. Comprehensive information on the underlying code and processing

is available in the "FISHtoFigure v1.0.1 User Guide" document in the tool's GitHub repository. Here, I used this feature to validate the cell type quantification of our pipeline. *Cd4* and *Cd79a* are well established markers for helper T-cells and B-cells respectively (Luckheeram et al., 2012; Mason et al., 1995). Spleen resident B-cells do not express *Cd4*, and T-cells do not express *Cd79a*. Therefore I used the double-positive *Cd4*+ *Cd79a*+ cell population as a metric for mis-categorisation of cells by FISHtoFigure. The naïve dataset comprised a total of 1229 cells of which 273 contained transcripts of *Cd4* or *Cd79a*. A total of 18 cells were labelled as *Cd4*+ *Cd79a*+, representing approximately 1.5% of all cells and 6.6% of transcript-expressing cells (figure 4.3B). The infected dataset comprised a total of 1487 cells of which 882 contained transcripts from either marker. The infected dataset showed a higher presumed mis-categorisation rate, with 171 cells (11.5% of all cells and 19.4% of transcript-expressing cells) labelled as *Cd4*+ *Cd79a*+ (figure 4.3B). Upon closer inspection of the quantified data, many of the apparently *Cd4*+ *Cd79a*+ cells contained a majority of transcripts from one gene, suggesting that mis-categorisation typically resulted from a small number of transcripts from the other gene. This could be plausibly explained if incorrect boundary approximations caused a small proportion of transcripts to be mis-allocated between highly localised cells. For example, a B-cell in close proximity to T-cell might appear to contain a single *Cd4* transcript due to cell boundary approximation (figure 4.3C). In such cases, it is reasonable to assume the cell identity based on the majority transcript. To address this, I introduced a thresholding feature so that users can define the minimum number of transcripts from each mRNA target required for cells to be included in analysis. By setting this threshold at two transcripts from each mRNA, the population of *Cd4*+ *Cd79a*+ cells was eliminated in the naïve dataset and substantially reduced (67 cells, representing 4.5% of all cells and 7.5% of transcript-expressing cells) in the infected dataset (figure 4.3B). This was consistent with the model that *Cd4*+ *Cd79a*+ cells were artefacts, and showed that thresholding allowed this source of error to be controlled.

Having demonstrated that FISHtoFigure can quantify cell types based on mRNA expression profiles, I progressed to a more challenging system containing cells with less regular boundaries. To do this I examined sections of mouse brains, which contain highly ramified cell types, using data from a study exploring the interactions between regulatory B-cells (Bregs) and microglia during infection with *T. brucei* (Quintana et al., 2022). The brain dataset comprised 17 images captured from brain sections of infected mice and 9 images captured from uninfected (naïve) controls and was originally generated by Dr. Juan Quintana as part of a seperate study (Quintana et al., 2022). Brain sections were stained using DAPI and probed for *Cd79a* (a B-cell marker), *Cx3cr1* (a microglia marker), *Il10* (an anti-inflammatory cytokine hypothesised to be involved in Breg–microglia interactions), and *Il10ra* (the receptor for *Il10* (Mason et al., 1995; Wolf et al., 2013). These images were quantified in QuPath and concatenated into two datasets comprising naïve control data and infected data. *Cx3cr1* is a well-established microglia marker (Wolf et al., 2013). B-cells do not express *Cx3cr1* and microglia do not express *Cd79a*. Similarly to the spleen dataset, in order to examine to what extent the thresholding function could improve cell type quantification in data containing ramified cells, presumptively mis-categorised *Cd79a*+ *Cx3cr1*+ cells were quantified. The naïve dataset contained 1631 cells, 914 of which contained transcripts. 30 cells were labelled *Cd79a*+ *Cx3cr1*+ double-positive (1.8% of all cells, 3.3% of transcript-expressing cells). The infected dataset contained 3907 cells, of which 3332 contained transcripts, 392 were labelled as *Cd79a*+ *Cx3cr1*+ double-positive (10% of all cells, 11.7% of transcript-expressing cells (figure 4.4A)). Applying a threshold of two transcripts per mRNA per cell reduced the number of *Cd79a*+ *Cx3cr1*+ double-positive cells to four in the naïve dataset (0.2% of all cells, 0.4% of transcript-expressing cells), and 76 in the infected dataset (1.9% of all cells, 2.3% of transcript-expressing cells (figure 4.4A). This demonstrated that applying thresholds for transcript abundance could allow accurate allocation of transcripts to cells even for cells with complex and irregular boundaries.

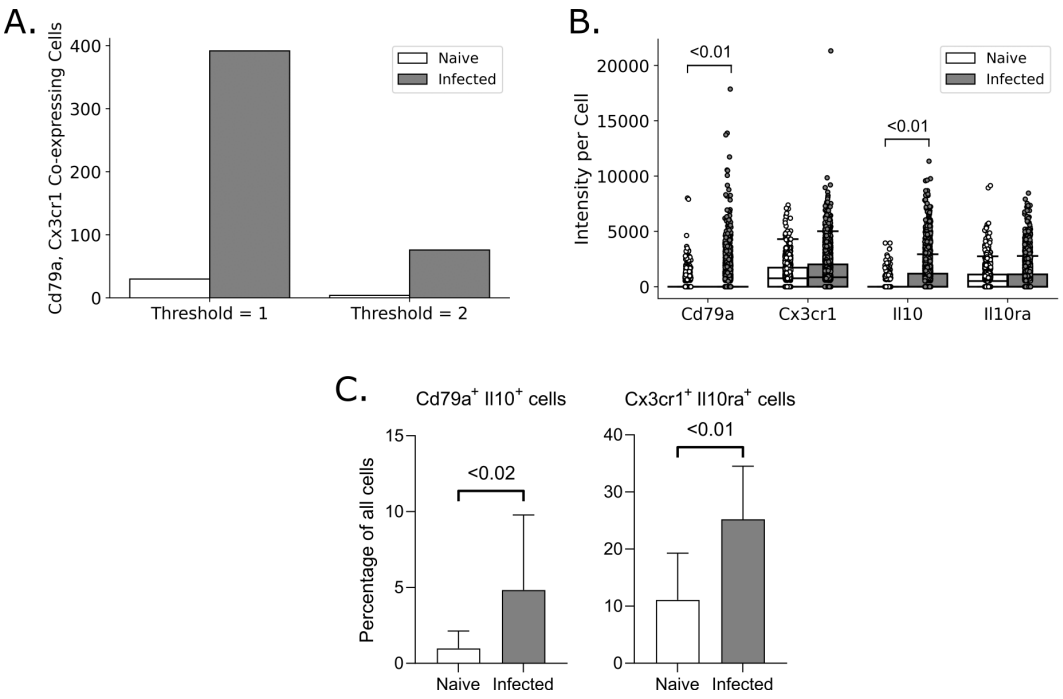

Figure 4.4: Examples of FISHtoFigure outputs from analysis of the brain dataset. (**a**) Total number of cells expressing *Cd79a* and *Cx3cr1* with threshold of either one or two transcripts per cell. (**b**) Fluorescence intensities for each mRNA for all cells, each point represents a cell. Box limits are defined by the interquartile range (IQR) with whiskers extending to the lowest/highest data point within 1.5 IQR. (**c**) Percentage of cells expressing both *Cd79a* and *Il10* (Bregs) and percentage expressing both *Cx3cr1* and *Il10ra* (Microglia). Bars represent mean values across all images in the naive (n=9) and infected (n=17) datasets, each dot represents a single image.

Finally, as a demonstration of the application of FISHtoFigure in an experimental workflow, I re-analysed data that was collected as part of a study of Breg-microglia crosstalk in the brains of mice infected with *T. brucei* (Quintana et al., 2022). Briefly, single cell and spatial transcriptomic analyses of infected mice revealed an upregulation of the anti-inflammatory cytokine *Il10*, along with Breg and microglia associated transcripts, in the brains of *T. brucei* infected mice. I tested the hypothesis that during infection *Il10* expression governed crosstalk between Bregs and microglia in the brain, using FISH and FISHtoFigure to investigate the localisation of transcripts. FISHtoFigure's "Transcript abundance analysis" func-

tion revealed a statistically significant upregulation in *Cd79a* and *Il10* expression in infected specimens compared to naïve controls, in agreement with results from single cell transcriptomics (Quintana et al., 2022 (figure 4.4B) ($p<0.01$, Mann-Whitney test; data from (Quintana et al., 2022). I then used a variety of analyses to validate that this crosstalk was driven by two specific cell types (*Il10*+ Bregs and *Il10ra*+ microglia), including visualising these cell types using FISH. Here, I expand on this analysis by using FISHtoFigure to directly quantify the abundance of two different double-positive cell types in infected and naïve mice. I used FISHtoFigure's "Multi-target transcript abundance" feature to analyse *Cd79a*+ *Il10*+ Breg populations and *Cx3cr1*+ *Il10ra*+ microglia populations in naïve and infected specimens. This analysis confirmed that during infection there was an upregulation of both *Cd79a*+ *Il10*+ Bregs (figure 4.4C) ($p<0.02$, Mann-Whitney test) and *Cx3cr1*+ *Il10ra*+ microglia (figure 4.4C) ($p<0.01$, Mann-Whitney test). In the context of the current paper, this demonstrates that FISHtoFigure can accurately quantify the abundance of specific cell types, including those with irregular boundaries, using multiplex expression profiles. Taken together, these findings demonstrate the value of FISHtoFigure in an experimental workflow.

4.2.2 FISH study of reassortment during IAV co-infection

Having developed tools capable of identifying populations of cells exhibiting combinations of RNA targets, I sought to use these tools to study interactions between co-infecting IAVs. The emergence of novel IAV strains through reassortment is reliant on co-infection such that genes from distinct variants can be packaged into single particles. In order to image reassortment events specific genes from co-infecting strains must be distinguishable. Many fluorescence methods exist for visualising IAV infection, however, these typically rely on immunostaining or endogenously fluorescent viruses. IAV immunostaining lacks specificity to distinguish between IAV subtypes, resulting in non-specific staining of co-infecting viruses. Endogenously fluorescent viruses encode a fluorophore during replication (Fukuyama et al., 2015; Pirillo et al., 2023). While this fluorophore is carried by a single

genome segment (and is therefore segment specific) fluorescently tagged IAVs typically encode only a single fluorophore gene, meaning only a single genome segment could be tracked. Additionally, the genome segment carrying the fluorophore encoding sequence is typically the same between tagged viruses (Segment 8) due to the relative tolerance for the incorporation of fluorophore sequence by this genome segment. Thus, reassortment events between co-infecting viruses involving segment 8 would simply swap the fluorophore, meaning reassortant viruses could not be distinguished from viruses naively expressing the fluorophore. The improved specificity of antibodies used in immunostaining enables the differentiation of similar genetic sequences. It was hypothesised that FISH probes designed against the surface glycoprotein encoding segments of two laboratory IAV strains of different subtype would be sufficiently specific to distinguish specific genes and thereby visualise reassortment events.

FISH probe design

FISH was performed using the RNAScope platform, as above. RNAScope provides a custom probe manufacture service by which users can have probes designed against a chosen nucleotide sequence. As mentioned above, this service comes with the significant caveat that the probe sequence is proprietary. The user provides a 1000 nucleotide sequence (with notes about specific subsequences to avoid based on similarity to other genes) against which the team at ACD-BioTechne design a probe. The probe will target a subsequence of this 1000 nucleotide sequence, however, the exact sequence of the probe is not released to the user. A panel of four probes was designed against the surface glyocoprotein encoding sequences of laboratory IAV strains PR8 (H1N1) and A/X31 (H3N2) (X31). The surface glyocoproteins, hemagglutinin (HA) and neuraminidase (NA), were selected as targets as these proteins govern the cell entry and egress of virus particles and are common drivers in the emergence of pandemic IAV strains through reassortment. X31 comprises the six internal genes of PR8 with the surface glycoproteins from the HK68 IAV strain (Kilbourne et al., 1971). Therefore, PR8 and X31 differ

only in the surface glycoproteins so are particularly appropriate for this study. RNAScope custom probe design (ACD-Biotechne) requires that users submit a nucleotide sequence of approximately 1000 bases, within which users can specify subsequences which should be avoided in probe design due to similarity to other genes, leading to non-specific binding. The primary non-specific binding concern was between segments encoding similar glycoproteins in each subtype (i.e. H1N1 HA and H3N2 HA). In order to identify subsequences within each gene which may result in non-specific binding, pair-wise alignments were conducted via nBLAST. The four surface glyocoprotein genes were aligned with one another, as well as the other six segments of the PR8 backbone shared by PR8 and X31. BLAST alignments yielded numerous sequences of significant alignment within each target gene (table 4.1). Sequences within each of the target genes which may result in non-specific probe binding with other IAV genes are shown in table 4.1 column two. The gene with which each given sequence aligns are shown in parenthesis in column two.

Table 4.1: Alignment of target genes for fluorescence *in situ* hybridisation experiments against relevant influenza A virus genomes

Gene	**Sequence position**
PR8 HA	1754-1775 (PR8: PB2, NP, NA, M, NS) 1053-1534 (X31: HA)
PR8 NA	18-64 (X31: NA) 804-880 (X31: NA) 1389-1413 (PR8:PB2, HA, NP, M, NS)
X31 HA	1042-1523 (PR8: HA, NS)
X31 NA	2-48 (PR8: NA) 588-607 (PR8: NS) 830-906 (PR8: NA)

Given that BLAST alignment is automated, each pair-wise alignment was also directly inspected by eye using JalView to check for similarity between sequences

not highlighted in BLAST analysis. An alignment of PR8 HA with the GAPDH sequence from yeast was performed to provide a baseline for the expected alignment resulting from random similarities between two unrelated genes. From the HA/GAPDH alignment, the following conditions for regions of high alignment were decided: regions of >300nt with an alignment of >70%, and regions adjacent to sequences identified during BLAST alignments with an alignment >70%. These conditions were determined based on conservative estimates of the HA/GAPDH alignment. Regions exceeding these conditions would be removed from probe designs.

JalView analysis revealed a high alignment region in the PR8 NA sequence not identified by BLAST. This region, from 1300-1480nt aligns with the PR8 polymerase basic protein 2 (PB2) sequence and is an extends the alignment between these two sequences identified during BLAST analysis. This exteneded sequence was removed from probe design along with the sequences determined to have significant alignment via JalView (table 4.1).

The remaining sequences from each target gene were aligned (again via BLAST) with both the reverse complement of each viral gene and the host (mouse) transcriptome. This analysis did not identify any further regions of alignment. Finally, promoter sequences in the terminal regions of IAV genes are shared between all viral genes (approximately comprising the 20nt at the 5' and 3' ends of the sequence), as such, these regions were removed from probe design. The target gene sequences and the above information on regions suitable for probe design were provided to the RNAScope custom probe design team. All designs were deemed feasible by the probe development team. Importantly, the RNAScope methodology relies on a series of complementary probes of 20-50nt which bind adjacent regions of the target gene. Therefore the nominal probe sequence can span regions listed as being inappropriate for probe design, but no probes will bind these regions. RNAScope probes were therefore designed to target the four genes of interest (table 4.2). Note that as mentioned above, the precise sequence of the probe oligos is not provided by ACD-BioTechne.

Table 4.2: Probe sequences for IAV target genes

Gene	**Probe target sequence**
PR8 HA	66-1048
PR8 NA	93-1178 (avoiding 803-881)
X31 HA	21-1682 (avoiding 1041-1524)
X31 NA	50-1412 (avoiding 587-608 and 829-907)

Use of probes in experiments

I validated probes *in vitro* via confocal microscopy. I infected Marin-Darby canine kidney (MDCK) cell monocultures with either PR8 or X31 at an MOI of 0.4 PFU/cell on coverglass (at biological safety level 2 - BSL2). Infections were fixed after 24 hours and probed via the RNAScope protocol described by ACD-Biotechne and briefly in section 2.4.4. In addition to FISH probes, cell nuclei were stained with DAPI. Cell monolayers were mounted and imaged via Zeiss LSM 710 (figure 4.5). Note that X31 panels are expected to be negative when probing with PR8 probes as this demonstrates that PR8 probes do not non-specifically bind with X31 genes, and vice versa for PR8 panels when probing with X31 probes.

Probes targeting PR8 HA and NA are clearly visible, as is the X31 HA probe. The X31 NA probe is barely visible by the human eye, however, the probe remains quantifiable. When analysing images of probes via image analysis platforms such as QuPath, the brightness of each fluorophore channel can be directly measured for each pixel. Pixels in X31 infected cells demonstrate above background fluorescence in the channel associated with the X31 NA probe, this is confirmed by eye if the brightness of channels is increased. This has not been done here in the interest of presenting minimally edited image data. The lower brightness of X31 NA is likely the result of lack of probe binding as increasing the concentration of fluorophore had no noticeable effect on brightness. As this probe can be quantified during analysis, it was deemed appropriate to continue pilot FISH co-infection experiments, however, improvements in this probe's binding would benefit future studies.

Probes were then used to investigate interactions between co-infecting viruses *in vivo*. Mice were co-infected with PR8 and X31 and lung tissue harvested at 6 dpi by collaborators at the CRUK. Infections were performed via a single cell instillation approach: MDCK cells were co-infected with PR8 and X31 each at an MOI of 3 PFU/cell, ensuring the majority of cells are co-infected. After five hours, cells were trypsinised and resuspended. Resuspended cells were then used as an inoculum for mouse infections. The timepoint of five hours ensures that virus will be released shortly after inoculation, increasing the likelihood of competent infection in the murine host. This approach increases the number of interacting lesions within the lung by seeding viruses in close proximity to one another rather than stochastically throughout the airway. Harvested lung tissues were formalin fixed paraffin embedded (FFPE) embedded and sections cut via microtome by University of Glasgow Veterinary Diagnostic Services.

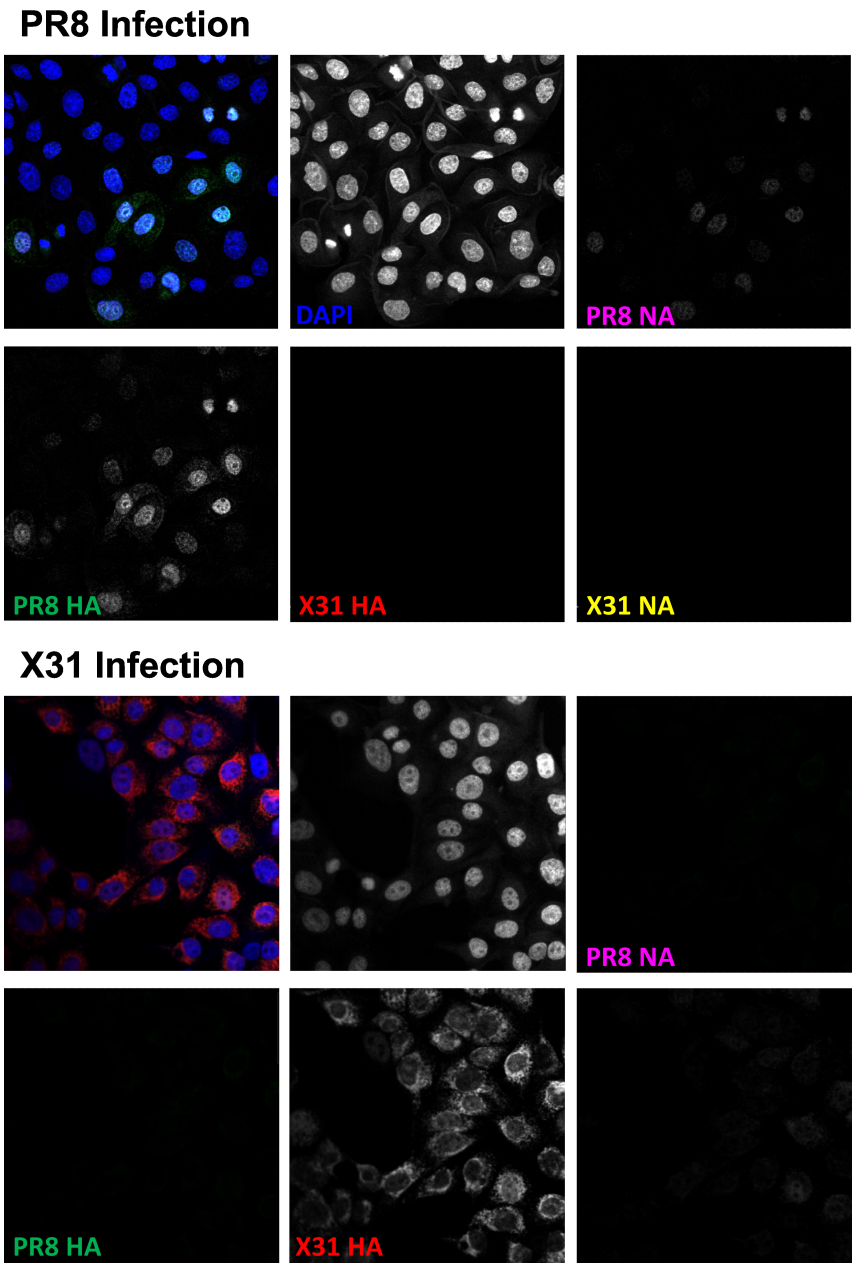

Figure 4.5: FISH probes against PR8 HA and NA and X31 HA and NA were validated via confocal microscopy. All probes targeted vRNA. Monolayers were infected with A: PR8 and B: X31. In both cases cells were incubated with all four probes. Cell nuclei are stained with DAPI (Blue). PR8 HA is shown in magenta (Opal 520 dye), PR8 NA in green (Opal 540 dye), X31 HA in red (Opal 570 dye), and X31 NA in yellow (Opal 650 dye). Probe channels are shown in grayscale for clarity. All images were gathered via Zeiss LSM 710 (40× objective).

Due to the cost of FISH probes and reagents, not all sections can be probed. This is an example of the limiations of RNAScope, had I used HCR probes this cost

issue would have been avoided. In order to identify sections containing infectious lesions, sets of three adjacent sections were cut at multiple depths across the tissue block. The top and bottom sections of each set of sections were stained for PR8 nucleoprotein (NP) and PR8 HA respectively via immunohistochemistry (IHC), the middle section being reserved for FISH analysis (figure 4.6). These sections show a high background, particularly in the section stained for NP. A possible means of avoiding this would have been to perform this staining via immunofluorescence rather than via IHC. However, a fluorescent slide scanner was not available at the time of conducting these experiments, and as such these experiments were performed via IHC.

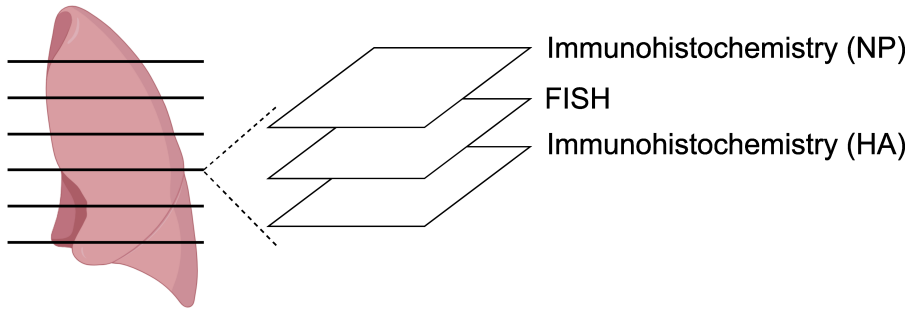

Figure 4.6: Sectioning schematic for IHC/FISH. Sets of three 10 μm thick serial sections were cut from 10 depths across the tissue in two lung blocks. Sections were cut by University of Glasgow Veterinary Diagnostic Services.

Conducting staining in the tissue section both above and below the section reserved for FISH ensures that any lesions identified via IHC will be present in the section analysed via FISH. Staining sections for PR8 NP and PR8 HA enables PR8 and X31 lesions to be distinguished. PR8 lesions will be co-stained while X31 (which lacks the PR8 HA and NA genes but comprises the other six PR8 genome segments) will be singly stained for PR8 NP. Thus, I can use this sectioning and staining method to identify co-infected tissue sections for FISH staining (figure 4.7).

Sections adjacent to those comprising PR8 and X31 lesions were then probed via FISH. Sections (n=8) were treated as per the RNAScope protocol. However, despite the presence of large visible lesions of both in adjacent IHC sections, no

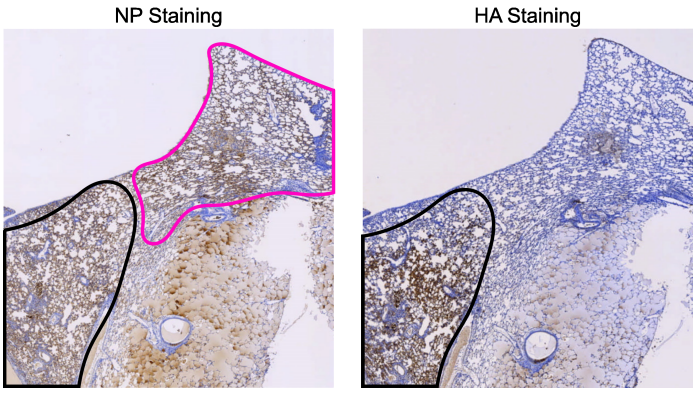

Figure 4.7: Immunohistochemical staining for PR8 NP and PR8 HA in the lungs of PR8/X31 co-infected mice. Single staining for NP signifies X31 infection (Magenta), dual staining for NP and HA signifies PR8 infection (Black). Background is characterised by homogeneous light brown staining and is not indicative of infection.

above background signal was observed for any target in FISH sections. Given the success in performing FISH *in vivo* described above, it is unclear why these attempts were unsuccessful. Due to financial constraints and reagent cost, experiments could not be repeated during this project.

4.3 Discussion

4.3.1 FISHtoFigure

FISHtoFigure automates the extraction and processing of transcriptomic data from QuPath-quantified FISH data, allowing users to analyse specific transcript expression profiles in datasets that would otherwise be very difficult to parse. Our tool is capable of analysing FISH data by any number of mRNA targets and quantifying cell types and expression profiles with a high accuracy. Furthermore, the graphical user interface allows users to specify a positivity threshold for transcript abundance analysis (i.e., the number of transcripts required for a cell to be marked as positive, and by extension, be included in analysis), allowing users to directly control the sensitivity of the FISHtoFigure platform individually for each set of analyses.

Current analysis packages for FISH data are largely focused on quantification and labelling of transcripts and only offer limited downstream transcript abundance analysis options, which require programming experience to implement. For example, FISH-quant provides a means to detect transcripts in FISH data and assign individual transcripts to cells and subcellular compartments (Imbert et al., 2021; Imbert et al., 2022; Mueller et al., 2013). FISH-quant offers downstream analysis options for mRNA expression, but this analysis is largely focused on the intracellular distributions of transcripts rather than the quantification of cells that express multiple mRNA targets. Another FISH analysis tool, dotdotdot, outputs quantified cell and transcript data in a format interpretable using R or Python. However, programming experience is required to implement downstream analysis (Maynard et al., 2020). As described earlier in this chapter, FISHQuant and BigFISH provide a means of analysing transcript localisation and clustering within cells, however, these tools are focused on the intracellular localisation of RNA species, rather than distinguishing cell types based on RNA expression profiles. FISHtoFigure facilitates custom differential transcript and cell type abundance analyses without the need for custom code. By providing multi-transcript analysis tools in an intuitive package, FISHtoFigure significantly broadens the accessibility of FISH analysis. Comparison of FISHtoFigure's spatial distribution plots with the confocal microscopy images from which they were derived demonstrates high levels of concordance between raw and quantified data (figure 4.2B). I demonstrate that FISHtoFigure can accurately determine cell profiles in different biological systems, and that the in-built thresholding feature can substantially reduce mis-categorisation caused by the close proximity of different cell types (figure 4.3). It must be noted that for this thresholding function to work, users must include at least two markers which are not shared by any cell type under any circumstances. This is crucial because the thresholding method implemented here relies on searching for quantified cells expressing combinations of markers which should not be expressed by any cell (for example the B-cell marker, Cd79a, and the microglial marker, Cx3cr1, in the brain dataset described above) to provide a proxy for how many cells are being mis-

categorised. If the users probe panel does not include a pair of exclusive markers like these, there will be no way to threshold cells accurately. It is generally possible to find exclusive markers for cell types present in the majority of samples, however this must be considered when designing the probe panel. As described above, using a membrane marker, rather than approximating cell boundaries based on nuclear staining, would circumvent this issue and no thresholding would be required. It is advised that users adjust this threshold to obtain the best results from different experimental designs. In order to determine the most appropriate value for this threshold for each experiment presented here, combinations of transcripts which were not expected to be representative of any cell type in each dataset were analysed. This allowed us to adjust the false discovery rate: the threshold was adjusted until the number of cells expressing these "impossible" combinations of transcripts was below a predetermined percentage of the total number of cells in the dataset. I suggest that users conduct similar analyses of their own data in order to determine an appropriate threshold value for each experiment. In the spleen dataset, applying a threshold of two transcripts per mRNA target per cell completely removed all mis-categorised cells in the naïve dataset and reduced mis-categorisation by $>$60% in the infected dataset (figure 4.3B). In the brain dataset, applying a threshold of two transcripts per mRNA target per cell reduced mis-categorisation of cell types by $>$80% in both the naïve and infected datasets (figure 4.4A). In the brain dataset, FISHtoFigure enabled rapid analysis of FISH data which would otherwise require considerable time investment and programming experience. FISHtoFigure analysis reveals a statistically significant ($p<0.01$, Mann-Whitney test) upregulation in expression of *Cd79a* and *Il10* during infection (figure 4.4B).The ability to analyse and plot cellular information for specific cell types with multiplex transcriptional profiles allowed us to identify the upregulation of *Cd79a*+ *Il10*+ Bregs and *Cx3cr1*+ *Il10ra*+ microglia in infected specimens compared with controls, a difference which would otherwise require custom code to assess (figure 4.4C).

Considerations and Limitations

The labeling of transcripts is the first step of our quantification pipeline and poor sensitivity or specificity at this step will have a compounding effect on the accuracy of cell type analysis performed by FISHtoFigure. Many FISH methods are available, and in this study I used the RNAScope assay, a well-established and widely-used method (F. Wang et al., 2012). As mentioned in the introduction to this chapter, alternative methods such as HCR-merFISH offer cheaper alternatives to RNAScope (Choi et al., 2008; Dirks and Pierce, 2004; Evanko, 2004). Additionally, smFISH enables quantification of single molecules via FISH probes (Femino et al., 1998). Single molecule inexpensive FISH (smiFISH) attempts to reduce the cost barrier to conducting smFISH experiments (Tsanov et al., 2016). —In a similar fashion to indirect immunofluorescence, smiFISH uses unlabelled primary probes which bind the RNA target with labelled secondary probes which bind the primary probe. Primary probes can be cheaply produced beacuse they are unlabelled. Sesecondary probes can be non-specific and capable of binding a range of primaries and thus less expensive and more generic. Collectively this reduces the number of fluorescently labelled probes which are required, since a single secondary probe can bind numerous primary probes, and reduces the cost of smFISH experiments. The RNAScope assay incorporates various features to ensure accurate and reproducible labeling of transcripts, such as a pair-wise probe design in which probes will not fluoresce unless adjacent probes also bind, significantly reducing the signal from non-specific binding (F. Wang et al., 2012). Additionally, the RNAScope assay includes a set of positive control probes specific to the species the tissue samples are taken from. These probes target common housekeeping genes present in all cell types in the sample. Because the abundance levels of these target genes are well characterised (and by extension fluorophores will bind to these targets at known levels), processing samples with these probes prior to the final experiment provide users with a means to check that fluorophores used to visualise target probes are binding correctly and are of approximately equal brightness. Finally, the assay includes a set of negative control probes which target

genes which are not expressed by any cell in the sample, and therefore any fluorescence observed in images of samples processed with these probes can be treated as background signal (generally arising from fluorophore remaining in the tissue after the wash steps). The maximum fluorescence for each fluorophore in these images can then be used to set minimum detection thresholds in experimental data (i.e. Any fluorescent signal below this threshold treated as background and is removed). Using this approach, I can be confident that quantified fluorescent spots in experimental data represent true signal from transcripts. Our pipeline cannot robustly identify single transcripts, as an smFISH method would, due in part to the means by which fluorescent spots are quantified in QuPath. QuPath quantifies subcellular fluorescent signals either as "spots" or as "clusters" depending on fluorescent intensity. In principle, "spots" should be individual transcripts, and "clusters" more than one transcript (with the specific number of transcripts comprising a cluster being estimated by QuPath based on fluorescent signal. In practice, this fluorescent intensity will depend on binding affinity of probes and amplifiers, the concentration of fluorophore used, among other factors. Therefore, we cannot describe our method as single molecule. However, given that our pipeline is primarily focused on distinguishing cell types based on RNA expression, quantifying single RNA transcripts is less crucial than in other applications (for example imaging of RNA-binding proteins). Provided there is sufficiently abundant RNA present in a cell that it can be detected by our pipeline, this RNA expression will be sufficient for cell type identification. The variety of FISH methods available means that users may wish to analyse different formats of input data. FISHtoFigure was designed for the analysis of QuPath output files, but I have intentionally built FISHtoFigure as a modular tool, separating the data harvesting step (in which data is pulled from the QuPath output) from the analysis steps. As a result, the data harvesting section can be adjusted easily, without interfering with any downstream analysis steps. At present, to modify FISHtoFigure to work with data quantified using another platform (e.g. CellProfiler) simply requires changes to the specific flags which the program uses to identify information in the quantified data file. Information on

how to make these changes to the tool are available in the "FISHtoFigure v1.0.1 User Guide" document in the FISHtoFigure GitHub repository. Regarding identifying cell boundaries, QuPath has the capacity to quantify cell boundaries based on nuclear staining, or via a fluorescent membrane marker. Here, cell nuclei were identified via fluorescent DAPI staining, and cell boundaries were approximated by applying a set radius based on tissue cell type composition to each identified nucleus using the "Cell Detection" function in QuPath. Though I demonstrate that this can allow the accurate quantification of cells, even for cell types with irregular boundaries, further improvements in the determination of cell boundaries, and by extension cell expression profiles, could likely be achieved through adjustments in sample preparation. For example, for challenging cell types users may wish to experiment with the use of membrane markers to further improve cell boundary quantificationThough the threshold function included within FISHtoFigure can be used to eliminate the majority of cell type misclassification events, the use of a membrane marker would further improve cell type quantification. I advise the inclusion of a membrane marker if users find that they cannot sufficiently eliminate misclassification events using the inbuilt thresholding function.

4.3.2 FISH analysis of IAV co-infection

The panel of FISH probes designed here were demonstrated to label the surface glycoprotein encoding segments of PR8 and X31 effectively, without cross-reactivity. This is a significant improvement over the cross-reactivity across subtypes observed in antibodies against these proteins (Beest et al., 2017). Fluorescence was visible by eye for the majority of probes. While the probe targeting X31 NA provided poor signal, being barely visible by eye, fluorescence was sufficiently above background levels for computational detection and quantification. However, in tissues exhibiting higher levels of autofluorescence in the channel colour channel chosen for this probe this low fluorescence may inhibit detection. Increasing fluorophore concentrations did not improve fluorescence signal for this probe. This suggests it is primary probe binding, rather than secondary fluorophore binding causing this

low signal. It is possible that this low signal is due to low abundance of X31 NA. However, this is unlikely as at 24 hpi multiple rounds of infection have taken place each comprising replication of NA. This is further evidenced by the proportion of cells positive for X31 HA in the X31-infected cell population.

FISH experiments using this panel of probes were unsuccessful, yielding no signal for any target gene despite IHC evidence of X31 and PR8 infection in adjacent tissue sections. The experiments performed during the development of FISHtoFigure were not performed in lung tissue, however, RNAScope is validated for use in the lung and examples exist in the literature (Sounart et al., 2022). As the FISH approach described here was unsuccessful in visualising IAV interactions *in vivo*, I decided to focus on a spatial transcriptomics approach for visualising these interactions which will be described in the next chapter. Despite this, the probes designed here will be useful in future FISH experiments on IAV infection. By enabling the differentiation of genes between co-infecting subtypes, this system enables analysis which cannot be performed using existing immunofluorescence methods.

4.4 Conclusion

The problem of balancing accessibility for non-specialist users and analytical scope is an important consideration in the development of software tools. Here, I present FISHtoFigure, an analytical platform for QuPath-quantified FISH data capable of analysing specific cell types and multiplex transcriptomic profiles and of generating a variety of differential transcript abundance analytics for cells expressing a user-specified combination of mRNA transcripts. In the interest of accessibility for users with all levels of computational image analysis experience, I have created a simple graphical user interface and packaged FISHtoFigure as an executable program, thus allowing transcript expression analysis without interaction with raw quantified image data or custom analysis scripts. FISHtoFigure can therefore expand the in-house analysis capabilities of many research groups investigating transcriptomics via FISH.

Chapter 5

Developing in vitro spatial transcriptomics methods

5.1 Introduction

In chapters 3 and 4, I have demonstrated that modern light microscopy methods enable high resolution imaging of a range of biological targets including proteins, via immunofluoresence, RNA, via fluorescence *in situ* hybridisation (FISH), and endogenous markers, via genetic modification of organisms and autofluorescence (Calvo-Alvarez et al., 2018; F. Wang et al., 2012). However, light imaging comes with caveats which complicate analysis of some samples, namely, number of targets which can be imaged and target specificity.

In order to accurately assign fluorescent signal to a biological marker, it is essential that the fluorescence spectra of markers in an image can be unmixed. Unlike lasers, fluorophores do not emit monochromatically, with emission intensity varying across a range of wavelengths, in some cases hundreds of nanometers (figure 1.7) (Hirano et al., 2022; Toseland, 2013). While many modern fluorophore systems have been designed, comprising fluorophores specifically designed to be spectrally separable (e.g. the opal fluorophores from Akoya Biosciences), overlap between emission spectra is difficult to avoid for high-plex imaging studies (AkoyaBioscience, 2024; Bhakdi and Thaicharoen, 2018). Advances in light mi-

croscopy have aided in multi-plexing, with spectral, lifetime, and cyclical imaging approaches.

Spectral imaging relies on separating fluorescent signals based on the emission response of fluorophores across the imaging spectrum. While two fluorophores may have similar maximum emission wavelengths, the emission profiles can differ significantly across the rest of the spectrum. By defining the emission of fluorophores across the spectrum, spectral imaging enables the differentiation of fluorophores based on their entire spectral profile rather than the emission peak alone (Garini et al., 2006; Tsurui et al., 2000).

Similarly, fluorescence lifetime imaging (FLIM) involves unmixing fluorophores which could not be separated using traditional confocal microscopy (Datta et al., 2020). The time for which electrons remain in the excited state varies between fluorophores. By measuring the fluorescence lifetime (the time for which electron remain in the excited state) of fluorophores, signals can be separated based on lifetime rather than emission wavelength. FLIM systems allow fluorophores with essentially identical emission spectra to be used in combination, provided they have sufficient differences in lifetime, vastly increasing the number of targets which can be imaged (Hwang et al., 2024).

Cyclical imaging approaches involve imaging the same samples multiple times, quenching fluorophores and relabeling targets with different colours between imaging sessions. This creates a fluorescent "barcode" associated with each target after numerous rounds of imaging, enabling the imaging of n^x targets, where n is the number of fluorophores and x the number of rounds of imaging. However, photodamage resulting from extensive imaging can result in variance in sample and image quality across rounds of imaging.

Additionally, specificity of antibodies and RNA probes is crucial to ensure that fluorescent signals are characterised correctly. Antibody cross-reactivity is well established with proteins binding to antibodies designed against similar structures (Beest et al., 2017). FISH probes improve on the specificity of antibodies by targeting specific gene sequences. Expanding on the example above, in section

4.2.2 FISH probes enabled the differentiation of influenza A virus (IAV) glycoprotein subtypes. However, this does not entirely alleviate specificity issues, with non-specific binding of FISH probes observed between similar sequences. This makes identification of single nucleotide polymorphisms (SNPs), for example in the study of genetic mutations during viral replication, unreliable using immunofluorescence or FISH approaches.

Sequencing based spatial transcriptomics approaches alleviate these issues by sequencing RNA directly, rather than relying on probes, while preserving spatial context. Direct sequencing allows the precise discrimination of similar sequences, offering improved genetic resolution in comparison to probe based approaches. The 10× Genomics Visium assay is an industry-leading spatial transcriptomics platform and involves the capture of RNA from tissue sections mounted on specially designed microscopy slides (Cheng et al., 2023; Rao et al., 2021). Each slide features four capture areas comprising an array of RNA capture spots. Capture spots contain oligoneuclitides comprising a poly-dT sequence capable of binding ploy-adenalated RNA and a spatial barcode specific to each capture spot (figure 5.1).

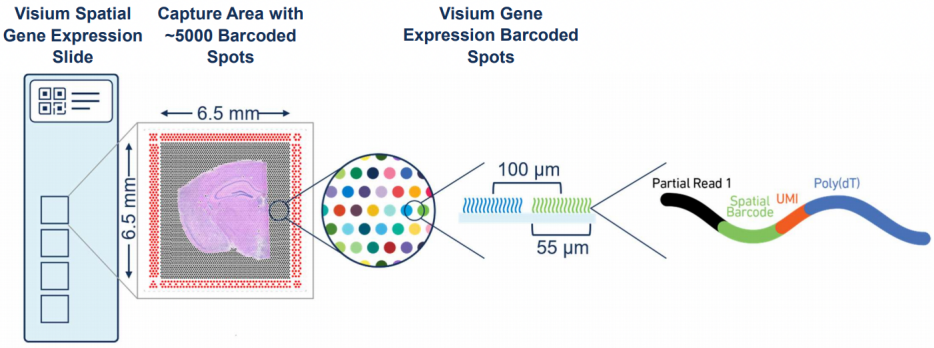

Figure 5.1: Visium spatial gene expression slide design (10xGenomics, 2025).

Following RNA capture and sequencing, the spatial distribution of sequencing data can be recapitulated using the spatial barcode associated with each capture spot. While the Visium spatial gene expression assay improves on the genetic specificity of techniques such as FISH, the assay compromises on spatial resolution. Capture spots are 55 μm in diameter with a centre to centre spacing of 110 μm. In lung tissue, capture areas contain between one and ten cells, with cellular density

varying between airway epithelium and parenchyma (Mothes et al., 2023).

The 10× Genomics Visium protocol has been used in a variety of tissues from a range of hosts (Fan, Gao, et al., 2024; Fan, Tao, et al., 2024; N. H. Gopee et al., 2024; Kats et al., 2024). By capturing all poly-adenelated RNA, the Visium platform enables researchers to study biological processes which are difficult to examine using probe based approaches such as isoforms (Joglekar et al., 2021; Lebrigand et al., 2023). These studies typically rely on coupling of the Visium assay and Oxford Nanopore Technology (ONT) to enable long read sequencing. Long read sequencing is not possible using only Illumina sequencing due to the destruction of long read sequence information during library preparation for Illumina sequencing (Ribarska et al., 2022). To conduct high-plex viral reassortment studies, one would have to identify variants of individual genes in tissues comprising many copies of similar viral gene sequences. The limitations of immunofluorescence and FISH approaches described above complicate such studies. Here, using a library of genetically barcoded IAVs developed by our collaborators Dr. Jinqi Fu and Dr. Laurence Tiley at the University of Cambridge, I use the Visium gene expression assay to study reassortment between IAVs during co-infection in the lungs of mice (Fu, 2018). These barcoded viruses comprise a series of mutations to synonymous codons in the genes encoding the polymerase basic protein 2 (PB2), haemagglutinin (HA), and nucleoprotein (NP) sequences of IAV A/Puerto Rico/8/34 (H1N1) (PR8), enabling the discrimination of gene variants without affecting the translated protein or viral fitness. Additionally, I develop and test an implementation of the Visium assay for use *in vitro*, demonstrating that this assay can harvest high quality RNA from *in vitro* samples and distinguish similar genes, namely the barcode sequences in the IAV library developed by Dr. Fu and Dr. Tiley.

5.2 Results

5.2.1 Validation of barcoded viruses

Table 5.1: Schematic of variable bases (X) in barcoded influenza A viruses

Segment	Start Position	End Position	Sequence
PB2	802	831	ttgatcatcgcXgcXagXaacatXgtXagX
HA	99	122	ggctaXcatgcXaaXaaXtcXacX
NP	553	573	tcgacXctXccXagXagXtcX

Working stocks of barcoded viruses were produced via forward passage of viral stocks supplied by Laurence Tiley (University of Cambridge). To ensure that barcode sequences in working stocks aligned with those stated by Jinqi Fu (table 5.1), RNA was extracted from virus stocks, reverse transcribed, and barcode regions were sequenced via Sanger sequencing.

MDCK cultures were infected with each barcoded virus stock at an multiplicity of infection (MOI) of 0.4 plaque forming units(PFU)/cell and incubated for 24 hours at 37°C. Following incubation cells were trypsinised, spun down and resuspended. RNA extractions were performed via Qiagen RNeasy kit (Qiagen). Eluted RNA was reverse transcribed and cDNA concentrations quantified via Nanodrop (Thermo Scientific Nanodrop One) (table 5.2).

Table 5.2: RNA concentrations for barcoded virus stocks

Sample	RNA (ng/ml)	A260/A280	A260/A230	ssDNA (ng/ml)
IAV_Barcode_1	1306	2.09	2.21	971
IAV_Barcode_2	1625	2.12	2.11	1003
IAV_Barcode_3	1474	2.11	2.08	1115
IAV_Barcode_4	1025	2.09	2.24	980
IAV_Barcode_5	1070	2.10	1.96	976

PCR primers were designed to allow targetting of the barcoded region in the PB2, HA, and NP gene segments. Where possible primers were designed such that amplicons would include mutliple hundred nucleotides at either end of the barcode sequence. This would enable binding of a dedicated sequencing primer (table 2.7) within the amplicon, and ensure reads within barcoded regions were not affected by anamolous reads typical of early bases in Sanger sequencing experiments. PCR primers were designed for each barcoded segment and are described in section 2.4.6. Primers were produced by SigmaAldrich.

DNA concentration of PCR products were measured via Nanodrop (table 5.3).

Table 5.3: dsDNA concentrations of barcoded IAV library PCR products

PB2	**ng/ml**	**HA**	**ng/ml**	**NP**	**ng/ml**
PB2_Barcode_1	1439	HA_Barcode_1	1483	NP_Barcode_1	1437
PB2_Barcode_2	1403	HA_Barcode_2	1405	NP_Barcode_2	1442
PB2_Barcode_3	1469	HA_Barcode_3	1424	NP_Barcode_3	1462
PB2_Barcode_4	1422	HA_Barcode_4	1322	NP_Barcode_4	1452
PB2_Barcode_5	1431	HA_Barcode_5	1449	NP_Barcode_5	1437

Prior to Sanger sequencing, PCR products were visualised via agarose electrophoresis (figure 5.2). All products were of the expected size and no bands representing contaminants were observed, so PCR products were sent for sequencing. Sequencing was performed by Eurofins.

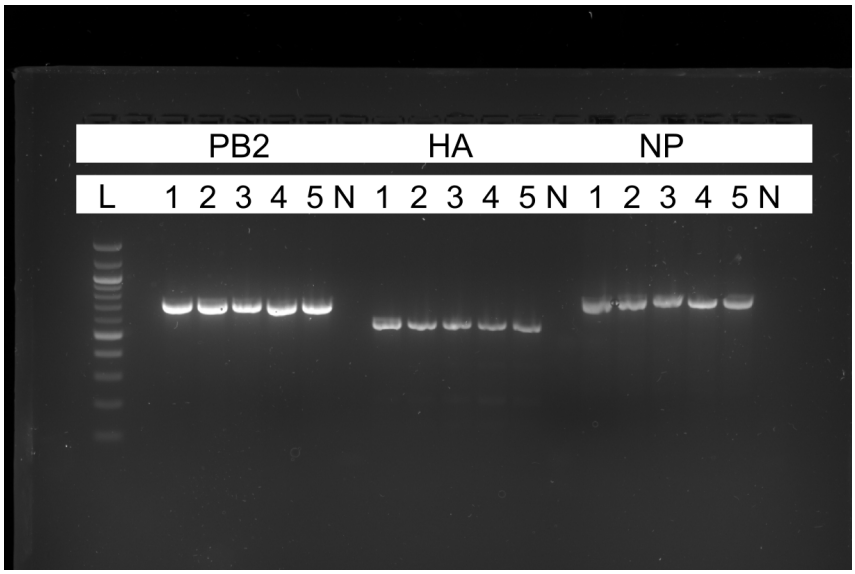

Figure 5.2: PCR products separated via gel electrophoresis.

Sequencing results for all barcoded amplicons were aligned with the reference sequences for each segment provided by Jinqi Fu (figure 5.3). Reference sequences for each segment were taken as the barcode 1 sequence for that segment. Therefore, for the barcodes in the amplicons sequenced by Eurofins to be deemed correct, barcode 1 should be identical to the reference sequence and all other barcodes should differ in the three or four bases not shared between that barcode and barcode 1. All barcodes in the PB2 and HA segments matched the expected sequences from Jinqi Fu. Three of five barcodes in NP matched the expected sequences, with barcodes 3 and 4 sequences failing to be definitively confirmed. In the case of barcode 3, the expected barcode sequence differs from the barcode 1 reference sequence in three positions; 561, 564, and 573. Of these positions only position 573 is representative of the expected barcode 3 sequence, with positions 561 and 564 and following the barcode 1 reference sequence. It is worth noting that the barcode 1 sequence is not the wildtype sequence, with mutations made at the wobble regions of codons used to encode the barcode. There are an additional three bases, all in the third bases of codons, which follow neither the barcode 1 reference sequence nor the expected barcode 3 sequence (positions 558 and 567 - which could not be read - and 570). Cumulatively, barcode 3 was not present in the expected form. These differences may be the result of mutations in the

barcoded virus during passage between sequencing of the original viral stock by Jinqi Fu and the sequencing of the stock produced from the original stock (the P+1 stock) which was used in the experiments here.

The results for NP barcode 4 were more promising. Barcode 4 differs from the barcode 1 reference sequence at four positions; 561, 564, 567, and 570. All four are correct in the sequencing results, matching the expected barcode 4 sequence. The results for barcode 4 only differ from the expected sequence in two positions; 555 and 556. Of these position 555 was swapped from G to T in the third position of the codon. This is in fact a synonymous mutation, with both sequences encoding serine, despite this codon not being used for encoding the barcode. As a result, it is unlikely this synonymous change would effect viral function or growth kinetics and would have no effect on barcode readability, it is therefore plausible that this mutation will have no bearing on experiments. Position 556 is swapped from A to T in the first position of the codon. This changes the encoded amino acid from a threonine to a serine. Cummulatively, these changes have no bearing on the readability of the barcode sequence as all barcode mutations are correct and match the expected barcode 4 sequence. The mutation at position 556 could affect viral stability or growth kinetics due to its impact on the amino acid sequence, however, all barcoded virus stocks were repeatedly passaged over six days (emulating the longest mouse infections to be performed) and no observable impact on the titre, nor barcode stability, in resultant viral progeny was observed in any of the five barcoded viruses. Given this, it was deemed that the read at position 556 had little bearing on any experiments to be performed using the barcoded library and therefore experiments with the library went ahead despite this.

Despite the inability to confirm the NP barcode 3 sequence, and the mutations in NP barcode 4, the majority of barcode sequences were confirmed and barcode fidelity was deemed sufficient to begin *in vivo* and *in vitro* experiments using the barcoded virus library.

PB2 Barcode Sequencing

Barcode 1

```
JF_PB2reference(Barcode1)       aatgatgatgttgatcaaAGCTTGATCATCGCTGCCAGGAACATTGTTAGGAGAgctgca   840
PB2_Barcode1(forwardprimer)     AATGATGATGTTGATCAAAGCTTGATCATCGCTGCCAGGAACATTGTTAGGAGAGCTGCA   497
                                ************************************************************
```

Barcode 2

```
JF_PB2reference(Barcode1)       aatgatgatgttgatcaaAGCTTGATCATCGCTGCCAGGAACATTGTTAGGAGAgctgca   840
PB2_Barcode2(forwardprimer)     AATGATGATGTTGATCAAAGCTTGATCATCGCTGCCAGGAACATAGTAAGAAGAGCTGCA   496
                                ********************************************:**:**.*********
```

Barcode 3

```
JF_PB2reference(Barcode1)       aatgatgatgttgatcaaAGCTTGATCATCGCTGCCAGGAACATTGTTAGGAGAgctgca   840
PB2_Barcode3(forwardprimer)     AATGATGATGTTGATCAAAGCTTGATCATCGCTGCTAGAAACATTGTTAGAAGAGCTGCA   495
                                ********************************** **.***********.*********
```

Barcode 4

```
JF_PB2reference(Barcode1)       aatgatgatgttgatcaaAGCTTGATCATCGCTGCCAGGAACATTGTTAGGAGAgctgca   840
PB2_Barcode4(forwardprimer)     AATGATGATGTTGATCAAAGCTTGATCATCGCTGCTAGAAACATAGTAAGGAGAGCTGCA   496
                                ********************************** **.*****:**:************
```

Barcode 5

```
JF_PB2reference(Barcode1)       aatgatgatgttgatcaaAGCTTGATCATCGCTGCCAGGAACATTGTTAGGAGAgctgca   840
PB2_barcode5(reverse)           AATGATGATGTTGATCAAAGCTTGATCATCGCAGCCAGAAACATTGTAAGGAGAGCTGCA   534
                                ********************************* ***** ******** ************
```

HA Barcode Sequencing

Barcode 1

```
jinqirefsequence    gtgcacttgcagctgcagatgcagacacaatatgtataGGCTACCATGCGAACAACTCCA   120
barcode1            -NNCNNNNNNGCTNNNNNNTGCANNNNCCATCTGTATAGGCTACCATGCGAACAACTCCA    59
                       *              ****    * ** ****************************
jinqirefsequence    CCGACACTgttgacacagtactcgagaagaatgtgacagtgacacactctgttaacctgc   180
barcode1            CCGACACTGTTGACACANTACTCGAGAAGAATGTGACAGTGACACACTCTGTTAACCTGC   119
                    ***************** ******************************************
```

Barcode 2

```
jinqirefsequence    gtgcacttgcagctgcagatgcagacacaatatgtataGGCTACCATGCGAACAACTCCA   120
barcode2            NNNNNNNNNNNNNNTGCN-----NNNNNNCNTCTGTATAGGCTACCATGCGAACAATTCAA    62
                                ***             * ********************** ** *
jinqirefsequence    CCGACACTgttgacacagtactcgagaagaatgtgacagtgacacactctgttaacctgc   180
barcode2            CTGACACTGTTGACACANTACTCGAGAAGAATGTGACAGTGACACNNTCTGTTAACCTGC   122
                    * *************** ************************** *************
```

Barcode 3

```
jinqirefsequence    gtgcacttgcagctgcagatgcagacacaatatgtataGGCTACCATGCGAACAACTCCA   120
barcode3            NNNNNNNNNNNNNNTGCN-----NNNNNNCATCTGTATAGGCTACCATGCAAATAACTCCA    60
                                ***             ** ***************** ** *******
jinqirefsequence    CCGACACTgttgacacagtactcgagaagaatgtgacagtgacacactctgttaacctgc   180
barcode3            CTGACACTGTTGACACANTACTCGAGAAGAATGTGACAGTGACACACTCTGTTAACCTGC   120
                    * *************** ******************************************
```

Barcode 4

```
jinqirefsequence    gtgcacttgcagctgcagatgcagacacaatatgtataGGCTACCATGCGAACAACTCCA   120
barcode4            NNNNNNNNNNNNNNNNNNNNNNNNNNNCCNTCTGTATAGGCTACCATGCAAATAATTCAA    61
                                      *  * ***************** ** ** ** * *
jinqirefsequence    CCGACACTgttgacacagtactcgagaagaatgtgacagtgacacactctgttaacctgc   180
barcode4            CCGACACTGTTGACACAGTACTCGAGAAGAATGTGACAGTGACACNNTNTGTTAACCTGC   121
                    ******************************************  * ************
```

Barcode 5

```
jinqirefsequence    gtgcacttgcagctgcagatgcagacacaatatgtataGGCTACCATGCGAACAACTCCA   120
barcode5            GNGCN--NNNNNNNNCA-----NNNNNNCATCTGTATAGGCTATCATGCGAATAACTCAA    59
                    * **           **            ** *********** ******** ***** *
jinqirefsequence    CCGACACTgttgacacagtactcgagaagaatgtgacagtgacacactctgttaacctgc   180
barcode5            CCGACACTGTTGACACAGTACTCGAGAAGAATGTGACAGTGACACACTCTGTTAACCTGC   119
                    ************************************************************
```

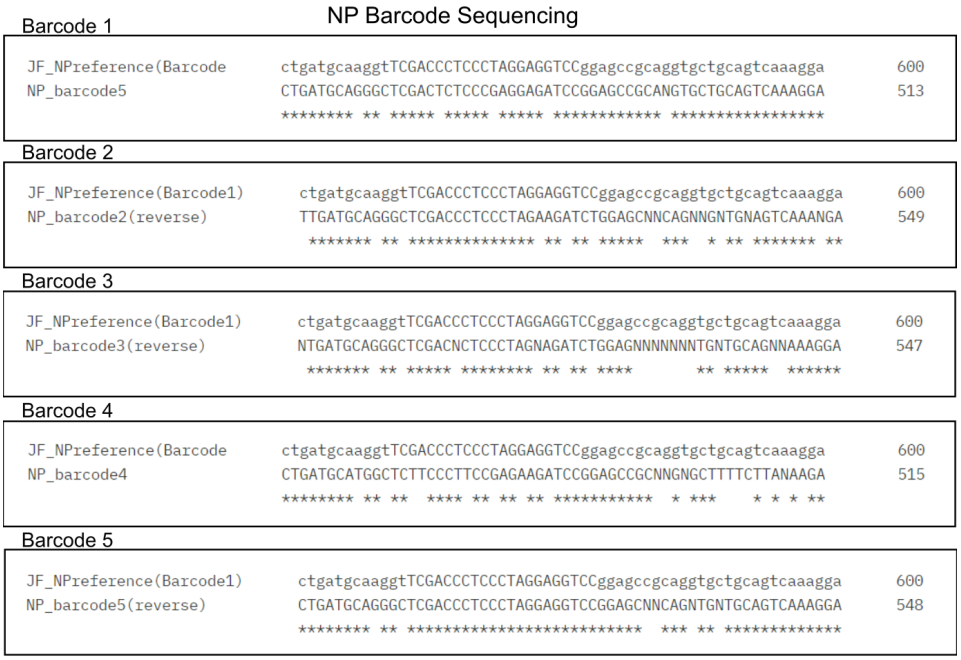

Figure 5.3: Sanger sequencing results for barcoded virus libraries comparing barcode regions to those documented by Jinqi Fu (Fu, 2018). Barcode regions are capitalised and shared bases are denoted by an asterisk. Alignment and analysis performed in ClustalOmega.

5.2.2 In vivo spatial transcriptomics study of IAV reassortment in mouse lungs

In order to better understand reassortment events occurring in the host leading to the emergence of novel IAV variants, spatial transcriptomics was performed on sections from the lungs of IAV co-infected mice. The Visium spatial gene expression assay is designed for *in vivo* studies and has been validated for lung tissue (Di Marco et al., 2024; X. Qiu et al., 2024). However, as described above the pooling of multiple cells into capture areas prevents single cell analysis. Previous studies of superinfection exclusion, as well as experiments performed in section 3.2.7, demonstrate that the co-infected region between interacting viruses is narrow, typically comprising 1-3% of infected cells (Sims, 2024). Co-infection is required for reassortment and therefore this region is of particular interest to this study. In order to determine the coverage of Visium capture spots, confocal data from a

previous mouse co-infection study was overlayed with a mask emulating the Visium capture spot array (figure 5.4) (Sims et al., 2022).

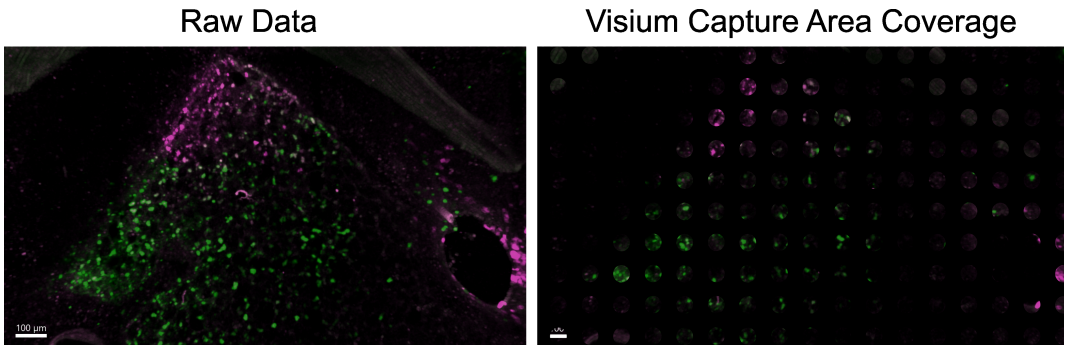

Figure 5.4: Visium capture spots reliably cover interstitial co-infected regions. Coverage of capture spots on the Visium spatial gene expression slide overlayed on an example confocal fluorescence image taken of a IAV-infected mouse lung section. Capture spots are 55 μm in diameter with a centre to centre spacing of 110 μm. Colour has been removed outside of areas covered by capture spots. Original confocal image captured by Anna Sims *et al.* (Sims et al., 2022).

The lower density of cells in the parenchyma results in a more diffuse co-infected region, makes determining the bounds of this co-infected region more difficult than in a denser cell culture or epithelium. However, mutliple capture spots cover the co-infected region with many spots containing cells expressing both green and red fluorophores. This demonstrates that the Visium spatial gene expression assay will provide sufficient spatial resolution to distiniguish adjacent IAV lesions and cover regions of co-infection.

Given that each capture spot contains multiple cells (figure 5.4), the question of whether we can truly identify reassortant viruses from these data arises. While the Visium technology used here is lacks single cell resolution, it can still be used to identify reassortant viral populations. If a capture area contains transcripts from multiple viruses we would expect to see barcodes from each of these viruses represented in this capture spot (i.e. Barcodes 1 and 2 from PB2, HA, and NP). In this case, there are three possibilities pertinent to the detection of reassortment; Some portion of the cells in this capture spot are co-infected. Or some population of cells in this capture area are infected with barcoded virus 1 and some other cells

infected with barcoded virus 2. Or some population of cells in this capture area are expressing a novel combination of transcripts from barcode 1 and barcode 2, arrising from reassortment (i.e. PB2 barcode 1, HA barcode 2, and NP barcode 2). In this case we cannot distinguish these outcomes, and therefore cannot identify any reassortant populations. However, if a capture area contains exclusively cells infected with a reassortant population (for example, in a reassortant virus-infected microdomain which is not exhibiting co-infection due to the effects of superinfection exclusion) then only a novel array of transcripts would be expressed in this spot (i.e. PB2 barcode 1, HA barcode 2, and NP barcode 2). In this case, the lack of the complimentary segments from each barcoded virus (i.e. the lack of HA and NP from barcoded virus 1 and the lack of PB2 from barcoded virus 2) definitionally tells us that barcoded viruses 1 and 2 are not present in this spot and therefore this spot is representative of a reassortant population.

The Visium assay relies on the permeabilisation of cells in order to release and capture RNA. As such, the assay includes a tissue optimisation step during which permeabilisation conditions which maximise RNA capture are identified. To do this, tissue sections from a sample analogous to the tissue being used during the Visium assay are mounted on a Visium tissue optimisation slide (comprising four capture areas, each containing an array of capture spots similar to the spatial gene expression slide, but without the spatial identifiers) (10xGenomics, 2025). Mounted tissue sections are then permeabilised with for increasing lengths of time between 6 and 30. Polyadenelated RNA from permeablised tissues is captured by the poly-dT oligos adhered to the slide. cDNA synthesis is performed using a proprietary reverse transcription mix comprising fluorescent nucleotides labelled with TRITC (a commonly used orange fluorophore), meaning optimal permeabilisation conditions will be proportional to TRITC fluorescence intensity. Tissue is then enzymatically removed from the slide and the slide imaged via fluorescence microscope. Isolated mouse RNA was used as a positive control. On our first attempt, all sections, including the positive control, showed very weak TRITC signal. In tissue sections this was likely the result of RNA degradation, however, it is unclear

why no signal was observed in the positive control (10xGenomics, 2025). As this was the first attempt, it was not understood what signal intensity was expected for successful permeabilisation using the imaging equipment available. Therefore, despite the lack of significant signal in all sections, the highest signal was selected and the used for the Visium assay (figure 5.5). A permeablisation time of 12 minutes yielded higher fluorescence than other sections, though still very weak, thus a permeabilisation time of 12 minutes was selected for the Visium gene expression experiment.

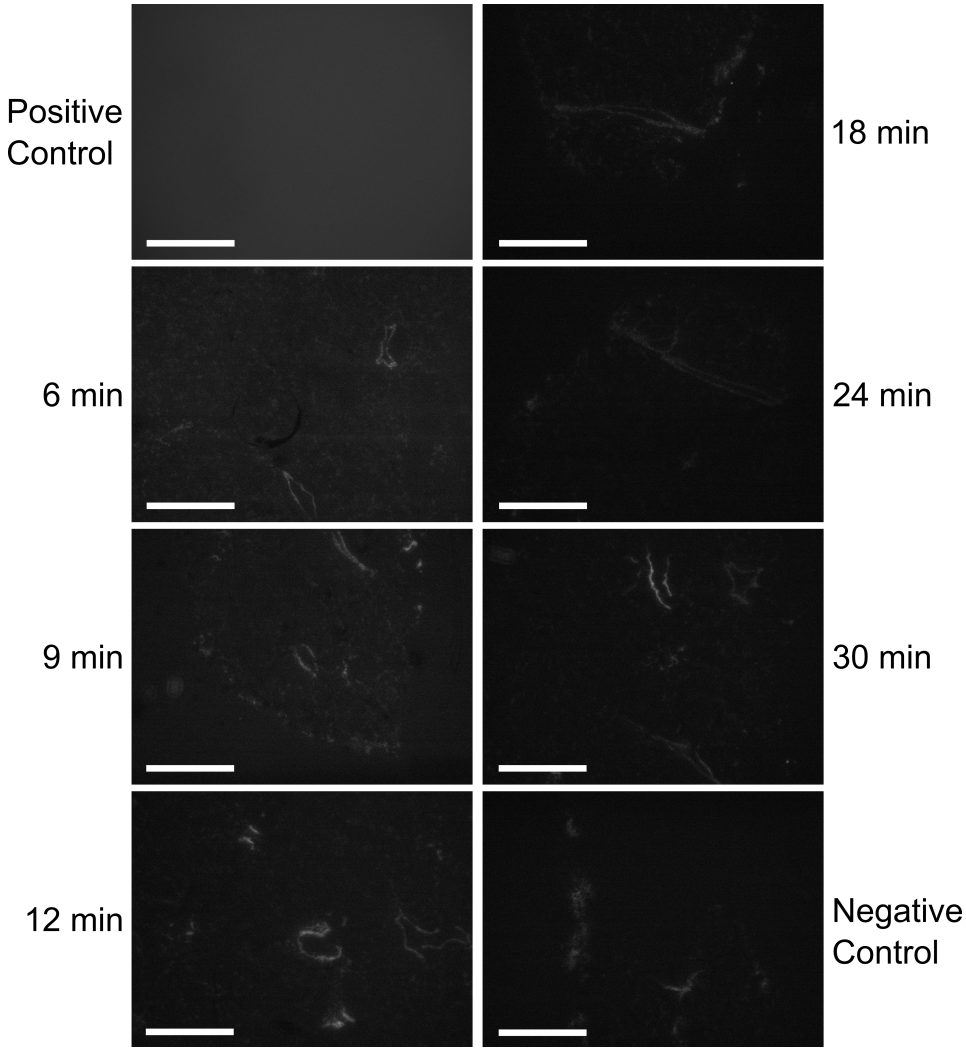

Figure 5.5: Tissue optimisation data for *in vivo* spatial transcriptomics on mouse lungs. Lung sections were 10 μm thick. Permeabilisation was performed using a proprietary Visium reagent. Permeabilisation times for each section are given in minutes. Due to a lack of availability of fluorescent slide scanner facilities, each section was imaged via widefield fluorescent microscope (EVOS) and the layout of sections shown here is representative of the tissue optimisation slide layout. All sections were imaged under identical illumination conditions (561 nm) using a 4$\times$ objective. TRITC (gray scale) signal is proportional to captured RNA quantity. I have rescaled images equally to better visualise differences in TRITC signal. Scale bar = 1000 μm.

Having determined the most appropriate permeabilisation time for lung tissue, spatial transcriptomics was carried out via the Visium assay. Mice were intranasally inoculated with a viral cocktail comprising the five barcoded viruses described above and BrightFlu-ZsGreen. BrightFlu-ZsGreen was included so that lung slices containing viral populations could be identified via fluorescence imaging prior to mounting sections. Typically, intranasal infections of mice are performed using viral particles in suspension. However, this results in a dispersed, and typically not overlapping, distribution of viral populations in the airway. In section 3.2.7, when imaging lung lobes from mice co-infected using this free virus particle inoculation method, it was found that interactions between co-infecting viruses were rare. I hypothesised that lack of interaction between co-infecting viruses was the result of this stochastic seeding of virus particles in the airway. To promote interaction between viral populations mice were instead intranasally instilled with cells which had been co-infected with the viral cocktail described above, thereby seeding mixed viral populations wherever cells land in the airway (figure 5.6). Given that these vector cells were infected prior to inoculation of the mouse, cytokine expression by these cells may affect the efficacy of this infection. However, given that this study aims to seed viruses in close proximity, it was preferable to ensure proximity of viral lesions (through seeding with co-infected cells) despite concerns over reduced infection efficacy. Infection was confirmed by immunofluorescence before sections were used for spatial transcriptomics to ensure that the sections being processed were positive for IAV.

These vector cells comprised MDCK cells which had been infected at an MOI of 0.5 PFU/cell for each virus in our cocktail (for a total MOI of 3 PFU/cell). Low titres of barcoded IAV stocks, on the order of 10^5 PFU/ml, meant that a relatively low total MOI was required when co-infecting cells. This ensured that the total volume of inoculum was contained in wells. The percentage of cells infected during an inoculation at a given MOI, m, follows a Poisson distribution:

$$P(k) = \frac{e^{-m}m^k}{k!} \tag{5.1}$$

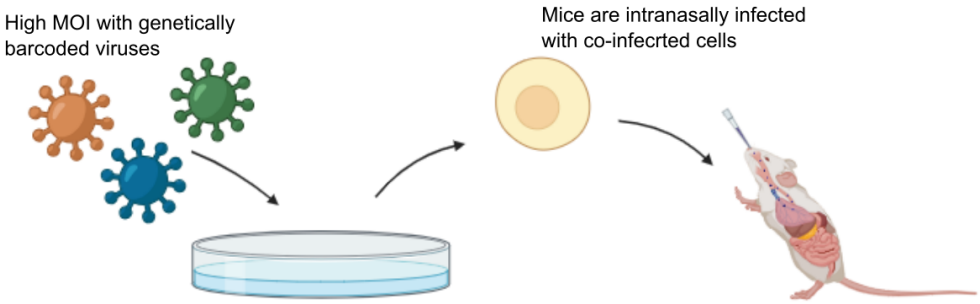

Figure 5.6: Infection methodology for mouse infections using multiply-infected vector cells.

Where $P(k)$ is the fraction of cells infected by k virus particles for a given MOI. It then follows that a total MOI of 3 PFU/cell results in $P(3) = 0.224 = 22.4\%$ and $P(4) = 0.168 = 16.8\%$. Thus, though not all cells will be infected with all viruses, at this MOI 22% of cells carry three viruses and 17% of cells carry four viruses. Additionally, $P(1) = 0.149$ meaning 15% of cells are not co-infected, thus in a section comprising multiple lesions, the majority will be co-infected. This demonstrates that a sufficient proportion of cells are co-infected to seed multiple viral populations in close proximity.

Following infection, vector cells were incubated for five hours before being resuspended for mouse inoculations, the incubation length was chosen to optimise for the release of viral progeny from infected cells immediately following inoculation (Baccam et al., 2006). Mice were intranasally instilled with 5000 vector cells. Mice were culled and lungs harvested and flash frozen at 3 and 6 dpi by collaborators at the Cancer research UK - Scotland Institute (CRUK). Lungs were cryosectioned (figure 5.7) and imaged via confocal fluorescence microscopy (figure 5.8) by the CRUK Histology facility.

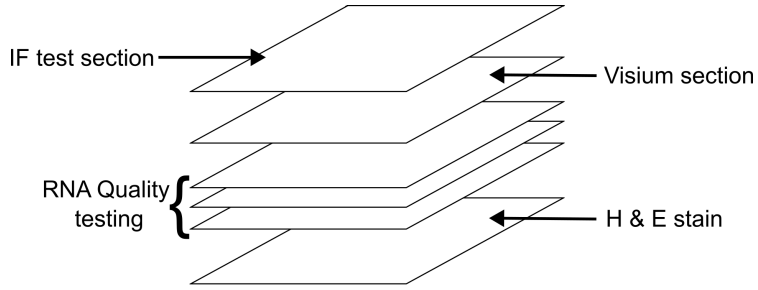

Figure 5.7: Sectioning scheme for mouse lung sections mounted for spatial transcriptomics. Sections taken for RNA quality testing were cut 40 μm thick, all other sections were cut 10 μm thick.

Based on the multiply infected cell seeding approach described above, fluorescence provides strong evidence for co-infection. Autofluorescence is strong in the green channel in lung tissue, as described earlier. In figure 5.8, some autofluorescence has been included for contextual understanding (i.e. how infection localises to structures such as airways). Signal was interpreted as IAV infection based on fluorescence above surrounding background autofluorescence. Ideally, images would have been captured and background removed based on uninfected controls prior to determining which sections were infected. In practice this was not possible as sections needed to be visualised in parallel with sections from the tissue block being cut and mounted for Visium analysis. The tissue block is serially sectioned and therefore once a section was cut and visualised, either the next section had to be cut and mounted on the Visium slide, or if there was no clear infection, a thicker section had to be removed from the tissue in order to search for infection at another depth. Given that sections cannot be restored back onto the tissue after cutting, it was not feasible to visualise sections and remove background before deciding whether the next section was appropriate for Visium analysis. For tissues where sufficient fluorescent lesions were observed in cryosections, a series of subsequent sections were cut (figure 5.7) and relevant sections were mounted for spatial transcriptomic analysis. Visium gene expression slides were stored for two weeks at -80°C before conducting the Visium assay.

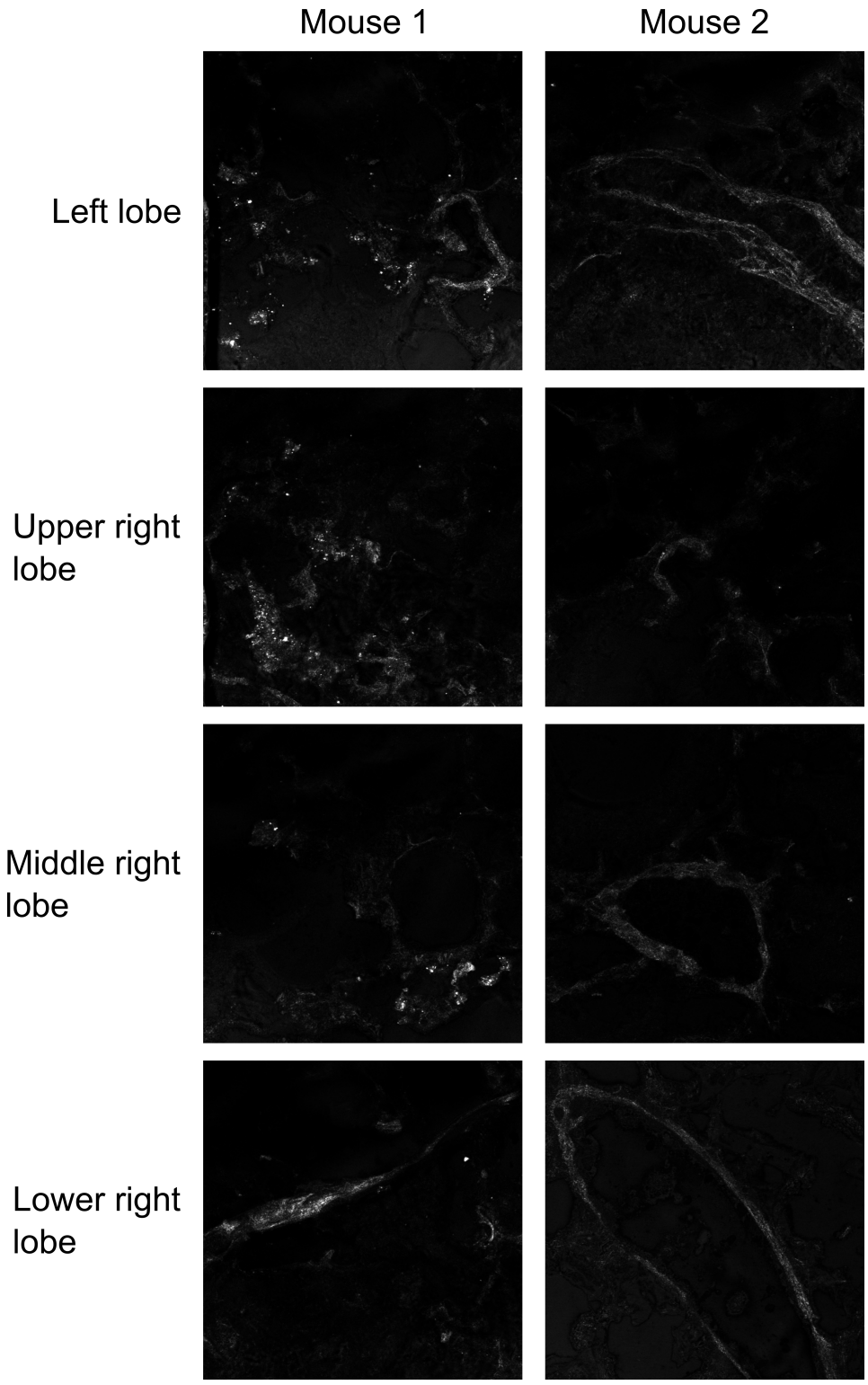

Figure 5.8: Fluorescence images of sections of lungs from mice co-infected using the vector cell protocol described above. Fluoresence (green) indicates BrightFlu-ZsGreen infection. Shown in gray scale for clarity. Imaged via Zeiss LSM 880, 10× objective, 488 nm illumination.

The Visium assay was performed as per the protocol described by 10× Genomics (10xGenomics, 2025). The protocol is described briefly here. Tissue sections were immunostained for PR8 NP and imaged via fluorescent slides scanner (Leica). The slide scanner image is used to align spatial transcriptomics information with tissue sections and enable comparison of RNA and protein expression. In this case, NP staining was used to visualise barcoded virus lesions, in addition to the endogenously fluorescent BrightFlu lesions. Following immunofluorescence imaging, cDNA and second strand synthesis is performed on the slide before aspirating DNA for sequencing. Aliquoted DNA is amplified via qPCR and stored at -20°C prior to Illumina and ONT long read sequencing.

qPCR results for DNA from all tissue sections returned high quantification cycle (C_q) numbers with thresholds set based on 10× Genomics guidelines (table 5.4) (10xGenomics, 2025). C_q number defines the number of amplification cycles required for a sample to reach a certain fluorescence threshold, since fluorescence is proportional to DNA concentration, the C_q value provides a proxy for the starting concentration of DNA in each sample (Ginzinger, 2002).

Table 5.4: C_q values for mouse lung sections processed via the Visium assay.

Section	**C_q**
1	17
2	17
3	18
4	19

10× Genomics state that a C_q value of <15 indicates that synthesised DNA is suitable for sequencing, with $15 < C_q < 20$ indicating poor RNA capture or degradation of RNA during the assay. Additonally, RNA intergrity number (RIN) scoring was performed via Tape Station. RIN scores quantify RNA quality by quantifying RNA fragment length via electropherogram, with samples comprising high quantities of short RNA fragments (indicating degradation) being given low RIN scores (Schroeder et al., 2006). 10× Genomics suggest that RIN scores of >7 are suit-

able for Visium experiments. Among the four samples analysed here, RIN scores averaged 2.5, providing further evidence of RNA degradation either prior to, or during, the Visium assay.

Due to the evidence of RNA degradation and high cost of sequencing, further analysis of *in vivo* samples was abandoned and no sequencing data was gathered for any of the *in vivo* samples. Following the RNA quality control issues encountered throughout the *in vivo* spatial transcriptomics experiments, it was decided that follow up spatial transcriptomics work would be performed *in vitro*. I hypothesised that RNA quality control would be simpler *in vitro* due to the relative lack of RNases present in cell cultures when compared with *in vivo* tissue, along with the logistical benefits of *in vitro* work (samples can be fixed, snap frozen etc. immediately rather than requiring numerous intermediate steps after tissue harvesting).

5.2.3 Developing an assay for in vitro spatial transcriptomics

The Visium gene expression assay is designed for RNA capture from tissue sections, with no spatial transcriptomics assays currently being supported for *in vitro* work. In addition to the complications of working with animal tissue described above, visualising viral dynamics in the airway comes with topological challenges. The majority of respiratory infection occurs in the airway epithelium, thus studies of IAV interaction and reassortment would benefit from mapping RNA expression across the epithelial surface (Denney and Ho, 2018; Hiller et al., 2022). When sectioning lungs, airways are almost exclusively cross-sectioned, limiting RNA capture to a 2D ring of epithelial cells. Even in the rare case that sectioning aligns perfectly with airway orientation, due to the thickness of tissue sections only a narrow section of epithelium is captured, rather then the entire circumfrence of the airway surface.

To study the interactions across a more significant portion of the epithelium, the airway would have to be "unwrapped" to create a flat, 2D surface which could be studied via existing spatial transcriptomics methods. I hypothesised that a transwell membrane could enable *in vitro* spatial transcriptomics studies of IAV interactions by providing a 2D surface emulating the airway epithelium. Cell cultures grown on

transwell membranes could then be permeablised and RNA captured as for tissue sections.

Before conducting spatial transcriptomics experiments, it was important to demonstrate that high quality RNA could be captured from cells cultured on transwell membranes. MDCK cells were grown on polycarbonate transwell membranes to confluence under cell culture conditions described in section 2.4.5. Membranes were then excised from transwells and incubated at room temperature for 10 minutes in RLT lysis buffer (Qiagen). RNA was then extracted via RNeasy kit (Qiagen). The purpose of the extended RLT incubation prior to RNA extraction was to allow buffer to permeate the transwell membrane and disrupt the monolayer. Typically, disruption would be performed prior to RNA extraction either by trypsinisation and resuspension of cells *in vitro*, or tissue shredding for *in vivo* samples. Given transwells share many properties with *in vivo* samples but could not be shredded since preserving spatial context is crucial for spatial transcriptomics, this extended incubation was employed in lieu of shredding. RNA quality control was performed via Tape Station (table 5.5). As described above, 10× Genomics recommend that RIN scores of >7 are sufficient for spatial transcriptomics so these data demosntrate that both the quantity and quality of RNA captured from transwell membranes is sufficient for the following Visium experiments.

Table 5.5: RIN scores for transwell membranes used in RNA quality control experiments.

Membrane	**RNA (ng/ul)**	**RIN score**
1	1840	9.9
2	1620	9.9

As for *in vivo* experiments, it was necessary to confirm that capture spots would provide sufficient coverage of lesions and co-infected regions *in vitro* (figure 5.9). The spot overlay approach described above was applied to images captured by Sims *et al.* of ColorFlu propagated under plaque assay conditions (figure 5.9) (Sims et al., 2022).

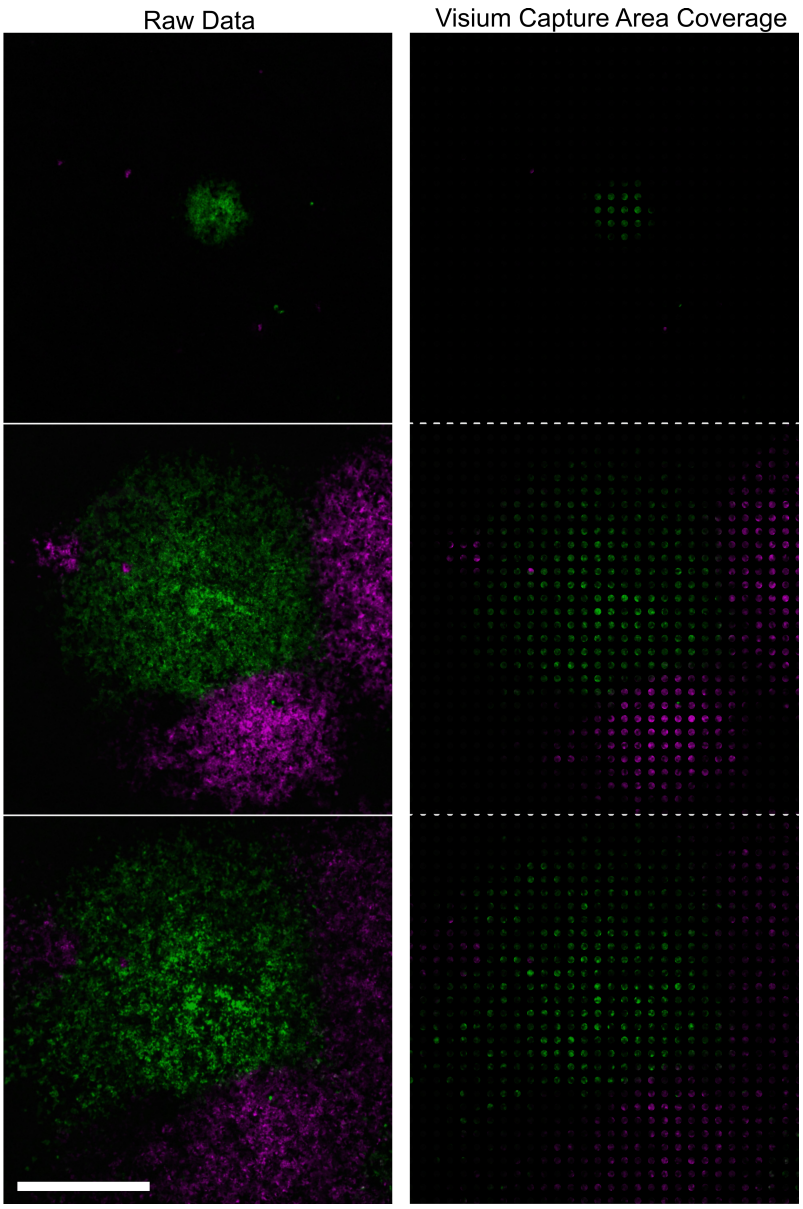

Figure 5.9: Example of data captured by Visium spatial gene expression capture areas in an *in vitro* plaque assay similar to the comet assay method employed here. Capture spots are 55 μm in diameter with a 110 μm centre to centre spacing. Colour has been included only within the regions covered by capture spots. Scale bar = 2 mm. Original confocal image captured by Anna Sims *et al.* (Sims et al., 2022).

The cell density within capture spots was higher *in vitro* when compared with *in vivo* due to the higher density of cells in culture. Additionally, *in vivo* lesions are smaller and less numerous than plaques observed *in vitro*. It is hypothesised that due to a lack of long range transport of virus particles grown under plaque

assay conditions *in vitro*, lesions would develop only in regions seeded during initial infection. Conversely, *in vivo*, long range particle transport would enable secondary seeding events leading to more numerous lesions, which could in turn restrict growth of surrounding lesions via superinfection exclusion. As a result, density of cells in capture spots overlayed on plaques *in vitro* is greater than that observed *in vivo* (figure 5.9).

Having demonstrated that capture spot coverage was sufficient for co-infection studies, means of propagating IAVs on transwell membranes were investigated. Monolayers of MDCKs cultured on transwell membranes were infected using the vector cell method described above and incubated under plaque assay conditions for 48 hours (figure 5.10).

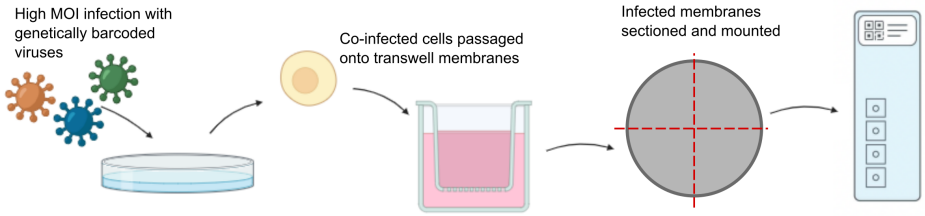

Figure 5.10: Methodology for *in vitro* spatial transcriptomics on transwells.

It was found that a traditional plaque assay approach - overlaying the monolayer with agarose - led to monolayers drying out from the underside of the membrane. To prevent this, two alternative conditions were investigated: hydrating the underside of the membrane with VGM or a mixture of VGM and agarose during incubation. These conditions were explored on two common membrane materials, polycarbonate and polyester (figure 5.11).

Polycarbonate membranes treated with VGM below the membrane provided consistent results, both in plaque size and abundance. However, in all cases the removal of agarose from the monolayer side of the membrane removed the cells in the centres of plaques, inhibiting the capture of RNA from, and transcriptomic analysis of, these cells. In order to preserve infected areas of the culture when harvesting, "comet assay" conditions were investigated. Unlike plaque assays, comet assays allow for the movement of virus particles across the culture during

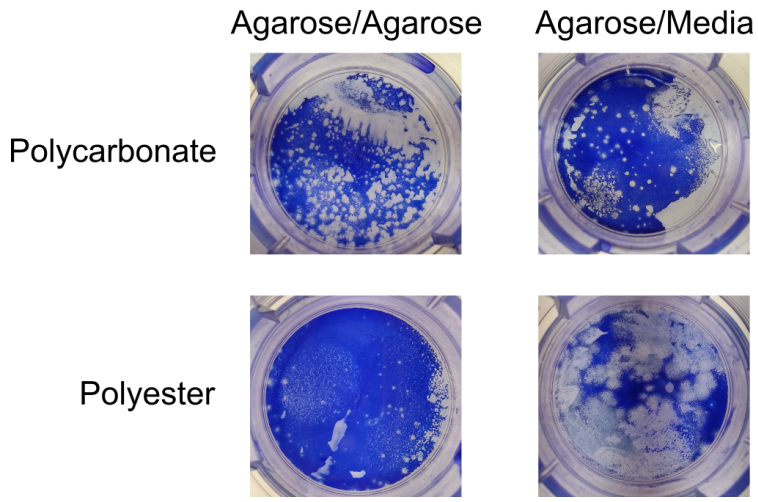

Figure 5.11: Plaque assays performed via the protocol described in section 2.4.1, stained with Coomasie brilliant blue. Agarose/Agarose refers to agarose both above and below the membrane. Agarose/Media refers to agarose above and media below the membrane.

incubation by using a liquid overlay. Provided the culture dish remains undisturbed for the duration of incubation, convection currents cause viruses to propagate towards the edge of the well, creating comets (figure 5.12). The lack of a semi-solid overlay such as agarose allows far more dead cells to remain adhered to the transwell membrane when harvesting comet assays. Comet assays were performed on MDCKs cultured on polycarbonate transwell membranes infected via the vector cell methodology for 48 hours, underlaying the membrane with VGM as above (figure 5.12).

While cellular density in comets is higher than that observed in plaques, staining still removed a significant portion of infected cells. I hypothesised that harvesting at an earlier timepoint would give sufficient time for viral populations to propagate and interact while preventing extensive cell death, and by extension, de-adherance from the membrane, preserving these cells for spatial transcriptomics analysis.

Having demonstrated that comet assays can be performed on transwell membranes without the loss of cells during harvesting, the permeability of transwell membranes to reagents was tested. The ability to immunostain cells through transwell membranes provides good evidence that membranes will be permeable to

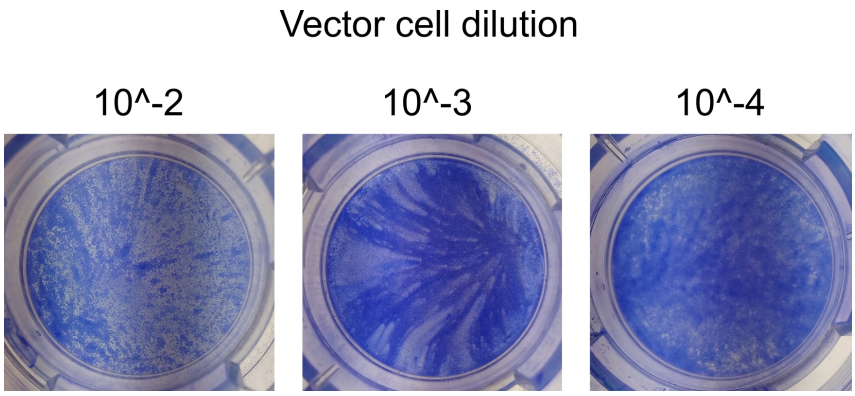

Figure 5.12: Example of a comet assays on polycarbonate transwell membrane 48 hours post infection. Membrane were fixed and stained with Coomasie brilliant blue solution mixed with acetic acid.

reagents used for RNA capture during the Visium assay, since antibodies are large relative to reagents involved in RNA harvesting. MDCK cultures grown on polycarbonate transwell membranes were infected with BrightFlu-ZsGreen as above were harvested 24 hours post infection and stained for IAV NP. Membranes were excised from transwells and mounted cell-side down on glass microscope slides. Cells were permeabilised and then stained for IAV PR8 NP through transwell membranes (figure 5.13). While NP staining was not well correlated with BrightFlu signal, the fact that NP stain is present (and loosely localised to cells) demonstrates that the antibodies used for staining successfully permeated through the membrane. The localisation to cells also demonstrates that this signal is not simply random secondary antibody stuck to the membrane, further demonstrating membrane permeability. Given that demonstrating the permeability of the membrane to reagents in preparation for Visium processing, this result was deemed sufficient to continue to Visium analysis. It is hypothesised that the poor correlation of staining and BrighFlu signal is due to poor permeabilisation. Permeabilisation conditions were not adjusted from a standard cells staining assay to account for penetration of permeabilisation reagents through the membrane, likely impacting permeabilisation efficacy.

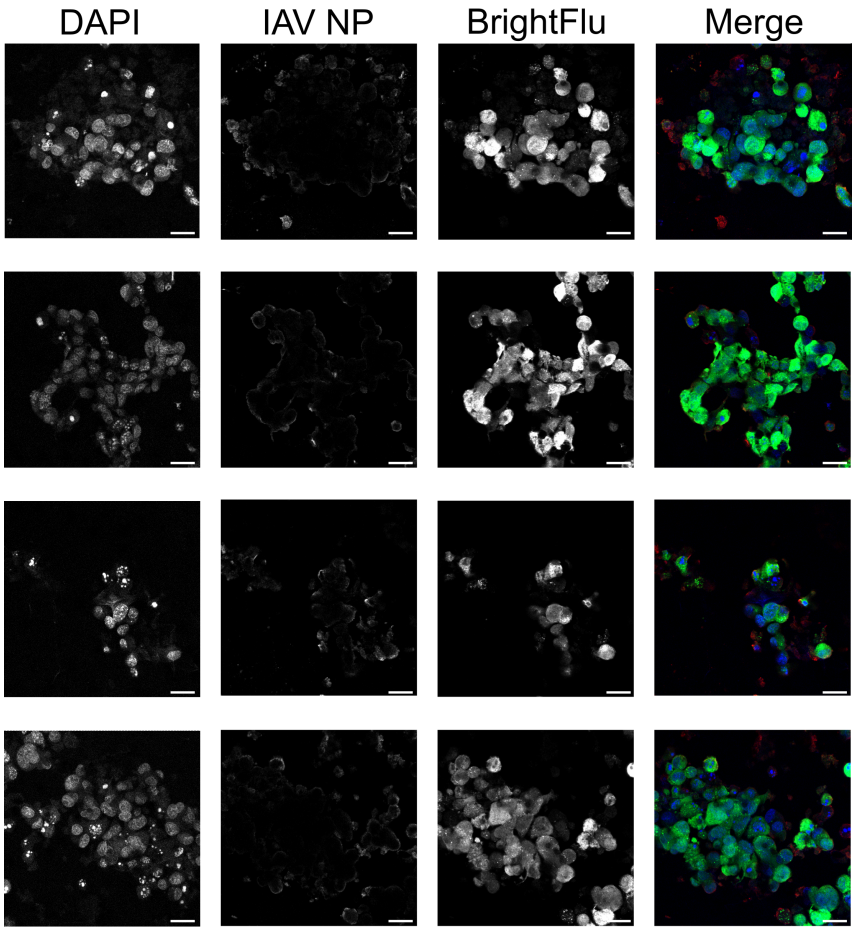

Figure 5.13: MDCK cultures on transwell membranes infected with BrighFlu-ZsGreen (Green) and stained for PR8 NP (Red). Channels are shown in gray scale for clarity. Cell nuclei are stained with DAPI (Blue). All scale bars = 20 μm.

The permeabilisation time used here was optimised for cells cultured on coverglass and did not account for reagents permeating the transwell membrane, leading to a lack of penetration of stain into cells. Given that the Visium assay contains a step to determine the permeabilisation time to optimise RNA yield the results observed here were deemed satisfactory. After validating virus growth conditions and permeability of transwell membranes, the Visium gene expression assay was carried out *in vitro*.

Permeabilisation time varies between tissue types and thus a specific step is included in the Visium protocol as described above. MDCK cells cultured on polycarbonate transwell membranes were infected with PR8 at an MOI of 0.4

PFU/cell and incubated for 24 hours at 37°C. Following incubation, transwell membranes were fixed in methanol at -20°C for 30 minutes, dissected into quarters, and mounted on a Visium tissue optimisation slide. Tissue optimisation was performed as described for *in vivo* samples. RNA extracted from MDCK cells grown on transwells during the RNA extraction experiments described above was used as a positive control. A permeabilisation time of 18 minutes was selected based on results of permeabilisation time optimisation experiments (figure 5.14). The fluorescence from all sections is significantly stronger than that observed during the *in vivo* study, providing further evidence to support the hypothesis that there had been significant degradation of RNA in lung samples (figure 5.5).

Having determined optimal permeabilisation conditions, MDCK vector cells were infected with five barcode variants and BrightFlu-ZsGreen for a total MOI of 3 PFU/cell and incubated for five hours before being resuspended. MDCK cells cultured on polycarbonate transwell membranes were infected by inoculation with vector cells, membranes were inoculated with a range of concentrations of vector cells. After 24 hours, membranes were fixed in methanol at -20°C for 30 minutes and imaged via widefield fluorescence microscope (EVOS) to identify membranes with an appropriate density of comets for spatial transcriptomic analysis (figure 5.15). Appropriate density was defined as having a sufficient number of comets in close proximity to ensure interactions between viral populations while maintaining the ability to distinguish between individual comets. A single membrane was chosen for spatial transcriptomic analysis, the chosen membrane was seeded with 1×10^3 vector cells.

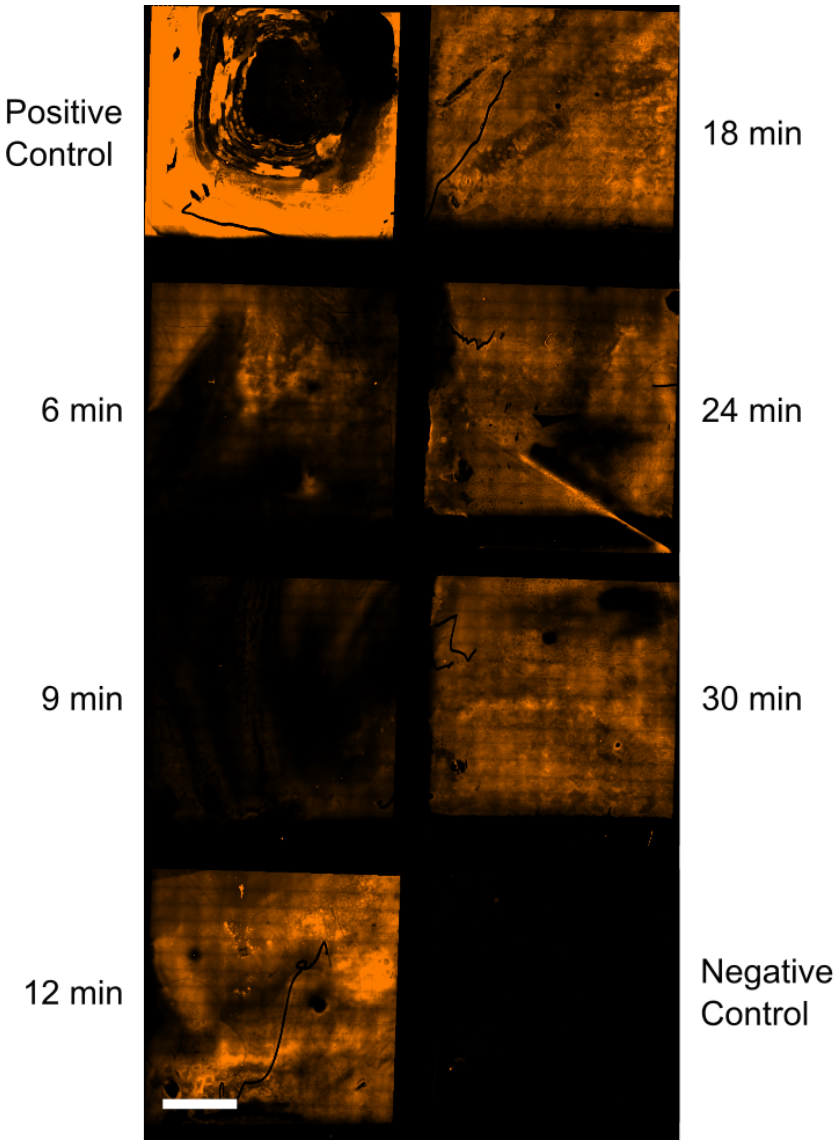

Figure 5.14: Tissue optimisation slide comprising six transwell membrane sections infected with IAV BrightFlu-Zsgreen permeabilised for between 6 and 30 minutes. TRITC (Orange) signal is proportional to captured RNA quantity. Scale bar = 2000 μm.

The chosen membrane was dissected into quarters, to fit capture areas on the Visium slide, and mounted. The Visium spatial gene expression assay was then carried out using the protocol recommended by 10$\times$ Genomics which is briefly described here (10xGenomics, 2025). Membrane sections were permeablised, resulting in RNA binding to capture spots on the slide.

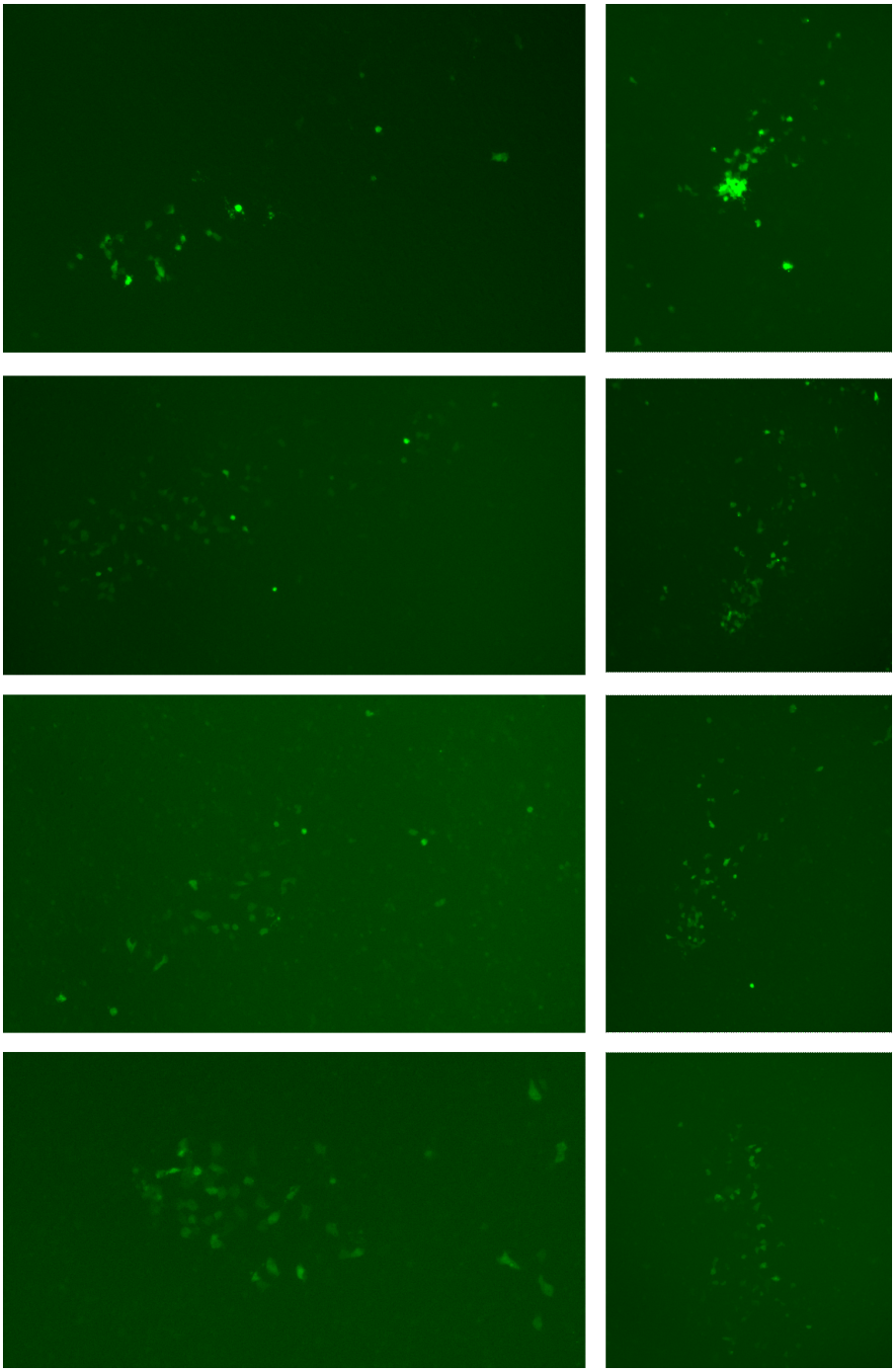

Figure 5.15: Fluorescence images of comets on transwell membrane chosen for spatial transcriptomics analysis. Imaged via EVOS, 10× objective, 488 nm illumination.

Reverse transcription and cDNA synthesis was performed on the slide and the quantity of RNA captured from each section was determined by qPCR (QuantStudio 3, ThermoFisher) (figure 5.16 and table 5.6). 10× Genomics state that for a cycle threshold set at approximately 25% of peak fluorescence, a quantification cycle (C_q) number <15 indicates suitable RNA capture for spatial transcriptomics analysis (10xGenomics, 2025).

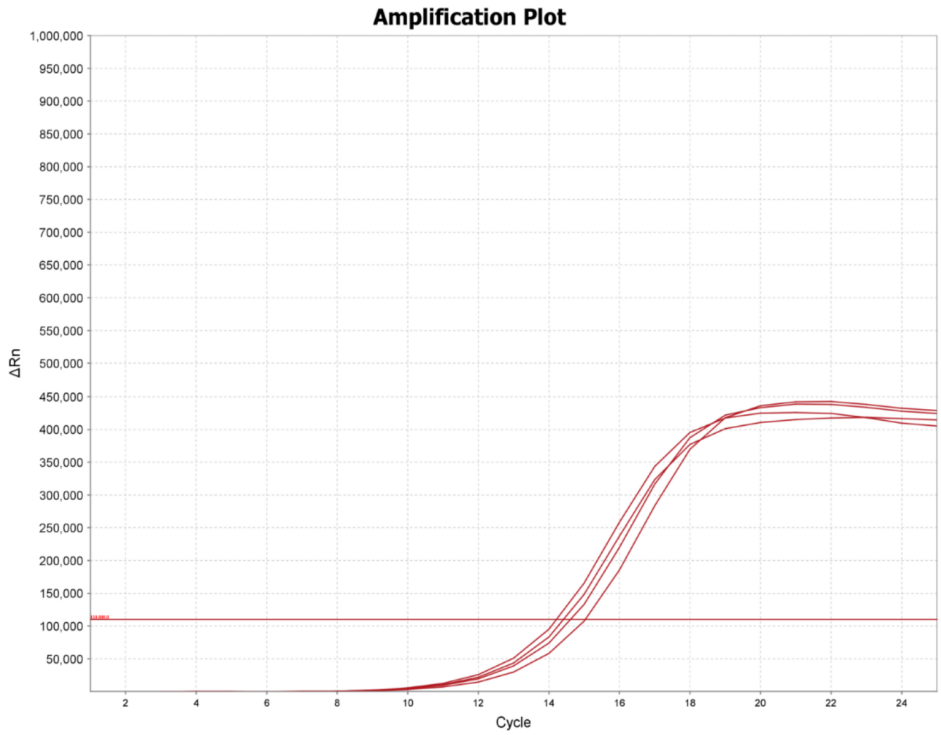

Figure 5.16: qPCR results for transwell membranes processed via the Visium spatial gene expression assay. Performed via QuantStudio 3 (ThermoFisher).

Table 5.6: C_q values for membrane sections processed via the Visium assay.

Membrane section	**Cq**
1	13.061
2	13.501
3	13.889
4	13.298

Note, the staining and imaging step described in the Visium protocol was not performed. Typically imaging is performed to provide a guide for aligning the resulting spatial transcriptomics data. Due to the homogenous structure of a transwell membrane, no features would appear in imaging that would assist in alignment. Additionally, imaging requires the removal of the gasket affixed to the slide during the Visium protocol. Cryosectioned or sectioned formalin fixed paraffin embedded tissue sections are adhered to the slide and are robust to gasket removal. In this case, wet transwell membrane sections were lightly adhered to the slide through surface tension and pinned in place by the surrounding gasket, this ensured that sections were stationary throughout the protocol but removal of the gasket would have likely dislodged samples, impacting results. It was therefore decided that the imaging step could be removed.

Following qPCR amplification, library preparation and sequencing via Illumina and ONT was carried out by the genomics department at the Centre for Virus Research (CVR). Library preparation for Illumina sequencing was carried out as advised by 10× Genomics.

5.2.4 Sequencing results for spatial transcriptomics on IAV co-infections

In order to validate that the method designed here for conducting spatial transcriptomics *in vitro* could accurately distinguish barcoded IAV genes, a preliminary analysis of barcode sequences was conducted. The Visium spatial gene expression slide features four tissue capture areas (A-D). Due to timings in the sequencing of Visium data, only sequencing data for capture area A was available within the timeline of this project. Therefore, this preliminary analysis was performed on data from capture area A. In collaboration with the CVR Viral Bioinformatics Facility, ONT sequencing results were first searched for sequences matching IAV genes (figure 5.17). It was determined that IAV genes accounted for 10.92% of all reads. The proportion of reads associated with each segment varied significantly, with the most abundantly captured segment being M, accounting for 3.12% of all reads,

and the lowest being PA, accounting for 0.26% of all reads (figure 5.17). The cause of the discrepancy in segment abundance is unclear. Irrespective of differences in abundance, these data demonstrate that RNA captured via the method designed here is sufficient for the identification of viral transcripts.

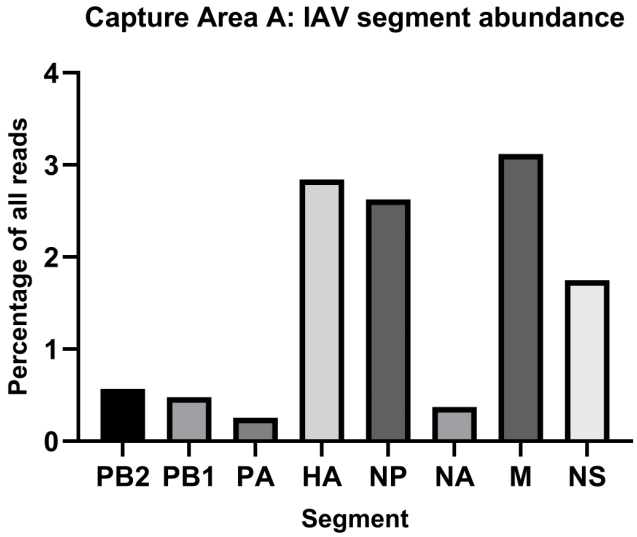

Figure 5.17: IAV segment abundance in long read sequencing data from Visium slide capture area A. Plotted using GraphPad PRISM.

Subsequently, ONT results were searched for sequences associated with the barcoded PB2, HA, and NP gene segments from the barcoded IAV library (table 2.5). For the PB2 and HA segments, all barcode sequences were identified as well as the wildtype sequence (figure 5.18 A/B). The wildtype sequence is present due to the inclusion of the unbarcoded BrightFlu-ZsGreen in the infection virus cocktail. For the NP segment, barcodes 1, 2, and 5 were identified, as well as the wildtype sequence (figure 5.18 C). A sequence similar to NP barcode 3, referred to as "Barcode 3 variant", was identified, however, this sequence included multiple non-specified bases making it impossible to definitively identify as barcode 3, even with the error correcting nature of the barcodes (figure 5.18 C). NP barcode 4 was not present in the ONT results.

Interestingly, NP barcode 3 and 4 were the only barcodes which could not be matched to Dr. Fu's reference sequences via Sanger sequencing of the original barcoded virus stocks (figure 5.3). It is therefore possible that the lack of these

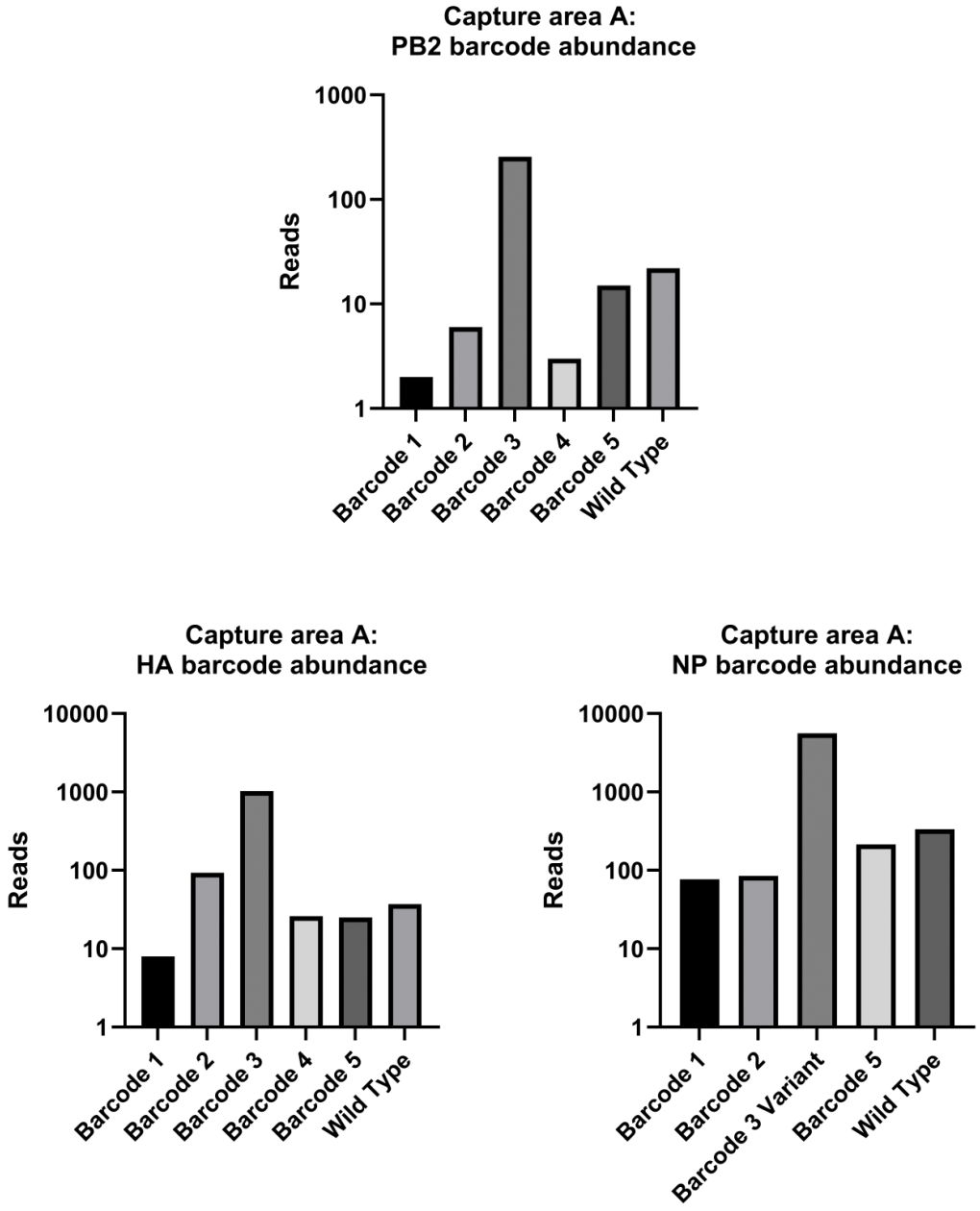

Figure 5.18: Barcode sequence abundance among reads for each of the barcoded IAV segments. Wild Type variants of each segment are also reported, representing BrightFlu-ZsGreen. NP barcodes 3 and 4 were not identified. A sequence highly correlated with NP barcode 3 was found in high abundance and is included as "Barcode 3 variant".

barcodes within the ONT sequencing data is due to mutations of the barcode sequence prior to infection of the transwell, rather than a lack of detection during the assay.

The prevalence of barcode 3 across sequencing data for all three genome segments provides further evidence that the assay designed here reliably captures accurate information on gene expression. Given each of the five barcoded viruses comprises three barcoded segments, an increase in prevalence of a virus should result in increased prevalence of each of the barcoded segments of this virus. It follows that if the HA barcode 3 sequence is highly abundant, the PB2 and NP barcodes should be similarly abundant, relative to the other barcodes. This provides evidence that the prevalance of barcode 3 observed in these data accurately represent viral burden across the sample.

The prevalence of barcode 3 relative to other barcodes aligns with the dominant strain emergence observed by Ganti *et al.* (Ganti et al., 2022). In ferrets co-infected with a library of barcoded IAVs, Ganti observes the stochastic emergence of a dominant strain from a mixed infection in both the nasal tract and lung as early as 1 dpi. The data presented here demonstrate a similar effect *in vitro*, with barcode 3 dominating the viral population. This correlation with the literature provides further evidence that the *in vitro* spatial transcriptomics assay designed here can accurately capture gene expression across cell cultures.

These findings demonstrate that this *in vitro* spatial transcriptomics assay can effectively distinguish the barcoded IAV genes of interest to this study. More generally, this provides evidence that this assay can distinguish highly similar genes, performing similarly to the *in vivo* Visium assay in distinguishing genes varying in only a small number of bases (Joglekar et al., 2021).

Due to the ONT sequencing taking longer than expected, similar analysis of capture areas B-D and the investigation of IAV interactions and reassortment events was not possible during the timeline of this project. I had hoped to perform on this data were not feasible within the project timeline. Analysis of IAV interactions will be performed using the suite of tools generated by 10$\times$ Genomics after

the conclusion of this project. This analysis will focus on establishing the genetic composition of IAV lesions across the cell culture.

Particular focus will be directed to studying viral genes within cells at the interface between lesions. Superinfection exclusion dictates that co-infection, and by extension reassortment, is restricted to these regions. By studying the viral genes harboured within cells in these interstitial regions, I aim to identify cells expressing novel combinations of barcoded genes, representing cells infected with viruses arising from reassortment events. Due to the size of capture areas in comparison to cells, multiple cells are included in each capture spot. As described above, in cases where there are multiple barcodes represented for each segment in a single capture area, this makes it impossible to distinguish co-infection from reassortment. It is possible that due to the width of these interstitial regions *in vitro*, capture areas covering these interstitial regions will often include cells from adjacent microdomains. In such cases, it will not be possible to identify reassortant viruses, however, given that we know reassortant progeny are common in late stage infections, these reasortant viruses likely seed microdomains of their own. In these microdomains, capture areas would contain only cells from within the microdomain, thereby enabling the identification of reassortant viruses. Identifying such cell populations would provide the first direct evidence that reassortant viruses emerge from these interstitial co-infected cell populations. Additionally, the comets in comet assays develop as convection currents within the well cause viral populations to migrate towards the edges of the well. As a result, the narrower "tail" of the comets closer to the centre of the well represent a earlier timepoint in the infection than the wider "head" of the comet. The comet therefore provides a visualisation of the infection timecourse. By identifying where cells harbouring reassortant viral populations localise along the comet, these data can also provide insights into whether there is a bias in when reassortment events occur during infection.

5.3 Discussion

5.3.1 In vivo spatial transcriptomics

In vivo spatial transcriptomics experiments performed here attempted to visualise infection dynamics between IAVs during co-infection. By using a barcoded library of viruses I hypothesised that spatial transcriptomics would enable more precise discrimination of viral strains than equivalent immunofluorescence and FISH studies. Here, quality of captured RNA was not sufficient

There are two notable possible reasons for this low RNA quality. Firstly, when flash freezing tissues for spatial transcriptomics, 10× Genomics advise that time between excising and freezing tissues is minimised. This is due to the presence of endogenous RNases which begin degrading host RNA immediately after culling the host. In pilot studies prior to this *in vivo* Visium experiment, RNA quality was tested from tissues frozen one hour after harvesting (a delay incurred due to transporting the tissue from the CRUK to the CVR for freezing). These pilot studies revealed significant degradation in harvested RNA. It was concluded that the time between harvesting and freezing was the cause of this degradation and it was determined that freezing would be performed at the CRUK to minimise this delay. By conducting freezing at the CRUK this delay was shortened to under 15 minutes (due to having to transport tissue from the animal unit to the primary laboratory). It was expected that this delay was sufficiently short to preserve RNA quality, however, upon further discussion with researchers familiar with RNA extraction from tissues and the Visium protocol it is likely that such a delay would lead to significant RNA degradation. Secondly, due to limitations on equipment availability at the CVR, namely access to a fluorescent slide scanner, the slide was transported between the CVR and CRUK for imaging during the Visium assay. This resulted in the assay lasting substantially longer than intended and by extension prolonged periods during which tissue sections were at room temperature before cDNA synthesis was performed. Due to the instability of RNA at room temperature, it is hypothesised that these prolonged incubations at room temperature lead to RNA

degradation (Chheda et al., 2024; N. V. Gopee and Howard, 2007).

Taken together, these compounding effects resulted in the extensive RNA degradation observed here. These opportunities for RNA degradation can be simply avoided in future Visium gene expression experiments by conducting flash freezing in the animal unit immediately after excising tissues. Additionally, the CVR now has in-house fluorescent slide scanner facilities minimising the need for extensive room temperature incubations. RNA degradation can also be avoided by fixing and paraffin embedding tissues, avoiding the need for flash freezing. However, fixation results in RNA no longer being directly recoverable and therefore this is inappropriate for use with the Visium platform used here. 10x Genomics does make a platform for RNA capture from fixed and embedded tissue, however, this relies on probes targeting RNA species of interest, rather than capture of all poly-adenylated RNA. Due to the cost of creating probes for this platform, this wasn't viable for all the barcoded sequences explored here.

5.3.2 In vitro methods development

Following the issues described above in performing *in vivo* spatial transcriptomics, coupled with the cost of Visium experiments, it was decided that the final Visium spatial gene expression slide would be used to attempt to develop the assay for use *in vitro*. This novel use of the Visium assay was not validated by 10× Genomics nor in the literature and therefore was not guaranteed to yield any useful data. Despite this, following multiple failures to extract high quality RNA from flash frozen tissues it was decided that the development of an *in vitro* assay was a more valuable use of the remaining slide and reagents than repeating *in vivo* experiments.

Here, I have developed and validated an *in vitro* application of the spatial transcriptomics assay for the first time. The assay has been rigorously tested for MDCK cells cultured on polycarbonate transwell membranes. This *in vitro* assay yielded high quality RNA (with an average RIN score of 9.9 for RNA extracted from cells cultured on membranes) at concentrations sufficient for analysis via the Visium spatial transcriptomics sequencing protocol (10xGenomics, 2025).

In this work, the primary application of this *in vitro* assay was the study of influenza virus co-infection. Despite having access to human airway epithelial cells (A549), canine kidney cells (MDCK) were used during the development and validation of the assay. A549 cells are well characterised in the literature and are of course more representative of the landscape of typical IAV infections than MDCKs (Giard et al., 1973). However, the primary goal of this study was to develop *in vitro* spatial transcriptomics methods, irrespective of application. MDCK monolayers are well-established as being structurally robust, typically remaining intact under harsher conditions than A549 monolayers, for example, during challenge with a pathogen. Given the chemical and physical agitation of the protocol established here (excising and disection of the transwell membrane, chemical fixation and permeabilisation), it was decided that the integrity of MDCK monolayers would improve the likelihood of capturing high quality RNA in the quantities required for Visium analysis. Finally, it is worth noting that our primary objective here focussed on the expression of viral genes rather than host genes. Prior work in our lab group suggests that IAV genes follow similar patters of interactions regardless of the cells they are cultured in (Sims et al., 2022).

Based on the pilot study presented here, this method would appear to be appropriate for any cell type which can be cultured on a transwell membrane and readily forms a monolayer, however further testing using the RNA quality control steps outlined here is required to validate each cell type. This assay could be applied to more complex differentiated cell culture systems such as those used in air-liquid interface (ALI) studies. ALIs emulate the airway epithelium, comprising co-cultures of ciliated, goblet, and basal cell types resident in the lung. ALIs are commonly cultured on permeable transwell membranes and have been used to study a variety of respiratory infections (Caves et al., 2018; D. Jiang et al., 2018). Such systems are common in immunofluorescence and FISH studies (Derichs et al., 2011; Prescott et al., 2023; Rani et al., 2023; Ziegler et al., 2021). The application of the methods developed here would likely be viable in such systems, greatly expanding on the depth and specificity of current ALI studies (the flattening of cilia would have

to be considered, but these considerations also have to be made in existing imaging based methods). While the focus of this work is the study of airway infection, the *in vitro* spatial transcriptomics methods developed here greatly expand the application of the Visium platform. These methods will enable spatial transcriptomics to be performed in systems for which *in vivo* experiments are not viable, such as studies of high-containment pathogens or those without appropriate laboratory host species, decreasing the animal burden of infection studies.

5.3.3 In vitro spatial analysis of IAV co-infection

Preliminary sequencing results demonstrated that high quality RNA was collected from *in vitro* samples processed using our adapted Visium protocol and that barcoded IAV genes were distinguishable in this data (figures 5.17 and 5.18). Further analysis of these data unfortunately fell outside of the timeframe of this project due to ONT sequencing and data processing taking significantly longer than anticipated. While 10× Genomics provide fairly user friendly tools to conduct downstream analysis and produce graphical outputs for spatial transcriptomics data, this analysis was not feasible within the project timeline. Given the quality of RNA recovered from tissue sections, and the presence of sequences associated with barcoded IAV variants within these data, it is likely that further analysis will provide insights into the spatial interactions between IAVs. These insights may reveal the presence of reassortant strains at the interface between IAV lesions, improving the understanding of novel strain emergence during co-infection.

Irrespective of whether the specific data generated here provide insights into IAV evolution upon further examination, the protocol designed here for *in vitro* spatial transcriptomics has been demonstrated to successfully harvest RNA from *in vitro* samples. This is the first example of the Visium assay being implemented *in vitro*.

5.4 Conclusion

Here, Visium spatial transcriptomics experiments were carried out in an attempt to visualise viral interactions during co-infection at a plexity and genetic resolution not afforded by imaging methods. *In vivo* experiments were unsuccessful in capturing RNA of a sufficient quality for sequencing, however, the issues in flash freezing and methodology optimisation resulting in RNA degradation can be easily rectified in future work, improving RNA capture in future Visium experiments at the CVR. I have also successfully developed an *in vitro* implementation of the Visium spatial transcriptomics assay for cells cultured on transwell membranes.

Building on this work beyond the scope of this thesis, downstream analysis of spatial transcriptomcis data will be performed, analysing the genetic composition of IAV lesions. This analysis will aim to identify whether lesions comprising novel combinations of genes from multiple barcoded strains emerge at the interface between co-infecting strains. This would expand on the findings of Ganti *et al.*, Amato *et al.*, and Fu by preserving spatial context underpinning these interactions, enabling reassortant strains to not only be identified, but also to be contextualised in the landscape of the co-infected tissue. The single cell sequencing methods employed by Ganti, Amato, and Fu rely on the homogenisation of lung tissue, removing spatial context. While spatial transcriptomics lacks single cell resolution, by preserving the spatial landscape of the tissue these technologies provide insights into spatial interactions between viruses not captured by the work of Ganti, Amato, and Fu. Despite the lack of time for downstream analysis, the experiments performed here have successfully implemented the Visium spatial gene expression assay *in vitro* for the first time.

This *in vitro* spatial transcriptomics assay design will significantly expand the application of the Visium platform, enabling researchers whose subject can be studied in cell culture but for whom no animal host is accessible does not have an existing laboratory host to conduct complex spatial genetic analysis which existing imaging methods are incapable of performing.

Chapter 6

General Discussion

6.1 Summary of key findings

In section 1.4.4, I outlined the three primary goals of this project. Here I will contextualise the findings of this project with respect to these goals:

6.1.1 Aim 1: Developing mesoscale imaging methods for imaging infection

In chapter 3, I detail the development and implementation of an adapted ethyl cinnamate (ECi) clearing protocol capable of clearing a range of tissues to a standard suitable for light sheet imaging. By using Ce3D as a "primer" in the clearing protocol developed here, this method improves on the transparency observed in tissues cleared using ECi alone (Masselink et al., 2019; Subiran Adrados et al., 2021). Additionally, the use of tertiary-butanol as a dehydrating agent rather than ethanol better preserves fluorescent signals, as described in the literature (Alves et al., 2016; Schwarz et al., 2015). Here I demonstrate that this clearing protocol is capable of optically clearing skin, bone, nerve, and lung tissue. I additionally clear melanised samples such as whole arthropods by incorporating a H_2O_2 bleaching step into the protocol. The protocol designed here provides comparable levels of clearing to popular clearing methods such as CUBIC, SeeDB, and CLARITY (Chung et al., 2013a; Ke et al., 2013; Ren et al., 2021; Susaki et al., 2014). This

clearing protocol is derived from the ECi protocol described in the literature, this protocol involves non-toxic compounds and can therefore be performed outwith a fumigated environment and safely used with open-top microscope systems without environmental control, unlike popular methods such as CUBIC. This clearing method is fast, clearing samples such as bone, lung and skin in three days or less. This is only an increase of approxiamtely 12-24 hours on ECi approaches described in the literature due to the inclusion of the Ce3D priming step. This improves on the clearing times associated with other popular methods which often exceed one week (L. Liu et al., 2021; Susaki et al., 2014). This reduction in clearing time directly correlates with improved fluorescence signal capture during imaging, improving the capture of low abundance fluorescent targets, as evidenced by the ability to image single *Trypanosoma brucei* parasites in the skin of infected mice. In all cases, cleared tissues were imaged via light sheet microscopy. Optical clearing was sufficient to identify structures at multiple length scales from tissue structures in bone and lungs to mesoscale lesions in influena A virus (IAV) infected lungs.

6.1.2 Aim 2: Developing microscale imaging methods for imaging infections

In chapter 4 I develop FISHtoFigure, a computational analysis tool for the quantification of fluorescence *in situ* hybridisation (FISH) data (Bentley-Abbot et al., 2024). This tool is open source and packaged such that it can be used by all researchers irrespective of coding or computational analysis experience. I validate this tool in the analysis of a cytokine-mediated crosstalk between cell types in the brains of *T. brucei*-infected mice. The tool has been published in *Scientific Reports* and the *T. brucei* research this tool supported is published in Nature Communications (Bentley-Abbot et al., 2024; Quintana et al., 2022). I aim to continue to develop FISH toFigure beyond this project. One such improvement which is already underway is the integration of FISHtoFigure into QuPath. QuPath features numerous plug-ins, many of which were developed as external tools before being integrated, integrating FIShtoFigure in this way would significantly decrease the

barrier to entry for use of the tool. Additionally, improvements to the cell quantification by membrane marker function in QuPath would improve the accuracy of downstream analysis in FIShtoFigure. Having discussed this with the QuPath team, this is a goal for an upcoming QuPath release. Finally, statistical analysis is currently performed downstream of FIShtoFigure, for example in GraphPad PRISM. I hope to integrate these analyses directly into FIShtoFigure in future versions. FISH experiments, using the RNAScope platform, were performed to investigate interactions between co-infecting IAVs (F. Wang et al., 2012). These experiments were performed both *in vivo* and *in vitro*. While probes against surface glycoprotein encoding segments of two IAV subtypes were designed and validated *in vitro*, *in vivo* experiments were unsuccessful in identifying IAV lesions in tissues via FISH. Following the issues faced using FISH, alternative methods of visualising infection on the microscale were attempted.

In chapter 5 I demonstrate the use of spatial transcriptomics in analysing IAV co-infections. This was first, unsuccessfully, attempted in fresh frozen lung tissue from mice infected with a barcoded library of IAVs. The failure to obtain sufficiently high quality RNA for genetic sequencing from *in vivo* samples was most likely the result of RNA degradation prior to freezing (Chheda et al., 2024; N. V. Gopee and Howard, 2007). The nature of the Cancer Research UK - Scotland institute complex necessitated the culling and freezing of tissues in separate buildings. Whilst attempts were made to minimise the time between culling and freezing, this time could only be reduced to approximately 15 minutes, during which time it is likely that much of the RNA in the sample was degraded.

Similar experiments were subsequently performed *in vitro*, using an adapted Visium spatial transcriptomics assay developed here. RNA quality from *in vitro* samples was sufficient for sequencing and provided results from which barcode sequences could be discerned. It is therefore reasonable to attribute the low quality RNA gathered from *in vivo* samples to RNA degradation. However, studies of RNA degradation in the skin of mice demonstrate that room temperature incubation of up to one hour has little effect on RNA integrity number (RIN) scores

(Chheda et al., 2024; N. V. Gopee and Howard, 2007). While skin and lung tissue composition differ, particularly in cellular density, RNases are present in both tissue types. It is possible that IAV infection alters the tissue environment resulting in increased presence of RNases. Irrespective of the extent to which RNases result in degradation of RNA prior to freezing, decreasing the interval between culling and freezing would improve RNA quality. In lieu of reducing this interval, the perfusion of the tissue with an RNase inhibitor followed by transport of tissues in RNase inhibitor between culling and freezing would likely reduce the degradation of RNA observed here.

In vitro experiments yielded sufficiently high quality RNA to justify genetic sequencing. Sequencing was performed via Illumina and Oxford Nanopore Technology, enabling the reading of whole IAV gene segments. Long read sequencing was required to identify barcode sequences accurately as the barcodes are distal from the spatial barcode sequence and thus are lost in library preparation for Illumina sequencing (Ribarska et al., 2022).

Sequencing was completed successfully, however, the project timeline only allowed for rudimentary analysis of these data to be performed and reported here. *In vitro* spatial transcriptomics data was analysed in collaboration with the centre for virus research Viral Bioinformatics Facility. This analysis focused on validating the efficacy of the *in vitro* assay, rather than investigating biological questions regarding IAV evolution and pandemic strain emergence. The reasons for focusing on methodological validation were two-fold; Validation of the *in vitro* assay via the identification of barcoded IAV genes was expected to require less time than visualisation of IAV interactions, therefore aligning better with the project timeline. And given the primary focus of this work is the development and validation of methods for the visualisation of infections, validating the method aligned more closely with the primary aims of this work than focusing on biological questions. This analysis demonstrated that barcoded IAV genes could be identified, and specific barcode sequences discriminated, in data gathered using the *in vitro* Visium assay developed here.

While analysis of IAV interactions and reassortant strain emergence were not reported here, these analyses will be performed following the conclusion of this project. I intend to conduct an analysis of the genetic composition of lesions to identify co-infected regions at the interface between strains. We know from the work of Sims *et al.* that co-infection is limited by superinfection exclusion and by examining the viral genetic composition of infected cells within these these interstitial regions, the data gathered here may enable the visualisation of reassortment events between co-infecting strains.(Sims et al., 2022 While the data presented by Ganti *et al.* and Amato *et al.* demonstrate that reassortment readily occurs in the respiratory tract during co-infection, these studies do not spatially contextualise these events (Amato et al., 2022; Ganti et al., 2022). By visualising these events, the data here may provide insight into the location, timepoint during infection, and kinetics of reassortant viral strain emergence. By better understanding the spread of these novel viruses and their interaction with surrounding viral lesions, we may be able to better predict the emergence of future novel strains with pandemic potential.

Despite the project timeline not allowing for biological analysis of the spatial transcriptomics data gathered here. The analysis presented demonstrates that the *in vitro* spatial transcriptomics assay developed here can robustly harvest RNA from cell cultures grown on transwell membranes while preserving the spatial context of the tissue. This implementation of the spatial transcriptomics assay is novel, with the Visium assay being developed, validated, and marketed solely for use *in vivo*. The work performed here significantly expands the scope of the Visium assay and spatial transcriptomics methods more generally, providing a means for researchers who cannot work *in vivo* due to biological or ethical limitations to conduct spatial transcriptomics experiments.

6.1.3 Aim 3: Coupling multi-length scale imaging methods to visualise IAV co-infection

Finally, this project aimed to couple these multi-length scale imaging approaches to better understand the pathology and influenza virus co-infection and the interactions between co-infecting viruses. Through light sheet imaging of whole lung lobes, optically cleared using the protocol developed in chapter 3, I have visualised influenza virus co-infection across the whole lung for the first time. This work demonstrated that, unlike the effects seen in previous microscale studies, infectious populations remain mixed on the mesoscale. These mixed populations appear predominantly around bifurcations inn the airway. I hypothesise that the localisation of these lesions to bifurcations is the result of turbulent airflow in these regions. Simulations of the respiratory tract have demonstrated that airflow in the bronchi and bronchioles is primarily laminar, with turbulent flow appearing at the bifurcations (Lazaridis, 2023). This turbulent flow results in slower air currents which impact airway walls more readily than under laminar flow. It follows that this would result in more aerosolised liquid droplets containing virus particles depositing in the epithelium.

The lightsheet imaging of influenza co-infection demonstrates that the pathology of co-infection on the mesoscale is largely unchanged from single infection. At 3 days post infection (dpi), infectious lesions are primarily located in the bronchi and major bronchioles proximal to the trachea. By 6 dpi, infectious lesions have cleared from the proximal airways with the remaining viral burden being isolated in the distal minor bronchioles. This reflects findings from single IAV infections (Pirillo et al., 2023).

The finding that lesions comprise mixed populations at the mesoscale is particularly interesting given the effects of superinfection exclusion (SIE) at the microscale (Sims et al., 2022). However, as described in Chapter 1, imaging of large tissues typically comes at the cost of resolution, as such these lightsheet analyses do not enable imaging at single cell resolution. As such I had concerns that these mixed populations may be an artifact of resolution. Additionally, there are numerous

factors involved in light sheet imaging of endogenously fluorescent viruses which may effect these experiments efficacy. Endogenous fluorophores, even GFP-derived fluorophores which are notably long-lived, decayed after approximately a month in lung tissue. Cumulatively, fixation, optical clearing, and imaging take a minimum of a week, tupically longer. Additionally, we must consider the quenching effects of dehydrants on fluorescence and the capacity for tagged viruses to drop the fluorophore encoding sequence through reversion to wildtype during replication. Cumulatively, these effects reduce the proportion of virus we detect during imaging, potentially introducing a sampling bias in which only regions of high viral burden remain at the point of imaging. These considerations prompted further imaging of samples with a shorter lead time and less need for chemical processing at higher resolution. Upon higher resolution imaging via thick section confocal on sections of infected mouse lungs, it was found that seemingly mixed mesoscale populations comprise singly infected microdomains exhibiting SIE. Furthermore, these investigations revealed that SIE restricts co-infection to around 2% of infected cells *in vivo*, aligning with results from *in vitro* studies in the literature (Sims et al., 2022).

Microscale studies via spatial transcriptomics enabled barcoded IAVs to be identified within Visium gene expression data gathered *in vitro*. These data enable the identification not only of specific IAV strains, but the discrimination of highly similar variants of IAV genes. This allows for the identification of cells infected with novel combinations of genes from multiple co-infecting strains arising from reassortment events. Further analysis of these data may reveal insights into the interactions occurring within the co-infected regions afforded by SIE, potentially explaining the origin of reassotant viruses within the spatial context of the tissue.

Collectively, these results demonstrate that multiscale imaging can provide significant insights into the pathology, replication, and evolution of infectious disease.

6.2 Development of approaches for imaging across scales

Technological advancements in microscopy have enabled the imaging of mesoscale samples on the scale of whole organs (Daetwyler and Fiolka, 2023). In recent years, even whole mice have been imaged without dissection (Cai et al., 2023). The imaging of large tissues is reliant on a combination of technologies and methodologies; infection of hosts and harvesting of tissues, optical clearing, imaging, and image analysis. Despite advancements in each of these areas, imaging of large tissues, primarily via light sheet microscopy, still fails to match the resolving power of modern confocal microscope systems (Elliott, 2020). Cutting-edge confocal microscope systems are capable of imaging samples at resolutions of tens of nanometers, surpassing the Abbe diffraction limit through innovative superresolution methods (Bates et al., 2008; Schmidt et al., 2008). However, these systems are limited in field of view, capable of imaging samples on the order of around millimeters in the lateral directions and hundreds of microns in the axial direction (Elliott, 2020). These limitations are exacerbated in the majority of superresolution approaches. In order to gain a comprehensive understanding of mesoscale biological systems, such as the respiratory tract infections focused on here, it is crucial to couple large field of view and high resolution technologies. Infection is a prevalent example of this, with mesoscale behavior often arising from microscale, in many cases subcellular, processes (X. Li et al., 2021; Matthews, 2005). The work presented here demonstrates the importance of imaging across length scales, visualising IAV infections from the scale of the whole lung to the processes occurring between infected cells. These experiments demonstrate the diversity between mesoscale spread of infection, where mixed populations reflect single virus pathology, and microscale spread, where SIE segregates viral populations. In order to gain these insights, this work has contributed to both mesoscale and microscale imaging and image analysis in the form of a novel optical tissue clearing method, tools for FISH data analysis, and the first implementation of spatial transcriptomics *in vitro*.

6.2.1 Advancements in mesoscale imaging of tissues

Light sheet microscopy has enabled the imaging of large samples, with advancements in technology enabling the imaging of samples on the scale of whole mice. This trend is likely to continue, with larger sample chambers, such as that of the Miltenyi Ultramicroscope Blaze, continuing to increase in size (Cai et al., 2023). However, without optical tissue clearing, the depth of imaging is limited to approximately 200 μm via traditional illumination, though this can be extended to at least 2mm using multi-photon illumination (Centonze and White, 1998; Hamdy et al., 2022; Soeller and Cannell, 1999). In addition to the transparency of cleared tissues, it is important to consider numerous other factors when selecting a clearing method. Namely, clearing time, effects of reagents on fluorophores or dyes, effects of reagents on sample morphology, and the toxicity of reagents.

The minimisation of clearing time is crucial for stained samples due to the degradation of fluorophores. This effect is exacerbated in thick tissues due to the autofluorescence of surrounding tissue (Jacob et al., 2024). Fluorescence from GFP-derived fluorophores, notably long-lived among fluorophores, was found to decay to background levels after approximately four weeks in lung tissues (Hirano et al., 2022). Due to the size of mesoscale samples, immunofluorescence or FISH staining times are longer, typically taking one week for whole murine organs, as antibodies or probes take longer to penetrate deep into tissues (Schneider et al., 2021). Though this can be improved by using nanobodies rather than traditional antibodies. Due to their size, nanobodies can penetrate deeper tissue regions than traditional antibodies. In the experiments presented here, labelling of endogenously expressed fluorophores with existing, commercially available nanobodies against GFP and mCherry would likely improve signal and mitigate quenching. Given that clearing protocols comprising delipidation or depigmentation steps, such as CUBIC, can take two weeks, this leaves little time for imaging of fluorophores (Ren et al., 2021).

In addition to fluorophore degradation over time, chemical degradation of fluorophores must be considered. Ethanol and methanol have been popular dehy-

dratants, removing low refractive index (RI) water from samples, since the inception of optical clearing. However, these alcohols significantly degrade fluorophore signals, particularly that of GFP-derived fluorophores, as described in the literature (Maillard et al., 2021). Additionally, high RI compounds used for RI matching can have similar fluorophore quenching effects (Becker et al., 2012; Chung et al., 2013b). Benzyl Alcohol/ Benzyl Benzoate (BABB) is a clearing method which has been used in a variety of tissues for decades, but will quench fluorescent proteins making it appropriate only for the study of endogenous tissue structures (Becker et al., 2012; Chung et al., 2013b).

Many clearing protocols, such as ECi and CUBIC, have been documented to alter the size of tissues following incubation (Masselink and Tanaka, 2023; Ren et al., 2021). In the case of individual organs, this is not a significant issue due to the heterogeneity of the tissue resulting in approximately isotropic alterations. However, in samples comprising multiple tissue types, such as whole organisms, researchers must carefully consider the effects of reagents on composite tissues. A more detrimental effect observed in the CUBIC protocol is the degradation of tissue structure, resulting in tissues with a viscous jelly-like structure (L. Liu et al., 2021; Ren et al., 2021). This is problematic for sample mounting, particularly on the Zeiss Z1 light sheet microscope in which samples are suspended from above. Early in this project, imaging of CUBIC-cleared brain samples was attempted via Zeiss Z1 as part of a collaborative study, however, imaging could not be performed because the samples could not be successfully mounted due to this degradation of structure.

Toxicity of reagents is a crucial consideration as many lightsheet microscope sample chambers are open (CarlZeissMicroscopy, 2011). In order to ensure refractive index matching between the objective lens and the sample, these chambers must be filled with a mounting solution of equal RI to that of the optical clearing solution. This is most easily acheived by simply using the clearing solution as a mounting solution, however, this is inappropriate for toxic reagents. Additionally, toxic clearing reagents simply make working with samples more involved during

the clearing process, therefore inert reagents are preferable.

The clearing method developed during this project was adapted from existing ECi clearing protocols (Masselink and Tanaka, 2023). This ECi protocol was selected due to the short clearing time - 48 to 96 hours - and the non-toxic reagents which were both appropriate for benchtop use and for use with the Zeiss Z1 light sheet microscope. Additionally, though samples do expand following ECi incubation, this morphological change is minimal in comparison to other methods and the integrity of tissues remains unchanged, enabling easy sample mounting (Masselink and Tanaka, 2023; Ren et al., 2021).

However, existing ECi protocols relied on ethanol dehydration. This was replaced with tertiary-butanol dehydration. Tertiary-butanol has been demonstrated to preserve the fluorescence of fluorophores quenched by ethanol (Alves et al., 2016; Schwarz et al., 2015). While this does increase the clearing time by approximately 48 hours, the total clearing time of approximately one week is still shorter than many commercial clearing protocols. Furthermore, the inclusion of the single-step clearing reagent, Ce3D, as a "primer" prior to the dehydration step improves transparency of cleared tissues (W. Li et al., 2019). The addition of this priming step notably improves the transparency of haem-rich samples, significantly improving the clarity of poorly perfused lungs. Finally, the incorporation of an optional bleaching step broadens the scope of the clearing method developed here. This clearing method improves on the transparency, signal retention, and scope of existing ECi clearing protocols, while retaining the speed, morphology and non-toxicity of methods described in the literature. While this project does not directly involve the development of mesoscopic imaging technology, the harnessing of these technologies locally at the Unviersity of Glasgow has been an integral part of the project. When beginning this project, the light sheet microscope facilities at the University of Glasgow Centre for Virus Research were underused. During this project I have adopted the day-to-day management responsibilities of the light sheet imaging facility at the Centre for Virus Research. This has involved the training of new users and the imaging of samples from both internal and external

collaborators. The experiments performed on bone, spinal cord, and mosquitoes are examples of such projects. The development of optical clearing and light sheet imaging facilities at the Centre for Virus Research has broadened the scope of mesoscale imaging at the University of Glasgow. This project has led to the training of researchers from numerous lab groups at the centre for virus research (CVR), enabling studies of coronavirus in the lungs, human papillomavirus in organoids, and multiple arboviruses. This project has also broadened the collaborative capacities of the CVR imaing facility, collaborating with users from the University of Glasgow Centre for Neuroscience, and Cancer Research UK.

6.2.2 Advancements in microscopic approaches

Following the issues with RNA quality in spatial transcriptomic analysis of *in vivo* samples described above, *in vitro* spatial transcriptomics methods were developed. The spatial transcriptomics platform used throughout this project was the Visium spatial gene expression assay produced by 10x Genomics (Cheng et al., 2023). The Visium assay was designed to analyse *in vivo* samples, either fresh frozen or formalin fixed paraffin embedded. The platform has been used successfully in a range of tissues types including brain, lung, and bone marrow from a range of host species. However, application has thus far been limited to *in vivo* samples. Here, I have developed a protocol for performing spatial transcriptomics *in vitro* and implemented this protocol for the first time. The assay designed here uses cell cultures grown on permeable transwell membranes in place of tissue sections traditionally used in the Visium assay. I robustly demonstrate that transwell membranes are permeable to reagents crucial to the Visium assay by performing permeabilisation and immunofluorescence staining of transwell-grown cultures. The protocol is then implemented to study interactions between barcoded IAV variants in a scenario analogous to IAV co-infection in the host. This experiment demonstrates that the protocol designed here can harvest RNA from *in vitro* samples to a standard suitable for spatial transcriptomics analysis, preserving the spatial context of RNA distribution via the spatial identifier sequences. The quality of harvested RNA is

sufficient to distinguish barcoded IAV strains, each of which has a hamming distance of 3/4 (Fu, 2018). This specificity demonstrates that the efficacy of this protocol is sufficient not only to distinguish genes, but also distinguish highly correlated genetic material such as isoforms of individual genes. This demonstrates that the *in vitro* protocol designed here is as effective as the existing *in vivo* protocol for conducting gene expression analysis. This protocol broadens the scope of the Visium assay, enabling researchers working with biological systems inappropriate for *in vivo* study to conduct spatial transcriptomics experiments.

In addition to the development of wet-lab technologies, this project has resulted in the development of FISHtoFigure, a computational image analysis tool for the analysis of FISH data (Bentley-Abbot et al., 2024). Many tools capable of conducting similar analysis to that of FISHtoFigure exist, however, these tools are either expensive (Indica Labs HALO suite) or require extensive coding experience (starFISH) (Horai et al., 2019). FISHtoFigure has been designed such that researchers without extensive computational experience can conduct these analyses. The tool is packaged as an executable file such that it can be downloaded and run immediately from the desktop. The tool is also built with a graphical user interface such that users do not need to interact with the underlying code running the analysis. FISHtoFigure is published on GitHub and is entirely open source and has been used both by internal collaborators at the University of Glasgow and by researchers from other academic institutions. As with all open source software, FISHtoFigure is under continual development, with integration into the image analysis platform QuPath being a key future development goal. FISHtoFigure presently acts as a downstream analysis tool for QuPath-quantified FISH data and direct integration of FISHtoFigure within QuPath would further lower the barrier to entry for researchers seeking to conduct FISH image analysis. Discussions about the integration of FISHtoFigure within QuPath are ongoing with the QuPath development team (Peter Bankhead, personal communication).

6.3 Insights into IAV infection across length scales

It is well established in the literature that influenza A virus co-infection results in complex behaviour which significantly differs across length scales (Amato et al., 2022; Fu, 2018; Ganti et al., 2022; Sims et al., 2022). Microscale behavior is dominated by the segregation of individual viral strains to microdomains by superinfection exclusion (Sims et al., 2022). Meanwhile on the mesoscale, similar segregation results in the emergence of dominant strains in lung lobes, though it is unclear whether this is the result of SIE or an alternative mechanism (Amato et al., 2022; Fu, 2018; Ganti et al., 2022). Though, given the size of microdomains resulting from SIE, it is unlikely these dominant strains directly arise from SIE. While visualisations, primarily *in vitro*, of SIE are well documented, imaging of co-infection dynamics on the larger scale of whole lung lobes have been missing from the literature. This project has enabled such imaging experiments for the first time, visualising IAV co-infection of whole lung lobes. Additionally, while literature on SIE provides of an understanding of how microscopic interactions govern spread of IAV, a deeper understanding of the mechanisms governing genetic exchange between viral strains is necessary to understand the emergence of novel viral strains. The *in vitro* spatial transcriptomics experiments conducted here generated data which may provide insights into reassortment events occurring in the interstitial co-infected regions between domains exhibiting SIE. Initial analysis of these spatial transcriptomics data suggest that co-infecting viral strains can be distinguished based on genetic barcode expression. By conducting imaging experiments at multiple length scales, this project has visualised both mesoscale and microscale interactions between IAVs for the first time. The diverse behavior observed between the micro- and mesoscale demonstrates the importance of developing pipelines capable of imaging samples across length scales.

6.3.1 Dominant strain emergence and IAV interaction

The work of Amato, Ganti, and Fu demonstrate the emergence of dominant strains over the course of IAV co-infection (Amato et al., 2022; Fu, 2018; Ganti et al., 2022). Amato and Ganti identify dominant strains in the lung lobes, while Fu shows that single strains dominate in the forward transmission of virus. The light sheet imaging studies performed here do not align with these findings, rather, these data suggest that the progression of disease during co-infection closely resembles that of single infections, both in spread and distribution in the airway. Viral burden spreads from the proximal major airways at 3dpi to the distal bronchioles at 6dpi, and foci of infection are primarily located at the bifurcation points of the airway. These findings reflect prior work performed by Pirillo *et al.* visualising single IAV infections in lung lobes (Pirillo et al., 2023). The experiments performed here investigate the left lung of infected mice. The murine left lung comprises a single lung lobe, thus these data are comparable to that of Ganti and Amato. Importantly, Amato and Ganti's studies were bulk transcriptomic studies and did not comprise imaging experiments (Amato et al., 2022; Ganti et al., 2022). Therefore, though the light sheet microscopy data presented here do not demonstrate a visible dominance of a single strain, it is possible that differences in viral burden between strains exist which are not perceptible on the mesoscale. This is further evidenced by the microdomains which comprise the seemingly mixed populations observed in these mesoscale data. I can therefore conclude from these data that while dominant strains emerge within co-infected lung lobes, these strains do not dominate the spatial landscape of the lung, with populations remaining mixed. Furthermore, the emergence of these dominant strains does not impact on the spread of infection and the progression of disease on the mesoscale, and nor do the effects of SIE. A significant difference between the studies presented here and those of Ganti, Amato, and Fu is the diversity of co-infecting viruses. Ganti, Amato and Fu use libraries of barcoded viruses comprising, at minimum, tens of variants (Amato et al., 2022; Fu, 2018; Ganti et al., 2022). The imaging studies here use a pair of fluorescently tagged IAVs. It is therefore possible that

these studies lack the necessary genetic diversity to observe effects documented by Ganti and Amato. There is a technological limitation on the number of fluorophores which can be imaged. This could be increased to 5-7 targets in cutting edge light sheet microscope or large sample confocal systems, however the Zeiss Z1 system is limited to three targets (CarlZeissMicroscopy, 2011). Given that the study presented here is primarily a pilot study involving the development of novel clearing and imaging methods, the pair of viruses used here is appropriate. As mesoscale imaging technologies develop further, imaging of more targets will likely be possible, potentially through cyclical methods seen in FISH studies. In future studies, these technological developments will enable imaging studies which better reflect the conditions investigated by Amato and Ganti, revealing whether these dominant strains can be visualised in larger viral populations.

6.3.2 SIE, reassortment and pandemic strain emergence

High resolution thick section confocal microscopy revealed that the populations which appear mixed on the mesoscale comprise tightly restricted singly infected microdomains. This microdomain structure reflects the findings of Sims *et al.* on super infection exclusion. Sims documented that SIE restricts co-infection to approximately 1-3% of cells *in vitro*, the thick section confocal study performed here found that a similar restriction occurs *in vivo*, with approximately 2% of infected cells being co-infected (Sims et al., 2022). This restriction has significant effects on the emergence of novel IAV strains via reassortment, as co-infection is required for genetic exchange during viral packaging (Jakob et al., 2022; X. Li et al., 2021).

Two methods for quantifying the emergence of novel strains through reassortment were explored here; FISH and spatial transcriptomics. The experiments performed here were unsuccessful in identifying co-infected cells and reassortant viral populations *in vivo* via FISH. However, a panel of FISH probes targeting the surface glycoprotein encoding segments of laboratory H1N1 and H3N2 viral strains were designed and validated *in vitro*. It is unclear why these experiments

were unsuccessful *in vivo*. *In vitro* and *in vivo* protocols differed only in the permeabilisation of the tissues, with permeabilisation times for lung samples being based on prior RNAScope experiments. The increased level of autofluorescence *in vivo* reduces signal to background ratio making detection more difficult that *in vitro*, however, RNAScope is primarily designed for *in vivo* use and the fluorophores used are designed to be detectable in animal tissues (F. Wang et al., 2012). The probes designed here will be useful in future IAV co-infection studies, both *in vitro* and *in vivo*, provided the issues with detection found here can be overcome.

Spatial transcriptomics experiments enabled the identification of individual IAV strains via *in situ* genetic barcodes. The timeline of this project did not enable in depth analysis of interactions between co-infecting strains. However, collected RNA was of high quality and the presence of barcoded IAV sequences in this data was readily apparent in initial analysis. This suggests further analysis of these data may yield insights into the interactions between co-infecting strains and the emergence of reassortant viruses within the spatial context of the co-infected tissue.

6.4 Conclusion

Collectively, this project aimed to develop methods for imaging *in vivo* samples across length scales and to employ these methods to better understand influenza A virus co-infection. This project has successfully achieved these goals. On the mesoscale, I have developed optical clearing and light sheet microscopy methods capable of imaging a range of murine organs. These methods have revealed influenza A virus co-infection pathology across the whole for the first time. On the microscale, I have developed tools and methods for performing analyses of RNA expression within a range of tissues. The spatial transcriptomics experiments performed here represent the first implementation of the Visium spatial gene expression assay *in vitro*, expanding the scope of spatial transcriptomics methods significantly. The experiments performed here have identified the intercellular processes governing co-infection *in vivo*, aligning with *in vitro* SIE data presented by Sims (Sims et al., 2022). Collectively, these experiments comprehensively explore the mutli-length scale nature of viral infection, developing methods for visualising infections from the meso- to the microscale. This work demonstrates the importance of developing pipelines capable of imaging tissues across length scales, as exemplified here in the murine lung.

References

10xGenomics. (2025). Cg000239visiumspatialgeneexpressionuserguide [Accessed: 26/05/2025]. https://www.10xgenomics.com/support/spatial-gene-expression-fresh-frozen

Abbe, E. (1873). Beiträge zur theorie des mikroskops und der mikroskopischen wahrnehmung. *Archiv für mikroskopische Anatomie*, *9*(1), 413–468.

AkoyaBioscience. (2024, January). Estimated spectral overlap between Opal fluors with Chroma filter sets_jdc.pdf.

Alberts, B., Johnson, A., Lewis, J., Raff, M., Roberts, K., & Walter, P. (2002). The Airways and the Gut. In *Molecular Biology of the Cell. 4th edition*. Garland Science. Retrieved July 4, 2025, from https://www.ncbi.nlm.nih.gov/books/NBK26875/

Alexakis, L., Buczkowski, H., Ducatez, M., Fusaro, A., Gonzales, J. L., Kuiken, T., Ståhl, K., Staubach, C., Svartström, O., Terregino, C., Willgert, K., Melo, M., & Kohnle, L. (2025). Avian influenza overview December 2024–March 2025. *EFSA Journal*, *23*(4), e9352. https://doi.org/10.2903/j.efsa.2025.9352

Alves, S., Bode, J., Bemelmans, A.-P., von Kalle, C., Cartier, N., & Tews, B. (2016). Ultramicroscopy as a novel tool to unravel the tropism of aav gene therapy vectors in the brain. *Sci Rep*, *6*. https://doi.org/10.1038/srep28272

Amato, K. A., Haddock, L. A., Braun, K. M., Meliopoulos, V., Livingston, B., Honce, R., Schaack, G. A., Boehm, E., Higgins, C. A., Barry, G. L., Koelle, K., Schultz-Cherry, S., Friedrich, T. C., & Mehle, A. (2022). Influenza A virus undergoes compartmentalized replication in vivo dominated by

stochastic bottlenecks. *Nature Communications*, *13*, 3416. https://doi.org/10.1038/s41467-022-31147-0

Ariel, P. (2018). Ultramicroscope ii – a user guide. *University of North Carolina, University Libraries*, *1*.

Azaripour, A., Lagerweij, T., Scharfbillig, C., Jadczak, A. E., Willershausen, B., & Van Noorden, C. J. F. (2016). A survey of clearing techniques for 3D imaging of tissues with special reference to connective tissue. *Progress in Histochemistry and Cytochemistry*, *51*(2), 9–23. https://doi.org/10.1016/j.proghi.2016.04.001

Baccam, P., Beauchemin, C., Macken, C. A., Hayden, F. G., & Perelson, A. S. (2006). Kinetics of influenza a virus infection in humans. *J. Virol.*, *80*, 7590–7599. https://doi.org/10.1128/JVI.01623-05

Bae, W., Yoon, T., & Jeong, C. (2021). Direct evaluation of self-quenching behavior of fluorophores at high concentrations using an evanescent field. *PLOS One*. https://doi.org/https://doi.org/10.1371/journal.pone.0247326

Bankhead, P., Loughrey, M. B., Fernández, J. A., Dombrowski, Y., McArt, D. G., Dunne, P. D., McQuaid, S., Gray, R. T., Murray, L. J., Coleman, H. G., James, J. A., Salto-Tellez, M., & Hamilton, P. W. (2017). QuPath: Open source software for digital pathology image analysis. *Scientific Reports*, *7*(1), 16878. https://doi.org/10.1038/s41598-017-17204-5

Bates, M., Huang, B., & Zhuang, X. (2008). Super-resolution microscopy by nanoscale localization of photo-switchable fluorescent probes. *Current Opinion in Chemical Biology*, *12*(5), 505–514. https://doi.org/10.1016/j.cbpa.2008.08.008

Battistella, E., Quintana, J. F., & McConnell, G. (2022). Application of Light-Sheet Mesoscopy to Image Host-Pathogen Interactions in Intact Organs. *Frontiers in Cellular and Infection Microbiology*, *12*. https://doi.org/10.3389/fcimb.2022.903957

Battistella, E., Schniete, J., Wesencraft, K., Quintana, J. F., & McConnell, G. (2022). Light-sheet mesoscopy with the Mesolens provides fast sub-cellular

resolution imaging throughout large tissue volumes. *iScience*, *25*(9), 104797. https://doi.org/10.1016/j.isci.2022.104797

Bauman, J. G. J., Wiegant, J., Borst, P., & van Duijn, P. (1980). A new method for fluorescence microscopical localization of specific DNA sequences by in situ hybridization of fluorochrome-labelled RNA. *Experimental Cell Research*, *128*(2), 485–490. https://doi.org/10.1016/0014-4827(80)90087-7

Becker, K., Jährling, N., Saghafi, S., Weiler, R., & Dodt, H.-U. (2012). Chemical Clearing and Dehydration of GFP Expressing Mouse Brains. *PLOS ONE*, *7*(3), e33916. https://doi.org/10.1371/journal.pone.0033916

Beest, D. E. t., Bruin, E. d., Imholz, S., Koopmans, M., & Boven, M. v. (2017). Heterosubtypic cross-reactivity of HA1 antibodies to influenza A, with emphasis on nonhuman subtypes (H5N1, H7N7, H9N2). *PLOS ONE*, *12*(7), e0181093. https://doi.org/10.1371/journal.pone.0181093

Bentley-Abbot, C., Heslop, R., Pirillo, C., Chandrasegaran, P., McConnell, G., Roberts, E., Hutchinson, E., & MacLeod, A. (2024). An easy to use tool for the analysis of subcellular mRNA transcript colocalisation in smFISH data. *Scientific Reports*, *14*(1), 8348. https://doi.org/10.1038/s41598-024-58641-3

Berezin, M. Y., & Achilefu, S. (2010). Fluorescence Lifetime Measurements and Biological Imaging. *Chemical reviews*, *110*(5), 2641–2684. https://doi.org/10.1021/cr900343z

Betzig, E., Patterson, G., Sougrat, R., Lindwasser, O., Olenych, S., Bonifacino, J., Davidson, M., Lippincott-Schwartz, J., & Hess, H. (2006). Imaging intracellular fluorescent proteins at nanometer resolution. *Science*. https://doi.org/10.1126/science.1127344

Beutner, E. H., & Jordon, R. E. (1964). Demonstration Of Skin Antibodies In Sera Of Pemphigus Vulklgaris Patients By Indirect Immunofluorescent Staining. *Proceedings of the Society for Experimental Biology and Medicine. Society for Experimental Biology and Medicine (New York, N.Y.)*, *117*, 505–510. https://doi.org/10.3181/00379727-117-29622

Bhakdi, S. C., & Thaicharoen, P. (2018). Easy Employment and Crosstalk-Free Detection of Seven Fluorophores in a Widefield Fluorescence Microscope. *Methods and Protocols*, *1*(2), 20. https://doi.org/10.3390/mps1020020

Bhatia, H. S., Brunner, A.-D., Ozturk, F., Kapoor, S., Rong, Z., Mai, H., Thielert, M., & Ali, M. (2022). Spatial proteomics in three-dimensional intact specimens. *University of North Carolina, University Libraries*, *185*. https://doi.org/p5040-5058.e19

Biorender [Accessed: 09/07/2025]. (2025).

Boudreau, C., Wee, T.-L. (, Duh, Y.-R. (, Couto, M. P., Ardakani, K. H., & Brown, C. M. (2016). Excitation Light Dose Engineering to Reduce Photo-bleaching and Photo-toxicity. *Scientific Reports*, *6*(1), 30892. https://doi.org/10.1038/srep30892

Cai, R., Kolabas, Z. I., Pan, C., Mai, H., Zhao, S., Kaltenecker, D., Voigt, F. F., Molbay, M., Ohn, T.-I., Vincke, C., Todorov, M. I., Helmchen, F., Van Ginderachter, J. A., & Ertürk, A. (2023). Whole-mouse clearing and imaging at the cellular level with vDISCO. *Nature Protocols*, *18*(4), 1197–1242. https://doi.org/10.1038/s41596-022-00788-2

Calvo-Alvarez, E., Cren-Travaillé, C., Crouzols, A., & Rotureau, B. (2018). A new chimeric triple reporter fusion protein as a tool for in vitro and in vivo multimodal imaging to monitor the development of African trypanosomes and Leishmania parasites. *Infection, Genetics and Evolution: Journal of Molecular Epidemiology and Evolutionary Genetics in Infectious Diseases*, *63*, 391–403. https://doi.org/10.1016/j.meegid.2018.01.011

Capewell, P., Cren-Travaillé, C., Marchesi, F., Johnston, P., Clucas, C., Benson, R. A., Gorman, T.-A., Calvo-Alvarez, E., Crouzols, A., Jouvion, G., Jamonneau, V., Weir, W., Stevenson, M. L., O'Neill, K., Cooper, A., Swar, N.-R. K., Bucheton, B., Ngoyi, D. M., Garside, P., . . . MacLeod, A. (2016). The skin is a significant but overlooked anatomical reservoir for vector-borne African trypanosomes. *eLife*, *5*, e17716. https://doi.org/10.7554/eLife.17716

CarlZeissMicroscopy. (2011). ZEISS Lightsheet Z.1 manual. *Zeiss Z1 Handbook*, 19.

Caswell, T. A., Droettboom, M., Lee, A., De Andrade, E. S., Hoffmann, T., Hunter, J., Klymak, J., Firing, E., Stansby, D., Varoquaux, N., Nielsen, J. H., Root, B., May, R., Elson, P., Seppänen, J. K., Dale, D., Lee, J.-J., McDougall, D., Straw, A., ... Ivanov, P. (2021, August). Matplotlib/matplotlib: REL: V3.4.3. https://doi.org/10.5281/ZENODO.5194481

Caves, E. A., Cook, S. A., Lee, N., Stoltz, D., Watkins, S., & Shair, K. H. Y. (2018). Air-liquid interface method to study epstein-barr virus pathogenesis in nasopharyngeal epithelial cells. *mSphere.*, *4*. https://doi.org/10.1128/mSphere.00152-18

Centonze, V. E., & White, J. G. (1998). Multiphoton excitation provides optical sections from deeper within scattering specimens than confocal imaging. *Biophysical Journal*, *75*(4), 2015–2024. https://doi.org/10.1016/S0006-3495(98)77643-X

Chang, B.-J., Dean, K. M., & Fiolka, R. (2020). Systematic and quantitative comparison of lattice and gaussian light-sheets. *Optics Express*. https://doi.org/https://doi.org/10.1364/OE.400164

Chang, J.-B., Chen, F., Yoon, Y.-G., Jung, E. E., Babcock, H., Kang, J. S., Asano, S., Suk, H.-J., Pak, N., Tillberg, P. W., Wassie, A. T., Cai, D., & Boyden, E. S. (2017). Iterative expansion microscopy. *Nature Methods*, *14*(6), 593–599. https://doi.org/10.1038/nmeth.4261

Chen, F., Tillberg, P. W., & Boyden, E. S. (2015). Expansion microscopy. *Science*, *347*(6221), 543–548. https://doi.org/10.1126/science.1260088

Chen, F., Wassie, A. T., Cote, A. J., Sinha, A., Alon, S., Asano, S., Daugharthy, E. R., Chang, J.-B., Marblestone, A., Church, G. M., Raj, A., & Boyden, E. S. (2016). Nanoscale imaging of RNA with expansion microscopy. *Nature Methods*, *13*(8), 679–684. https://doi.org/10.1038/nmeth.3899

Chen, X., Zheng, B., & Liu, H. (2011). Optical and digital microscopic imaging techniques and applications in pathology. *Analytical Cellular Pathology (Amsterdam)*, *34*(1-2), 5. https://doi.org/10.3233/ACP-2011-0006

Cheng, M., Jiang, Y., Xu, J., Mentis, A.-F. A., Wang, S., Zheng, H., Sahu, S. K., Liu, L., & Xu, X. (2023). Spatially resolved transcriptomics: A comprehensive review of their technological advances, applications, and challenges. *Journal of Genetics and Genomics*, *50*(9), 625–640. https://doi.org/10.1016/j.jgg.2023.03.011

Chheda, U., Pradeepan, S., Esposito, E., Strezsak, S., Fernandez-Delgado, O., & Kranz, J. (2024). Factors Affecting Stability of RNA – Temperature, Length, Concentration, pH, and Buffering Species. *Journal of Pharmaceutical Sciences*, *113*(2), 377–385. https://doi.org/10.1016/j.xphs.2023.11.023

Choi, H. M. T., Schwarzkopf, M., Fornace, M. E., Acharya, A., Artavanis, G., Stegmaier, J., Cunha, A., & Pierce, N. A. (2008). Third-generation in situ hybridization chain reaction: Multiplexed, quantitative, sensitive, versatile, robust. *Nature Methods*. https://doi.org/https://doi.org/10.1038/nmeth.1253

Chozinski, T. J., Halpern, A. R., Okawa, H., Kim, H.-J., Tremel, G. J., Wong, R. O. L., & Vaughan, J. C. (2016). Expansion microscopy with conventional antibodies and fluorescent proteins. *Nature Methods*, *13*(6), 485–488. https://doi.org/10.1038/nmeth.3833

Chung, K., Wallace, J., Kim, S.-Y., Kalyanasundaram, S., Andalman, A. S., Davidson, T. J., Mirzabekov, J. J., Zalocusky, K. A., Mattis, J., Denisin, A. K., Pak, S., Bernstein, H., Ramakrishnan, C., Grosenick, L., Gradinaru, V., & Deisseroth, K. (2013a). Structural and molecular interrogation of intact biological systems. *Nature*, *497*(7449), 332–337. https://doi.org/10.1038/nature12107

Chung, K., Wallace, J., Kim, S.-Y., Kalyanasundaram, S., Andalman, A. S., Davidson, T. J., Mirzabekov, J. J., Zalocusky, K. A., Mattis, J., Denisin, A. K.,

Pak, S., Bernstein, H., Ramakrishnan, C., Grosenick, L., Gradinaru, V., & Deisseroth, K. (2013b). Structural and molecular interrogation of intact biological systems. *Nature*, *497*(7449), 332–337. https://doi.org/10.1038/nature12107

Coons, A. H., & Kaplan, M. H. (1950). Localization Of Antigen In Tissue Cells. *The Journal of Experimental Medicine*, *91*(1), 1–13. https://doi.org/10.1084/jem.91.1.1

Czakó, R., Vogel, L., Lamirande, E. W., Bock, K. W., Moore, I. N., Ellebedy, A. H., Ahmed, R., Mehle, A., & Subbarao, K. (2017). In Vivo Imaging of Influenza Virus Infection in Immunized Mice. *mBio*, *8*(3), 10.1128/mbio.00714–17. https://doi.org/10.1128/mbio.00714-17

Daetwyler, S., & Fiolka, R. P. (2023). Light-sheets and smart microscopy, an exciting future is dawning. *Communications Biology*, *6*(1), 502. https://doi.org/10.1038/s42003-023-04857-4

Datta, R., Heaster, T. M., Sharick, J. T., Gillette, A. A., & Skala, M. C. (2020). Fluorescence lifetime imaging microscopy: Fundamentals and advances in instrumentation, analysis, and applications. *Journal of Biomedical Optics*, *25*(7), 071203. https://doi.org/10.1117/1.JBO.25.7.071203

Davidovits, P., & Egger, M. (1969). Scanning laser microscope. *Nature*. https://doi.org/https://doi.org/10.1038/223831a0

de Matos, L. L., Trufelli, D. C., de Matos, M. G. L., & da Silva Pinhal, M. A. (2010). Immunohistochemistry as an Important Tool in Biomarkers Detection and Clinical Practice. *Biomarker Insights*, *5*, 9–20. https://doi.org/10.4137/bmi.s2185

De Niz, M., Brás, D., Ouarné, M., Pedro, M., Nascimento, A. M., Henao Misikova, L., Franco, C. A., & Figueiredo, L. M. (2021). Organotypic endothelial adhesion molecules are key for Trypanosoma brucei tropism and virulence. *Cell Reports*, *36*(12), 109741. https://doi.org/10.1016/j.celrep.2021.109741

Dempsey, G. T., Vaughan, J. C., Chen, K. H., Bates, M., & Zhuang, X. (2011). Evaluation of fluorophores for optimal performance in localization-based super-resolution imaging. *Nature methods*, *8*(12), 1027–1036. https://doi.org/10.1038/nmeth.1768

Denney, L., & Ho, L.-P. (2018). The role of respiratory epithelium in host defence against influenza virus infection. *Biomedical Journal*, *41*(4), 218–233. https://doi.org/10.1016/j.bj.2018.08.004

Derichs, N., Jin, Y., B-J andSong, Finkbeiner, W. E., & Verkman, A. S. (2011). Hyperviscous airway periciliary and mucous liquid layers in cystic fibrosis measured by confocal fluorescence photobleaching. *Mehtods Mol. Biol.*, *7*, 2325–32. https://doi.org/10.1096/fj.10-179549

Di Marco, F., Nicola, F., Giannese, F., Saliu, F., Tonon, G., de Pretis, S., Cirillo, D. M., & Lorè, N. I. (2024). Dual spatial host-bacterial gene expression in Mycobacterium abscessus respiratory infections. *Communications Biology*, *7*(1), 1–8. https://doi.org/10.1038/s42003-024-06929-5

Dickson, R., Cubitt, A., Tsien, R., & Moerner, W. E. (1997). On/off blinking and switching behaviour of single molecules of green fluorescent protein. *Nature*. https://doi.org/https://doi.org/10.1038/41048

Diefenbacher, M., Sun, J., & Brooke, C. B. (2018). The parts are greater than the whole: The role of semi-infectious particles in influenza A virus biology. *Current opinion in virology*, *33*, 42–46. https://doi.org/10.1016/j.coviro.2018.07.002

Dirks, R. M., & Pierce, N. A. (2004). Triggered amplification by hybridization chain reaction. *PNAS*. https://doi.org/https://doi.org/10.1073/pnas.0407024101

Dou, D., Revol, R., Östbye, H., Wang, H., & Daniels, R. (2018). Influenza A Virus Cell Entry, Replication, Virion Assembly and Movement. *Frontiers in Immunology*, *9*, 1581. https://doi.org/10.3389/fimmu.2018.01581

Elliott, A. D. (2020). Confocal Microscopy: Principles and Modern Practices. *Current protocols in cytometry*, *92*(1), e68. https://doi.org/10.1002/cpcy.68

Enders, P. (1996). Huygens' principle and the modelling of propagation. *European Journal of Physics*, *17*(4), 226. https://doi.org/10.1088/0143-0807/17/4/014

Endesfelder, U., & Heilemann, M. (2015). Direct stochastic optical reconstruction microscopy (dSTORM). *Methods in Molecular Biology (Clifton, N.J.)*, *1251*, 263–276. https://doi.org/10.1007/978-1-4939-2080-8_14

Ertürk, A., Becker, K., Jährling, N., Mauch, C. P., Hojer, C. D., Egen, J. G., Hellal, F., Bradke, F., Sheng, M., & Dodt, H.-U. (2012). Three-dimensional imaging of solvent-cleared organs using 3DISCO. *Nature Protocols*, *7*(11), 1983–1995. https://doi.org/10.1038/nprot.2012.119

Evanko, D. (2004). Hybridization chain reaction. *Nature Methods*. https://doi.org/https://doi.org/10.1038/nmeth1204-186a

Fahrbach, F. O., Gurchenkov, V., Alessandri, K., Nassoy, P., & Rohrbach, A. (2013). Light-sheet microscopy in thick media using scanned bessel beams and two-photon fluorescence excitation. *Optics Express*. https://doi.org/https://doi.org/10.1364/OE.21.013824

Fan, G., Gao, R., Xie, T., Li, L., Tang, L., Han, X., & Shi, Y. (2024). DKK1+ tumor cells inhibited the infiltration of CCL19+ fibroblasts and plasma cells contributing to worse immunotherapy response in hepatocellular carcinoma. *Cell Death & Disease*, *15*(11), 1–15. https://doi.org/10.1038/s41419-024-07195-3

Fan, G., Tao, C., Li, L., Xie, T., Tang, L., Han, X., & Shi, Y. (2024). The co-location of MARCO+ tumor-associated macrophages and CTSE+ tumor cells determined the poor prognosis in intrahepatic cholangiocarcinoma. *Hepatology*, 10.1097/HEP.0000000000001138. https://doi.org/10.1097/HEP.0000000000001138

Feinberg, D. A., Beckett, A. J. S., Vu, A. T., Stockmann, J., Huber, L., Ma, S., Ahn, S., Setsompop, K., Cao, X., Park, S., Liu, C., Wald, L. L., Polimeni, J. R., Mareyam, A., Gruber, B., Stirnberg, R., Liao, C., Yacoub, E., Davids, M., … Dietz, P. (2023). Next-generation MRI scanner designed for ultra-

high-resolution human brain imaging at 7 Tesla. *Nature Methods*, *20*(12), 2048–2057. https://doi.org/10.1038/s41592-023-02068-7

Femino, A. M., Fay, F. S., Fogarty, K., & Singer, R. H. (1998). Visualization of single rna transcripts in situ. *Science*. https://doi.org/DOI:10.1126/science.280.5363.585

Fischer, W. A., Gong, M., Bhagwanjee, S., & Sevransky, J. (2014). Global burden of Influenza: Contributions from Resource Limited and Low-Income Settings. *Global heart*, *9*(3), 325–336. https://doi.org/10.1016/j.gheart.2014.08.004

Foster, D. S., Nguyen, A. T., Chinta, M., Salhotra, A., Jones, R. E., Mascharak, S., Titan, A. L., Ransom, R. C., da Silva, O. L., Foley, E., Briger, E., & Longaker, M. T. (2019). A Clearing Technique to Enhance Endogenous Fluorophores in Skin and Soft Tissue. *Scientific Reports*, *9*(1), 15791. https://doi.org/10.1038/s41598-019-50359-x

Fpbase [Accessed: 18/07/2025]. (2025).

Fu, J. (2018). *A tool of barcoded viruses to study influenza virus transmission dynamics* [Doctoral dissertation, University of Cambridge].

Fujii, S., Muranaka, T., Matsubayashi, J., Yamada, S., Yoneyama, A., & Takakuwa, T. (2020). The bronchial tree of the human embryo: An analysis of variations in the bronchial segments. *Journal of Anatomy*, *237*(2), 311–322. https://doi.org/10.1111/joa.13199

Fukuyama, S., Katsura, H., Zhao, D., Ozawa, M., Ando, T., Shoemaker, J. E., Ishikawa, I., Yamada, S., Neumann, G., Watanabe, S., Kitano, H., & Kawaoka, Y. (2015). Multi-spectral fluorescent reporter influenza viruses (Color-flu) as powerful tools for in vivo studies. *Nature Communications*, *6*(1), 6600. https://doi.org/10.1038/ncomms7600

Gall, J. G., & Pardue, M. L. (1998). Formation and detection of rna-dna hybrid molecules in cytological preparations. *PNAS*. https://doi.org/https://doi.org/10.1073/pnas.63.2.378

Ganti, K., Bagga, A., Carnaccini, S., Ferreri, L. M., Geiger, G., Joaquin Caceres, C., Seibert, B., Li, Y., Wang, L., Kwon, T., Li, Y., Morozov, I., Ma, W., Richt, J. A., Perez, D. R., Koelle, K., & Lowen, A. C. (2022). Influenza A virus reassortment in mammals gives rise to genetically distinct within-host subpopulations. *Nature Communications*, *13*(1), 6846. https://doi.org/10.1038/s41467-022-34611-z

Garini, Y., Young, I. T., & McNamara, G. (2006). Spectral imaging: Principles and applications. *Cytometry Part A*, *69A*(8), 735–747. https://doi.org/10.1002/cyto.a.20311

Gaush, C. R., & Smith, T. F. (1968). Replication and Plaque Assay of Influenza Virus in an Established Line of Canine Kidney Cells. *Applied Microbiology*, *16*(4), 588–594. https://doi.org/10.1128/am.16.4.588-594.1968

Genina, E. A. (2022). Tissue Optical Clearing: State of the Art and Prospects. *Diagnostics*, *12*(7), 1534. https://doi.org/10.3390/diagnostics12071534

Gerhard, C. (2021). On the History, Presence, and Future of Optics Manufacturing. *Micromachines*, *12*(6), 675. https://doi.org/10.3390/mi12060675

Germroth, P. G., Gourdie, R. G., & Thompson, R. P. (1995). Confocal microscopy of thick sections from acrylamide gel embedded embryos. *Microscopy Research and Technique*, *30*(6), 513–520. https://doi.org/10.1002/jemt.1070300608

Giard, D. J., Aaronson, S. A., Todaro, G. J., Arnstein, P., Kersey, J. H., Dosik, H., & Parks, W. P. (1973). In vitro cultivation of human tumors: Establishment of cell lines derived from a series of solid tumors. *J. Natl. Cancer Inst.*, *5*. https://doi.org/10.1093/jnci/51.5.1417

Ginzinger, D. G. (2002). Gene quantification using real-time quantitative PCR: An emerging technology hits the mainstream. *Experimental Hematology*, *30*(6), 503–512. https://doi.org/10.1016/S0301-472X(02)00806-8

Gog, J., Edos Afonso, S., Dalton, R., Leclercq, I., Tiley, L., Leton, D., von Kirchbach, J., Naffakh, N., Escriou, N., & Digard, P. (2007). Codon conservation

in the influenza a virus genome defines rna packaging signals. *Nucleic Acid Res.*, *35*, 1897–907. https://doi.org/doi:10.1093/nar/gkm087.

Goossen-Schmidt, N. C., Schnieder, M., Hüve, J., & Klingauf, J. (2020). Switching behaviour of dSTORM dyes in glycerol-containing buffer. *Scientific Reports*, *10*(1), 13746. https://doi.org/10.1038/s41598-020-70335-0

Gopee, N. V., & Howard, P. C. (2007). A time course study demonstrating RNA stability in postmortem skin. *Experimental and Molecular Pathology*, *83*(1), 4–10. https://doi.org/10.1016/j.yexmp.2006.11.001

Gopee, N. H., Winheim, E., Olabi, B., Admane, C., Foster, A. R., Huang, N., Botting, R. A., Torabi, F., Sumanaweera, D., Le, A. P., Kim, J., Verger, L., Stephenson, E., Adão, D., Ganier, C., Gim, K. Y., Serdy, S. A., Deakin, C., Goh, I., ... Haniffa, M. (2024). A prenatal skin atlas reveals immune regulation of human skin morphogenesis. *Nature*, *635*(8039), 679–689. https://doi.org/10.1038/s41586-024-08002-x

Grover, V. P., Tognarelli, J. M., Crossey, M. M., Cox, I. J., Taylor-Robinson, S. D., & McPhail, M. J. (2015). Magnetic Resonance Imaging: Principles and Techniques: Lessons for Clinicians. *Journal of Clinical and Experimental Hepatology*, *5*(3), 246–255. https://doi.org/10.1016/j.jceh.2015.08.001

Haghnegahdar, A., Zhao, J., & Feng, Y. (2019). Lung Aerosol Dynamics of Airborne Influenza A Virus-Laden Droplets and the Resultant Immune System Responses: An In Silico Study. *Journal of aerosol science*, *134*, 34–55. https://doi.org/10.1016/j.jaerosci.2019.04.009

Hamdy, O., Abdel-Salam, Z., & Abdel-Harith, M. (2022). Optical Characterization of Biological Tissues Based on Fluorescence, Absorption, and Scattering Properties. *Diagnostics*, *12*(11), 2846. https://doi.org/10.3390/diagnostics12112846

Hampson, K. M., Turcotte, R., Miller, D. T., Kurokawa, K., Males, J. R., Ji, N., & Booth, M. J. (2021). Adaptive optics for high-resolution imaging. *Nat Rev Mehtods Primers*. https://doi.org/10.1038/s43586-021-00066-7

Hawkes, R. C., Holland, G. N., Moore, W. S., & Worthington, B. S. (1980). Nuclear Magnetic Resonance (NMR) Tomography of the Brain: A Preliminary Clinical Assessment with Demonstration of Pathology. *Journal of Computer Assisted Tomography*, *4*(5), 577. Retrieved June 25, 2025, from https://journals.lww.com/jcat/abstract/1980/10000/Nuclear_Magnetic_Resonance__NMR__Tomography_of_the.1.aspx

Hecker, H., & Brun, R. (1982). Comparative morphometric analysis of bloodstream and lymph forms of *Trypanosoma (T.) brucei brucei* grown *in vitro* and *in vivo*. *Transactions of the Royal Society of Tropical Medicine and Hygiene*, *76*(5), 692–697. https://doi.org/10.1016/0035-9203(82)90241-3

Heim, R., & Tsien, R. Y. (1996). Engineering green fluorescent protein for improved brightness, longer wavelengths and fluorescence resonance energy transfer. *Current Biology*, *6*(2), 178–182. https://doi.org/10.1016/S0960-9822(02)00450-5

Herbert, S., Soares, H., Zimmer, C., & Henriques, R. (2012). Single-molecule localization super-resolution microscopy: Deeper and faster. *Microscopy and Microanalysis*, *18*, 1–11. https://doi.org/10.1017/S1431927612013347

Hiller, B. E., Yin, Y., Perng, Y.-C., de Araujo Castro, Í., Fox, L. E., Locke, M. C., Monte, K. J., López, C. B., Ornitz, D. M., & Lenschow, D. J. (2022). Fibroblast growth factor-9 expression in airway epithelial cells amplifies the type I interferon response and alters influenza A virus pathogenesis. *PLoS Pathogens*, *18*(6), e1010228. https://doi.org/10.1371/journal.ppat.1010228

Hirano, M., Ando, R., Shimozono, S., Sugiyama, M., Takeda, N., Kurokawa, H., Deguchi, R., Endo, K., Haga, K., Takai-Todaka, R., Inaura, S., Matsumura, Y., Hama, H., Okada, Y., Fujiwara, T., Morimoto, T., Katayama, K., & Miyawaki, A. (2022). A highly photostable and bright green fluorescent protein. *Nature Biotechnology*, *40*(7), 1132–1142. https://doi.org/10.1038/s41587-022-01278-2

Hofmann, J., Gadjalova, I., Mishra, R., Ruland, J., & Keppler, S. J. (2021). Efficient Tissue Clearing and Multi-Organ Volumetric Imaging Enable Quantitative Visualization of Sparse Immune Cell Populations During Inflammation. *Frontiers in Immunology*, *11*. https://doi.org/10.3389/fimmu.2020.599495

Hooke, R. (1665). *Micrographia: Or Some Physiological Descriptions of Minute Bodies Made by Magnifying Glasses With Observations and Inquiries Thereupon.* The Royal Society.

Horai, Y., Mizukawa, M., Nishina, H., Nishikawa, S., Ono, Y., Takemoto, K., & Baba, N. (2019). Quantification of histopathological findings using a novel image analysis platform. *Journal of Toxicologic Pathology*, *32*(4), 319–327. https://doi.org/10.1293/tox.2019-0022

Hu, D.-N., Simon, J. D., & Sarna, T. (2008). Role of ocular melanin in ophthalmic physiology and pathology. *Photochem. Photobiol.*, *3*, 639–44. https://doi.org/10.1111/j.1751-1097.2008.00316.x

Huang, B., Babcock, H., & Zhuang, X. (2010). Breaking the Diffraction Barrier: Super-Resolution Imaging of Cells. *Cell*, *143*(7), 1047–1058. https://doi.org/10.1016/j.cell.2010.12.002

Huang, J., Brenna, C., Khan, A. u. M., Daniele, C., Rudolf, R., Heuveline, V., & Gretz, N. (2019). A cationic near infrared fluorescent agent and ethyl-cinnamate tissue clearing protocol for vascular staining and imaging. *Scientific Reports*, *9*(1), 521. https://doi.org/10.1038/s41598-018-36741-1

Huber, D., Voith von Voithenberg, L., & Kaigala, G. V. (2018). Fluorescence *in situ* hybridization (FISH): History, limitations and what to expect from micro-scale FISH? *Micro and Nano Engineering*, *1*, 15–24. https://doi.org/10.1016/j.mne.2018.10.006

Huisken, J., Swoger, J., Del Bene, F., Wittbrodt, J., & Stelzer, E. H. K. (2004a). Optical Sectioning Deep Inside Live Embryos by Selective Plane Illumination Microscopy. *Science*, *305*(5686), 1007–1009. https://doi.org/10.1126/science.1100035

Huisken, J., Swoger, J., Del Bene, F., Wittbrodt, J., & Stelzer, E. H. K. (2004b). Optical sectioning deep inside live embryos by selective plane illumination microscopy. *Science (New York, N.Y.)*, *305*(5686), 1007–1009. https://doi.org/10.1126/science.1100035

Hwang, W., Raymond, T., McPartland, T., Jeong, S., & Evans, C. L. (2024). Fluorescence Lifetime Multiplexing (FLEX) for simultaneous high dimensional spatial biology in 3D. *Communications Biology*, *7*(1). https://doi.org/10.1038/s42003-024-06702-8

Im, K., Mareninov, S., Diaz, M. F. P., & Yong, W. H. (2019). An introduction to Performing Immunofluorescence Staining. *Methods in molecular biology (Clifton, N.J.)*, *1897*, 299–311. https://doi.org/10.1007/978-1-4939-8935-5_26

Imbert, A., Meuller, F., Walter, T., & Ouyang, W. (2021). https://fish-quant.github.io

Imbert, A., Ouyang, W., Safieddine, A., Coleno, E., Zimmer, C., Bertrand, E., Walter, T., & Mueller, F. (2022). FISH-quant v2: A scalable and modular tool for smFISH image analysis. *RNA*, *28*(6), 786–795. https://doi.org/10.1261/rna.079073.121

Irvin, C. G., & Bates, J. H. (2003). Measuring the lung function in the mouse: The challenge of size. *Respiratory Research*, *4*(1), 4. https://doi.org/10.1186/rr199

IX. An account of Mr. Leeuwenhoek's microscopes. (n.d.). https://doi.org/10.1098/rstl.1739.0085

Jacob, A. M., Lindemann, A. F., Wagenpfeil, J., Geiger, S., Layer, Y. C., Salam, B., Panahabadi, S., Kurt, D., Wintergerst, M. W. M., Schildberg, F. A., Kuetting, D., Attenberger, U. I., Abdullah, Z., & Böhner, A. M. C. (2024). Autofluorescence-based tissue characterization enhances clinical prospects of light-sheet-microscopy. *Scientific Reports*, *14*(1), 18033. https://doi.org/10.1038/s41598-024-67366-2

Jakob, C., Paul-Stansilaus, R., Schwemmle, M., Marquet, R., & Bolte, H. (2022). The influenza A virus genome packaging network — complex, flexible and yet unsolved. *Nucleic Acids Research*, *50*(16), 9023–9038. https://doi.org/10.1093/nar/gkac688

Jelley, J. V. (1983). Cherenkov Radiation: Its Properties, Occurrence, and Uses. In K. C. Smith (Ed.), *Photochemical and Photobiological Reviews: Volume 7* (pp. 275–318). Springer US. https://doi.org/10.1007/978-1-4684-4505-3_6

Jiang, D., Schaefer, N., & Chu, H. W. (2018). Air-liquid interface culture of human and mouse airway epithelial cells. *Mehtods Mol. Biol.*, 91–109. https://doi.org/10.1007/978-1-4939-8570-8_8

Jiang, S., Li, R., Du, L., & Liu, S. (2010). Roles of the hemagglutinin of influenza A virus in viral entry and development of antiviral therapeutics and vaccines. *Protein & Cell*, *1*(4), 342–354. https://doi.org/10.1007/s13238-010-0054-6

Joglekar, A., Prjibelski, A., Mahfouz, A., Collier, P., Lin, S., Schlusche, A. K., Marrocco, J., Williams, S. R., Haase, B., Hayes, A., Chew, J. G., Weisenfeld, N. I., Wong, M. Y., Stein, A. N., Hardwick, S. A., Hunt, T., Wang, Q., Dieterich, C., Bent, Z., . . . Tilgner, H. U. (2021). A spatially resolved brain region- and cell type-specific isoform atlas of the postnatal mouse brain. *Nature Communications*, *12*(1), 463. https://doi.org/10.1038/s41467-020-20343-5

Johnson, C., Exell, J., Lin, Y., Aguilar, J., & Welsher, K. D. (2022). Capturing the start point of the virus-cell interaction with high-speed 3D single-virus tracking. *Nature Methods*, *19*(12), 1642–1652. https://doi.org/10.1038/s41592-022-01672-3

Johnson-Delaney, C. A., & Orosz, S. E. (2011). Ferret Respiratory System: Clinical Anatomy, Physiology, and Disease. *Veterinary Clinics: Exotic Animal Practice*, *14*(2), 357–367. https://doi.org/10.1016/j.cvex.2011.03.001

Juškaitis, R. (2006). Measuring the Real Point Spread Function of High Numerical Aperture Microscope Objective Lenses. In J. B. Pawley (Ed.), *Handbook Of Biological Confocal Microscopy* (pp. 239–250). Springer US. https://doi.org/10.1007/978-0-387-45524-2_11

Kaplan, I. G. (2020). The Pauli Exclusion Principle and the Problems of its Theoretical Substantiation1. *Russian Physics Journal*, *63*(8), 1305–1321. https://doi.org/10.1007/s11182-020-02174-5

Kats, I., Simovic-Lorenz, M., Schreiber, H. S., Sant, P., Mallm, J.-P., Körber, V., Li, A., Velmurugan, P., Heuer, S., Kües, L., Devens, F., Sill, M., Jugold, M., Moustafa, M., Abdollahi, A., Winkler, F., Korshunov, A., Pfister, S. M., Stegle, O., & Ernst, A. (2024). Spatio-temporal transcriptomics of chromothriptic SHH-medulloblastoma identifies multiple genetic clones that resist treatment and drive relapse. *Nature Communications*, *15*(1), 10370. https://doi.org/10.1038/s41467-024-54709-w

Kaufmann, A., Mickoleit, M., Weber, M., & Huisken, J. (2012). Multilayer mounting enables long-term imaging of zebrafish development in a light sheet microscope. *Development*, *139*(17), 3242–3247. https://doi.org/10.1242/dev.082586

Ke, M.-T., Fujimoto, S., & Imai, T. (2013). SeeDB: A simple and morphology-preserving optical clearing agent for neuronal circuit reconstruction. *Nature Neuroscience*, *16*(8), 1154–1161. https://doi.org/10.1038/nn.3447

Keller, P. J., Schmidt, A. D., Wittbrodt, J., & Stelzer, E. H. (2008). Reconstruction of Zebrafish Early Embryonic Development by Scanned Light Sheet Microscopy. *Science*, *322*(5904), 1065–1069. https://doi.org/10.1126/science.1162493

Khan, R., Gul, B., Khan, S., Nisar, H., & Ahmad, I. (2021). Refractive index of biological tissues: Review, measurement techniques, and applications. *Photodiagnosis and Photodynamic Therapy*, *33*, 102192. https://doi.org/10.1016/j.pdpdt.2021.102192

Kilbourne, E., Schulman, J., Schild, G., Schloer, G., Swanson, J., & Bucher, D. (1971). Correlated studies of a recombinant influenza-virus vaccine. i. derivation and characterization of virus and vaccine. *J. Infec. Dis.*, *124*, 449–462. https://doi.org/https://doi.org/10.1093/infdis/124.5.449

Klingberg, A., Hasenberg, A., Ludwig-Portugall, I., Medyukhina, A., Männ, L., Brenzel, A., Engel, D. R., Figge, M. T., Kurts, C., & Gunzer, M. (2017). Fully Automated Evaluation of Total Glomerular Number and Capillary Tuft Size in Nephritic Kidneys Using Lightsheet Microscopy. *Journal of the American Society of Nephrology*, *28*(2), 452–459. https://doi.org/10.1681/ASN.2016020232

Kontny, A., Stoyanov, D., Pavlov, P., Wagner, N., Kolev, N., Zlatarov, A., Kalinov, T., & Tonchev, A. B. (2024). On-slide clearing and imaging of 100-µm-thick histological sections using ethyl cinnamate and epifluorescence. *Folia Medica*, *66*(3), 380–385. https://doi.org/10.3897/folmed.66.e122790

Kubalová, I., Němečková, A., Weisshart, K., Hřibová, E., & Schubert, V. (2021). Comparing Super-Resolution Microscopy Techniques to Analyze Chromosomes. *International Journal of Molecular Sciences*, *22*(4), 1903. https://doi.org/10.3390/ijms22041903

Kutschera, U. (2023). Antonie van Leeuwenhoek (1632–1723): Master of Fleas and Father of Microbiology. *Microorganisms*, *11*(8), 1994. https://doi.org/10.3390/microorganisms11081994

Lakdawala, S. S., Jayaraman, A., Halpin, R. A., Lamirande, E. W., Shih, A. R., Stockwell, T. B., Lin, X., Simenauer, A., Hanson, C. T., Vogel, L., Paskel, M., Minai, M., Moore, I., Orandle, M., Das, S. R., Wentworth, D. E., Sasisekharan, R., & Subbarao, K. (2015). The soft palate is an important site of adaptation for transmissible influenza viruses. *Nature*, *526*(7571), 122–125. https://doi.org/10.1038/nature15379

Laperchia, C., Palomba, M., Seke Etet, P. F., Rodgers, J., Bradley, B., Montague, P., Grassi-Zucconi, G., Kennedy, P. G. E., & Bentivoglio, M. (2016). Trypanosoma brucei Invasion and T-Cell Infiltration of the Brain Parenchyma

in Experimental Sleeping Sickness: Timing and Correlation with Functional Changes. *PLoS Neglected Tropical Diseases*, *10*(12), e0005242. https://doi.org/10.1371/journal.pntd.0005242

Lazaridis, M. (2023). Modelling approaches to particle deposition and clearance in the human respiratory tract. *Air Quality, Atmosphere & Health*, *16*(10), 1989–2002. https://doi.org/10.1007/s11869-023-01386-1

Lebrigand, K., Bergenstråhle, J., Thrane, K., Mollbrink, A., Meletis, K., Barbry, P., Waldmann, R., & Lundeberg, J. (2023). The spatial landscape of gene expression isoforms in tissue sections. *Nucleic Acids Research*, *51*(8), e47. https://doi.org/10.1093/nar/gkad169

Lee, S., Lee, K., Shin, S., & Park, Y. (2017). Generalized image deconvolution by exploiting the transmission matrix of an optical imaging system. *Scientific Reports*, *7*(1), 8961. https://doi.org/10.1038/s41598-017-07937-8

Lelek, M., Gyparaki, M. T., Beliu, G., Schueder, F., Griffié, J., Manley, S., Jungmann, R., Sauer, M., Lakadamyali, M., & Zimmer, C. (2021). Single-molecule localization microscopy. *Nature Reviews Methods Primers*, *1*(1), 39. https://doi.org/10.1038/s43586-021-00038-x

Li, W., Germain, R. N., & Gerner, M. Y. (2019). High-dimensional cell-level analysis of tissues with Ce3D multiplex volume imaging. *Nature protocols*, *14*(6), 1708–1733. https://doi.org/10.1038/s41596-019-0156-4

Li, X., & Wang, C.-Y. (2021). From bulk, single-cell to spatial RNA sequencing. *International Journal of Oral Science*, *13*(1), 36. https://doi.org/10.1038/s41368-021-00146-0

Li, X., Gu, M., Zheng, Q., Gao, R., & Liu, X. (2021). Packaging signal of influenza A virus. *Virology Journal*, *18*, 36. https://doi.org/10.1186/s12985-021-01504-4

Liu, L., Xia, X., Xiang, F., Gao, Y., Li, X., Li, H., & Zheng, W. (2021). F-CUBIC: A rapid optical clearing method optimized by quantitative evaluation. *Biomedical Optics Express*, *13*(1), 237–251. https://doi.org/10.1364/BOE.442976

Liu, Z., Niu, M., Kuang, Z., Ren, N., Wu, S., Cong, L., Wang, X., Sang, Z., Williams, C., & Yang, Y. (2022). High resolution detectors for whole-body PET scanners by using dual-ended readout. *EJNMMI Physics*, *9*(1), 29. https://doi.org/10.1186/s40658-022-00460-4

Long, Y., Zheng, X., Wang, Y., Du, P., Li, X., Chen, J., & Shao, Y. (2025). Recent advances in performance enhancement technologies for structured illumination microscopy: A comprehensive review. *Optics and Lasers in Engineering*. https://doi.org/https://doi.org/10.1016/j.optlaseng.2025.109203

Luckheeram, R. V., Zhou, R., Verma, A. D., & Xia, B. (2012). CD4+T Cells: Differentiation and Functions. *Clinical and Developmental Immunology*, *2012*, 925135. https://doi.org/10.1155/2012/925135

Luker, K. E., & Luker, G. D. (2010). Bioluminescence Imaging of Reporter Mice for Studies of Infection and Inflammation. *Antiviral research*, *86*(1), 93–100. https://doi.org/10.1016/j.antiviral.2010.02.002

Machado, H., Bizarra-Rebelo, T., Costa-Sequeira, M., Trindade, S., Carvalho, T., Rijo-Ferreira, F., Rentroia-Pacheco, B., Serre, K., & Figueiredo, L. M. (2021). Trypanosoma brucei triggers a broad immune response in the adipose tissue. *PLoS pathogens*, *17*(9), e1009933. https://doi.org/10.1371/journal.ppat.1009933

MacLean, L., Reiber, H., Kennedy, P. G. E., & Sternberg, J. M. (2012). Stage Progression and Neurological Symptoms in Trypanosoma brucei rhodesiense Sleeping Sickness: Role of the CNS Inflammatory Response. *PLoS Neglected Tropical Diseases*, *6*(10), e1857. https://doi.org/10.1371/journal.pntd.0001857

Maillard, J., Klehs, K., Rumble, C., Vauthey, E., Heilemann, M., & Fürstenberg, A. (2021). Universal quenching of common fluorescent probes by water and alcohols. *Chemical Science*, *12*(4), 1352–1362. https://doi.org/10.1039/D0SC05431C

Mansell, A., & Tate, M. D. (2017). In Vivo Infection Model of Severe Influenza A Virus. *Inflammation and Cancer*, *1725*, 91–99. https://doi.org/10.1007/978-1-4939-7568-6_8

Martynov, V. I., Pakhomov, A. A., Popova, N. V., Deyev, I. E., & Petrenko, A. G. (2016). Synthetic Fluorophores for Visualizing Biomolecules in Living Systems. *Acta Naturae*, *8*(4), 33–46. Retrieved July 8, 2025, from https://www.ncbi.nlm.nih.gov/pmc/articles/PMC5199205/

Marx, V. (2021). Method of the Year: Spatially resolved transcriptomics. *Nature Methods*, *18*(1), 9–14. https://doi.org/10.1038/s41592-020-01033-y

Marx, V. (2023). Method of the year: Long-read sequencing. *Nature Methods*, *20*(1), 6–11. https://doi.org/10.1038/s41592-022-01730-w

Mason, D. Y., Cordell, J. L., Brown, M. H., Borst, J., Jones, M., Pulford, K., Jaffe, E., Ralfkiaer, E., Dallenbach, F., & Stein, H. (1995). CD79a: A novel marker for B-cell neoplasms in routinely processed tissue samples. *Blood*, *86*(4), 1453–1459.

Masselink, W., Reumann, D., Murawala, P., Pasierbek, P., Taniguchi, Y., Bonnay, F., Meixner, K., Knoblich, J. A., & Tanaka, E. M. (2019). Broad applicability of a streamlined ethyl cinnamate-based clearing procedure. *Development (Cambridge, England)*, *146*(3), dev166884. https://doi.org/10.1242/dev.166884

Masselink, W., & Tanaka, E. M. (2023). Ethyl Cinnamate-Based Tissue Clearing Strategies. *Methods in Molecular Biology (Clifton, N.J.)*, *2562*, 123–133. https://doi.org/10.1007/978-1-0716-2659-7_7

Matthews, K. R. (2005). The developmental cell biology of Trypanosoma brucei. *Journal of cell science*, *118*(Pt 2), 283–290. https://doi.org/10.1242/jcs.01649

Maynard, K. R., Tippani, M., Takahashi, Y., Phan, B. N., Hyde, T. M., Jaffe, A. E., & Martinowich, K. (2020). Dotdotdot: An automated approach to quantify multiplex single molecule fluorescent in situ hybridization (smFISH) images

in complex tissues. *Nucleic Acids Research*, *48*(11), e66. https://doi.org/10.1093/nar/gkaa312

McAuley, J. L., Gilbertson, B. P., Trifkovic, S., Brown, L. E., & McKimm-Breschkin, J. L. (2019). Influenza Virus Neuraminidase Structure and Functions. *Frontiers in Microbiology*, *10*. https://doi.org/10.3389/fmicb.2019.00039

McConnell, G., & Amos, W. B. (2018). Application of the Mesolens for subcellular resolution imaging of intact larval and whole adult Drosophila. *Journal of Microscopy*, *270*(2), 252–258. https://doi.org/10.1111/jmi.12693

McConnell, G., Trägårdh, J., Amor, R., Dempster, J., Reid, E., & Amos, W. B. (2016). A novel optical microscope for imaging large embryos and tissue volumes with sub-cellular resolution throughout (M. E. Bronner, Ed.). *eLife*, *5*, e18659. https://doi.org/10.7554/eLife.18659

McLatchie, A. P., Burrell-Saward, H., Myburgh, E., Lewis, M. D., Ward, T. H., Mottram, J. C., Croft, S. L., Kelly, J. M., & Taylor, M. C. (2013). Highly Sensitive In Vivo Imaging of Trypanosoma brucei Expressing "Red-Shifted" Luciferase. *PLoS Neglected Tropical Diseases*, *7*(11), e2571. https://doi.org/10.1371/journal.pntd.0002571

Miles, R. B., Lempert, W. R., & Forkey, J. N. (2001). Laser Rayleigh scattering. *Measurement Science and Technology*, *12*(5), R33. https://doi.org/10.1088/0957-0233/12/5/201

MiltenyiBiotechnology. (2023). Miltenyi ultramicroscope blaze user manual. *Miltenyi User Manual*, 56.

MiltenyiBiotechnology. (2025). Miltenyi ultranmicrscope blaze product specifications [Accessed 22/05/2025]. https://www.miltenyibiotec.com/GB-en/products/ultramicroscope-blaze.html

Moerner, W. E., & Kador, L. (1989). Optical detection and spectroscopy of single molecules in a solid. *Physical Review Letters*. https://doi.org/https://doi.org/10.1103/PhysRevLett.62.2535

Moody, A. S., Dayton, P. A., & Zamboni, W. C. (2021). Imaging methods to evaluate tumor microenvironment factors affecting nanoparticle drug de-

livery and antitumor response. *Cancer Drug Resistance*, *4*(2), 382–413. https://doi.org/10.20517/cdr.2020.94

Moses, W. W. (2011). Fundamental Limits of Spatial Resolution in PET. *Nuclear instruments & methods in physics research. Section A, Accelerators, spectrometers, detectors and associated equipment*, *648 Supplement 1*, S236–S240. https://doi.org/10.1016/j.nima.2010.11.092

Mostafa, A., Nogales, A., & Martinez-Sobrido, L. (2025). Highly pathogenic avian influenza H5N1 in the United States: Recent incursions and spillover to cattle. *npj Viruses*, *3*(1), 54. https://doi.org/10.1038/s44298-025-00138-5

Mothes, R., Pascual-Reguant, A., Koehler, R., Liebeskind, J., Liebheit, A., Bauherr, S., Philipsen, L., Dittmayer, C., Laue, M., von Manitius, R., Elezkurtaj, S., Durek, P., Heinrich, F., Heinz, G. A., Guerra, G. M., Obermayer, B., Meinhardt, J., Ihlow, J., Radke, J., ... Hauser, A. E. (2023). Distinct tissue niches direct lung immunopathology via CCL18 and CCL21 in severe COVID-19. *Nature Communications*, *14*(1), 791. https://doi.org/10.1038/s41467-023-36333-2

Mueller, F., Senecal, A., Tantale, K., Marie-Nelly, H., Ly, N., Collin, O., Basyuk, E., Bertrand, E., Darzacq, X., & Zimmer, C. (2013). Fish-quant: Automatic counting of transcripts in 3d fish images. *Nature Methods*. https://doi.org/https://doi.org/10.1038/nmeth.2406

Murakami, T. C., Mano, T., Saikawa, S., Horiguchi, S. A., Shigeta, D., Baba, K., Sekiya, H., Shimizu, Y., Tanaka, K. F., Kiyonari, H., Iino, M., Mochizuki, H., Tainaka, K., & Ueda, H. R. (2018). A three-dimensional single-cell-resolution whole-brain atlas using CUBIC-X expansion microscopy and tissue clearing. *Nature Neuroscience*, *21*(4), 625–637. https://doi.org/10.1038/s41593-018-0109-1

Neuman, K., Chadd, E., Liou, G., Bergman, K., & Block, S. (1999). Characterization of photodamage to escherichia coli in optical traps. *Biophysical Journal*, *77*(5), 2856–2863. https://doi.org/10.1016/S0006-3495(99)77117-1

Neupane, B., Ligler, F. S., & Wang, G. (2014). Review of recent developments in stimulated emission depletion microscopy: Applications on cell imaging. *Journal of Biomedical Optics*, *19*(8), 080901. https://doi.org/10.1117/1.JBO.19.8.080901

Nikolić, M. Z., Sun, D., & Rawlins, E. L. (2018). Human lung development: Recent progress and new challenges. *Development*, *145*(16), dev163485. https://doi.org/10.1242/dev.163485

Nobusawa, E., & Sato, K. (2006). Comparison of the Mutation Rates of Human Influenza A and B Viruses. *Journal of Virology*, *80*(7), 3675–3678. https://doi.org/10.1128/JVI.80.7.3675-3678.2006

Oethinger, M. D., & Campbell, S. M. (2009, January). Chapter 3 - Infection and Host Response. In W. B. Coleman & G. J. Tsongalis (Eds.), *Molecular Pathology* (pp. 41–61). Academic Press. https://doi.org/10.1016/B978-0-12-374419-7.00003-2

Petrova, V. N., & Russell, C. A. (2018). The evolution of seasonal influenza viruses. *Nature Reviews Microbiology*, *16*(1), 47–60. https://doi.org/10.1038/nrmicro.2017.118

Pirillo, C., Al Khalidi, S., Sims, A., Devlin, R., Zhao, H., Pinto, R., Jasim, S., Shearer, P. A., Shergold, A. L., Donnelly, H., Bravo-Blas, A., Loney, C., Perona-Wright, G., Hutchinson, E., & Roberts, E. W. (2023). Cotransfer of antigen and contextual information harmonizes peripheral and lymph node conventional dendritic cell activation. *Science Immunology*, *8*(85), eadg8249. https://doi.org/10.1126/sciimmunol.adg8249

Platkov, M., Tirosh, R., Kaufman, M., Zurgil, N., & Deutsch, M. (2014). Photobleaching of fluorescein as a probe for oxidative stress in single cells. *Photochem. Photobiol. B*, *140*, 306–14. https://doi.org/10.1016/j.jphotobiol.2014.08.016

Ponte-Sucre, A. (2016). An Overview of Trypanosoma brucei Infections: An Intense Host–Parasite Interaction. *Frontiers in Microbiology*, *7*, 2126. https://doi.org/10.3389/fmicb.2016.02126

Poologasundarampillai, G., Haweet, A., Jayash, S. N., Morgan, G., Moore, J. E., & Candeo, A. (2021). Real-time imaging and analysis of cell-hydrogel interplay within an extrusion-bioprinting capillary. *Bioprinting*, *23*, e00144. https://doi.org/10.1016/j.bprint.2021.e00144

Prescott, R. A., Pankow, A. P., Vries, M., Crosse, K. M., Patel, R. S., Alu, M., Loomis, C., Torres, V., Koralov, S., Ivanova, E., Dittmann, M., & Rosenberg, B. R. (2023). A comparative study of in vitro air–liquid interface culture models of the human airway epithelium evaluating cellular heterogeneity and gene expression at single cell resolution. *Respiratory Research*, *24*, 2325–32. https://doi.org/10.1186/s12931-023-02514-2

Qiu, M., Huang, S., Luo, C., Wu, Z., Liang, B., Huang, H., Ci, Z., Zhang, D., Han, L., & Lin, J. (2021). Pharmacological and clinical application of heparin progress: An essential drug for modern medicine. *Biomedicine & Pharmacotherapy*, *139*, 111561. https://doi.org/10.1016/j.biopha.2021.111561

Qiu, X., Zhong, P., Yue, L., Li, C., Yun, Z., Si, G., Li, M., Chen, Z., Tan, Y., & Bao, P. (2024). Spatial transcriptomic sequencing reveals immune microenvironment features of *Mycobacterium tuberculosis* granulomas in lung and omentum. *Theranostics*, *14*(16), 6185–6201. https://doi.org/10.7150/thno.99038

Quintana, J. F., Chandrasegaran, P., Sinton, M. C., Briggs, E. M., Otto, T. D., Heslop, R., Bentley-Abbot, C., Loney, C., de Lecea, L., Mabbott, N. A., & MacLeod, A. (2022). Single cell and spatial transcriptomic analyses reveal microglia-plasma cell crosstalk in the brain during Trypanosoma brucei infection. *Nature Communications*, *13*(1), 5752. https://doi.org/10.1038/s41467-022-33542-z

Raj, A., van den Bogaard, P., Rifkin, S. A., van Oudenaarden, A., & Tyagi, S. (2008). Imaging individual mRNA molecules using multiple singly labeled probes. *Nature methods*, *5*(10), 877–879. https://doi.org/10.1038/nmeth.1253

Rani, A. Q., Nurmemet, D., Liffick, J., Khan, A., Mitchell, D., Li, J., Zhao, B., & Liu, X. (2023). Conditional cell reprogramming and air–liquid interface modeling life cycle of oncogenic viruses (hpv and ebv) in epithelial cells and virus-associated human carcinomas. *Viruses*, *6*. https://doi.org/10.3390/v15061388

Rao, A., Barkley, D., França, G. S., & Yanai, I. (2021). Exploring tissue architecture using spatial transcriptomics. *Nature*, *596*(7871), 211–220. https://doi.org/10.1038/s41586-021-03634-9

Reback, J., Jbrockmendel, McKinney, W., Van Den Bossche, J., Roeschke, M., Augspurger, T., Hawkins, S., Cloud, P., Gfyoung, Sinhrks, Hoefler, P., Klein, A., Petersen, T., Tratner, J., She, C., Ayd, W., Naveh, S., Darbyshire, J., Shadrach, R., ... Li, T. (2022, June). Pandas-dev/pandas: Pandas 1.4.3. https://doi.org/10.5281/ZENODO.3509134

Ren, Z., Wu, Y., Wang, Z., Hu, Y., Lu, J., Liu, J., Chen, Y., & Yao, M. (2021). CUBIC-plus: An optimized method for rapid tissue clearing and decolorization. *Biochemical and Biophysical Research Communications*, *568*, 116–123. https://doi.org/10.1016/j.bbrc.2021.06.075

Renier, N., Wu, Z., Simon, D. J., Yang, J., Ariel, P., & Tessier-Lavigne, M. (2014). iDISCO: A Simple, Rapid Method to Immunolabel Large Tissue Samples for Volume Imaging. *Cell*, *159*(4), 896–910. https://doi.org/10.1016/j.cell.2014.10.010

Reuman, P., Ayoub, E., & Small, P. (1983). Influenza infection in the infant mouse. *Pediatr Res*, *17*, 338–343. https://doi.org/https://doi.org/10.1203/00006450-198305000-00006

Ribarska, T., Bjørnstad, P. M., Sundaram, A. Y. M., & Gilfillan, G. D. (2022). Optimization of enzymatic fragmentation is crucial to maximize genome coverage: A comparison of library preparation methods for Illumina sequencing. *BMC Genomics*, *23*(1), 92. https://doi.org/10.1186/s12864-022-08316-y

Richard, M., van den Brand, J. M. A., Bestebroer, T. M., Lexmond, P., de Meulder, D., Fouchier, R. A. M., Lowen, A. C., & Herfst, S. (2020). Influenza A

viruses are transmitted via the air from the nasal respiratory epithelium of ferrets. *Nature Communications*, *11*, 766. https://doi.org/10.1038/s41467-020-14626-0

Richardson, D. S., & Lichtman, J. W. (2015). Clarifying Tissue Clearing. *Cell*, *162*(2), 246–257. https://doi.org/10.1016/j.cell.2015.06.067

Rodriguez-Frandsen, A., Martin-Sancho, L., Gounder, A. P., Chang, M. W., Liu, W.-C., De Jesus, P. D., von Recum-Knepper, J., Dutra, M. S., Huffmaster, N. J., Chavarria, M., Mena, I., Riva, L., Nguyen, C. B., Dobariya, S., Herbert, K. M., Benner, C., Albrecht, R. A., García-Sastre, A., & Chanda, S. K. (2020). Viral Determinants in H5N1 Influenza A Virus Enable Productive Infection of HeLa Cells. *Journal of Virology*, *94*(4), e01410–19. https://doi.org/10.1128/JVI.01410-19

Rodriguez-Gatica, J. E., Iefremova, V., Sokhranyaeva, L., Yeung, S. W. C. A., Breitkreuz, Y., Brüstle, O., Schwarz, M. K., & Kubitscheck, U. (2022). Imaging three-dimensional brain organoid architecture from meso- to nanoscale across development. *Development*, *149*(20), dev200439. https://doi.org/10.1242/dev.200439

Rong, J., Haider, A., Jeppesen, T. E., Josephson, L., & Liang, S. H. (2023). Radiochemistry for positron emission tomography. *Nature Communications*, *14*(1), 3257. https://doi.org/10.1038/s41467-023-36377-4

Rooney, L. M., Bottura, B., Baxter, K., Amos, W. B., Hoskisson, P. A., & McConnell, G. (2024). Addressing multiscale microbial challenges using the Mesolens. *Journal of Microscopy*, *296*(2), 139–144. https://doi.org/10.1111/jmi.13172

Rust, M., Bates, M., & Zhuang, X. (2006). Sub-diffraction-limit imaging by stochastic optical reconstruction microscopy (storm). *Nature Methods*. https://doi.org/https://doi.org/10.1038/nmeth929

Sandell, J. L., & Zhu, T. C. (2011). A review of in-vivo optical properties of human tissues and its impact on PDT. *Journal of Biophotonics*, *4*(11-12), 773–787. https://doi.org/10.1002/jbio.201100062

Sarkar, D., Kang, J., Wassie, A. T., Schroeder, M. E., Peng, Z., Tarr, T. B., Tang, A.-H., Niederst, E. D., Young, J. Z., Su, H., Park, D., Yin, P., Tsai, L.-H., Blanpied, T. A., & Boyden, E. S. (2022). Revealing nanostructures in brain tissue via protein decrowding by iterative expansion microscopy. *Nature Biomedical Engineering*, *6*(9), 1057–1073. https://doi.org/10.1038/s41551-022-00912-3

Scherer, K. M., Manton, J. D., Soh, T. K., Mascheroni, L., Connor, V., Crump, C. M., & Kaminski, C. F. (2021). A fluorescent reporter system enables spatiotemporal analysis of host cell modification during herpes simplex virus-1 replication. *Journal of Biological Chemistry*, *296*, 100236. https://doi.org/10.1074/jbc.RA120.016571

Schmidt, R., Engelhardt, J., & Lang, M. (2013). 4pi microscopy. *Methods Mol Biol*. https://doi.org/10.1007/978-1-62703-137-0_3

Schmidt, R., Wurm, C. A., Jakobs, S., Engelhardt, J., Egner, A., & Hell, S. W. (2008). Spherical nanosized focal spot unravels the interior of cells. *Nature Methods*, *5*(6), 539–544. https://doi.org/10.1038/nmeth.1214

Schneider, F., Sych, T., Eggeling, C., & Sezgin, E. (2021). Influence of nanobody binding on fluorescence emission, mobility, and organization of GFP-tagged proteins. *iScience*, *24*(1), 101891. https://doi.org/10.1016/j.isci.2020.101891

Schönbach, C. (2013). Respiratory Tract, Upper and Lower. In *Encyclopedia of Systems Biology* (pp. 1851–1852). Springer, New York, NY. https://doi.org/10.1007/978-1-4419-9863-7_748

Schroeder, A., Mueller, O., Stocker, S., Salowsky, R., Leiber, M., Gassman, M., Lightfoot, S., Menzel, W., Granzow, M., & Ragg, T. (2006). The rin: An rna integrity number for assigning integrity values to rna measurements. *BMC Mol. Biol.*, *7*. https://doi.org/10.1186/1471-2199-7-3

Schwarz, M. K., Scherbarth, A., Sprengel, R., Engelhardt, J., Theer, P., & Giese, G. (2015). Fluorescent-Protein Stabilization and High-Resolution Imaging

of Cleared, Intact Mouse Brains. *PLOS ONE*, *10*(5), e0124650. https://doi.org/10.1371/journal.pone.0124650

Scientific, E. (2025). White paper: Silicone immersion objectives answer the call for higher resolution. https://evidentscientific.com/en/learn/white-papers/silicone-immersion-objectives-for-higher-resolution

Shariati B. K., B., Ansari, M. A., Khatami, S. S., & Tuchin, V. V. (2023). Multimodal optical clearing to minimize light attenuation in biological tissues. *Scientific Reports*, *13*(1), 21509. https://doi.org/10.1038/s41598-023-48876-x

Sharma-Chawla, N., Sender, V., Kershaw, O., Gruber, A. D., Volckmar, J., Henriques-Normark, B., Stegemann-Koniszewski, S., & Bruder, D. (2016). Influenza A Virus Infection Predisposes Hosts to Secondary Infection with Different Streptococcus pneumoniae Serotypes with Similar Outcome but Serotype-Specific Manifestation. *Infection and Immunity*, *84*(12), 3445–3457. https://doi.org/10.1128/IAI.00422-16

Shnaider, T., & Pristyazhnyuk, I. (2021). CLARITY and Light-Sheet microscopy sample preparation in application to human cerebral organoids. *Vavilov Journal of Genetics and Breeding*, *25*(8), 889–895. https://doi.org/10.18699/VJ21.103

Šíma, M., Havelková, H., Quan, L., Svobodová, M., Jarošíková, T., Vojtíšková, J., Stassen, A. P. M., Demant, P., & Lipoldová, M. (2011). Genetic Control of Resistance to Trypanosoma brucei brucei Infection in Mice. *PLoS Neglected Tropical Diseases*, *5*(6), e1173. https://doi.org/10.1371/journal.pntd.0001173

Simpson, J., & Hawes, P. C. (2022). Preparation of Immunofluorescently Labeled Tissue Sections for Imaging at Low and High Magnifications in the Confocal Microscope. *Methods in Molecular Biology (Clifton, N.J.)*, *2503*, 51–61. https://doi.org/10.1007/978-1-0716-2333-6_3

Sims, A. (2024). Phd thesis: Respiratory virus coinfection and superinfection exclusion. *University of Glasgow, UK*.

Sims, A., Tornaletti, L. B., Jasim, S., Pirillo, C., Devlin, R., Hirst, J., Loney, C., Wojtus, J., Sloan, E., Thorley, L., Boutell, C., Roberts, E., & Hutchinson, E. (2022). *Superinfection exclusion creates spatially distinct influenza virus population* (tech. rep.). University of Glasgow. https://doi.org/10.1101/2022.06.06.494939

Smith, F. W., Hutchison, J. M., Mallard, J. R., Johnson, G., Redpath, T. W., Selbie, R. D., Reid, A., & Smith, C. C. (1981). Oesophageal carcinoma demonstrated by whole-body nuclear magnetic resonance imaging. *British Medical Journal (Clinical Research Ed.)*, *282*(6263), 510–512. https://doi.org/10.1136/bmj.282.6263.510

Soeller, C., & Cannell, M. B. (1999). Two-photon microscopy: Imaging in scattering samples and three-dimensionally resolved flash photolysis. *Microscopy Research and Technique*, *47*(3), 182–195. https://doi.org/10.1002/(SICI)1097-0029(19991101)47:3⟨182::AID-JEMT4⟩3.0.CO;2-4

Sounart, H., Lázár, E., Masarapu, Y., Wu, J., Várkonyi, T., Glasz, T., Kiss, A., Borgström, E., Hill, A., Jurek, A., Niesnerová, A., Druid, H., Bergmann, O., & Giacomello, S. (2022, March). Dual spatially resolved transcriptomics for SARS-CoV-2 host-pathogen colocalization studies in humans. https://doi.org/10.1101/2022.03.14.484288

Splateholz, W. (1914). On the translucency of human and animal specimens and its theoretical conditions, with appendix: On bone staining. *S. Hirzel*.

Subiran Adrados, C., Yu, Q., Bolaños Castro, L. A., Rodriguez Cabrera, L. A., & Yun, M. H. (2021). Salamander-Eci: An optical clearing protocol for the three-dimensional exploration of regeneration. *Developmental Dynamics*, *250*(6), 902–915. https://doi.org/10.1002/dvdy.264

Suki, B., Stamenović, D., & Hubmayr, R. (2011). Lung Parenchymal Mechanics. In *Comprehensive Physiology* (pp. 1317–1351). John Wiley & Sons, Ltd. https://doi.org/10.1002/cphy.c100033

Susaki, E. A., Tainaka, K., Perrin, D., Kishino, F., Tawara, T., Watanabe, T. M., Yokoyama, C., Onoe, H., Eguchi, M., Yamaguchi, S., Abe, T., Kiyonari,

H., Shimizu, Y., Miyawaki, A., Yokota, H., & Ueda, H. R. (2014). Whole-Brain Imaging with Single-Cell Resolution Using Chemical Cocktails and Computational Analysis. *Cell*, *157*(3), 726–739. https://doi.org/10.1016/j.cell.2014.03.042

Tan, G., Opitz, L., Schlapbach, R., & Rehrauer, H. (2019). Long fragments achieve lower base quality in Illumina paired-end sequencing. *Scientific Reports*, *9*(1), 2856. https://doi.org/10.1038/s41598-019-39076-7

Toseland, C. P. (2013). Fluorescent labeling and modification of proteins. *Journal of Chemical Biology*, *6*(3), 85–95. https://doi.org/10.1007/s12154-013-0094-5

Trombetta, C. M., Kistner, O., Montomoli, E., Viviani, S., & Marchi, S. (2022). Influenza Viruses and Vaccines: The Role of Vaccine Effectiveness Studies for Evaluation of the Benefits of Influenza Vaccines. *Vaccines*, *10*(5), 714. https://doi.org/10.3390/vaccines10050714

Trotter, J., Pantel, A. R., Teo, B.-K. K., Escorcia, F. E., Li, T., Pryma, D. A., & Taunk, N. K. (2023). Positron Emission Tomography (PET)/Computed Tomography (CT) Imaging in Radiation Therapy Treatment Planning: A Review of PET Imaging Tracers and Methods to Incorporate PET/CT. *Advances in Radiation Oncology*, *8*(5), 101212. https://doi.org/10.1016/j.adro.2023.101212

Tsanov, N., Samacoits, A., Chouaib, R., Traboulsi, A.-M., Gostan, T., Weber, C., Zimmer, C., Zibara, K., Walter, T., Peter, M., Bertrand, E., & Mueller, F. (2016). Smifish and fish-quant – a flexible single rna detection approach with super-resolution capability. *Nucleic Acids Res*. https://doi.org/10.1093/nar/gkw784

Tsurui, H., Nishimura, H., Hattori, S., Hirose, S., Okumura, K., & Shirai, T. (2000). Seven-color Fluorescence Imaging of Tissue Samples Based on Fourier Spectroscopy and Singular Value Decomposition. *J. Histochem. Cytochem.*, *48*. https://doi.org/10.1177/002215540004800509

Tyson, A. L., & Margrie, T. W. (2022). Mesoscale microscopy and image analysis tools for understanding the brain. *Progress in Biophysics and Molecular Biology*, *168*, 81–93. https://doi.org/10.1016/j.pbiomolbio.2021.06.013

Ugolini, F., Baroni, G., Nassini, R., De Logu, F., & Massi, D. (2021). A fast and automated melanin-bleaching method for histopathologic evaluation of pigmented melanoma tissues. *Appl. Immunohistochem. Mol. Morphol.*, *4*, 311–16. https://doi.org/10.1097/PAI.0000000000001004

Van Den Abbeele, J., Claes, Y., Van Bockstaele, D., Le Ray, D., & Coosemans, M. (1999). *Trypanosoma brucei* spp. development in the tsetse fly: Characterization of the post-mesocyclic stages in the foregut and proboscis. *Parasitology*, *118*(5), 469–478. https://doi.org/10.1017/S0031182099004217

Van Den Abbeele, J., Caljon, G., De Ridder, K., De Baetselier, P., & Coosemans, M. (2010). Trypanosoma brucei Modifies the Tsetse Salivary Composition, Altering the Fly Feeding Behavior That Favors Parasite Transmission. *PLoS Pathogens*, *6*(6), e1000926. https://doi.org/10.1371/journal.ppat.1000926

Van Leeuwenhoek, A. (1675). *Observations*. Bloomsbury Publishing.

Varble, A., Albrecht, R. A., Backes, S., Crumiller, M., Bouvier, N. M., Sachs, D., García-Sastre, A., & tenOever, B. R. (2014). Influenza A virus transmission bottlenecks are defined by infection route and recipient host. *Cell host & microbe*, *16*(5), 691–700. https://doi.org/10.1016/j.chom.2014.09.020

Vidarsson, G., Dekkers, G., & Rispens, T. (2014). IgG Subclasses and Allotypes: From Structure to Effector Functions. *Frontiers in Immunology*, *5*, 520. https://doi.org/10.3389/fimmu.2014.00520

Wang, D., Cheung, A., Mawdsley, G. E., Liu, K., Yerofeyeva, Y., Thu, K. L., Yoon, J.-Y., & Yaffe, M. J. (2024). A modified bleaching method for multiplex immunofluorescence staining of ffpe tissue sections. *Appl. Immunohistochem. Mol. Morphol.*, *10*, 447–52. https://doi.org/10.1097/PAI.0000000000001228

Wang, F., Liu, G., Lu, Y., Hlasny, M., Liu, Q., & Zhou, Y. (2020). Acquisition of Avian-Origin PB1 Facilitates Viral RNA Synthesis by the 2009 Pandemic H1N1 Virus Polymerase. *Viruses*, *12*(3), 266. https://doi.org/10.3390/v12030266

Wang, F., Flanagan, J., Su, N., Wang, L.-C., Bui, S., Nielson, A., Wu, X., Vo, H.-T., Ma, X.-J., & Luo, Y. (2012). RNAscope: A novel in situ RNA analysis platform for formalin-fixed, paraffin-embedded tissues. *The Journal of Molecular Diagnostics : JMD*, *14*(1), 22–29. https://doi.org/10.1016/j.jmoldx.2011.08.002

Wang, H. (2011). A Kind of Performance Improvement of Hamming Code. In M. Zhu (Ed.), *Information and Management Engineering* (pp. 315–318). Springer. https://doi.org/10.1007/978-3-642-24097-3_47

Wang, Q., Bechet, N. B., & Lindstedt, S. (2023). Automated Vibratome Sectioning of Agarose-Embedded Lung Tissue for Multiplex Fluorescence Imaging. *Journal of Visualized Experiments: JoVE*, *200*. https://doi.org/10.3791/65943

Wang, S., Li, B., & Zhang, F. (2020). Molecular Fluorophores for Deep-Tissue Bioimaging. *ACS Central Science*, *6*(8), 1302–1316. https://doi.org/10.1021/acscentsci.0c00544

Waskom, M. (2021). Seaborn: Statistical data visualization. *Journal of Open Source Software*, *6*(60), 3021. https://doi.org/10.21105/joss.03021

Wassie, A. T., Zhao, Y., & Boyden, E. S. (2019). Expansion microscopy: Principles and uses in biological research. *Nature Methods*, *16*(1), 33–41. https://doi.org/10.1038/s41592-018-0219-4

Weisshart, K. (2025). The Basic Principle of Airyscanning [Accessed: 20/07/2025].

Wolf, Y., Yona, S., Kim, K.-W., & Jung, S. (2013). Microglia, seen from the CX3CR1 angle. *Frontiers in Cellular Neuroscience*, *7*, 26. https://doi.org/10.3389/fncel.2013.00026

Wollman, A. J. M., Nudd, R., Hedlund, E. G., & Leake, M. C. (2015). From Animaculum to single molecules: 300 years of the light microscope. *Open Biology*, *5*(4), 150019. https://doi.org/10.1098/rsob.150019

Worobey, M., Han, G.-Z., & Rambaut, A. (2014). Genesis and pathogenesis of the 1918 pandemic H1N1 influenza A virus. *Proceedings of the National Academy of Sciences*, *111*(22), 8107–8112. https://doi.org/10.1073/pnas.1324197111

Wu, Z., Xu, X., & Xi, P. (2021). Stimulated emission depletion microscopy for biological imaging in four dimensions: A review. *Microscopy Research and Technique*, *84*(9), 1947–1958. https://doi.org/10.1002/jemt.23750

Yang, B., Lange, M., Millett-Sikking, A., Zhao, X., Bragantini, J., VijayKumar, S., Kamb, M., Gómez-Sjöberg, R., Solak, A. C., Wang, W., Kobayashi, H., McCarroll, M. N., Whitehead, L. W., Fiolka, R. P., Kornberg, T. B., York, A. G., & Royer, L. A. (2022). DaXi—high-resolution, large imaging volume and multi-view single-objective light-sheet microscopy. *Nature Methods*, *19*(4), 461–469. https://doi.org/10.1038/s41592-022-01417-2

Young, T. (1802). On the theory of light and colours (the 1801 bakerian lecture). *Philosophical Transactions of the Royal Society*, *92*, 12–48.

Yu, C.-C., Barry, N. C., Wassie, A. T., Sinha, A., Bhattacharya, A., Asano, S., Zhang, C., Chen, F., Hobert, O., Goodman, M. B., Haspel, G., & Boyden, E. S. (2020). Expansion microscopy of C. elegans (A. F. Dernburg & D. Ron, Eds.). *eLife*, *9*, e46249. https://doi.org/10.7554/eLife.46249

Yu, T., Zhu, J., Li, D., & Zhu, D. (2021). Physical and chemical mechanisms of tissue optical clearing. *iScience*, *24*(3), 102178. https://doi.org/10.1016/j.isci.2021.102178

Zheng, Q., Jockusch, S., Zhou, Z., & Blanchard, S. C. (2014). The contribution of reactive oxygen species to the photobleaching of organic fluorophores. *Photochemistry and Photobiology*, *90*(2), 448–454. https://doi.org/10.1111/php.12204

Zhou, J., Lin, J., Zhou, C., Deng, X., & Xia, B. (2011). Cytotoxicity of red fluorescent protein DsRed is associated with the suppression of Bcl-xL translation. *FEBS letters*, *585*(5), 821–827. https://doi.org/10.1016/j.febslet.2011.02.013

Zhuang, Y., & Shi, X. (2023). Expansion microscopy: A chemical approach for super-resolution microscopy. *Current Opinion in Structural Biology*, *81*, 102614. https://doi.org/10.1016/j.sbi.2023.102614

Ziegler, P., Tian, Y., Bai, Y., Abrahamsson, S., Bäckerholm, A., Reznik, A. S., Green, A., Moore, J. A., Lee, S. E., Myerburg, M. M., Park, H. J., Tang, K.-W., & Shair, K. H. Y. (2021). A primary nasopharyngeal three-dimensional air-liquid interface cell culture model of the pseudostratified epithelium reveals differential donor- and cell type-specific susceptibility to epstein-barr virus infection. *PLOS Path.*, *17*. https://doi.org/10.1371/journal.ppat.1009041